Reactor Safety Research Quarterly Report January-March 1983 Volume 25

Reactor Safety Research Department 6420

Prepared for
U. S. NUCLEAR REGULATORY COMMISSION

REACTOR SAFETY RESEARCH
QUARTERLY REPORT
January-March 1983

Reactor Safety Research Program
Sandia National Laboratories
Albuquerque, NM 87185

Printed: July 1984

APPROVED:

Jack V Walker

Manager, Reactor Safety Research

Clifton Ruzer

Director, Nuclear Fuel Cycle Programs

Sandia National Laboratories
Albuquerque, New Mexico 87185
operated by
Sandia Corporation
for the
U.S. Department of Energy

FOREWORD

Sandia National Laboratories is conducting, under USNRC's sponsorship, phenomenological research related to the safety of commercial nuclear power reactors.

The overall objective of this work is to provide NRC a comprehensive data base essential to (1) defining key safety issues, (2) understanding risk-significant accident sequences, (3) developing and verifying models used in safety assessments, and (4) assuring the public that power reactor systems will not be licensed and placed in commercial service in the United States without appropriate consideration being given to their effects on health and safety.

Together with other programs, the Sandia effort is directed at assuring the soundness of the technology base upon which licensing decisions are made.
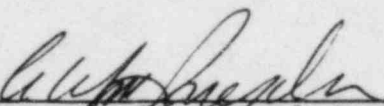
This report describes progress in a number of activities dealing with current safety issues relevant to both light water and breeder reactors. The work includes a broad range of experiments to simulate accidental conditions to provide the required data base to understand important accident sequences and to serve as a basis for development and verification of the complex computer simulation models and codes used in accident analysis and licensing reviews. Such a program must include the development of analytical models, verified by experiment, which can be used to predict reactor and safety system performance under a broad variety of abnormal conditions.

Current major emphasis is focused on providing information to NRC relevant to (1) its deliberations and decisions dealing with severe LWR accidents and (2) its safety evaluation of the proposed Clinch River Breeder Reactor.

CONTENTS

ILLUSTRATIONS

ILLUSTRATIONS (Continued)

TABLES

EXECUTIVE SUMMARY

1. CORE DEBRIS BEHAVIOR

1.1 EX-VESSEL CORE DEBRIS INTERACTIONS

Protracted interaction of hot, but not molten, core debris with concrete is an issue sometimes neglected in severe reactor accident analyses. The interaction of the hot solids with concrete, while not as dramatic as molten core debris/concrete interactions, can continue for very long times. The duration of hot solid interactions will determine when a severe accident is finished. In the case of very strong reactor containments, these interactions may determine when or if pressures in the containment caused by noncondensible gas will lead to containment rupture.

The recent FRAG tests examined long-term, hot solid interactions with concrete and the effects water coolant might have on the interactions. Analyses of the FRAG test results are reported to ascertain how the results would scale to a real reactor accident. These analyses indicate:

a. Hot solid attack on concrete could continue for over 200 h if the debris beds in a reactor accident are about 28 cm thick.

b. Hydrogen production from water vapor evaporating from the concrete can be predicted with equilibrium thermochemical arguments whether the debris is steel, stainless steel, or UO_2. Kinetic effects are unimportant even at the low temperatures of hot solid interactions.

c. The strength of concrete crusts formed over the debris is quite scale-dependent. The precise nature of this dependence is determined by the assumed mode of crust failure but can vary as the square of the scale.

The VANESA model describes aerosol production during core debris/concrete interactions. A key element of this model is the assumption that aerosols are produced by the mechanical processes of gas bubbles breaking at a melt surface. This assumption was based on simulant experiments with water and air. A scoping test was conducted to confirm that this mechanical aerosol formation occurs in more realistic melts. Mechanically generated aerosols (1 to 5 µm in size) were indeed observed when argon bubbles broke through melts of basaltic concrete.

The Zion Probabilistic Safety Study (ZPSS) proposed that when reactor core melts were ejected from a pressurized reactor vessel, they would be dispersed over a broad region and thus be rendered readily coolable. The Systems Pressure Injection Tests (SPIT tests) were designed as a means to confirm this proposal. First tests of this type showed that ejected melt behaved in a manner quite different than hypothesized in the ZPSS. Further, the tests demonstrated that

formidable aerosol generation occurred during pressurized melt ejection. These first scoping tests have led to a more systematic study of the melt ejection process. The matrix of tests to be conducted in the SPIT test series has been developed. The matrix consists of three major elements:

1. A factorial design matrix of 10 tests in which pressure, gas solubility in the melt, and melt temperature are varied.

2. Three tests in which melt is injected into a water pool.

3. A test in which melt is injected into a 1/20-scale mock-up of the reactor cavity at the Zion Nuclear Power Plant.

Coherence of the ejected melt jet, aerosol generation, melt dispersal, and the heat flux imposed by the jet will be monitored in these tests. Results of the tests will be the basis for the design and conduct of the 1/10 linearly scaled test with an 80-kg melt ejected into a scale mock-up of the Zion cavity.

1.2 CORE RETENTION MATERIALS ASSESSMENT

The Core Retention Materials Assessment program involves both experiments and analysis designed to (1) determine the fundamental limitations of candidate core retention materials and concepts and (2) develop a data base for use by the NRC in licensing review of proposed ex-vessel core retention devices. The program is currently focused on magnesia brick crucibles, thoria and alumina particle beds, and high-alumina concrete liners.

The third test in the SWA series was carried out during the current reporting period. A 5-kg pool of molten UO_2/ZrO_2 formed by the inductive-ring susceptor technique was deposited onto a layered alumina particle bed. The molten material quickly penetrated the large particles at the top of the bed. Penetration was stopped by a layer of small particles in the middle of the bed. There were no indications of particle flotation.

The SWA-3 test also demonstrated that the inductive-ring susceptor (IRIS) technique can be used to form larger pools of molten oxides than those obtained in the SOT series of tests. In the first part of SWA-3, a 17.6-kg pool of molten UO_2/ZrO_2 was formed from a total charge of 34.4 kg. In the final SOT test, the molten pool was only 30% of an 11-kg charge.

The SWA-3 results lend confidence to the IRIS designs presented in the last quarterly report. The IRIS test, scheduled for execution in the third quarter of FY83, will involve the melting of 100 to 200 kg of UO_2/ZrO_2 by the IRIS technique and the deposition of this melt onto an alumina particle bed.

The design of the test bed is presented. The central portion of the bed consists of large alumina sphere designed to absorb and quench approximately 20 kg of the melt. Downward penetration of the melt will be stopped by a layer of small alumina particles below the large particles. Lateral penetration is also controlled by small alumina particles. The central section is surrounded by an annulus. The top surface of the annulus slopes upward from the center to form a dish-shaped bed capable of containing as much as 200 kg of melt.

1.3 SODIUM CONTAINMENT AND STRUCTURAL INTEGRITY

The SLAM computer model of sodium interactions with limestone concrete is being developed as a part of the Sodium Containment Structural Integrity program. During this quarter, laboratory-scale tests of the interactions were performed and these test results have been compared to predictions by SLAM. Excellent agreement has been obtained in the onset, magnitude, and termination of energetic reaction between sodium and concrete. The validations, particularly of the chemistry models embodied in SLAM, add credence to the use of this mechanistic model as a predictive tool. If the predictions of SLAM are further verified when applied to other tests, SLAM will be incorporated in the CONTAIN model of LMFBR containment response during core-disruptive accidents.

An omission in the existing-data base concerning sodium interactions with concrete is the absence of tests with some simulant of core debris present. Speculation on how core debris might behave has included the suggestion that products of the sodium-concrete interaction are sufficiently viscous that the debris would not sink. Measurements of the viscosity of sodium-concrete reaction products were made this quarter. The viscosity was found to be about 20 poises over the temperature range of 773 to 873 K (500° to 600°C). The viscosity was found to be shear rate-dependent. These results suggest core debris would sink through the reaction product layer. This layer would occlude sodium from the debris and raise a question of coolability.

At NRR request, reviews were prepared of the CRBR project papers on (1) aerosol production during sodium/concrete interactions and (2) the extent of core debris attack on concrete. Reviewers generally agreed with the assessments in both these reports.

1.4 DEBRIS BED COOLABILITY

The Debris Bed Coolability program addresses issues concerned with the deposition of solid fuel debris on horizontal surfaces within the containment vessel and its subsequent coolability. This debris remains capable of generating significant power through the decay of fission products. Should natural processes fail to provide sufficient cooling, the debris could remelt and threaten containment. The Debris Bed Coolability program seeks to determine the natural cooling of such debris.

Work this quarter included materials tests and design evaluations for the D10/D13 test crucible. The materials evaluation was completed in March. High- and low-temperature tests were conducted of several refractory materials exposed to sodium and UO_2, and three viable materials for crucible fabrication were identified, Ta-10W, Mo41Re, and T-111. Stress analysis was performed for four different crucible designs. Thermal expansion can be accommodated easily by all the materials investigated. However, varying thermal expansion of the inner and outer crucible walls dictates the use of a single material for the crucible. High-temperature C-type thermocouples will be developed and fabricated at HEDL. Low- and high-temperature tests were run on the ultrasonic thermometers to insure satisfactory operation. The results are being studied.

The PAHR debris bed model was modified to predict the coolability of postaccident debris. The model includes various effects of laminar and turbulent flow, two-phase friction, gravity, and capillary force and predicts channel length, liquid fraction, dryout power, dry zone thickness, and downward heat removal.

1.5 DRY DEBRIS COOLABILITY

After a major reactor accident, if the core-material debris is uncoolable, it will progress to a molten state. The progression of the debris to a molten state and the interaction of the core melt with structural and core retention material are being investigated experimentally in the Dry Capsule program. This program, the follow-on to the Molten Pool Studies, interfaces closely with both the Ex-Vessel Core Debris Interactions and the Debris-Bed Coolability programs. High-temperature, laboratory-furnace tests and the first-of-a-kind, neutronically heated experiments are providing significant data on many coolability-related issues, including the thermal response of dried UO_2 and steel particulate beds to internally heated molten fuel material and the interaction of hot fuel debris with core structure and retention material. As with other safety research programs, investigators are using the experimental results to develop and verify analytical models that will be used to study reactor behavior under a wide variety of accident conditions.

The next in-pile experiment, DC 1, will investigate the thermal characteristics of an internally heated UO_2 debris bed from 1273 K (1000°C) to melt and the phenomenology and thermal characteristics of a molten UO_2 pool. The bed will consist of 2 kg of UO_2 particulate and will be top- and bottom-cooled and side-insulated. The maximum molten mass during the experiment is estimated to be from 0.7 to 1.0 kg.

During this quarter the final experiment assembly was essentially completed and is scheduled to run in April. Modeling of postdryout phenomena has continued. The one-dimensional model for analyzing the

postdryout behavior of debris beds has been extended to two dimensions. Improvements to the melt relocation module were also completed.

2. HIGH-TEMPERATURE FISSION-PRODUCT CHEMISTRY AND TRANSPORT

The purpose of the High-Temperature Fission-Product Chemistry and Transport program is to establish the data base necessary to predict fission-product behavior properly during severe accidents. This experimental task is being pursued by three interrelated activities:

a. Definition of thermodynamic data and chemical reaction characteristics of particular fission products of interest.

b. Examination of the transport properties of fission products in prototypic environments of steam and hydrogen.

c. Comparison of the observed behavior of the fission products with predictions made by purely thermodynamic considerations.

The study of chemistry of the control rod material, boron carbide (B_4C), in steam continued with experiments that examine the behavior of CsI vapor in a B_4C and steam environment. Analysis of condensed steam showed that very little cesium got through the steam system when B_4C was present, compared to previous experiments without B_4C where more cesium was detected. The iodine level in the steam condensate was about the same in either case. Some cesium reacted with the Inconel coupons, while no iodine was detected. A high level of cesium was detected on the B_4C coupons, but no iodine was found. Conclusions are that most of the cesium is retained in the reactor tube.

A new series of experiments to examine the reaction between tellurium vapor and structural materials in a steam/hydrogen environment was begun. Inconel coupons were placed in different areas along the reaction tube. Mass gains for the Inconel bands varied, due to oxidation. The rate of deposition is about the same as observed in previous experiments.

Several experiments were run in which tellurium vapor was equillibrated with urania particulate. A nickel coupon was used to remove tellurium from the gas stream. The rate of mass gain by the nickel coupon was a direct measure of the tellurium content in the gas. No extensive interaction was found of tellurium vapor with urania in experiments run between 773 to 1073 K (500° to 800°C). However, a slight interaction occurred in experiments run at the lower temperature.

3. CONTAINMENT ANALYSIS

The goal of this task is the development of CONTAIN, a general and comprehensive systems code that will analyze a variety of accident

sequences following the breach of the primary containment vessel through the breach of the secondary containment. It will provide detailed treatments of phenomena such as material interactions, heat transfer, aerosol behavior, and fission-product transport. The models will be sufficiently general to apply to all advanced reactor and LWR containment systems.

The testing of CONTAIN is continuing. Many features of CONTAIN have been tested, and a large number of tests have been completed and documented. The results of this testing work are being compiled into a comprehensive report that will summarize the results of the CONTAIN test program to date. This report will include CONTAIN Test Reports, Input Data Sets, and Supporting Analyses.

A simple sodium/concrete interaction model has been developed to provide a means of estimating gas release to the reactor cavity and to provide a check on the performance of more complex, mechanistic models. The code was tested using the CRBR extreme concrete-penetration rate (3 mm/min) and a preliminary validation calculation was made for Sandia Test 3. The calculations appear to agree with the experimental results to within a factor of 2; a more detailed comparison is underway.

Tests have been performed to check out the moving interface capability of the LMFBR reactor-cavity model. With a slowly moving interface and a very small node next to a large one, severe instabilities resulted initially. By making a small change in the algorithm, the instabilities were eliminated, and the solution algorithm now works well under a number of moving-node conditions. With the completion and demonstration of the moving-interface capabilities of the new model, the input and control routines were prepared for the implementation of various physical models. These routines, plus an added source option, have been completed and tested. Initial development and testing of the transport mechanisms of the new reactor-cavity model have also been completed. The technique used by Werner et al seems to work well for physical models in which there are only one or two materials. However, this approach has been developed only recently and needs to be tested further to verify the potential that it appears to have.

A working version of the MEDICI LWR cavity model/code has been produced in accordance with the structure diagrams and "structured documents" that were generated over the past few months. In the spirit of top-down code design and development, this code is a skeleton of the final version, containing most of the required logic and data management, but using dummy subroutines for many of the physics modules. Most of the effort for this code went into developing and debugging an efficient, interactive input processor.

A substantial effort was directed this quarter toward providing input to a document being prepared as part of the MELCOR code development project. This document is intended to be a guide for code developers and to provide a rationale for model choices.

Development work on the MAEROS aerosol module continued. One concern successfully addressed was the modeling of evaporation and condensation of water on aerosols; treatment of these processes appears to dominate the execution time in the LWR problems that are now being run. Execution time can be reduced substantially by simply changing the boundary conditions at the maximum and minimum particle sizes.

The tasks required for the modeling of radionuclide transport within and of radionuclide release from containment following severe accidents in LMFBR systems have been identified. Processes that require modeling to treat radionuclide redistribution between the various host materials (e.g., sodium, fuel, structures, aerosols, and atmosphere gases) have also been identified.

Development of various engineered safety systems continues. Modeling and initial coding of the heat exchanger and recirculation model have been completed. Development of the ice-condenser model has been initiated, and the fan-cooler models in existing containment codes have been reviewed.

With the revived interest in the Clinch River Breeder Reactor (CRBR), high priority is being given to completing the development of the models needed for studies of the containment response to various hypothetical accidents in the CRBR. One of the more critical models tests water release from heated concrete. This water release can be important in LMFBR accident scenarios because the sodium-water reaction is highly energetic and produces hydrogen. Checks of this model have established that water is being released from heated concrete, but that some of the water present is not being adequately accounted for. Work has been initiated to ensure that the water migration model is working properly.

Following the peer review of the LWR source-term work in January, a detailed review was performed of the then-current draft of NUREG-0956, "Radionuclide Release Under LWR Specific Accident Conditions, Vol. I: A PWR Analysis." This review included the checking of computer calculations reported in NUREG-0956 against simple analytical calculations.

4. ELEVATED TEMPERATURE MATERIALS ASSESSMENT

The primary objectives of the Elevated Temperature Materials Assessment studies are to (1) determine how microstructures evolve due to thermochemical history, which results in mechanical property changes, and (2) evaluate the validity of material damage and evaluate nondestructive evaluation techniques.

Materials that are currently under study include Inconel 718, 304 stainless steel, and 316 stainless steel. Optical metallography has been performed on Inconel 718 specimens. Biaxial deformation testing has been planned for both specimens of the stainless steel.

5. ADVANCED REACTOR ACCIDENT ENERGETICS

The Advanced Reactor Accident Energetics program is directed toward developing a data base for the understanding of the key in-core events in a core disruptive accident that determine the progression and severity of a reactor accident. For the advanced reactor, understanding in-core events is particularly important because significant energy release from the core is possible. The magnitude of this energy release, and therefore the ultimate threat to the containment, is determined by the competing positive and negative reactivity effects caused by the motion and temperature of fuel, cladding, and coolant.

This program, currently focused on postulated CRBR accidents, involves experimental and analytical efforts to determine the magnitude and characteristics of these reactivity effects in the two phases of a core disruption accident in an advanced reactor. These phases are:

1. Initiation Phase -- Fuel Dynamics

2. Transition Phase -- Fuel Freezing and Streaming.

5.1 INITIAL PHASE - FUEL DYNAMICS

The last two experiments, FD4.4 and FD4.5, in the FD2/4 experiments program were performed to investigate solid-state cracking, a special case of fuel disruption that may lead to early fuel dispersal in some types of LMFBR accidents. In FD4.4, solid-state fuel ejection was achieved without the destruction of the fuel pin. These fuel samples are available for PIE studies to examine the microscopic mechanisms that are causing the cracking phenomena. Experiment FD4.5 investigated the behavior of German-fabricated fuel under similar heating conditions that produced cracking in the U.S.-fabricated fuel. The KfK fuel was found similar to that of U.S. fuel.

5.2 TRANSITION PHASE - FUEL FREEZING AND STREAMING

Major activities in the TRAN program included the initiation of the TRAN B-Series tests (B-1), continuation of postirradiation examination (PIE) of TRAN Series I experiments, and preliminary design of the GAP-Series of tests.

The first TRAN B-Series (B-1) test was performed on February 15. The B-1 test addressed the question of full crust stability on convex (clad) surfaces vs concave (tube) surfaces. The use of thermocouples

allowed measurement of the leading-edge fuel velocity. These fuel "slug" velocity data are useful in confirming the accuracy of the PLUGM code, and so the B-1 experiment was analyzed with PLUGM. An improvement to the code has been developed that accounts for the effect of Taylor instabilities on film deposition. Modifications were made to the TRAN B-Series design for the fuel housing. PIE results will be available in a few months. Posttest examination work was done on the Series-I test TRAN-2, with steel found in the blockages and the end of the crust layer. The steel was presumably entrained in the fuel flow as it passed by the channel entrance.

The TRAN G-Series design (Gap Experiment) has begun. Preliminary engineering drawings were made and heat transfer calculations were performed. A new laboratory area is being set up for the assembly of the GAP experiments.

6. LIGHT WATER REACTOR (LWR) DAMAGED FUEL PHENOMENOLOGY

Sandia's LWR Damaged Fuel Phenomenology program includes analyses and experiments that are part of the integrated NRC Severe Fuel Damage (SFD) Research program. Sandia is investigating, both analytically and in separate-effects experiments, the important "in-vessel" phenomenology associated with severe LWR accidents. This investigative effort provides for three related research programs, the Melt-Progression Phenomenology (MPP) program, the Damaged Fuel Relocation (DFR) program, and the Damaged-Core Coolability (DCC) program. These programs are key elements in the NRC research effort to provide a data base to assess the progression and consequences of severe core-damaging accidents.

6.1 MELT PROGRESSION PHENOMENOLOGY

The objective of this program is to provide balanced perspectives and capabilities applicable to that phase of severe LWR accidents starting with initial core damage and progressing through to breach of the reactor vessel and discharge of core materials into the containment environment.

The formal elements comprising this program are:

a. Core Damage Sensitivity Studies.

b. Severe Accident Uncertainty Analysis.

c. Melt Progression Model (MELPROG) Development.

The core damage sensitivity studies are directed toward identifying the most influential phenomena governing the behavior of an LWR reactor core during an accident. The phenomena include both those governing the degradation of the core in an unterminated sequence and those occurring during attempts to terminate a severe accident

sequence. Most of the study of a two-level factorial approach designed to investigate the influence of external factors in an accident has been completed.

Because of the current importance of PRA in nuclear regulatory activities, an improved definition is necessary of the effects of uncertainty on the magnitude of risk estimates. This goal is pursued by the Severe Accident Uncertainty Analysis (SAUNA) project. A report of project findings is underway.

A formal system for integrating knowledge gained through improved understanding of the physical processes governing severe damage during the in-vessel phase of the accident can be constructed by developing computer-based models. The Melt Progression Model (MELPROG) is a program that calculates such sequences from rubble/debris formation through vessel failure. MELPROG is being developed from an existing code at Los Alamos. Coding of the model has begun.

6.2 LIGHT WATER REACTOR (LWR) FUEL DAMAGE EXPERIMENT PROGRAM

This program is directed toward examining the key phenomena that determine the core-damage configuration during the progression of a core melt sequence in an LWR core-uncovering accident. This program uses the information and perspectives gained in current LWR safety programs and focuses on the design of experiments that can contribute to the resolution of important severe-damage issues.

The two major areas of interest regarding in-vessel phenomena are:

a. The behavior of fuel and cladding during the stages of major core deformation from rod-bundle geometry to a severely degraded geometry and

b. The response of the severely damaged fuel to reintroduction of coolant from the emergency core cooling system (ECCS), especially the questions of redistribution of quenched material, short-term cooldown, increased steam generation, and oxidation reaction kinetics.

Current work under this subtask focuses on the in-pile applications because neutronic heating allows prototypic heat generation under severely damaged conditions.

A series of ACRR experiments is planned that addresses the above-described severe core damage issues:

a. Damaged Fuel Relocation Experiments (DF) -- Visually observed fuel damage in a flowing steam environment using neutronic heating in rod sections and multirod configurations.

b. Damaged Fuel Quench Experiments (DQ) -- Postmortem observation of damage configuration after ECCS flooding of damaged core materials.

c. Damaged Core Coolability Experiments (DCC) -- Coolability studies using DQ configurations.

Analysis of the DFR experiment matrix using DFR MOD3 code has continued. The experiment matrix was reviewed and several modifications were recommended. Design of the in-pile steam supply skid was completed and components were ordered. An analysis and evaluation of the shield plug design was completed. It was recommended that all penetrations contain two right-angle bends to prevent radiation streaming.

Experimenters completed the design for the detailed electrically heated out-of-pile test section. Components for the simplified (preliminary) out-of-pile test apparatus have arrived. Preliminary boiler operational checks have been completed.

6.3 LIGHT WATER REACTOR (LWR) DEGRADED-CORE COOLABILITY (DCC) PROGRAM

Sandia National Laboratories is pursuing a program to determine the coolability of the LWR degraded cores. The main purpose is to provide an experimental data base for use in evaluating the applicability of LMFBR coolability models to LWR-specifc conditions. This will be accomplished by performing a limited number of in-pile experiments using fission heating of UO_2 rubble to simulate the source of decay power in a severe-fuel-damage accident. This year, the scope of the DCC program encompasses the following:

a. Continue design, acquisition of parts, and assembly of the first two DCC experiment packages.

b. Perform DCC-1, the first in-pile coolability experiment containing a UO_2 rubble bed in a water bath.

c. Analyze the DCC-1 results, compared to current coolability models, and develop and improve models where necessary.

During the current quarter, the DCC program effort focused on the following activities.

a. Acquisition of the DCC-1 experiment hardware continued. Delays in delivery of some critical path components (primarily the urania fuel and the pressure vessels) put off the start of final assembly of the DCC-1 experiment package.

b. Considerable progress was made in fabricating and assemblying test facilities for the DCC-1 experiment. These facilities include a new lab and assembly area, a multilevel platform

for final assembly, and a leak-test bell jar capable of enclosing the entire experiment package.

c. Sandia staff members reviewed the particle size distributions for the first three experiments and concluded that DCC-1 will contain a small-sized particle distribution (typical of debris from a partial steam explosion) and DCC-2 will contain a large-sized particle distribution (typical of thermally fractured fuel).

d. Because of the small-sized particle distribution for DCC-1, some design and hardware changes were required for the DCC-1 experiment package. These include the addition of an electric heater, the exclusion of the liquid nitrogen precooler from the cooling loop, and the operation of the cooling loop with nitrogen instead of helium.

e. Most of the hardware and process development tests for DCC-1 were completed. Also, the final package test sequence to insure experiment reliability was formalized.

f. Safety calculations for the DCC-1 experiment were performed. These will be included as part of the experiment plan to be submitted to the Sandia reactor safety review committees.

g. Programmatic responsibilities were satisfied and included the presentation of papers on analytical development information, exchanges with other scientists in debris coolability research, and the completion of the draft for the DCC program plan.

REACTOR SAFETY RESEARCH

QUARTERLY REPORT

JANUARY-MARCH 1983

1. CORE DEBRIS BEHAVIOR

1.1 EX-VESSEL CORE DEBRIS INTERACTIONS
(D. A. Powers, 6422; D. R. Bradley, 6425; J. E. Gronager, 6422; J. E. Brockmann, 6422)

If core debris formed during a severe reactor accident is not coolable, the debris will penetrate the reactor vessel and interact with structural material in the reactor cavity. This interaction could lead to gas generation, production of flammable species, and intense emission of radioactive aerosols, in addition to erosion of the reactor basemat.

Study of the phenomena associated with ex-vessel interaction of core debris with structural material found in the reactor cavity is the purpose of the Ex-Vessel Core Debris Interactions program. In the recent past, the major part of this program was the study of core debris interaction with concrete. Penetration of core debris through steel liners has also been examined.

1.1.1 Application of the FRAG Results to a Reactor Accident

The Fragmented Debris test series (FRAG) was designed to investigate the interaction between hot, but not molten, core debris and prototypic reactor concretes. Inductively heated, mild steel spheres were used to simulate core debris that has undergone an energetic water/melt interaction with subsequent cooling to a solid, fragmented state.

1.1.1.1 Test Conclusions

From the data gathered in the four completed FRAG tests, the following conclusions can be drawn:

1. Oxidation of the mild steel debris by the concrete decomposition gases, H_2O and CO_2, produced equilibrium concentrations of the flammable species, H_2 and CO.

2. Molten concrete was transported through the debris and subsequently formed a crust layer either in the interior of the bed (limestone-common sand concrete) or above the surface of the bed (basaltic concrete).

3. Although the crust allowed gases to percolate through, it was impermeable to any water added following the formation. Hence, the debris bed was uncoolable and concrete ablation continued.

1

In order to determine the applicability of these results to the reactor case, the following questions must be answered:

1. What reactor power levels would produce similar debris-concrete interactions?

2. How do H_2 and CO production rates in a reactor case compare to those in the FRAG tests?

3. For the larger debris bed geometry of the reactor case, will the crust fail and thereby allow coolant to contact the debris?

1.1.1.2 Equivalent Reactor Decay Power Levels

In order to apply the FRAG results to a reactor accident situation, the reactor decay heat required to produce an equivalent debris-concrete interaction must be determined. This analysis begins with an energy balance for the debris bed:

$$mc \frac{dT}{dt} = \dot{Q}_D - \dot{q}_b A_b - \dot{q}_s A_s - \dot{q}_t A_t \qquad (1.1)$$

where the left-side term refers to the rate of change of energy stored in the bed, Q_D is the decay heat, and the last three terms refer to heat losses out the bottom, side, and top of the bed. This equation can be simplified by making the following assumptions:

1. The debris bed has reached a steady state, so $dT/dt = 0$.

2. The top surface of the debris has the same area as the bottom surface.

3. The heat flux to the concrete is uniform, i.e., $\dot{q}_c = \dot{q}_b = \dot{q}_s$

Hence,

$$\dot{Q} = \dot{q}_c (A_b + A_s) + q_t A_t \qquad (1.2)$$

This equation can be used to relate the power delivered to the debris in the experiment and the equivalent reactor accident. Substituting the appropriate dimensions for cylindrically shaped debris beds in the two cases yields the following relation:

$$\frac{\dot{Q}_{rea}}{\dot{Q}_{exp}} = \frac{\dot{q}_c(\pi R^2 + 2\pi RH) + \dot{q}_t \pi R^2}{\dot{q}_c(\pi r^2 + 2\pi rh) + \dot{q}_t \pi r^2} \qquad (1.3)$$

2

where the additional assumption has been made that since the experimen and accident interactions are equivalent, the heat fluxes, $\dot{q}_c$ and $\dot{q}_t$, are also equal in the two cases. Rewriting the $\dot{Q}$ terms as power density times bed volume, and then performing some algebraic manipulations on the resulting equation, produces the following simplified relation:

$$\frac{P_{rea}}{P_{exp}} = \frac{\left[\dfrac{\dot{q}_c}{\dot{q}_t}\left(1 + 2\dfrac{H}{R}\right) + 1\right]\left(\dfrac{h}{H}\right)}{\dfrac{\dot{q}_c}{\dot{q}_t}\left(1 + 2\dfrac{h}{r}\right) + 1} \qquad (1.4)$$

where P is the power density in W/cm^3. By choosing the dimensions of the accident debris bed and the ratio $\dot{q}_c/\dot{q}_t$, the reactor and experimental power densities can be related.

Table 1-I presents the calculated power density ratios for some typical parameter values. Two sets of calculations were performed: one for an accident debris height equivalent to the experimental height (h/H = 1, where h = 26.7 cm) and another for an accident debris height one-half the experimental value (h/H = 2). When concrete erosion began in the experiments, the radiative heat flux from the top of the debris was roughly twice the heat flux to the concrete. For this value of the heat flux ratio, the reactor power density required to produce an equivalent debris/concrete interaction is either 40% of the experimental value for the deep debris bed or 80% for the shallow bed. In the FRAG tests, the power density was on the order of 0.45 to 0.90 W/cm^3 (deep bed) or 0.36 to 0.72 W/cm^3 (shallow bed). For the two debris depths that were examined, this is equivalent to a range of 0.18 to 0.36 w/cm^3 (deep bed) or 0.36 to 0.72 w/cm^3 (shallow bed). On a per-unit-mass basis, these values convert to 0.1 to 0.2 W/g for FRAG and 0.04 to 0.08 W/g (deep bed) or 0.08 to 0.16 W/g (shallow bed) for the reactor case. (These calculations assume a debris bed porosity of 40% and a solid density of 8.0 g/cm^3.)

In relating these specific power levels to a time after accident initiation, several accident parameters must be specified. These are reactor power, mass of melted core material, and fraction of decay power produced by nonvolatile fission products. Assuming a reactor power of 3410 MW, a core debris mass of 130×10^3 kg, and a nonvolatile fraction of 70% results in the specific power levels shown in Table 1-II.

3

Table 1-I

The Ratio of Reactor to Experiment Power
for Typical Parameter Values

$$\frac{P_{rea}}{P_{exp}} \quad \text{for} \quad \begin{array}{l} h/H = 1 \\ (h/H = 2) \end{array}$$

$\dot{q}_t/\dot{q}_c$	H/R 1/10	1/20	1/30
1.0	.317	.303	.298
	(.634)	(.606)	(.596)
2.0	.403	.390	.386
	(.806)	(.780)	(.772)
3.0	.470	.459	.455
	(.940)	(.918)	(.910)

Table 1-II

Reactor Decay Power vs Time

Time (hr)	Specific Decay Power (W/g)
1	0.235
10	0.122
24	0.096
50	0.078
75	0.069
100	0.064
200	0.052

1.1.1.3 Applicability of FRAG Gas Composition to a Reactor Accident

The simulant debris used in the FRAG tests was made of mild steel, which is composed almost entirely of iron. Flammable gas production resulting from the oxidation of the FRAG debris may be quite different from that in the reactor case where the core debris is composed of a uranium dioxide, zirconium, and stainless steel mixture. In determining the applicability of the FRAG results, it is necessary to determine whether the oxidation of the core debris is sufficiently rapid to produce equilibrium H_2 and CO concentrations. This question can be answered by considering the relative reaction rates for iron, zirconium, stainless steel, and uranium dioxide.

4

rapid to produce equilibrium H_2 and CO concentrations. This question can be answered by considering the relative reaction rates for iron, zirconium, stainless steel, and uranium dioxide.

Assuming that the oxidation reaction is controlled by diffusion of reactants through the oxide layer building up on the outside of the debris particles, the reaction rate is given by an equation of the form

$$W^2 = K_p^\circ \exp(-E/RT) \cdot t \qquad (1.5$$

where W is the cumulative H_2/CO released per unit area, R is the universal gas constant, T is the absolute temperature, and K_p° and E are empirical parameters. To determine a reaction rate, this equation is differentiated with respect to time. The resulting parabolic reaction rates are given by

$$\frac{dW}{dt} = \frac{1}{2} \left(K_p^\circ \right)^{0.5} \exp \left(\frac{-E}{2RT} \right) t^{-0.5} \qquad (1.6)$$

For iron, Type 304 stainless steel, zirconium, and uranium dioxide, the rate expressions for oxidation by steam are given by the following:

For Fe, $\quad \frac{dW}{dt} = 0.3973 \exp[-9000/T] t^{-0.5}$

For S.S., $\quad \frac{dW}{dt} = 9.682 \times 10^4 \exp[-2.121 \times 10^4/T] t^{-0.5}$

For Zr, $\quad \frac{dW}{dt} = 127.0 \exp[-1.145 \times 10^4/T] t^{-0.5}$

For UO_2 $\quad \frac{dW}{dt} = 30.86 \exp[-1.311 \times 10^4/T] t^{-0.5}$

In these equations, W is the mass of H_2 (in mg) produced per cm^2 of exposed surface, and t is time in seconds.

The hydrogen production rates given by these equations are a strong function of temperature. The relative rates of H_2 production are given by the magnitude of the lead constants. Table 1-III presents the rate constants calculated for three temperatures: 867 K (594°C), 1100 K (827°C), and 1373 K (1100°C).

As shown in Table 1-III, except at relatively low temperatures (867 K [594°C]) hydrogen production rates would be even greater in a reactor accident than in the FRAG tests. Hence, the equilibrium concentrations would be obtained even more readily than in FRAG. Although similar calculations cannot be performed for CO production

because experimental data are unavailable, oxidation by CO_2 is expected to proceed at a rate similar to that of steam. Thus, equilibrium CO concentrations will also be achieved in a reactor debris bed.

Table 1-III

Rate Constants, K_r,* for Oxidation of Four Materials

Material	Temperature (K)		
	867	1100	1373
Fe	1.22×10^{-5}	1.11×10^{-4}	5.65×10^{-4}
S.S.	2.3×10^{-6}	4.09×10^{-4}	1.89×10^{-2}
Zr	2.34×10^{-4}	3.83×10^{-3}	3.03×10^{-2}
UO_2	8.36×10^{-6}	2.06×10^{-4}	2.20×10^{-3}

*Kr is defined by $dW/dt = K_r t^{-0.5}$

1.1.1.4 Analysis of Crust Strength

The concrete slag crusts formed in the FRAG tests were strong enough to support a column of water and sometimes a significant portion of the debris without failing. In order to extrapolate these results to the reactor scale, potential failure mechanisms should be evaluated. Two mechanisms will be considered here: failure due to excessive deflection at the center of the crust layer and detachment of the crust from the concrete sidewalls.

Consider the crust to be represented as a flat circular plate (of radius r) with fixed edges and a uniform thickness (ℓ). It is assumed to be uniformly loaded by a pressure (p). Under these conditions, the maximum stress occurs at the center of the plate and is given by

$$\sigma_{max} = \frac{3pr^2(1 + \nu)}{8\ell^2} \tag{1.7}$$

where ν is Poisson's ratio. If the assumption is made that the crust fails when the yield stress is exceeded, appropriate scaling laws can be derived. Equating the experiment and reactor accident stresses and cancelling common terms yields

$$\left(\frac{pr^2}{\ell^2}\right)_{exper} = \left(\frac{pr^2}{\ell^2}\right)_{accident} \tag{1.8}$$

The three independent variables of importance are then the applied pressure, the thickness of the crust, and the radius of the containing vessel.

The applied pressure may be from an overlying pool of water, encountered when basaltic concrete was used in the FRAG test, or from a combination of debris and a water pool, encountered with lime-stone/common sand concrete. If the mass of debris above the crust level is neglected, the pressure an be related to the depth of the water pool by

$$p = \rho g h \tag{1.9}$$

where ρ and h are the density and depth of the water pool. Substituting this expression into Equation 1.8 yields

$$\left(\frac{hr^2}{\ell^2} \right)_{exper} = \left(\frac{hr^2}{\ell^2} \right)_{accident} \tag{1.10}$$

Equations 1.8 and 1.9 indicate a strong dependence of crust failure on both the lateral dimension of the crust and on the crust's thickness. For example, in a 1/10-scale experiment (i.e., $r_{exper} = (0.1)r_{accident}$), the pressure required to fail the crust would be 100 times what would be required under reactor accident conditions. Therefore, no conclusions can be made as to the stability of reactor scale crusts based solely on what was observed in the FRAG tests.

A second failure mode, detachment of the crust from the concrete sidewall, might also provide coolant pathways to the debris. If S_s is the load applied by the water pool (or water/debris combination) to cause failure, then

$$S_s = p \pi r^2 = \rho g h \pi r^2 \tag{1.11}$$

At failure,

$$S_s = Y_s \, 2 \pi r \ell \tag{1.12}$$

where Y_s is the failure shear stress and $2 \pi r \ell$ is the area of attachment. Equating the experiment and accident shear stresses, the following relationships are obtained

$$\left(\frac{pr}{\ell}\right)_{exp} = \left(\frac{pr}{\ell}\right)_{acc}$$

and

$$\left(\frac{hr}{\ell}\right)_{exp} = \left(\frac{hr}{\ell}\right)_{acc} \qquad (1.13)$$

Again, the three variables p (or h), r, and ℓ can be used to relate crust failure conditions in experimental and accident geometries. In this case, however, the variables are linearly related.

The two analyses discussed above assume that similar crusts will be formed in the experiment and the accident. Although considerable argument has been voiced that the formation mechanisms are scale-dependent and that cavities of sufficient size will not crust over, observations of crust formation in the FRAG tests indicate that the mechanisms may be independent of scale. This is especially true of the crusts formed from basaltic concrete. In the FRAG1 test, the videotape clearly indicates that the molten concrete bubbles uniformly through the bed and then forms a domed crust of uniform thickness. Because the molten concrete moves through the debris bed and not around it, no reason exists to expect a larger geometry to prevent or inhibit crust formation. In a reactor scale, however, a flat rather than a domed crust would be expected. Although formation of the limestone/common sand slag crust could not be observed, the uniformity of the resulting crust layer also indicates equal flow throughout the bed.

In summary, this analysis indicates that although crust formation is independent of scale, crust failure depends very strongly on the applied load and dimension of the crust. Without large-scale experiments, no conclusion can be made at this time as to the stability of the crust in a reactor geometry.

1.1.2 The VANESA Model

Mechanistic modeling of the aerosol and fission-product source term from the ex-vessel core debris interactions is performed by the VANESA model. Two series of model validation tests are being planned. One series addresses vaporization release from a melt with gas bubbling through it. The other addresses aerosol formation by bubble bursting. A scoping test has been completed for the latter series.

The VANESA model of aerosol production and fission-product release during melt interactions with concrete has yielded two important predictions:

1. Bursting of bubbles at the melt surface mechanically creates aerosols that can persist long after the melt has cooled while vaporization is negligible.

2. Tellurium not released from the core debris during the process of core meltdown will be sparged from the melt during core debris/concrete interactions.

Initial validation of the VANESA model focuses on these two predictions.

A scoping test of aerosol production by bubble bursting was conducted in February. About 3 kg of basaltic concrete was melted inductively and sparged with argon. The melt was "tagged" with non-volatile ZrO_2 so that aerosols produced by mechanical processes could be distinguished from those produced by vaporization. Techniques for counting bubbles by measuring pressure surges in the sparge gas line were demonstrated successfully. This allows measurement of the number of particles produced per bubble burst, a critical input to the VANESA model.

One problem that did appear was that vaporization of Na_2O and K_2O from the melt masked the bubble-burst-generated aerosol. The obscuring of the bubble burst aerosol formation could be relieved by either prolonged heating of the melt to rid it of Na and K or by using a "synthetic" concrete that is free of Na and K.

The scoping test demonstrated the following:

a. A clay-graphite crucible can be used to inductively melt concrete and contain it up to 1823 K (1550°C).

b. Exposed junction thermocouples (type S) function acceptably up to 1773 K (1500°C) but may fail at higher temperatures. Sheathed junctions in alumina tubing prove less fragile and more reliable at the higher temperatures. Sheathed junctions will be used in future tests, since response times are not critical.

c. Melt sampling may be accomplished by inserting an alumina tube (1/4 in. OD, 1/8 in. ID) into the melt and withdrawing it. The melt adheres to the outside of the tube and cools.

d. Monitoring the pressure of the gas sparging line (alumina tube of 3/8 in. OD, 1/4 in. ID) allows bubbles to be counted individually at rates up to two bubbles per second. A shorter line or larger diameter line may allow counting of higher bubbling rates.

Three filter samples and corresponding melt samples were taken during the test with qualitative results.

The first sample was analyzed for Zr by inductively coupled plasma (ICP) optical emission spectrometry. The melt showed 2.1 w/o Zr (±10% relative error). If no ZrO_2 was vaporized, indications are that 10% of the aerosol came from bubble bursting.

The second sample, analyzed by spark source emission spectrometry showed that 1.5 w/o Zr was in the melt, and no detectable Zr (less than 5×10^{-3} w/o) was in the aerosol. This result was found at higher temperatures and higher flow rates. The analysis revealed that some elements such as Cu, Ga, Sn, and B had higher concentrations in

the aerosols than in the melt. Other elements such as Zr, Ca, Fe, Mg, Ti, Sr, and Ba had much lower concentrations in the aerosols than in the melt. These first two filter samples contained 200 to 300 mg of aerosol. Most of the aerosol was assumed to have come from the vaporization.

The third sample, taken at a lower melt temperature, contained 0.13 mg of material. An electron micrograph of this is shown in Figure 1.1-1, in which spherical particles on the order of 1 μm in diameter are seen. These are assumed to come from bubble bursting. Energy dispersive spectroscopy in the scanning electron microscope (SEM) did not reveal Zr because 2 w/o Zr expected in bubble burst aerosol particles is below the detectability limits.

The use of ZrO_2 for bubble burst aerosols is dependent on finding vaporization information on ZrO_2 from concrete melts.

1.1.3 System Pressure Injection Test (SPIT) Experiments

The SPIT test program was initially conceived to provide a cost-effective means of developing the melt generation and ejection techniques that are required for the High-Pressure Melt Streaming (HIPS) program. The physical size and complexity of the equipment for the HIPS apparatus requires long lead times for procurement and fabrication. To avoid unnecessary delay in the program, the smaller scale SPIT equipment was fabricated and installed.

The Phase I SPIT tests that have been performed have demonstrated the validity of using a sacrificial melt crucible and fusable melt plug.[1-1] In addition to achieving the initial program objective, the tests also demonstrated a number of unique jet behavior character-istics not previously identified. These characteristics include the appearance of noncoherent jet streams and a large aerosol source term. The deviation from the stable jet hypothesized in the ZPSS [1-2] is attributed to the absorption and subsequent diffusion of gas in the melt at pressure and the inherent nature of a turbulent submerged jet.[1-3] The jet emanating from the vessel consists of the liquid melt and gas in solution; the rapid change in the ambient conditions causes the gas to nucleate into bubbles that expand to disrupt the jet stream.

The dissolved gas also serves as a source of aerosols as the bubbles migrate to the surface of the stream and burst into fragments. The size distribution of the aerosols is at least trimodal, suggesting the presence of other generation mechanisms. Assuming that the mech-anisms are prototypic, the aerosol represents a large potential for the release of fission products from the melt stream envisioned in an accident situation.

The Phase I SPIT test results are qualitative because of the initial emphasis on technique development. The limited amount of quantitative data obtained indicates that the phenomena associated with high-pressure melt ejection may be significantly different from that assumed in the ZPSS analysis. It is necessary, therefore, to

10
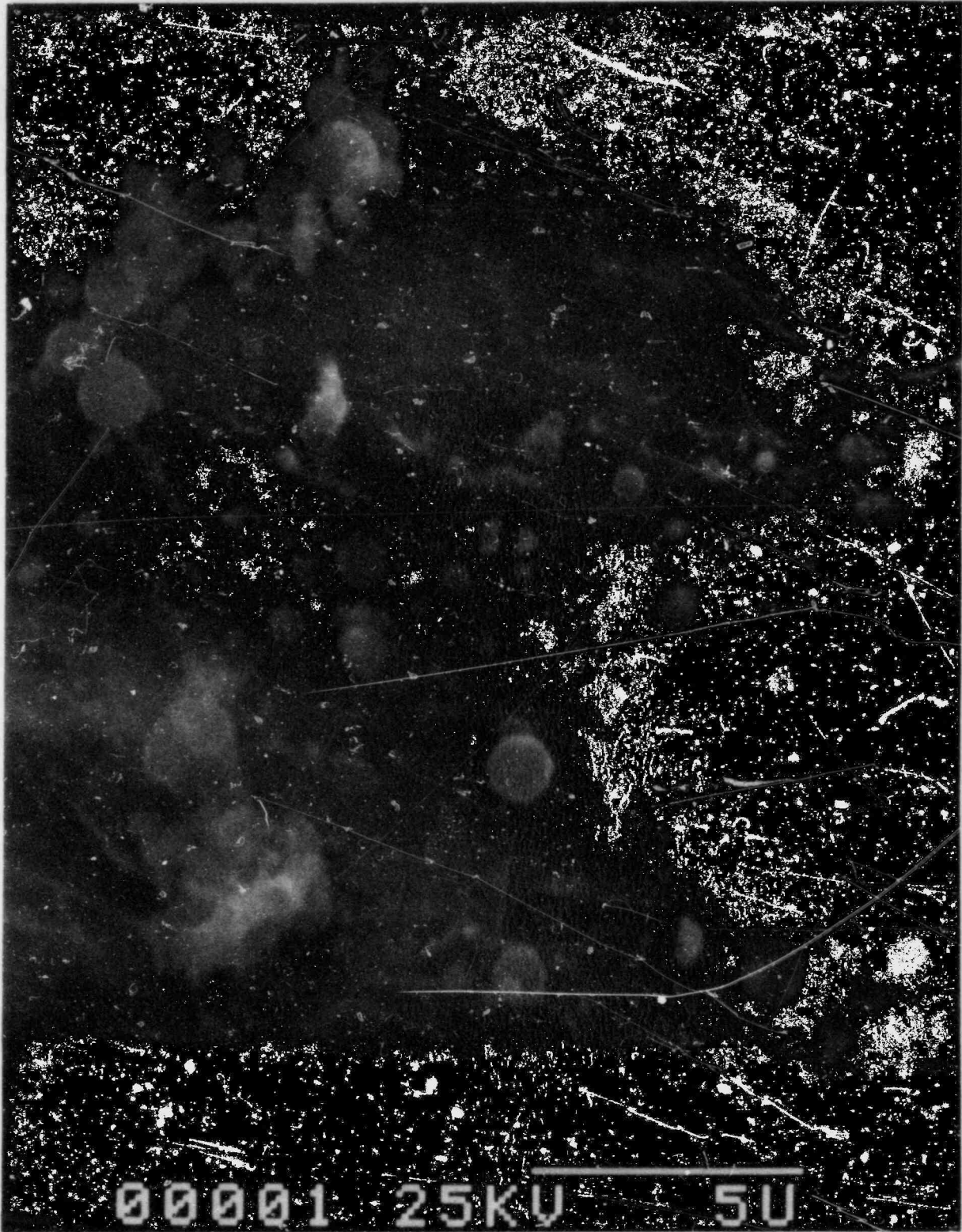
Figure 1.1-1.   Bubble Burst Particles from VANESA Validation Scoping
Test

substantiate this premise by performing a second phase of SPIT experiments prior to initiating the larger scale HIPS tests. This second phase of testing is considered essential to the HIPS program for the following reasons:

a. The SPIT apparatus allows a cost-effective means of obtaining system response information over the entire range of accident sequence input conditions.

b. Comparing the SPIT and HIPS data will provide scaling criteria (1/20- to 1/10-scale) and verification of the scaling laws.

c. Diagnostic techniques are available in SPIT that cannot be used in the HIPS cavity tests due to limitations in size or access to the jet.

d. The SPIT apparatus is more readily modified to address other test conditions, such as the presence of water or geometrical features.

The Phase II SPIT test matrix has been developed using the knowledge gained during the Phase I experiments. The matrix has three objectives:

a. Characterize the melt jet phenomena (velocity, shape, aerosol generation, fission-product source term) over the range of accident conditions.

b. Study the melt behavior in a scaled cavity to understand the phenomena expected during the HIPS tests.

c. Address the influence of water in the cavity to properly design the HIPS-scaled cavities and instrumentation.

The following develops the experimental strategy to be used to satisfy the objectives of the Phase II tests.

1.1.3.1 Phase II SPIT Test Strategy

The first step in developing a test strategy using a "statistical" approach is to identify the physical mechanisms that may affect the process.[1-4] From these mechanisms, the experimental factors can be listed and their range of influence evaluated. Those variables that have a significant influence are carried forward in the test matrix, while the others are held constant.

The Phase I SPIT tests served to screen the physical mechanisms of the melt ejection process. The dominant variables are pressure, gas solubility, and melt temperature. Melt mass can also be considered, but the limited capacity range of the SPIT apparatus cannot significantly alter the dependent variables (test outcomes). Table 1-IV identifies the range of each of these variables and dependent variables that they influenced.

Table 1-IV

Independent and Dependent Test Variables

Independent Variable	Range	Influenced Dependent Variable
Pressure	13.6 to 150 atm	Jet velocity Incident heat flux
Gas solubility	Low, high	Aerosol generation Jet dispersion
Temperature	(1773 K to 3273 K) (1500°C to 3000°C)	Heat flux Aerosol generation

The pressure used for the experiments is easily controlled and measured. The principal difficulty is the possible increase in the initial value induced during the thermite burn. Gas solubility is related to the types of materials involved, the pressure, and to a lesser extent, the temperature. Establishing a value of gas solubility for each test is therefore complicated by the factors involved and by the uncertainty of their interrelationship. For the Phase II SPIT tests, the gas solubility will be discretized by using two gases with presumably different degrees of solubility. The low solubility of carbon dioxide represents a lower bound on the conditions expected for prototypic situations (i.e., steam and hydrogen over molten corium). Selecting nitrogen as the second gas provides an upper bound on the expected behavior.

The temperatures achieved during the thermite reactions appear to be a function of the constituents involved (particularly contaminants), pressure, and the length of time the material resides in the vessel. The observations during the Phase I tests indicate that reducing the porosity of the powder bed causes improved heat transfer and hence a faster burn rate and reduced temperature losses. Thus, the highest temperatures will be achieved for highly tamped charges containing no additional materials other than the stoichiometric composition. Conversely, temperature can be lowered by adding iron powder to the thermite charge to cause energy to be absorbed in heating the nonreacting materials.

The existence of three factors at two levels (low and high) allows a factorial strategy to be implemented. Figure 1.1-2 represents this strategy as a three-dimensional cube in the form of a perspective drawing on two-dimensional paper. Each cube dimension represents one factor of the experiment: pressure, gas solubility, or temperature. The volume contained within the boundaries of the cube represents the factor space, or all possible combinations of the three factors.
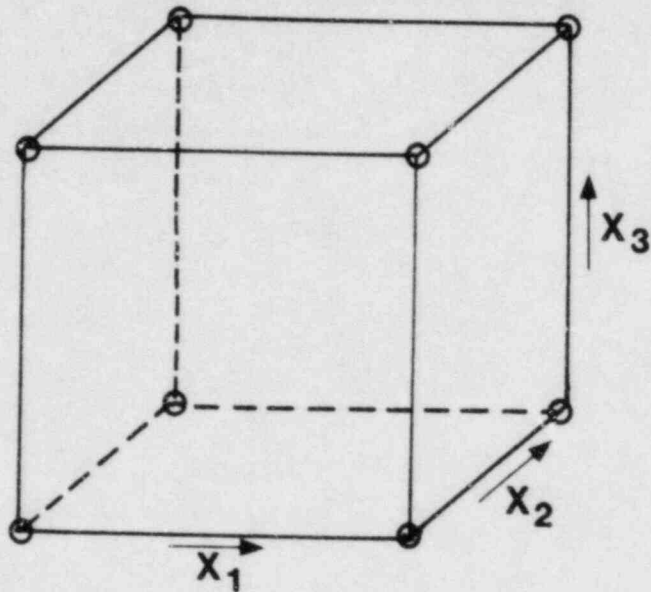
Figure 1.1-2. 2^3 Factorial Design

The intersections at the corners of the cube represent design points or conditions where the factors are at their extremes. This design pattern is called a "two-level" factorial--three factors at two levels each. The two-level factorial can determine the "main effect" of each factor, plus the "interactions" of the factors in combination. The main effect of X_1 is based on a comparison of the response values at the left and right planes of the cube (Figure 1.1-3). Along the lower front edge of the cube, the values of X_2 and X_3 are constant and at the ends of the line are two experimental points that differ with respect to X_1. Comparison of the response values at these two points gives an estimate of the effect of X_1. There are three other edges of the cube that can be treated in a similar manner. Each of the four edges gives an estimate of the effect of X_1. The "main effect" of X_1 is define as the average of the estimates from the four edges. Equivalently, the procedure considers the difference in average response between the right and left planes in Figure 1.1-3.

Because all combinations of X_2 and X_3 are represented in comparing planes, any main effect found will be known to apply over the ranges of X_2 and X_3, not just a particular combination of X_2 and X_3. The main effect of X_2 can be found in a similar manner by comparing the front and back planes of the cube. The effect of X_3 is determined by comparing the top and bottom cube surfaces.
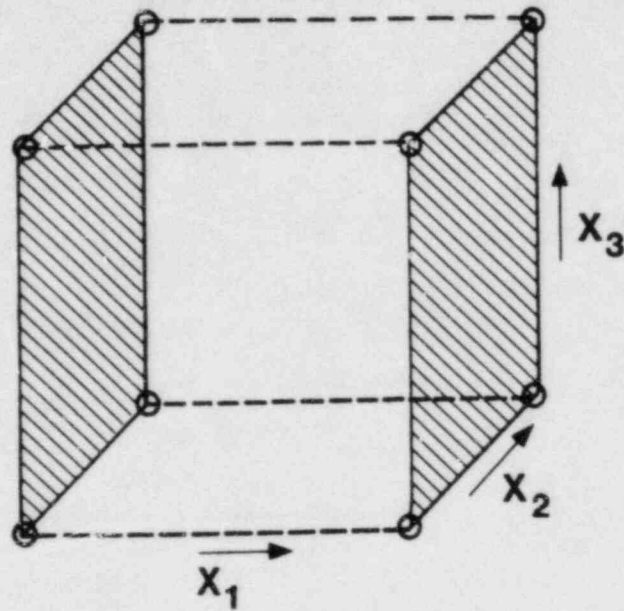
Figure 1.1-3.   Factor Effect X_1

By using all eight experimental points to determine the effect of a particular X, "hidden replication" of the data is achieved. Each factor effect and each interaction effect is based on all of the data points. Because the effect is the difference between two averages, the data is essentially "replicated" in the comparison. Effects determined in this way are mathematically orthogonal so that they can be interpreted as truly separate estimates of separate characteristics of the physical system being evaluated.

The improved precision of the factorial approach due to hidden replication can be estimated from the precision ratio (PR):

$$PR = \frac{\sigma_{FE}}{\sigma} = \frac{2}{(n)^{1/2}} \qquad (1.14)$$

where

   σ_{FE} = standard deviation of a factor effect
   σ = standard deviation of a single observation
   n = total number of observations = KZ^P
   K = number of replicates
   P = number of factors

15

For the experiment under consideration, K = 1 (no replication of data points) and P = 3 (pressure, gas solubility, temperature). Thus,

$$PR = \frac{\sigma_{FE}}{\sigma} = \frac{2}{(8)^{1/2}} = \frac{2}{2.82} = 0.707 \qquad (1.15)$$

Performing one replication at any data point would improve the PR ratio markedly:

$$PR = \frac{2}{\left(2 \cdot 2^3\right)^{1/2}} = 0.5 \qquad (1.16)$$

The type of experimental design illustrated in Figure 1.1-2 does not give any estimate of curvature of the response in the experimental region. To estimate the curvature of each response individually would require an increase in the number of tests by 50% to 100%. An estimate of curvature can be made economically by performing tests at the middle points of all factors. The severity of curvature can then be estimated by the difference between the average of the design point (corner intersection) and the average of the center points. If the curvature is severe, linear model assumptions will be accurate only near the corners of the cube.

Factor effects can be calculated from response data and compared to the "minimum significant factor effect" to determine if the factor is important to the response. The curvature effect can be calculated and compared to the "minimum significant curvature effect" in a similar manner. The formulas for the minimum significant factor effect (MIN) and minimum significant curvature effect (MINC) are as follows:

$$MIN = T's \, (2/mk)^{1/2} \qquad (1.17)$$

$$MINC = T's \, (1/mk + 1/C)^{1/2} \qquad (1.18)$$

where

T' = t-distribution statistic for the desired probability level and degree of freedom in the estimate

s = pooled standard deviation of a single response observation

$m = 2^{p-1}$ where p is the number of degrees of freedom

k = number of replicates of each trial

c = number of center points

Comparing the individual factor effects to MIN establishes the relative importance of that factor. The largest factors (in absolute value) are the most important, relative to the response of the system. Similarly, if the computed curvature effect is larger than MINC, then at least one variable has a nonzero curvature associated with it.

More sophisticated analyses recognize the need to consider the linear, interaction, and curvature effects with respect to all the independent variables. To estimate curvature, a full three-level factorial is required to provide orthogonal estimates. For 3 independent variables, a 3-level factorial requires a minimum of 27 tests. A variation developed by Box and Behnken uses 13 of the 27 points, plus two replicates at the center point, for a total of 15 points.[1-5] This technique allows a better estimate of error and curvature and permits developing polynomial expressions for the response function in terms of the independent variables. The disadvantage is near doubling of the required number of runs.

1.1.3.2 Jet Characterization Tests

The previous section established several strategies that could be used to characterize the melt jet over the range of the independent variables. The Phase II SPIT test matrix is based on a two-factorial strategy, principally due to the confines of time and resources available. A 2-level factorial matrix with 2 additional center points will be used, giving a total of 10 tests. The two center points provide a replicate data to reduce the PR and to allow an estimate of curvature in the response factors.

As indicated above, the three independent variables are pressure, temperature, and gas solubility. The factors can be expressed in any meaningful scale and remain applicable for the response consideration. Because some responses (velocity, gas solubility) are proportional to the square-root of the system pressure, expressing the scale in this manner would reduce the degree of curvature (i.e., the span of the scale is numerically reduced). This procedure also shifts the center-of-range value to a lower absolute value that would be found using the actual system pressures.

Another important aspect of the matrix is that the gas solubility and temperature are neither well-controlled nor well-measured input parameters. Thus, the data obtained will be affected by the accuracy at which these variables can be inferred. Table 1-V illustrates the "coded" and actual input parameters for the Phase II SPIT tests. The coding is based on using "-", "0" and "+", for the low, center, and high values of each variable, respectively.

The systematic trial order given in Table 1-V will not be the sequence by which the tests will be performed. Random ordering is considered beneficial in identifying the effects of bias errors that may be present in the results. Experimental constraints, such as equipment availability, will cause a degree of random ordering; the choice of test order beyond the constraints will be as random as possible.

17

Table 1-V

SPIT Phase II Jet Characterization Test Matrix

	Coded Variable			Actual Variable		
Trial	X_1	X_2	X_3	(ATM)	GAS	K(°C)
1	-	-	-	13	CO_2	1773 (1500)
2	+	-	-	150	CO_2	1773 (1500)
3	-	+	-	13	N_2	1773 (1500)
4	+	+	-	150	N_2	1773 (1500)
5	-	-	+	13	CO_2	3273 (3000)
6	+	-	+	150	CO_2	3273 (3000)
7	-	+	+	13	N_2	3273 (3000)
8	+	+	+	150	N_2	3273 (3000)
9	0	0	0	63	CO_2/N_2	2993 (2720)
10	0	0	0	63	CO_2/N_2	2993 (2720)

Performing the above tests and analyzing the results will allow development of models to relate the system responses to the input variables. These models can then be used over the entire response volume to the accuracy identified in the error analyses of the data.

1.1.3.3 Aerosol Characterization

Aerosol measurements have been made during the Phase I SPIT tests and are planned for the Phase II Jet Characterization tests. Both test series are conducted outdoors, which impose limitations on the aerosol data collected. The aerosol cloud is sampled as it drifts by the sampling instruments so that aerosol concentration can be estimated based only on the observed transit time of the cloud. Total mass of aerosol cannot be estimated because the volume of the cloud is not known. What is known from the Phase I tests is the general tri-modal nature of the aerosol distribution. Sampling efficiency of larger (i.e., 65-μm) particles is not certain but may be estimated from sampling theory, but transport of these larger particles in the aerosol cloud is not known. To eliminate the limitations of "grabbing" samples from the passing cloud, the aerosol must be thoroughly mixed and contained in a known volume. Samples from the volume permit calculation of total mass aerosolized and thus the fraction of melt that was aerosolized.

For this reason, the SPIT Phase II test matrix will contain a series of aerosol characterization tests employing a free jet inside an instrumented container. The measured and calculated quantities to be obtained are:

a. Total aerosol mass concentration

b. Total fraction of melt aerosolized

c. Size distribution of aerosol

d. Mass, mean size, and spread of each mode

e. Elemental composition of aerosol

f. Size-dependent elemental composition

The objectives of the aerosol characterization test series are twofold: as a mean effects tests to determine the relationship of the four identified input variables on aerosol generation, and to provide a well-defined data base for future efforts at developing a mechanistic model of melt ejection aerosol generation. In addition to the three variables considered in the jet characterization matrix, the aerosol generation also appears to be a function of the time the jet is exposed to the ambient atmosphere. Thus, the four input variables for aerosol characterization are:

1. Pressure

2. Melt temperature

3. Cover gas

4. Jet propagation distance

As indicated in the jet characterization discussion, these factors cannot all be set precisely nor easily measured during the test. Variable 1, pressure, is a precise measurement during the test, but controlling the absolute value is not easily accomplished. Variable 2, melt temperature, cannot be set before the test and is not an easily measureable quantity. Means to infer melt temperature are being developed. Variable 3, cover gas, is being used in lieu of the more desirable variable, degree of gas solubility. Gases of widely varying solubility (N_2 - soluble, and CO_2 - insoluble) will be employed during the tests. The amount of dissolved gas depends on pressure, melt temperature, and cover gas. This amount is a more desirable variable because it is assumed to be the driving parameter for film breakup particle generation. The use of cover gas as a substitute variable has been selected to avoid the inaccuracies involved in attempting to calculate solubility. If, at a later time, solubility can be calculated, the data will be available. The most desirable course of action now under consideration is a means of directly measuring the dissolved gas. Variable 4, jet propagation distance, is easily and precisely set before the test.

A fractional factorial test matrix is proposed, consisting of eight tests with parameter vectors comprised of high and low values (corner points) and two replicants of a vector of intermediate values (center point). This is a main effects test, which permits the fitting of a response surface of the form:

$$R = \sum_{i=1}^{L} b_i x_i + b_o \qquad (1.19)$$

where

R = response

$x_i = i^{th}$ variable

b_i = the coefficient of the ith variable

b_o = intercept

Eighteen tests, all 16 corner points, and 2 replicants of the center point, would be required to fit the interaction terms $x_i x_j$ where $i \neq j$. It should be noted that the additional eight tests may be run if deemed necessary. The choice of the fractional factorial matrix is dictated by the compromise between maximizing information and reducing the quantity of resources required for the matrix.

An advantage of this matrix is that the conditions of the tests from the jet characterization test matrix may be duplicated in the aerosol characterization test matrix.

The tests will be performed in a random order, within the constraints of the apparatus, to minimize bias errors. The aerosol characterization test matrix is given in Table 1-VI. The notation convention, "-", "0", "+", for the low, middle, and high values of the variables, respectively, is used. Separate matrices are required because of conflicting instrumentation requirements on the two types of tests. For example, flash X-ray is used to define the shape of the jet for characterization, but the equipment for this technique cannot be used inside the chamber utilized to contain the aerosol cloud.

1.1.3.4 Jet/Water Interaction Tests

An additional objective of the Phase II SPIT tests is to study the interaction between high-pressure jet streams and water pools. The objectives of these tests are (1) to determine the type and location of the interaction, and (2) to identify and quantify the loads generated during the interaction for designing the HIPS test fixture and instrumentation.

The first objective is concerned with identifying the instrumentation that will be required to properly diagnose the interaction when visual access is not available. For example, the ZPSS assumes

that a cavity filled with water will cause a steam bubble to form; the growth of the bubble subsequently causes the cavity to be completely purged of water with no net effect on the debris dispersal mechanisms. SPIT tests using transparent cavities will be used to verify this hypothesis and to study the behavior of the steam bubble.

Table 1-VI

Aerosol Characterization Test Matrix

	Coded Variable				Actual Variable			
Trial	X_1	X_2	X_3	X_4	Pressure (atm)	Gas	Temp K(°C)	Jet Height (m)
1	0	0	0	0	63	N_2/CO_2	2523 (2250)	0.9
2	.	+	+	+	150	N_2	3273 (3000)	1.6
3	−	+	+	−	13	N_2	3273 (3000)	0.2
4	+	−	+	−	150	CO_2	3273 (3000)	0.2
5	−	−	+	+	13	CO_2	3273 (3000)	1.6
6	+	+	−	−	150	N_2	1773 (1500)	0.2
7	--	+	−	+	13	N_2	1773 (1500)	1.6
8	+	−	−	+	150	CO_2	1773 (1500)	1.6
9	−	−	−	−	13	CO_2	1773 (1500)	0.2
10	0	0	0	0	63	N_2/CO_2	2523 (2250)	0.9

The second test objective is concerned with measuring the potentially large hydraulic loads that can be generated during a melt/water interaction. It is anticipated that a fully filled cavity will generate significantly larger forces than a partially filled cavity because the expansion is more confined. The information will be used to confirm that the design of the HIPS structure will prevent catastrophic damage from occurring. The ZPSS showed that the conditions existing at the time of the accident and the subsequent response of the system will determine the amount of water existing in the cavity. Similarly, the temperature of the water will also depend on the source of water (break in the primary system or discharge of a stored volume), the extent of steam condensation, and the degree of passive cooling that has occurred. Pool depth can range from a dry cavity to one that is filled to the bottom of the reactor pressure vessel (RPV). The ZPSS analyzes these two extremes of water depth, plus a third situation involving 0.5-m water depth.

21

The above discussion suggests that the interaction process involves a number of independent variables, e.g., pool depth, water temperature, melt velocity, and melt temperature. The range of these variables could be used as input to developing a factorial representation of their effect. The objective of these tests, however, is not to fully characterize the interaction process but only to provide enough information to allow designing the cavity tests. Therefore, a complete factorial test strategy will not be used. Instead, a select number of tests will be conducted to address the specific aspects of the objectives stated above.

To simplify the test strategy, it is assumed that the melt/water interactions fall into one of two accident categories: sequences with either fully filled cavities or where the melt will propagate through the atmosphere before contacting the water. The distance of propagation appears to affect the velocity and perhaps the diameter of the melt, but the former effect in the high-pressure discharge is not significant compared to the pressure-induced velocity.

Two experiments will be used to study the case of the water-filled cavity. The first test will use a container of water having a large mass relative to the quantity of melt. Dimensions of the box are 0.6 by 0.6 m in lateral directions by 1.1 m in depth. The water pool will be placed just under the melt generator to simulate a water-filled cavity. The objective of the test will be to monitor the steam bubble growth and propagation.

The ZPSS estimates bubble growth by assuming that all the material coming out of the pressure vessel is instantly quenched. The pressure within the bubble continues to increase and the bubble to expand. The rate of bubble growth as derived from the basic equations given in the ZPSS is:

$$\frac{dP_b}{dt} = \frac{3}{r_b}\left[\frac{RT}{2\pi r_b^2}(\dot{m}_q - \dot{m}_c) - P_b\frac{2}{3}\left(\frac{P_b - P_\infty}{P_\ell}\right)^{1/2}\right] \tag{1.20}$$

where

P_o = pressure in the bubble (instantaneous)

r_b = bubble radius

R = gas constant

T = absolute temperature

t = time

m_q = steam formation rate

22

m_c = condensation rate

P = atmospheric pressure

P_b = pressure in the water away from the bubble

The ZPSS derivation of this dP_b/dt expression from the same basic equations does not include the $(1/2 \, r_b^2)$ factor in the first term in the equation. The steam formation and condensation rates are given by:

$$\dot{m}_q = \dot{m}_F C_F (T_F - T_{sat})/h_{fg}$$

$$= A_f [2\rho_F (P_o - P_b)]^{1/2} C_F (T_F - T_{sat})/h_{fg} \qquad (1.21)$$

$$\dot{m}_c = h_b (2\pi r_b^2)(T_{sat} - T_B)/h_{fg} \qquad (1.22)$$

where

A_F = area of breach in melt generator

ρ_f = density of melt

P_o = melt specific heat

T_F = temperature of melt

T_{sat} = saturation temperature in the bubble

h_{fg} = heat of vaporization

h_b = heat transfer coefficient at the surface of the bubble

T_B = temperature of the water away from the bubble

The pressure in the water (P_ℓ) must be known to allow calculating the pressure in the bubble. For the geometry in the reactor, the expansion of the bubble is transmitted to the walls of the cavity and a portion reflected back at some fraction of the incident pressure. The velocity of the propagation is assumed to be given by the compressive wave velocity. The interactions of the reflected wave patterns are complicated by the geometry of the cavity; waves returned by the side walls will be out of phase with those returned from the floor and instrumentation tunnel. These interactions are not considered in the

23

ZPSS analysis; only the wave propagation in the instrument tunnel to the free surface on the containment floor is included. The calculated bubble and cavity pressure histories are given in Figure 1.1-4 (Ref. 1-2, Figure 3.2.9-6). The influence of the open instrument tunnel causes the cavity pressure to decrease after the initial rise.

The walls of the rectangular box described above for the SPIT test are not prototypic in that they are neither completely rigid nor of the same composition. This means that the mean pressure in the water (cavity pressure) will be proportionally less than seen in the reactor case with rigid walls. The floor of the box is firmly supported and will be assumed to be rigid. The presence of the free upper surface will allow the expansion of the bubble to be absorbed as movement of the water surface. The net effect of these changes will be to underpredict the influence of the water pressure on the bubble growth. In other words, the bubble growth rate will be greater in the experiment than in the accident. To a first approximation, the response of the system can be evaluated by considering the mechanical impedances of the water and interface material. The impedance of a material is given by [1-6]:

$$Z = \rho \mu_o \qquad (1.23)$$

where

Z = impedance

ρ = density

μ_o = longitudinal bulk sound speed

Four materials are of interest in the experiments and accident: water, plexiglass, steel, and concrete. Standard material properties are obtained from Ref. 1-7 and 1-8 and are given in Table 1-VII.

A compressional wave in water incident on an interface will cause a "partitioning" of the incident stress based upon the relative impedances of the materials. A simple approximation of the relative magnitudes can be found from the expressions:

$$P_T = P_o \frac{2Z_A}{Z_A + Z_B} \qquad (1.24)$$

$$P_r = P_o \frac{(Z_B - Z_A)}{(Z_B + Z_A)} \qquad (1.25)$$

24
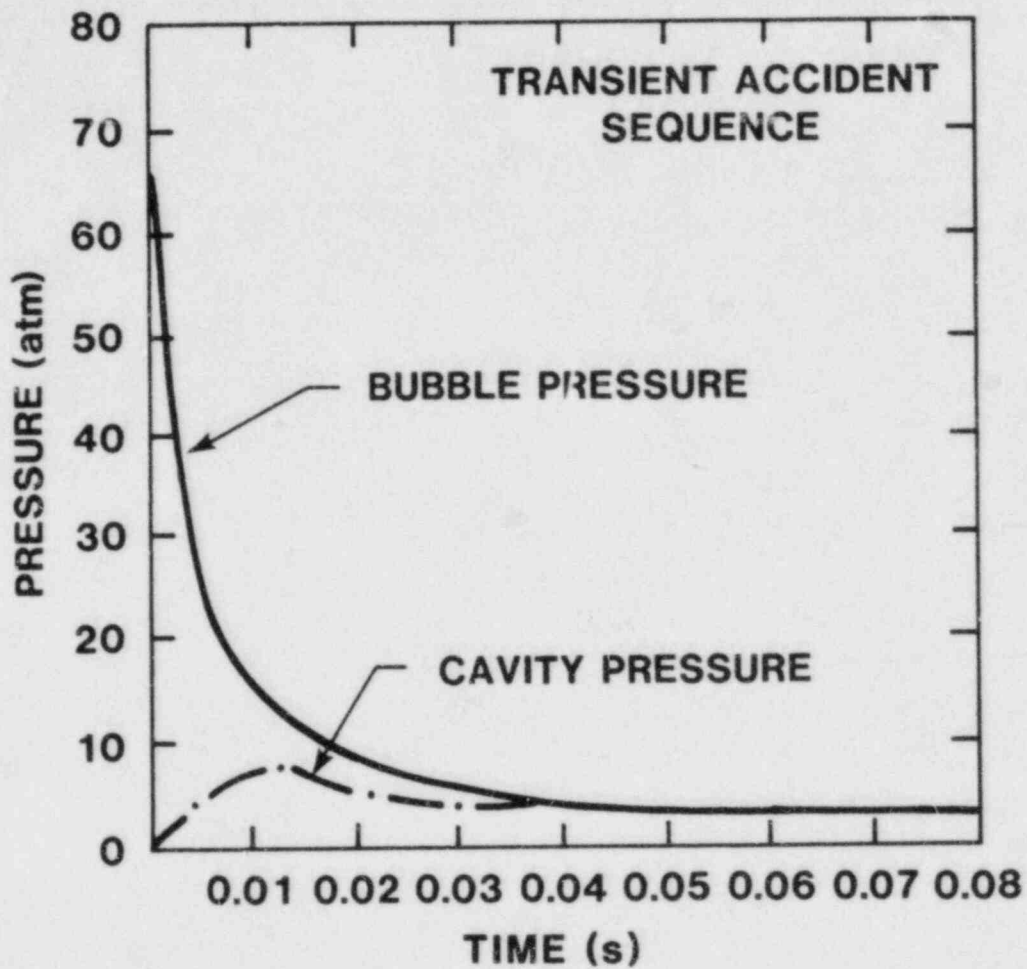
Figure 1.1-4. Bubble and Cavity Pressure Histories for a Water-Filled Cavity

where

P_o = incident stress level

P_T = transmitted stress into material B

P_r = reflected stress

Z_L = impedance of material i

Table 1-VII

Material Properties for Impedance Calculations

Material	Density (kg/m^3)	Sound Speed (m/s)	Impedance
Water	1000	1500	1.5×10^6
Plexiglass	1180	2680	3.2
Steel	7850	5960	46.7
Concrete	2340	4000	9.4

In Equation 1.25, P_r represents the pressure that is reflected back into the incident material and superimposed on the initial stress level. In the limiting case of a free surface ($Z_B = 0$) then $P_r - P_o$, and the pressure at the interface has the magnitude of twice the incident pressure (P_o incident plus P_o reflected). If P_o is constant at the source, then the reflected rarefaction from the interface travels back to the source at nominally the bulk sound speed, but the free-field stress is doubled.

The other limiting case is when material B is of infinite impedance so that $P_r = 0$ and no reflection occurs at the interface. The pressure on the wall is then P_o. In this situation, the thickness and rigidity of the second material must be considered to determine whether any stress is returned to the incident material by subsequent interface reflections.

The adequacy of using a plexiglass box to simulate the concrete cavity can be estimated by comparing the reflected pressure levels for both situations.

26

For plexiglass:

$$P_r = P_o \frac{(3.2 - 1.5)}{(3.2 + 1.5)}$$

$$= 0.36 \ P_o \qquad\qquad (1.26)$$

For concrete:

$$P_r = P_o \frac{(9.4 - 1.5)}{(9.4 + 1.5)}$$

$$= 0.72 \ P_o \qquad\qquad (1.27)$$

Thus, the reflection of a plane wave from a plane surface is one-half the magnitude for plexiglass as for concrete. Thus, the pressure in the water (P_ℓ) will be less in the experiment than in the accident. Even though the plexiglass walls are not rigid, the relative impedances will cause the water to maintain contact even as the wall moves outward. Therefore, the reflected stress from the wall will be maintained until the displacement of the wall causes the elastic limit to be exceeded and permanent deformation occurs.

The same analogy can be used if the upper water surface is exposed to the atmosphere. Pressure pulses propagated to the interface will reflect at twice the initial amplitude. If the reactor cavity is filled with water, then the presence or absence of trapped air pockets will affect the magnitude of the reflected wave. Assuming that no air exists in the accident dictates that the water box be covered in the experiment. For better simulation, wave interactions in the reactor are very complicated because of geometric and bubble geometries. The forces acting on the initial bubble generation suggest the geometry to be hemispheric. The compression waves emanating from the bubble will then be curvilinear as opposed to planar. Thus, reflections from interfaces will be returned in the same manner so that the arrival times at the bubble are sequential. Likewise, waves incident at other than normal to a plane surface will reflect at a complementary angle and not back toward the source location. Plane- or curved-wave fronts incident on curved surfaces such as the cavity wall will be reflected in a distorted manner.

The period of time when the walls in the experiment do not influence the steam bubble can be estimated by considering wave interaction times. Considering the initial steam generation as a point source, the wave transit time is given by the dimensions of the box and the sonic water velocity:

$$t_1 = \frac{2\Delta x}{C} = \frac{2(30 \ cm)}{0.15 \ cm/\mu s} = 400 \ \mu s \quad (horizontal) \qquad (1.28)$$

27

$$t_2 = \frac{2 \Delta Y}{C} = \frac{2(110 \text{ cm})}{0.15 \text{ cm}/\mu s} = 1.47 \text{ ms (vertical)} \qquad (1.29)$$

The dimension in t_1 (30 cm) represents the horizontal distance from the center of the stream to the nearest edge of the box. The times, t_1 and t_2, represent the transit times of the initial compressional. As the bubble expands, the distance will become less, depending on the growth of the bubble and the motion of the sidewalls. The calculated transit times are short compared to the discharge time of the generator, suggesting that pressure excursions due to reflection from the walls will be quickly equilibrated in the system.

The results from above can be compared to that expected during an accident. For this case, the transit time corresponds to the radius or depth of the reactor cavity.

$$t_1 = \frac{2(260 \text{ cm})}{0.15 \text{ cm}/\mu s} = 3.5 \text{ ms} \qquad (1.30)$$

$$t_2 = \frac{2(450 \text{ cm})}{0.15 \text{ cm}/\mu s} = 6 \text{ ms} \qquad (1.31)$$

Comparing these times to those of the experiments indicates that the times are scaled in the range of 1 to 10 to 1 to 4.

The above analysis for the jet into a water-filled box suggests that the experiment will underpredict the influence of the reflected expansion waves on the bubble growth pattern. Thus, if a bubble is not observed during the experiment, it is highly likely that bubble growth will not be manifested during the reactor accident. The converse, however, is not true; the low magnitude of the reflected stress may not be sufficient to prevent the establishment and growth of the bubble. Stress waves reflected from the concrete cavity will be roughly doubled in magnitude and very likely different in pattern from the experiment.

Performing the above experiment may establish the existence of a steam bubble but will not determine the influence of the subsequent wave interactions from side walls or the probability that the water will be expelled. In the reactor cavity, the compressional waves will propagate away from the boundary of the steam bubble until an interface is contacted, either the cavity walls, the RPV, or the free surface of the pool. The interactions of the waves are very complex due to the differences in the geometry of the bubble, cavity floor, and vessel. Focusing of the reflected waves may cause instabilities in the bubble, inducing destructive fragmentation and dissipation of the bubble energy. The waves may also constructively interact at an interface boundary to concentrate pressure loadings on portions of the cavity.

The second jet/water interaction test is designed to cause the wave interactions to occur in a prototypic manner to find the amount of expelled water and the structural loads placed on the cavity by the hydraulic forces in the water pool. For this test, a scaled-cavity geometry will be used to maintain the correct wave interaction transit times. Linear scaling can be used because the wave transit time is proportional to first power of the distance traveled. The cavity will be constructed of aluminum to simulate the impedance of the reactor cavity. Using the relationship for reflected pressure:

$$P_r = P_o \frac{(17.3 - 1.5)}{(17.3 + 1.5)} = 0.84 \ P_o \qquad (1.32)$$

The strength of the reflected shock waves will underpredict the reactor case by approximately 20%. The strength of the returned waves is assumed to be detrimental to the bubble formation and growth. Thus, if the bubble is not manifested in the scaled-cavity test, it is also assumed not to exist in the accident.

The second objective of the test is to determine the hydraulic loads placed on the cavity structure by the jet/water interaction. Pressure transducers placed in the sidewall and floor of the cavity will measure the value of P_r at that location. Mapping the values of P_r for all locations allows determination of the total load placed upon the structure.

The magnitude of the pressure-pulse can be estimated from a presumed thermal-to-mechanical conversion efficiency. Typical values of conversion efficiency for energetic interactions are estimated to be on the order of 1% or less.[1-9] Using 1% as a basis and assuming that all of the melt contributes to the mechanical energy in the form of pressure/volume work yields the following:

Total adiabatic thermal energy = 10 kg x 3.6 MJ/kg

= 36 MJ

Mechanical work = 0.01 x 36 MJ = 0.36 MJ

For an expansion process, the work is equal to the applied force, F, integrated over distance or the displacement, ds.

$$\text{Work} = \int F ds = \int (PdV + VdP) = \int VdP \qquad (1.33)$$

where the PdV term is zero for a closed system in which the volume does not change. When the expanding pressure wave reaches the cavity wall or floor, the existence of the free surface at the end of the

keyway is not yet a factor and the volume, V, can be approximated by the cylindrical cavity alone. Therefore,

$$\text{Work} = V \int dP = V(P_2 - P_1) = V\Delta P \qquad (1.34)$$

$$\Delta P = \frac{\text{Work}}{V} = \frac{0.36 \text{ mJ}}{2.13 \times 10^{-2} \text{ m}^3} = 1.69 \times 10^7 \frac{\text{Nt}}{\text{m}^2}$$

$$= 167 \text{ atm}$$

This value represents the incident pressure on the sidewall, P_o. The pressure the cavity must withstand is given by the sum of P_r and P_o.

$$P_{wall} = P_o + P_r = P_o(1 + 0.84) = 308 \text{ atm} \qquad (1.35)$$

This value can be used to compute the thickness of the cylindrical side wall by allowing the hoop stress to be equal to the yield value of the material, (42,000 psi for 6061-T6).[1-10] The hoop stress in a thick-wall pipe is given by the expression [1-11]:

$$\text{Stress} = \frac{P_a^2}{c^2 - a^2}\left(1 + \frac{c^2}{a^2}\right) \qquad (1.36)$$

where

a = inner radius

b = outer radius

P = internal pressure

Solving the equation above, using a = 13 cm, gives a minimum value for the outer radius of 16.5 cm. Thus, the 1/20-scale cavity will be constructed of commercially available aluminum shapes, using welds to insure a leakproof structure.

The two tests described above do not indicate the behavior when the cavity is partially filled with water. When only a portion of the cavity is filled with water, the free surface will expand, causing water to be thrown away from the pool. The free surface also causes a near-total reflection of the incident pressure wave. The specific purpose of the remaining two SPIT jet/water tests is to determine the

location and characteristics of the interaction, particularly the disposition of the water and the magnitude of the hydrodynamic pressures involved. Two scaled cavities will be used, one of plexiglass and the other of aluminum. The clear cavity will allow visualization of the interaction region with high-speed cameras in order to determine location and behavior. These data will be compared to the previous water-filled tests to aid in developing the HIPS test strategy and instrumentation requirements. The results will also confirm the ZPSS assumption concerning the fine fragmentation of the melt stream during the interaction. The plexiglass will not have adequate strength to allow a prototypic interaction to proceed to completion. This fact can be illustrated by the magnitude of the stress pulse that is transmitted into the plexiglass.

$$P_t = P_o \frac{2Z_A}{Z_A + Z_B} = \frac{2(1.5)}{(1.5 + 3.2)} \, (308 \text{ atm})$$

$$= 196 \text{ atm} \tag{1.37}$$

The transmitted stress will propagate through the plexiglass until the wave reaches the wall/air interface where it is reflected as a rarefaction wave. The wave will then return to the inner wall interface where a partitioning of the stress will occur due to the water impedance. The result will be a large amount of momentum transferred into the relatively weak plexiglass structure. The trapped momentum will cause gross deformations and failure due to bending stress or separation of bonds between sections of the structure.

The duration of the interaction can be estimated by considering the time required for the pulse to propagate through the water, plus the time required for the plexiglass to equilibrate to the transmitted stress level. This is normally assumed to require five reverberations of the stress pulse (double transit times).

$$t = \frac{a}{V_{H_2O}} + \left(5 \times 2 \times \frac{thk}{V_{PMMA}} \right) \tag{1.38}$$

where

thk = thickness of plexiglass

V = velocity of shock pulse

31

$$t = \frac{127}{1.5} = \frac{5 \times 2 \times 6}{2.7}$$

$$= 106.9 \ \mu s$$

Thus, gross motion of the plexiglass walls is estimated to begin approximately 0.1 ms after the jet first contacts the water.

The amount of melt ejected from the crucible is equivalent to the jet mass flow rate times the time required for the jet front to propagate to the water pool. The lower bound on the time is for the highest velocity discharge, combined with the deepest water pool.

$$m = \dot{m} \left(\frac{h}{V_{jet}} \right) \tag{1.39}$$

where

$\dot{m}$ = mass flow rate

h = height from vessel to pool surface

V_{jet} = velocity of the jet

$$m = \frac{212 \ kg}{s} \left(\frac{0.17 \ m}{71 \ m/s} \right) = 0.51 \ kg$$

For the worst-case sequence, only 1/20 of the melt mass will be outside the vessel when the jet contacts the water surface. Additional fine fragmentation beyond this amount will then depend on the time delay until the interaction occurs, plus other interactions that may occur with delivery of new material.

The second test article was constructed of aluminum to simulate the infinitely rigid structure of the reactor cavity. As indicated in the previous discussion of the water-filled chamber, the aluminum closely matches the impedance of concrete so that the wave interactions will be prototypic. The rigid walls also allow pressure sensors to be installed in the side walls and other locations to monitor the hydrostatic and gas pressure pulses. These data will be used to correlate with the ZPSS predictions and also allow assessment of the survivability of the proposed HIPS cavity geometry and instrumentation.

1.1.3.5 SPIT Scaled-Cavity Tests

The remaining objective of the Phase II SPIT test matrix will be to obtain quantitative data on the jet stream behavior in a 1/20-scale concrete cavity. The test is intended to be a verification of the instrumentation techniques and test methodology for HIPS, but the results will be important, together with HIPS, in determining scale effects. The test provides the first opportunity to study jet behavior and debris removal mechanisms in a realistic geometry, using a prototypic concrete.

Figures 1.1-5 and 1.1-6 illustrate some of the features of the concrete test article that has been constructed for this test. Not all of the features of the Zion plant are included, such as the instrumentation tube bundle and the sump pit at the end of the tunnel. The fixture is constructed with a parting line located along the ceiling of the instrumentation tunnel. This feature allows separating the unit after the test for inspection and cleanup. The concrete is generic limestone-common sand of composition given in Ref. 1-12.

The SPIT pressure vessel is accommodated in the cavity by using a cast-in-place flange cover at the scaled height of the reactor vessel. The cover also provides pressure sealing of the cavity from the region above the vessel to simulate the biological shield used in the Zion installation.

Meeting the objectives of the matrix may require that more than one cavity test be performed. The first experiment will be conducted at clearly established test conditions based on the jet characterization results. Subsequent tests with the same cavity may not be suitable for assessing debris relocation because damage to the cavity may have been incurred. A marginally damaged cavity would be acceptable for observing other phenomena such as jet/water interations, cavity pressurization, aerosol generation and transport, and debris fragmentation.

The test fixture will be installed in a closed chamber to contain the debris and aid in the assessment of aerosol behavior. The chamber is in the form of a horizontal cylinder, approximately 2 m in diameter and 3.4 m long with flat-plate covers on each end.

1.1.3.6 SPIT Phase II Test Matrix

Table 1-VIII summarizes the experimental matrix to be performed to satisfy the objective of the Phase II SPIT test program. As indicated previously, the characterization and aerosol tests have conflicting instrumentation requirements. A reduction in the total number of tests will be realized when the jet characterization experiments are moved into the closed chamber. This action will be implemented when the melt-stream pulsed X-ray data are adequate to allow predicting the system over the response surface.
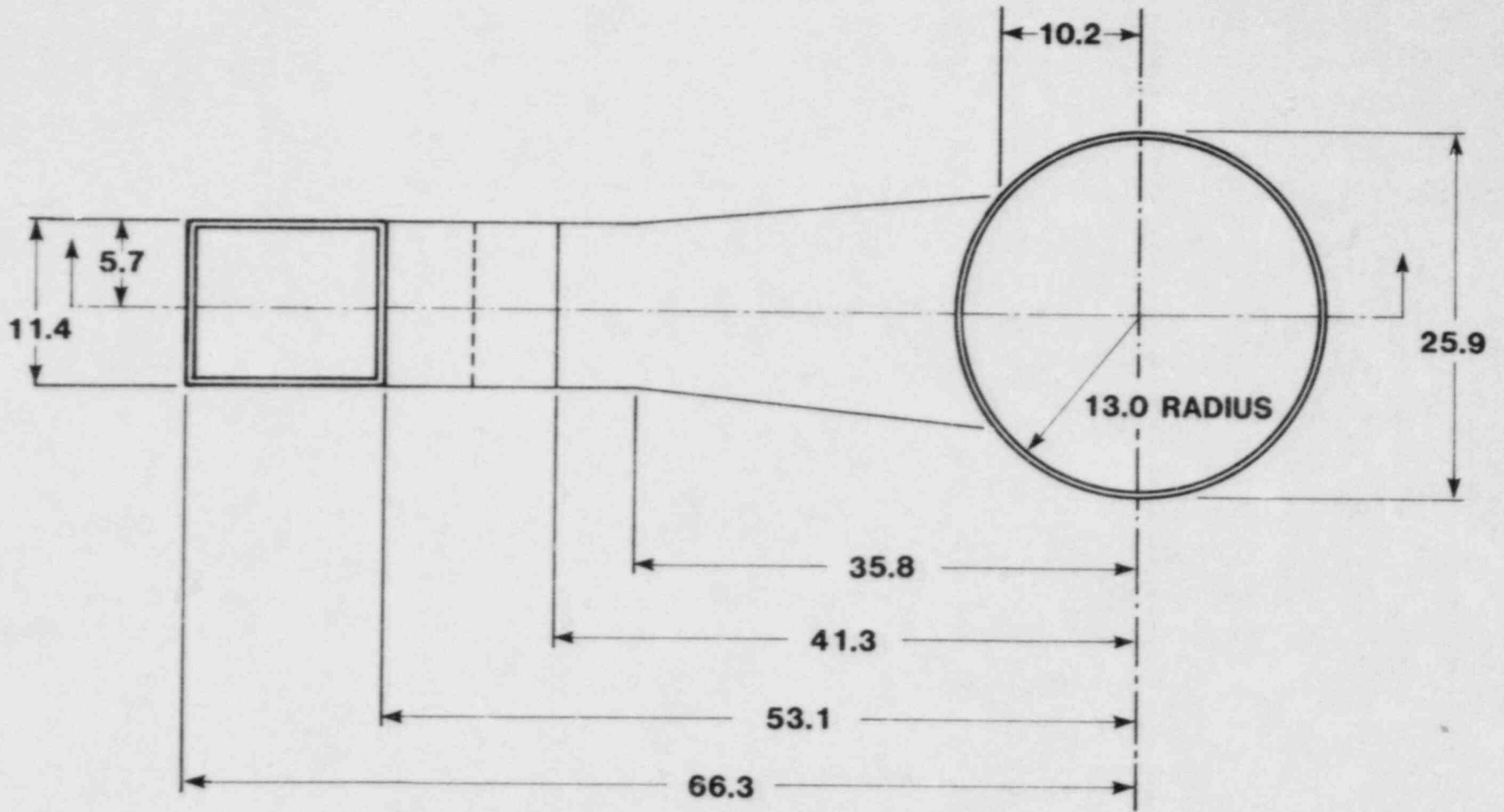
Figure 1.1-5.   SPIT 1/20-Scale Cavity Dimensions - Top View (cm)
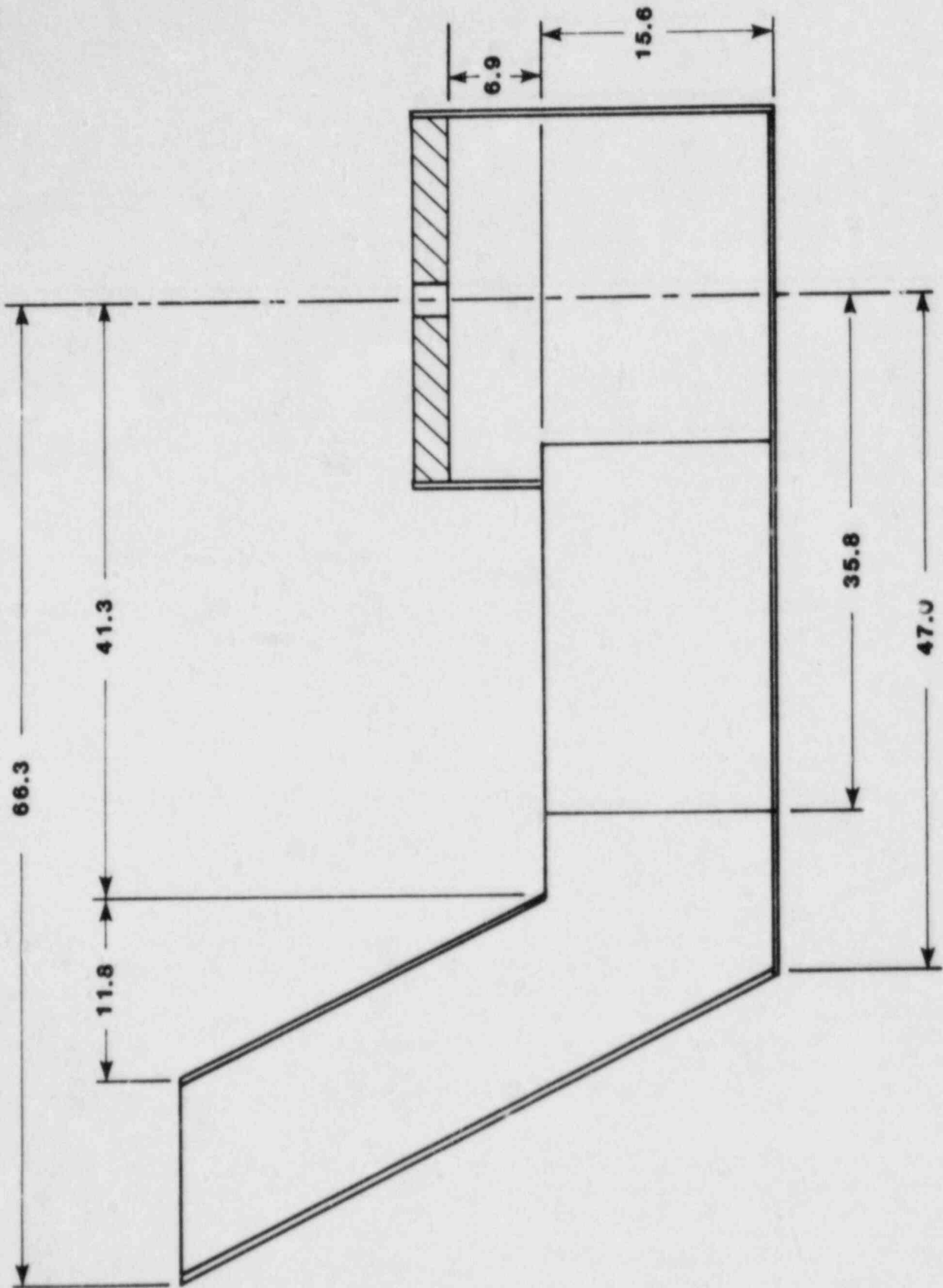
Figure 1.1-6. SPIT 1/20-Scale Cavity Dimensions - Section A-A (cm)

Table 1-VIII

SPIT Phase II Test Matrix

Number of Tests	Purpose	Characteristics
10	Jet characterization	Temperature, pressure, and gas solubility varied to assess affect on jet behavior
10	Aerosol tests	Temperature, pressure, cover gas, and jet height varied to assess type and extent of aerosol generation
4	Jet/water interaction	Determine existance of steam bubble, location and character of interaction, extent of water removal, debris fragmentation
1	Scaled cavity	Observe debris removal mechanisms, verify instrumentation techniques and devices

1.2 CORE RETENTION MATERIALS ASSESSMENT
(J. D. Fish, 6422; M. Pilch, 6425; E. R. Copus, 6422;
T. Y. Chu, 7537; F. E. Arellano, 6422; J. H. Bentz, 7537)

1.2.1 Introduction

The Core Retention Materials Assessment program involves both ex-
periments and analysis designed (1) to determine the fundamental limi-
tations of candidate core retention materials and concepts and (2) to
develop a data base for use by the NRC in licensing review of proposed
ex-vessel core retention devices. The program is currently focused on
magnesia brick crucibles, thoria and alumina particle beds, and high-
alumina concrete liners.

1.2.2 SWA-3 Test

The first practical application of the inductive-ring susceptor
(IRIS) technique was carried out during the current reporting period.
The objectives of this test were to:

a. Demonstrate that the IRIS technique could form a larger mass
   of molten material than those formed during the SOT series.

b. Demonstrate passive tapping of the melt crucible by erosion of the center of a zirconia board placed in the bottom of it.

c. Demonstrate that a UO_2-based melt would penetrate a layer of 1- to 2-cm alumina particles but would be stopped by a layer of 0.3- to 0.4-cm alumina particles.

d. Determine if alumina particles would float in the more dense melt.

A melt crucible 45.7 cm high and 19 cm in diameter was formed by joining two alumina sleeves. The core material and equally-spaced tungsten rings were packed into the upper three quarters of the crucible. The lower quarter of the crucible contained an alumina particle bed. A 2.5-cm zirconia board separated the two parts of the test fixture. Based on TAC2D calculations, the ring susceptors would melt the charge material, which would then eat through the zirconia board and pour down on the alumina test bed (Figures 1.2-1 and 1.2-2).[1-13]

SWA-3 was assembled during the week of 14 February. In order to increase the molten pool mass, three types of "core material" were employed:

1. Dense chunks ($\rho \simeq 10$) of solidified material taken from the remains of SOT III and IV. These chunks were a mixture of 45% U/40% UO_2/15% ZrO_2 and 80% UO_2/20% ZrO_2 and had a total mass of 7.6 kg.

2. A relatively dense ($\rho \simeq 5$) mixture of 48% UO_2/40% U/11.5% ZrO_2. This powder (16.8 kg) was poured down the center of the alumina sleeve in an effort to densify the most probable melt zones.

3. A less dense ($\rho \simeq 4$) mixture of 63% UO_2/22% U/15% ZrO_2 was poured around the inside diameter of the alumina sleeve. This had a mass of 10.0 kg and was expected to have a lower thermal conductivity than either of the other two types of "core material."

Thus, the total charge weighed 34.4 kg and had an average density of 5.2 g/cm^3. Of the 34.4 kg, nearly 20 kg were in the central 40% of the sleeve volume. This was expected to form the bulk of the central pool.

A pretest X-ray of SWA-3 showed that the central portion of the charge was indeed more dense than the periphery, that the bottom ring of the assembly had tilted slightly, and that the zirconia board had slipped about 1.5 cm. Nonetheless, SWA-3 was loaded into an inert argon environment and run on 17 February. This test was run for 10 hr at an average power level of 11 kW (Figure 1.2-3). Thermocouple data monitored during the test indicated that a large pool had formed and that the pool was slowly penetrating downward. Downward penetration was much slower than anticipated, however, and after 10 hr, the test
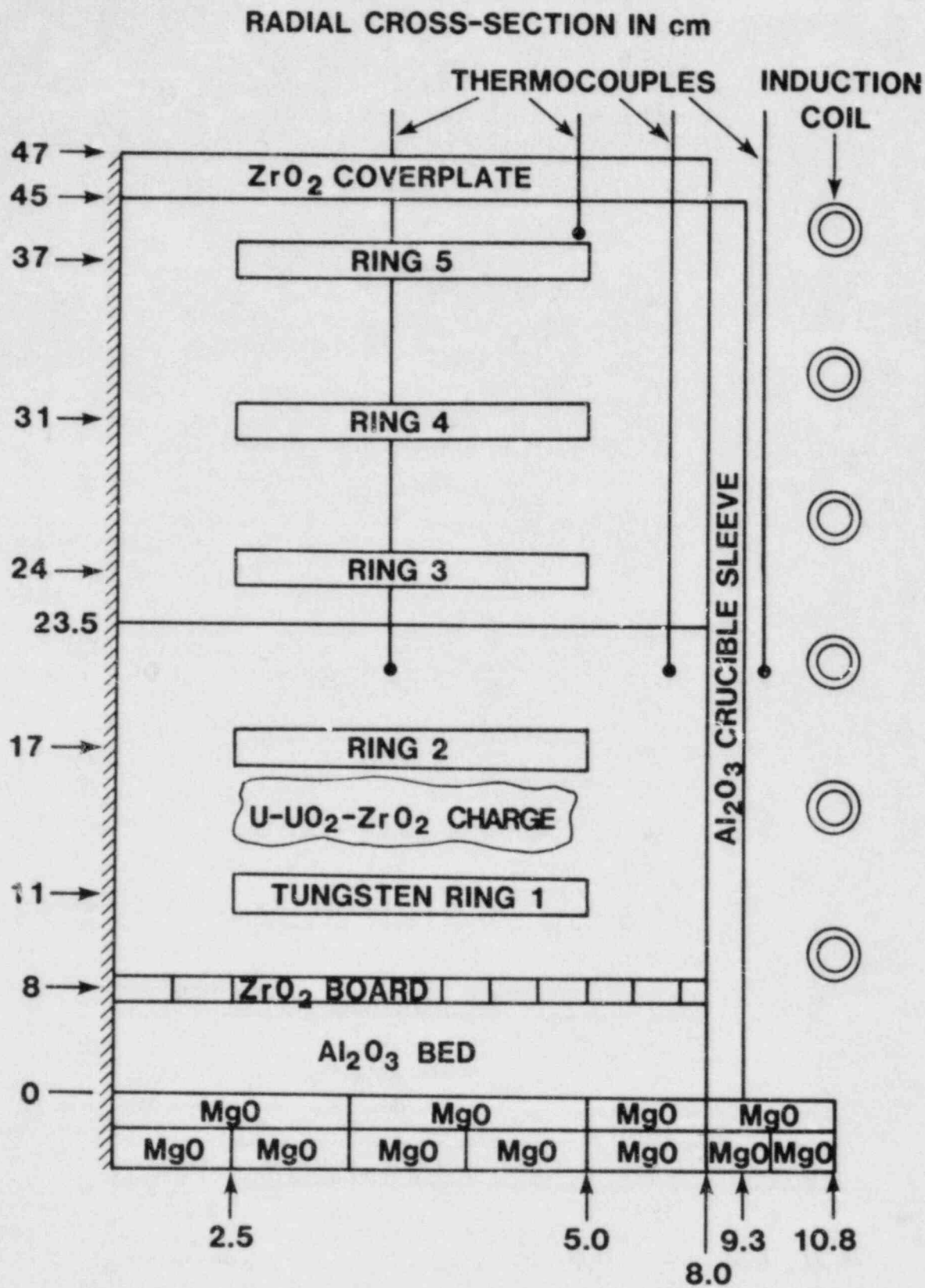
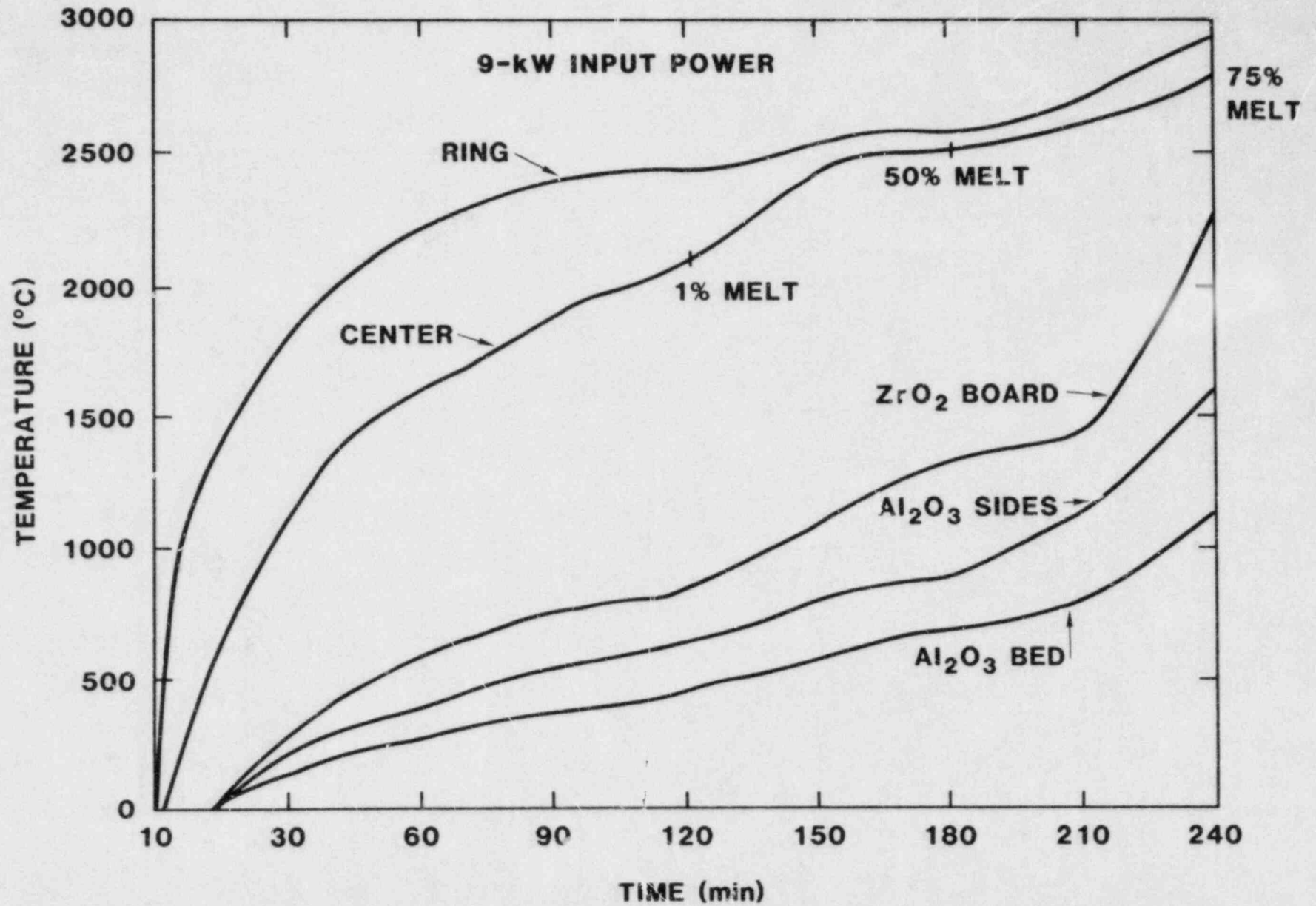Figure 1.2-1.   SWA-3 Pretest Configuration

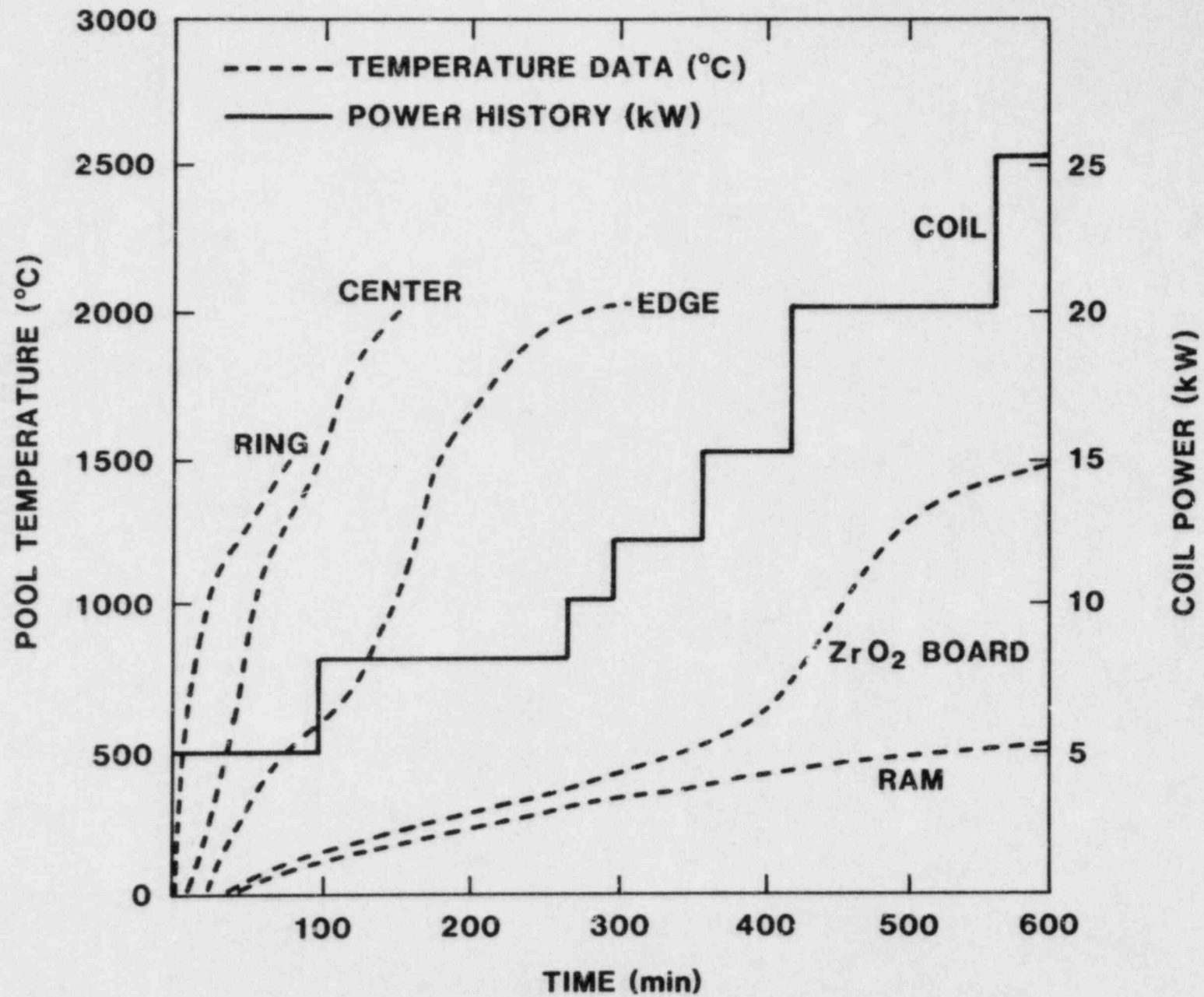Figure 1.2-2. Pretest SWA-3 Temperature Profiles

Figure 1.2-3. SWA-3A Power and Temperature Data

was postponed due to a series of abnormal thermocouple readings along with a loss of coupling efficiency.

A posttest X-ray indicated that a large pool had formed in the alumina sleeve but that the zirconia board was only partially eaten away. It also appeared that four of the five tungsten rings were missing and that the sidewalls of the sleeve were penetrated along the upper edge of the molten pool. Consequently, the alumina sleeve was dismantled and the contents were examined. The one remaining ring (top ring) was intact and showed no signs of corrosion. The area below the top ring was void down to a solid slug (17.6 kg) that filled the section of the sleeve just above the zirconia board. Sidewall penetration of the sleeve had occurred near the top of the slug. The remaining four rings were found together well within the solidified slug. All four seemed to be intact, relatively unharmed, and tilted some 20° off the horizontal. These posttest observations seem to indicate that the anomalies that terminated the test were caused, at least in part, by the collapse of the ring support structure and that excessive heat losses had prevented a more rapid penetration of the zirconia board.

The experiment was redesigned and SWA-3B was constructed during the week of 21 February (Figure 1.2-4). Three deficiencies in the original design were addressed: (1) the distance between the bottom ring and the zirconia board was reduced from 5.5 to 2 cm, (2) the thickness of the zirconia board was reduced from 2.5 to 1.3 cm, and (3) the test bed was housed in a smaller crucible that was heavily insulated with alumina silicate fiber.

The charge material for SWA-3B weighed 20 kg. Most of this mass (11.8 kg) was in the form of the SWA-3A slug. This slug also contained four of the five original rings. The top ring from SWA-3A was positioned below the slug on 6-mil tungsten struts, and a sixth ring was positioned above the slug (also on struts). The central region was filled with 6.2 kg of 63% UO_2/22% U/15% ZrO_2 powder, and 2.0 kg of pure UO_2 was poured around the periphery.

SWA-3B was run on 24 February. The power history and the results are shown in Figures 1.2-5 and 1.2-6. Evaluation of the thermocouple data showed that the zirconia board disintegrated in 110 min at a power level of 10 kW. Initial penetration of molten core material appeared to stop somewhere above the small gravel and proceeded slowly until a power increase to 15 kW drove it downward again at the 150-min mark. Shortly thereafter, all remaining thermocouples in a bed failed simultaneously. A posttest X-ray of the SWA-3 configuration showed that a significant pool of UO_2 core material had formed and that the melt had penetrated the alumina bed down to the small gravel interface. The X-rays also showed that the melt had penetrated the sidewall of the alumina sleeve and had poured down the side of the crucible onto the bed thermocouple leads. Disassembly of the SWA-3 test confirmed that the thermocouples had been destroyed by the molten stream. Approximately 5 kg of core material penetrated the top layer of the alumina bed. This penetration stopped cleanly at the small gravel interface. Spheres at this interface remained mostly intact
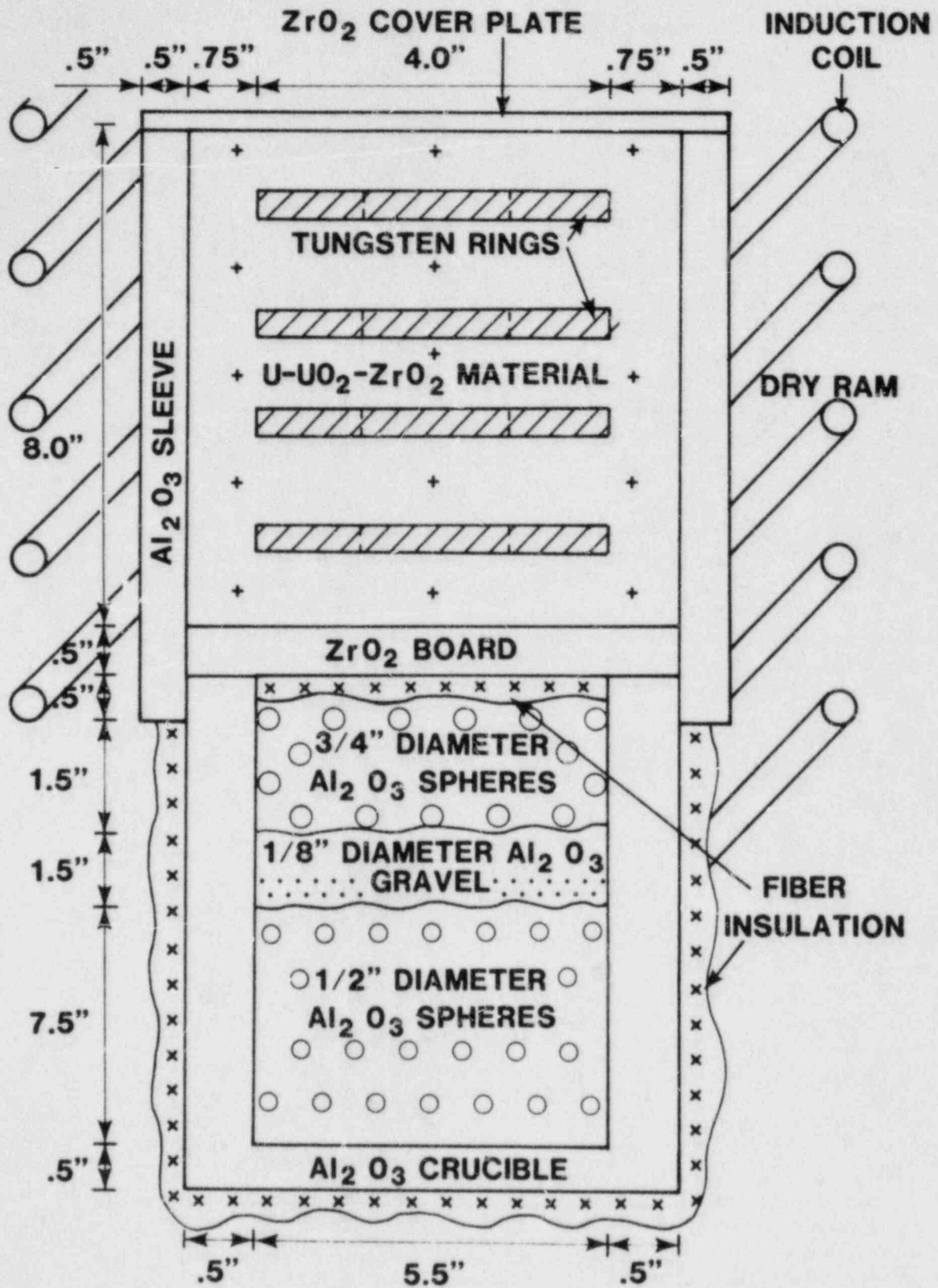
Figure 1.2-4.   SWA-3B Test Configuration

42
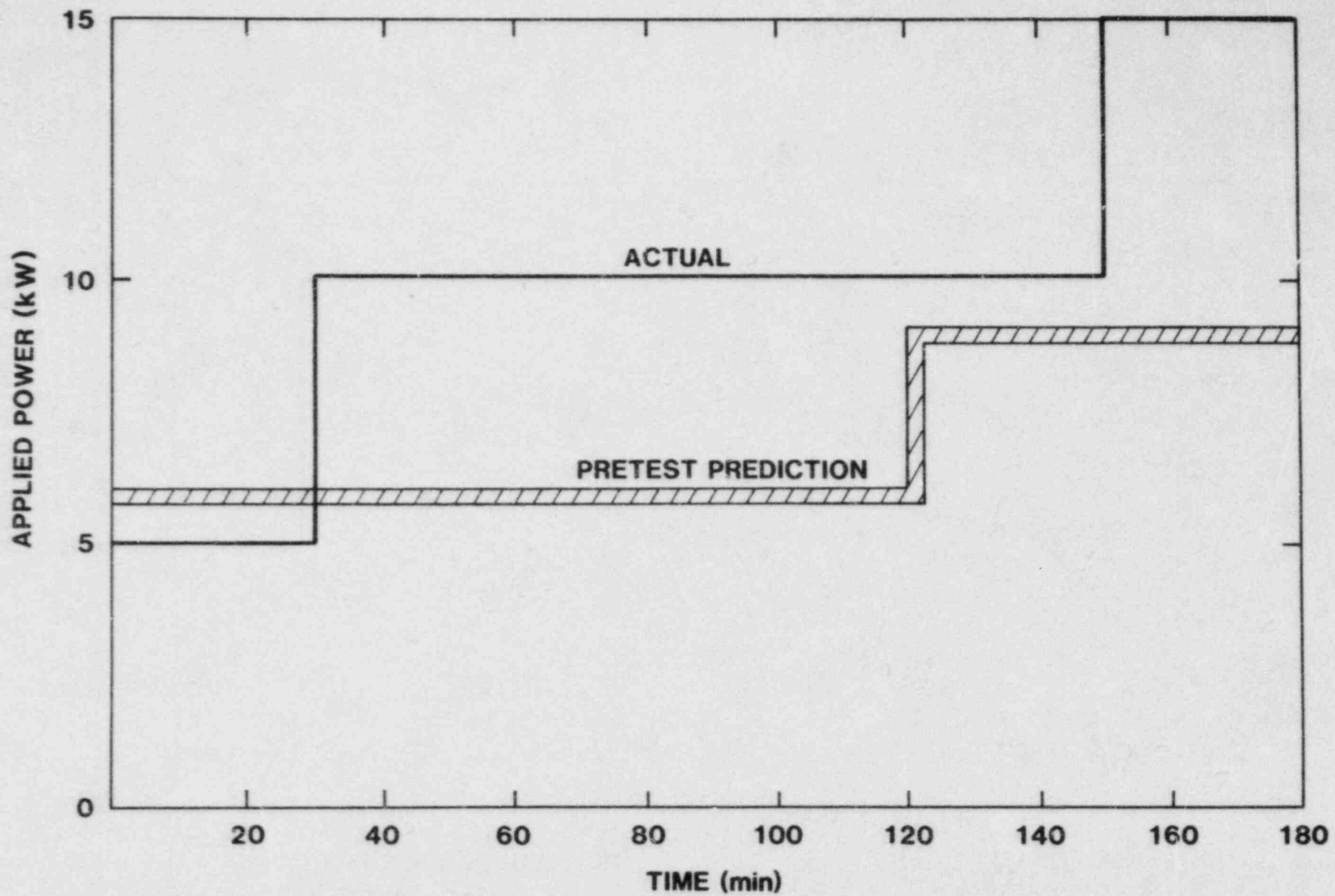
Figure 1.2-5. SWA-3B Power History
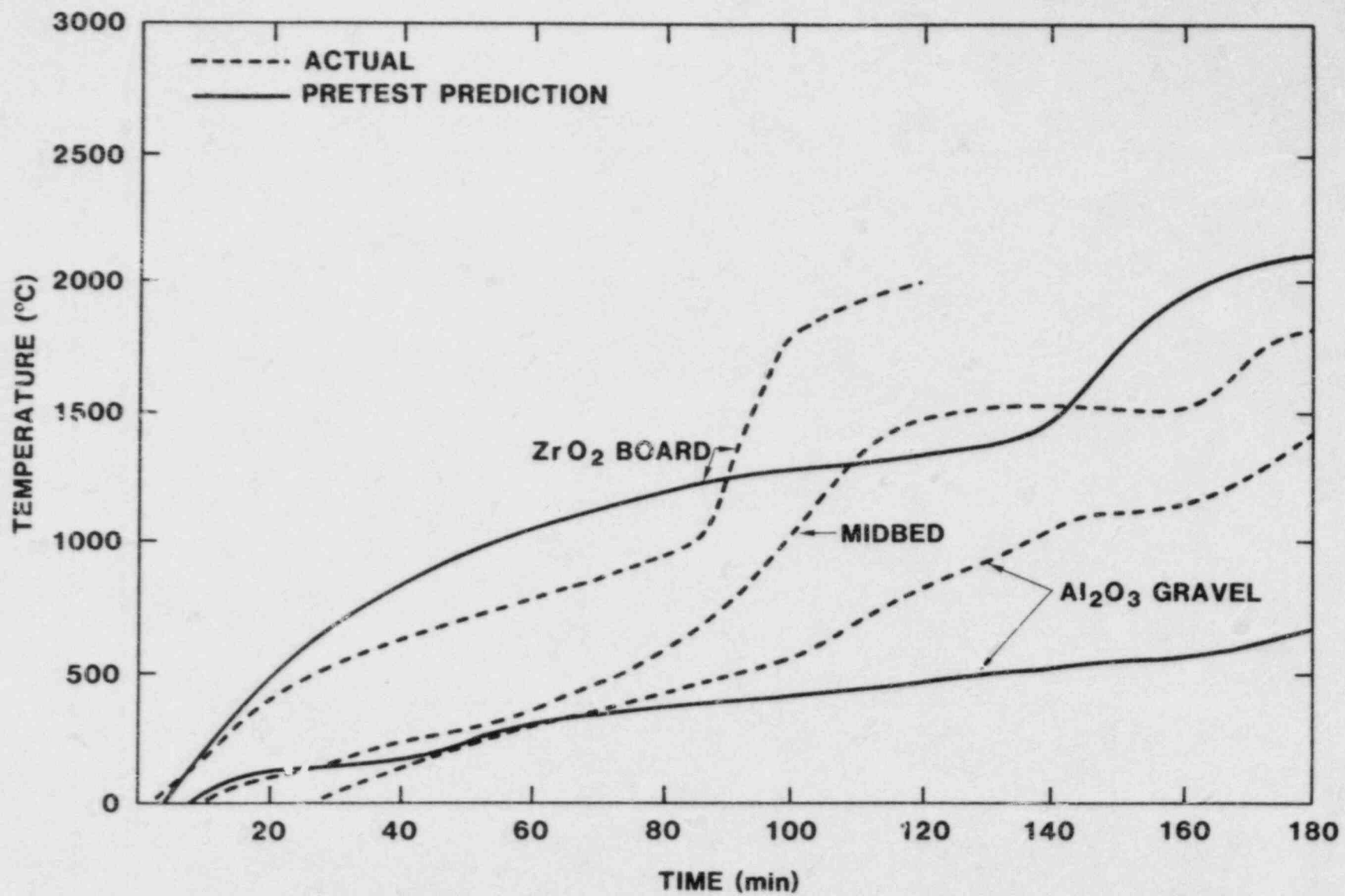
Figure 1.2-6. SWA-3B Temperature Data

whereas those above the interface had melted into the UO_2 core mixture, forming an Al_2O_3-UO_2 slag. The surface of the slag pool was smooth and showed no evidence that any of the Al_2O_3 spheres had floated or become detached from the bed.

The remainder of the charge was mostly molten but had not fallen down to the lower ring assembly. All six rings were recovered from the SWA-3B assembly intact and unharmed.

This test demonstrated that larger pools of UO_2 material can be achieved by preferentially loading the center of the crucible with high-density material. The SWA-3A test was three times larger than the SOT tests, and the molten pool was 50% of the total charge as compared to a 25% to 30% pool for the SOT III and SOT IV experiments. SWA-3B demonstrated that a slug of UO_2 material could be remelted using the original rings and that this remelt can be much faster.

Overall, the SWA-3 test demonstrated that a scale-up of the ring susceptor technique is feasible but that proper crucible insulation, proper ring spacing and support, and a proper power history are essential. It is quite likely that the SWA-3A test would have been successful if the power history and ring spacing had more closely matched the pretest calculations. Up to now, TAC2D code results have been used mostly as a measure of feasibility—hereafter these analyses may well be used as a predictive control parameter.

SWA-3 also demonstrated that small-diameter alumina gravel will control initial penetration of alumina particle-bed core retention schemes, that large Al_2O_3 spheres do not readily float upward following such a penetration, and that a UO_2-alumina slag forms on top of the melt as it penetrates the core retention bed.

1.2.3 Particle Bed for IRIS

The IRIS test, scheduled for execution in the third quarter of FY83, will involve the melting of 100 to 200 kg of UO_2/ZrO_2 by the IRIS technique and the deposition of this melt onto an alumina particle bed.

A cross section of the circular bed is shown in Figure 1.2-7. The center of the bed is a cylindrical section of 1.9-cm alumina spheres. The section is 28 cm in diameter and 10 cm thick. The rest of the bed consists of 0.3- to 0.4-cm alumina particles. The top surface of the small particles slopes toward the center of the bed at an angle of 30° from the horizontal (3° to 5° less than the angle of repose for detrital matter). Small masses of material splashing onto this surface should not disturb the slope.

The final levels of the molten pool for four delivered masses are shown. The amounts range from the minimum mass of delivered molten material that can be expected to the mass of the total charge. The particular configuration of the bed was chosen to insure that the head of molten material above the large particles is at least several particle diameters.
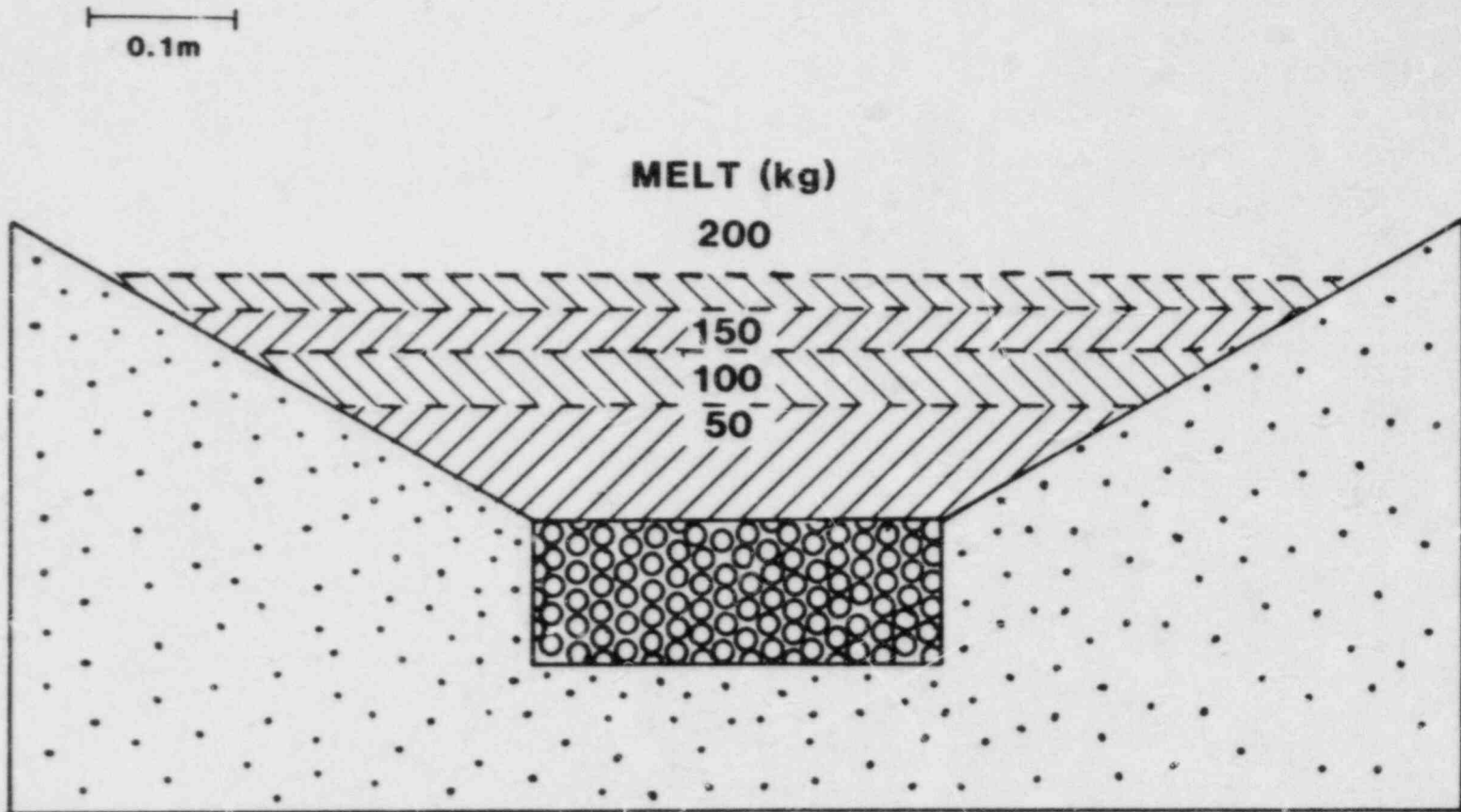
Figure 1.2-7. Cross Section of the Circular Bed for the IRIS Test

Based on PLUGM code predictions and on the results of SWA-3, the molten material will quickly penetrate the large particles.[1-14] No penetration of the small particles is expected.

The bed will be instrumented to ascertain quenching of the melt within the bed, heat flux distributions, and melting of the alumina particles. Flotation of the alumina particles in the denser core material will be determined by visual inspection and chemical analyses of the posttest fixture.

1.3 SODIUM CONTAINMENT AND STRUCTURAL INTEGRITY
(E. Randich, 6422; R. U. Acton, 7537; A. Suo-Anttila, 6425)

The four areas of work this quarter were (1) completion of laboratory-scale tests of calcite and dolomite aggregate concete, including SLAM predictions of the results, (2) viscosity measurements of the AA/AB calcite concrete test debris, (3) review of HEDL documents for NRR, and (4) report preparation and publication. A brief summary of each of these areas is outlined below.

1.3.1 Laboratory Scale Tests

The series of laboratory-scale experiments that were designed to identify the important heat-producing and concrete-eroding chemical reactions between sodium and limestone concrete was completed this quarter. These experiments were designed to evaluate the effects of water content, cement, and aggregate on sodium concrete interactions. Sodium-limestone aggregate reactions were found to be responsible for the bulk of the exothermic heat produced in sodium-concrete tests. The threshold temperatures for the energetic reactions were found to be about 853 K (580°C) for calcite and dolomite aggregate and calcite concrete but were ill-defined for dolomite concrete. Dehydrated concrete exhibited sharper exothermic peaks and threshold temperatures of about 813 K (540°C). Major reaction products include sodium oxide or sodium carbonate (depending upon the initial sodium/concrete ratio), calcium oxide, and elemental carbon. At high Na/concrete ratios, sodium oxide is produced. At low Na/concrete ratios, sodium carbonate is produced. When water is present, sodium hydroxide forms, which causes a slow erosion of the concrete with little or no heat production. The reaction products of the sodium or sodium hydroxide-concrete reactions as well as the presence of the sodium hydroxide itself appear to inhibit direct reaction between sodium and concrete. This is assumed to be caused by limitation of the mass transport of sodium through the reaction product or sodium hydroxide layer.

The SLAM computer code was used to simulate selected sodium-limestone concrete reactions. The time-temperature profiles predicted by SLAM are compared with the experimental profiles for experiments with Na/concrete ratios ranging from 7.0 to 0.14 in Figures 1.3-1 through 1.3-5. Calibration runs on sodium and reaction products were used to determine the heat transfer coefficients in SLAM. Similar laboratory-scale experiments were used to adjust the reaction kinetic parameters in SLAM, as discussed in the last quarterly report, to obtain a best fit for the exothermic peaks seen in the laboratory-scale tests. As Figures 1.3-1 through 1.3-5 show, there is good
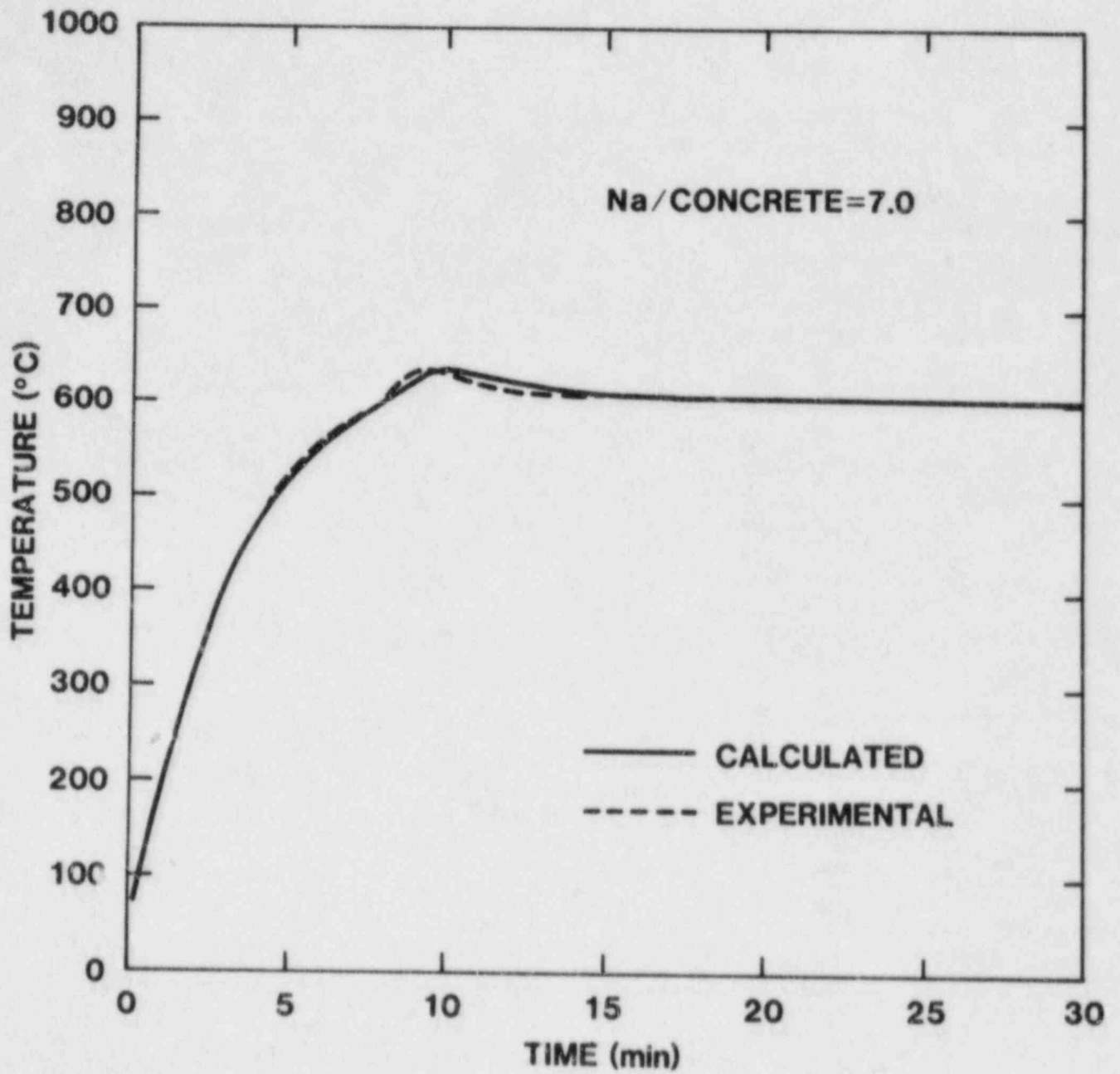
Figure 1.3-1. Calculated and Experimental Sodium/Concrete
Heating Curves

48
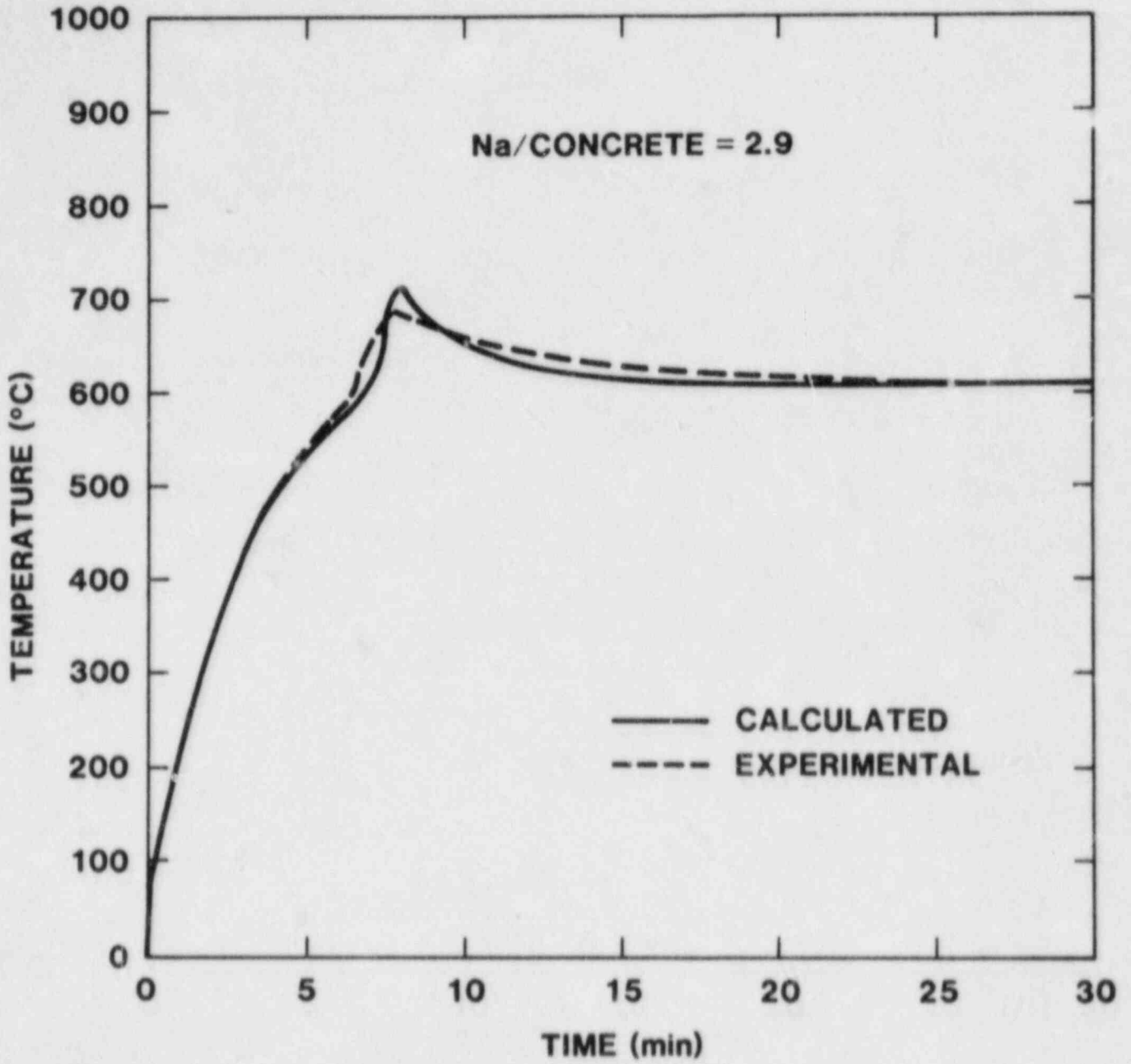
Figure 1.3-2. Calculated and Experimental Sodium/Concrete
             Heating Curves

49
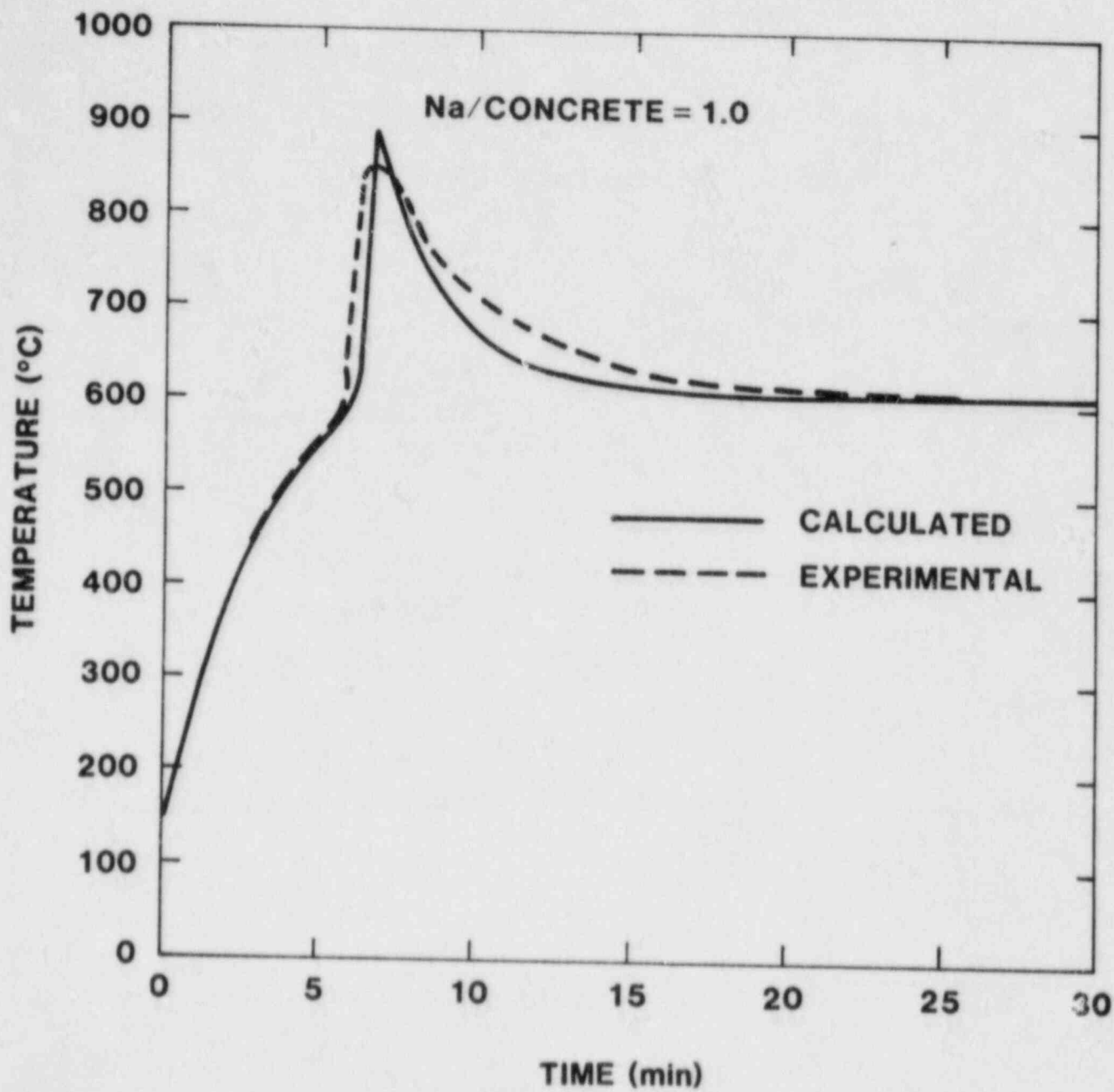
Figure 1.3-3. Calculated and Experimental Sodium/Concrete Heating Curves
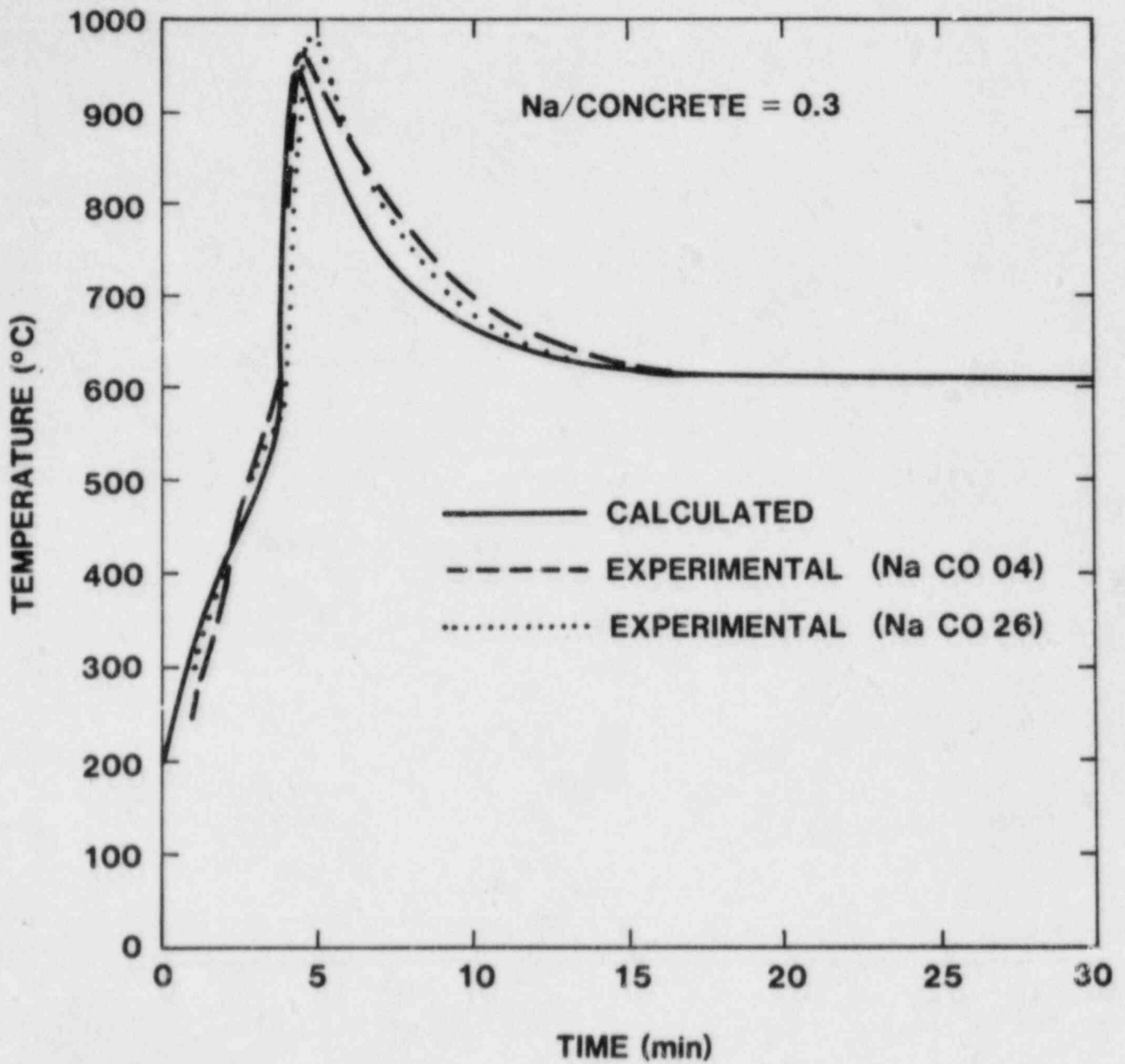
Figure 1.3-4.   Calculated and Experimental Sodium/Concrete
Heating Curves

51
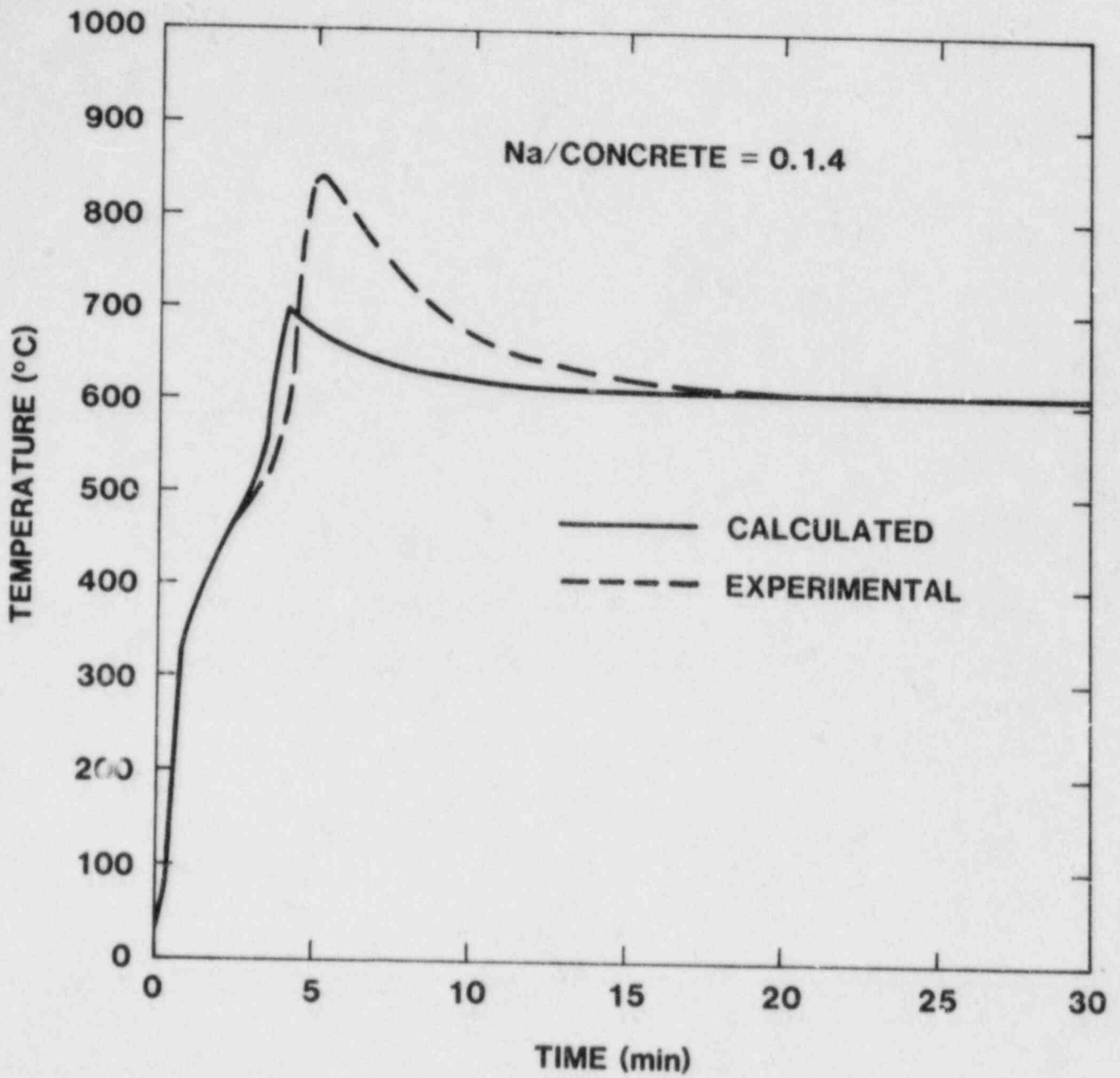
Figure 1.3-5. Calculated and Experimental Sodium/Concrete Heating Curves

agreement between calculated and experimental time/temperature curves when comparing peak size, shape, threshold temperature, vertical slope, and delay time. Only when the sodium/concrete ratio is low does a significant difference exist between the calculated and the experimental curves.

1.3.2 Viscosity Measurements

High-temperature viscosity measurements were made on the reaction debris from the AA/AB calcite concrete test performed in August 1982. The rheological behavior of the material was measured over a temperature range of 743 to 873 K (470° to 600°C). A Brookfield model LVTD digital viscometer with a concentric 316 stainless steel cylinder spindle (LV-3) was used to measure the viscosity. Measurements were made in a glove box under an argon atmosphere. Approximately 60 g of the debris was used for the measurements.

The heated sample softened at approximately 623 to 648 K (350° to 375°C). Viscosity measurements were continuously recorded from 743 to 868 K (470° to 595°C). A rotational speed of 12 rpm was used for the majority of the tests. Figure 1.3-6 plots the viscosity as a function of temperature. The viscosity varied from 5310 centipoise at 743 K (470°C) to 1900 centipoise at 868 K (595°C). The sheer rate dependence of the debris viscosity was measured at 868 K (595°C) by varying the spindle speed from 6 to 30 rpm. The viscosity decreased to 1040 centipoise at the 30-rpm speed and increased to 3510 centipoise at the 6-rpm speed. The results are consistent for a non-Newtonian pseudo-plastic material where increasing sheer rate results in a decreasing viscosity.

The results of these tests show that the reaction debris produced by the sodium-concrete reactions is quite viscous even at reaction temperatures. The high viscosity of the material suggests that the debris layer would probably not mix well with the relatively low viscosity sodium metal during the reaction. This is particularly true since the density difference of the materials is also significant (0.8 g/cm^3 for Na and 2.5 g/cm^3 for the debris).

1.3.3 Review of Documents for NRR

Two documents were reviewed for NRR by investigators in this program.

1. TMBDB Melting Scenario.

2. Aerosol Release from Sodium-Concrete Reactions, by L. D. Muhlestein and R. P. Colburn

The first of these documents addressed the containment consequences should core debris in the CRBR cavity become uncoolable prior to sodium boil-dry. Review analyses were conducted based on experimental data from the FRAG tests conducted as part of the Ex-Vessel Core Debris Containment program at Sandia. These calculations as well as the title document were done with the assumption that core-debris
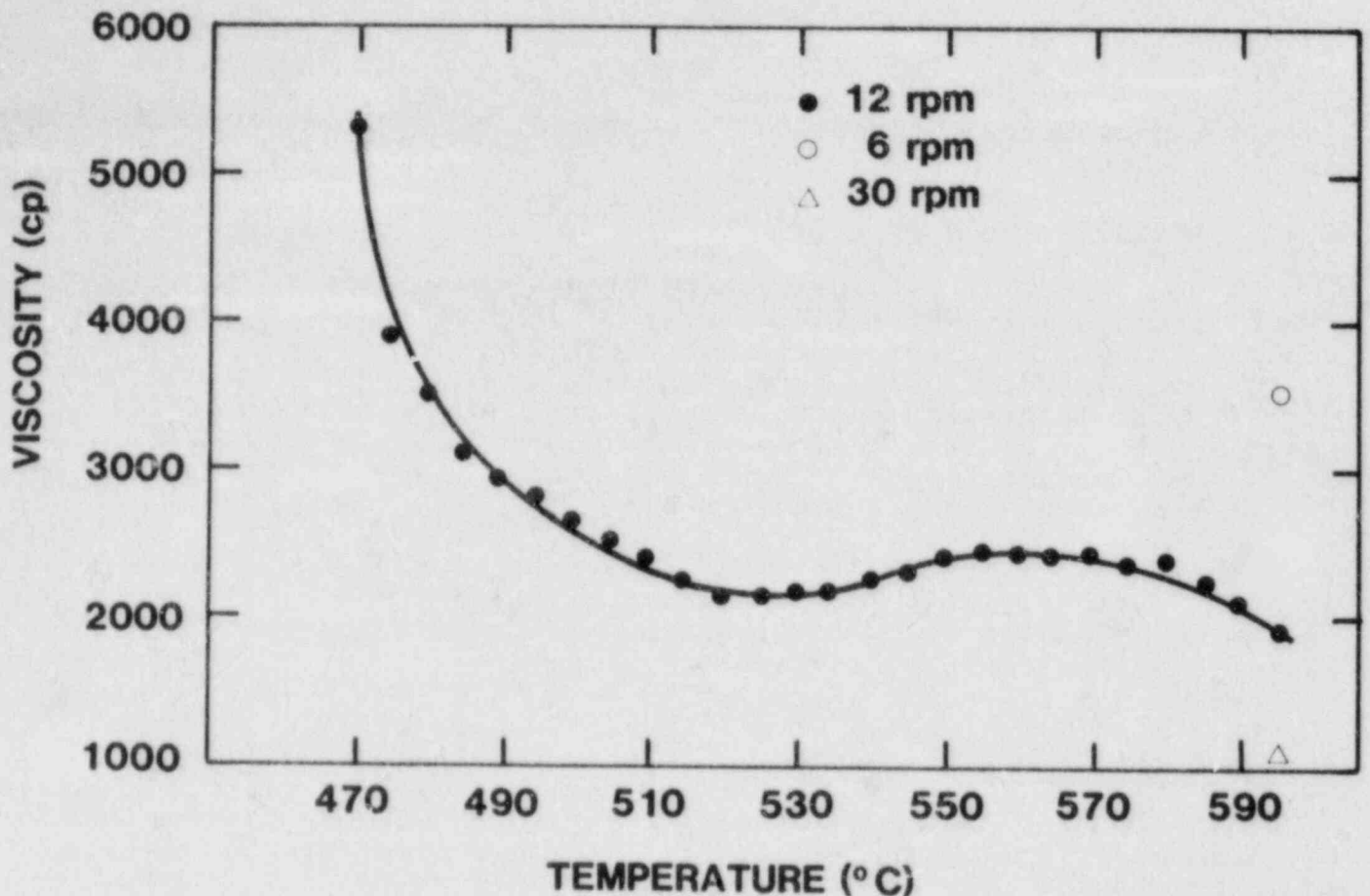
Figure 1.3-6.   Temperature vs Viscosity Results for the HEDL
Calcite No. 1 Sodium Debris Sample

interactions with concrete and sodium interactions with concrete can
be treated separately. No data are available to support this conten-
tion. Arguments in the reviewed document indicate that the combined
sodium/core-debris/concrete interaction should be less severe than
core-debris/concrete interactions alone, whereas Sandia arguments
based on the chemistry of sodium attack indicate the combined inter-
action would be more severe.

If the separability assumption is accepted, the review analysis
showed that the calculations in the TMBDB Melting Scenario are con-
servative. More realistic formulations of the problem lead to lower
concrete erosion than was calculated. Lateral erosion of the concrete
can be neglected. The only serious uncertainty is the separability
assumption described above.

Reviewers of the second document, Aerosol Generation Release from
Sodium-Concrete Interactions, generally agreed with the main thrust of
this article. They pointed out, however, that the issues concerning
fission products and aerosols during "beyond-design-basis" accidents
go considerably beyond those addressed in this article. The most
important of the issues raised by the reviewers were:

a. The existing data base and analyses are inadequate to estimate refractory fission-product release during the ex-vessel phase of a "beyond-design-basis" accident.

b. The data base available on aerosol source term is inadequate to form input to codes that predict aerosol behavior in the CRBR containment. This could lead to nonconservative estimates of fission-product behavior.

c. Aerosol behavior codes that assume the aerosol sizes are lognormally distributed yield conservative predictions of the amount of aerosol that must be filtered, but they yield nonconservative estimates of the particle size.

d. Questions remain on the ability of aerosols to pass through filters and to plug flow passages. These questions are particularly serious with regard to protecting instrumentation sensors in containment.

1.3.4 Report Preparation

Two topical reports were completed this quarter. The topical report Large-Scale Exploratory Tests of Sodium/Limestone Concrete Interactions, NUREG/CR-3000, SAND82-2315 by E. Randich, J. Smaardyk, and R. U. Acton was published this quarter. The topical report Large-Scale Exploratory Tests of Sodium/Magnetite Concrete Interactions, NUREG/CR-3189, SAND83-356 by E. Randich and R. U. Acton was completed this quarter.

Two topical reports are in preparation with publication anticipated next quarter. The first of these is the report Intermediate Scale Tests of Sodium Interactions with Calcite and Dolomite Aggregate Concretes by E. Randich and R. U. Acton, which summarizes results of the HEDL-SNLA AA/AB tests. The major findings of this report are summarized below. Two intermediate-scale tests were performed to compare the behavior of calcite and dolomite concretes when attacked by molten sodium. The tests were performed as part of an interlaboratory comparison between SNLA and HEDL. The results show that both calcite and dolomite aggregate concretes exhibit similar exothermic reactions with molten sodium. The large differences in reaction vigor suggested by thermodynamic considerations of CO_2 release from calcite and dolomite are not realized. Penetration rates of 1.4 to 1.7 mm/min were observed for short periods of time (less than 1 hr) with reaction zone temperatures of about 1073 K (800°C) during the energetic attack. The penetration was not uniform over the sodium-concrete contact and erosion may be localized due to inhomogeneities in the concrete. The reaction intensity varied considerably during the tests. The reaction zone is less than 1 cm thick for the calcite concrete but is about 7 cm thick for the dolomite concrete. This difference in reaction zone thickness is apparently caused by the lower thermal decomposition temperature of dolomite. Chemical analysis of the reaction debris suggests that the major chemical reactions of importance are the sodium-water reaction that produces sodium hydroxide and the sodium-limestone concrete reaction that produces sodium carbonate, calcium oxide, magnesium oxide, and hydrogen.

The second report in preparation is entitled Laboratory-Scale Sodium-Concrete Interactions by H. R. Westridge, H. W. Stockman, and A. Suo-Anttila. Publication of this report is anticipated in June 1983. The report summarizes the laboratory-scale experiments discussed in Section 1 of this quarterly.

1.4 DEBRIS BED COOLABILITY
(G. W. Mitchell, 6421; C. A. Ottinger, 6421; R. J. Lipinski, 6425)

The Debris Bed Coolability program addresses issues concerned with the deposition of solid fuel debris on horizontal surfaces within the containment vessel and its subsequent coolability. This debris remains capable of generating significant power through the decay of fission products. Should natural processes fail to provide sufficient cooling, the debris could remelt and threaten containment. The Debris Bed Coolability program seeks to determine the natural cooling of such debris. During this period, experiments and analysis of debris bed studies continued.

1.4.1 Debris Bed Experiments D10/D13 - Results and Analysis

1.4.1.1 Materials Evaluation

The materials evaluation program was delayed somewhat due to difficulties encountered in accurately measuring the oxygen content of the sodium used in the tests. To solve the difficulties, an oxygen analysis capability was established to provide faster analyses. After much consideration, the Sandia staff concluded that the oxygen analysis technique has inherent uncertainties, but oxygen levels could be established with a reasonable degree of uncertainty, based on oxygen solubility data in sodium.

After resolution of these difficulties, the materials evaluation program proceeded and was completed late in March. All low-temperature tests were conducted between 573 and 1073 K (300 and 800°C), 2- to 100-ppm oxygen in the sodium, and with durations of 10 to 130 hr. These tests indicated that four alloys, MO41Re, Re, Ta-10W, and T-111, retain sufficient mechanical properties after sodium exposure to be viable crucible materials for the D10/D13 experiments.

The high-temperature tests of these materials were conducted at Los Alamos National Laboratory by loading tubes fabricated from the material to be tested with 85 g of UO_2 and 12 g of sodium containing 400-ppm oxygen. These tests were conducted by heating the bottom 1 cm of the tube in five, 1-hr temperature cycles from 973 to 2423 K (700 to 2150°C). Although no catastrophic failure of the tubes occurred, some degradation of the rhenium (separation along grain boundaries) was observed. This separation was not due to attack by the sodium or UO_2, since it was observed primarily along the outer surface of the tube. The separation appeared to be related to grain growth in the material. From the results of these tests, Ta-10W, Mo-41Re, and T-111 were concluded to be viable materials for crucible fabrication.

1.4.1.2 Crucible Design

In parallel with the materials evaluation program, an evaluation of crucible design concepts was initiated. This program consisted of stress evaluations of four different designs to characterize important effects and to evaluate joining concepts for the double-walled crucible. This program will help to decrease time required for final design once a material is selected. The results indicate that thermal stresses due to the dry zone temperature gradients are relatively modest and can be accommodated by any of the three candidate materials. Attempts to accommodate differential expansion between the inner and outer crucible walls by using dissimilar materials (stainless steel or Inconel outer wall) would not appear appropriate due to the very large radial expansion mismatches that occur in that configuration. The stress calculations would appear to support crucible construction from a single material. Additionally, a liquid metal thermal bond at the bottom of the crucible has the effect of eliminating stresses in the crucible except for those imposed by the dry zone.

1.4.1.3 Thermocouple Fabrication

A contract to develop and fabricate the high-temperature C-Type thermocouple used in the D10/D13 experiments was placed with HEDL in January. HEDL has been successful in developing similar thermocouples for LOFT applications as well as for the DC-1 experiment. Development efforts ended successfully with testing of a prototype thermocouple incorporating BeO insulation and an Re sheath at 2573 K (2300°C) for 100 hr. Output drift was less than 2%. The design, including required seals and transitions for incorporation into the D10/D13 experiments, was reviewed with HEDL by Sandia project personnel. No major difficulties appeared in fabricating experiment thermocouples in time for the experiments as currently scheduled.

1.4.1.4 Component Status

Orders were placed for all major experiment components, including the containment vessels, gas flow components, manifolds, thermocouples, and pressure transducers. Deliveries of these components are expected during July and August.

1.4.1.5 Ultrasonic Thermometer Testing

Two tests of the ultrasonic thermometer (UT) intended to be used in the D10/D13 experiments were conducted in January and March. The test in January used a thoriated tungsten sensor wire partially enclosed in a thoria tube, with a tantalum sheath. The March test incorporated more complete coverage of the sensor with the thoria tube and a rhenium sheath. Both tests included low-temperature cycling between 1173 and 1473 K (900° and 1200°C) and high-temperature operation at various temperatures between 1473 and 2773 K (1200° and 2500°C). Each test encompassed about 30 hr of UT operation. Although initial low-temperature operation appeared satisfactory and the capability to measure temperatures at 2773 K (2500°C) was demonstrated, the long-term operation at modest temperatures (below 2273 K [2000°C]) appeared

to be unsatisfactory. High-temperature irreversible effects probably related to mass transfer occurred, which altered the calibration of the UT. Additionally, undesirable temperature sensitivity of the coil was observed. These phenomena are being studied for possible solutions.

1.4.2 PAHR Debris Bed

The one-dimensional model reported previously for steady-state boiling heat removal and dryout in particulate debris was modified slightly during this quarter.[1-15] The current model may be used for predicting the coolability of postaccident debris from a nuclear reactor (either LWR or LMFBR). The model includes the effects of both laminar and turbulent flow, two-phase friction, gravity, capillary force, and channels at the top of the debris. The model is applicable to debris on permeable supports with liquid entering the debris bottom or to debris on impermeable plates. In the latter case, the plate may be either adiabatic or cooled on the bottom.

The model predicts channel length, the liquid fraction within the debris as a function of elevation, the incipient dryout power, the dry zone thickness as a function of power, and the existence of downward heat removal by boiling (in bottom-cooled debris), all for both uniform and stratified debris. The recent modifications to the model will be described, and a comparison to the present debris-cooling data base will be made.

1.4.2.1 Model Modifications

In the previous model development, it had been assumed that the relative permeability for two-phase flow through a porous medium for turbulent flow was approximately equal to that for laminar flow. Recently, Reed extended the theoretical laminar-flow derivation for relative permeability to the turbulent flow regime.[1-16] An approximation for his turbulent expressions (which permit later simplification of the dryout expression) is

$$\eta_v = (1 - s)^5 \tag{1.40}$$

$$\eta_1 = s^5 \tag{1.41}$$

where s is the effective saturation (liquid fraction) in the debris. These new forms yield slighty better agreement with recent dryout data.

Another model modification regards the Leverett function, which relates the capillary pressure in debris to the effective saturation.[1-17] The Leverett function suggested in the previous development is

$$J = \frac{(s^{-1} - 1)^{\gamma}}{\sqrt{5}} \tag{1.42}$$

where γ was taken to be 0.175.[1-14] Analysis of recent debris heat removal data yields better general agreement if γ is taken to be 0.175 for sodium, but 0.30 for the other fluids commonly used (water, Freon-113, acetone, methanol, and isopropanol). This difference may be due to the large surface tension in sodium causing second order effects to be visible.

With the above considerations, the overall one-dimensional equation for the saturation within volume-heated debris is

$$\sqrt{150}\, \frac{\sigma \cos\theta\, (1 - \epsilon)}{\epsilon d} \frac{dJ}{ds} \frac{ds}{dz} + \sqrt{150}\, \sigma \cos\theta\, J \frac{d}{dz}\left[\frac{1 - \epsilon}{\epsilon d}\right] - (\rho_\ell - \rho_v)g$$

$$+ \frac{1.75\,(1 - \epsilon)q^2}{h_{\ell v}^2\, \epsilon^3\, d}\left[\frac{1}{\rho_v(1 - s)^5} \pm \frac{1}{\rho_\ell s^5}\right] + \frac{150(1 - \epsilon)^2 q}{h_{\ell v}\, \epsilon^3\, d^2}\left[\frac{\mu_v}{\rho_v(1 - s)^3} + \frac{\mu_\ell}{\rho_\ell s^3}\right]$$

$$+ \frac{(1 - \epsilon)w}{\rho_\ell\, \epsilon^3\, d}\left[\frac{1.75w}{s^5} \mp \frac{3.5q}{s^5\, h_{\ell v}} - \frac{150(1 - \epsilon)\mu_\ell}{s^3\, d}\right] = 0 \tag{1.43}$$

where θ is the contact angle between the liquid and solid ($\cos\theta$ typically is 1 for sodium, 0.8 for other fluids), ϵ is bed porosity, d is average particle diameter, z is elevation in the debris measured from the plane of zero heat flow, ρ_ℓ and θ_v are liquid and vapor densities, respectively, g is gravitational acceleration, q is bed heat flux at elevation z, $h_{\ell v}$ is heat of vaporization, μ_ℓ and μ_v are liquid and vapor dynamic viscosity, respectively, w is liquid mass flux (kg/m$^2\cdot$s) entering the base of the debris, and where the upper sign applies for $q > wh_{\ell v}$, and the lower sign applies for $q < wh_{\ell v}$. All bed properties may be functions of elevation; thus, the equation is valid for both uniform debris and stratified debris (where the particle diameter, porosity, and volumetric source may vary with elevation).

The first two terms in Eq. 1.43 are the capillary pressure gradients due to variations in the saturation and particle diameter. The second term is operative only in stratified beds and works to reduce the dryout power in stratified beds. The third term is the hydrostatic pressure gradient. The fourth and fifth terms are the laminar and turbulent flow resistances, respectively. The last term is the added resistance from any liquid flow entering the bed bottom. Eq. 1.43 may be solved numerically once the bed characteristics are chosen and a top boundary condition is determined.

Eq. 1.43 applies only to the packed boiling region of the bed. A top boundary condition must be used to accommodate channels. The

equations for this condition have been reported previously [1-16] and are reproduced here for convenience.

$$L_c = \frac{\sqrt{150} \; \sigma \; \cos\theta \; J}{(\rho_p - \rho_\ell) \; g \; \varepsilon \; d} \tag{1.44}$$

$$\frac{(1 - \varepsilon)q_c}{\rho_v g h_{\ell v} \varepsilon^3 d} \left[\frac{1.75 \; q_c}{(1 - s)^5 h_{\ell v}} + \frac{150(1 - \varepsilon)\mu_v}{(1 - s)^3 d} \right]$$

$$= (1 - \varepsilon)\rho_p + \varepsilon\rho_\ell \tag{1.45}$$

where L_c is the channel length and q_c is the heat flux at the base of the channeled region.

Since q_c is a function of L_c, Eq. 1.44 and 1.45 must be solved simultaneously to obtain the channel length and saturation at the top of the packed boiling zone (which sets the boundary conditions for Eq. 1.43). However, a quick estimate of the channel length can be obtained by using $s = 0.5$ in Eq. 1.42 and 1.44 (e.g., for 0.5-mm UO_2 debris in water, $L_c = 0.018$ m).

The model predicts channel length, the liquid fraction within the debris as a function of elevation, the incipient dryout power, the dry zone thickness as a function of power, and the existence of downward heat removal by boiling (in bottom-cooled debris), all for both uniform and stratified debris. The dryout power is determined by varying the debris power until Eq. 1.43 yields a saturation equal to zero somewhere in the bed.

1.4.2.2 Comparison of Model with Data

The predicted incipient dryout flux for a uniform bed on an adiabatic plate is shown in Figure 1.4-1 as a function of average particle diameter for various bed thicknesses and for either water or Freon-113 as a coolant. (Some of the curves in the figure are terminated because the channel length in the bed exceeds half the bed thickness, and the model is not accurate in that regime.) The curves show that the dryout flux is strongly dependent on particle diameter with small particles and deep beds but less so for large particles because of turbulence or for shallower beds because of capillary force. The curves also show that the dryout flux is independent of bed thickness if the bed thickness or particle diameter is large. The relevance of Freon-113 is that it shows the effect of changing material properties that occur with saturated water as the pressure in the containment building or reactor vessel changes.

Also shown in Figure 1.4-1 are dryout data from various sources. [1-18 through 1-25] Only data from beds near 200 mm thick are shown,

60
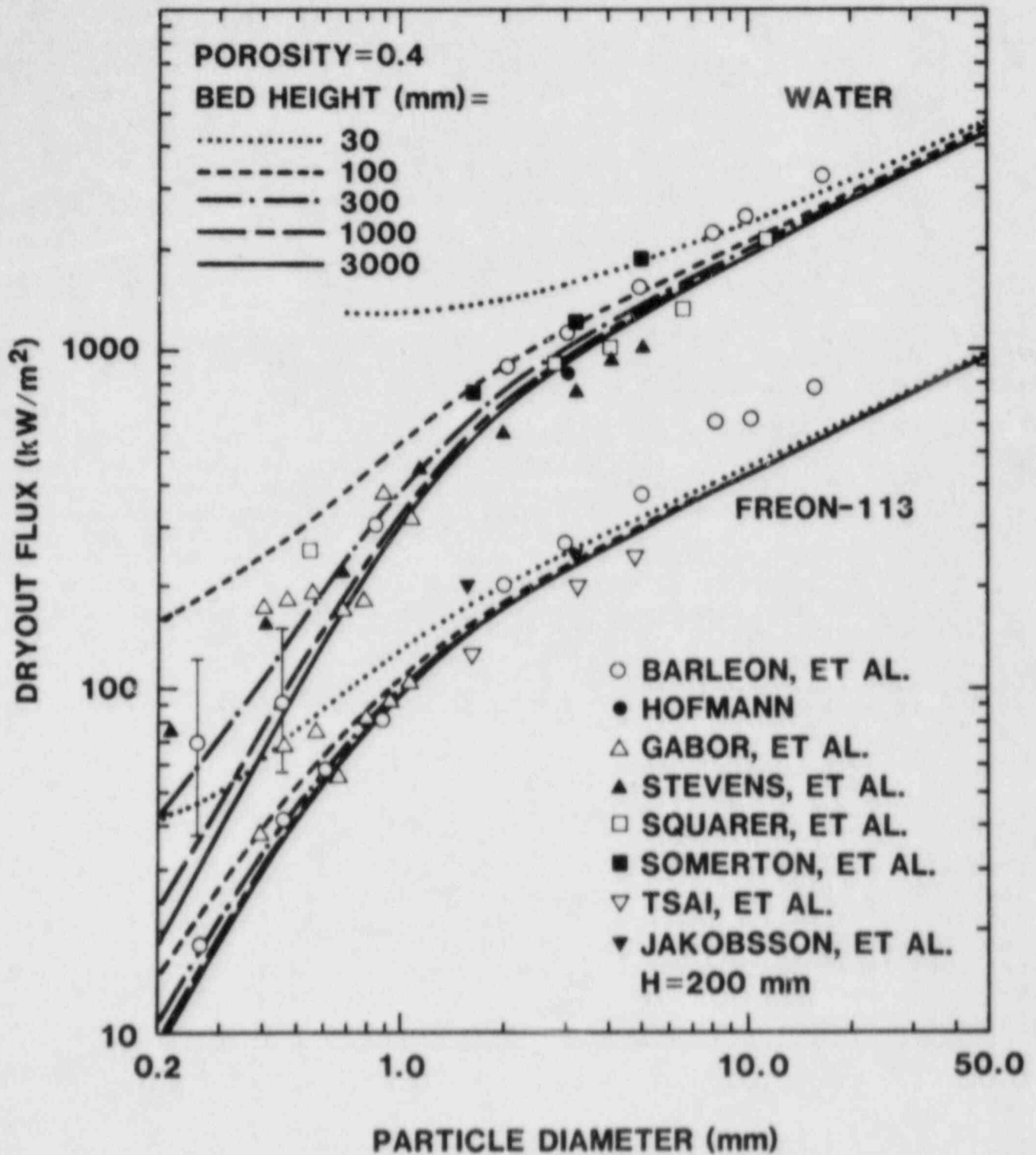
Figure 1.4-1. Dryout Heat Flux vs Particle Diameter in Water and Freon

except for large particles where the dryout flux is independent of bed thickness. In addition, data from beds with a porosity other than 40% have been normalized to 40% via $\epsilon^3/(1 - \epsilon)^2$ for d < 1.5 mm and via $(\epsilon^3/(1 - \epsilon))^{1/2}$ for d > 1.5 mm since the dryout flux is predicted to vary with porosity in that manner for the laminar and turbulent regimes, respectively. (This primarily affects the data of Barleon et al and is at most a 37% change.)[1-18]

An average error for n points may be defined as

$$ E = \frac{1}{n} \sum \frac{|q_{p,i} - q_{m,i}|}{q_{p,i}} \tag{1.46} $$

where $q_{p,i}$ and $q_{m,i}$ are the predicted and measured dryout fluxes for the ith point. The average error for the model predictions for the data shown in Figure 1.4-1 is 26%.

Figure 1.4-2 shows the predicted dryout flux vs bed thickness for a bed on an impermeable support with nonsubcooled sodium as the coolant. The dryout flux approaches an asymptotic value as the bed thickness increases to a "deep bed" limit. The nondeep regime has two components. The "shallow" regime occurs when the channel length (see Eq. 1.44) is not negligible compared to the bed thickness. However, the dryout flux can still depend on bed thickness even when channels are negligible because of the effect of capillary force within the bed. The regime between the shallow and deep bed regimes may be called the "moderate" regime. The moderate bed regime ends when the bed is much thicker than the capillary head, λ_c, which is the distance coolant can be drawn up into the bed by capillary force:

$$ \lambda_c = \frac{6 \, \sigma \, \cos\theta \, (1 - \epsilon)}{d \, \epsilon \, (\rho_\ell - \rho_v) \, g} \tag{1.47} $$

Channels have a greater effect on the dryout flux than internal capillary force. First, they allow the heat generated in the packed zone to exit in parallel with that generated in the channeled zone. Second, they reduce the thickness of the packed zone and thus allow internal capillary force to increase the dryout flux from that region. With this consideration, the three debris thickness regimes may be proposed to be

$$ H_{shallow} < 6L_c < H_{moderate} < 3\lambda_c < H_{deep} \tag{1.48} $$

These regimes are indicated in Figure 1.4-2.

Also shown in Figure 1.4-2 are the dryout data of Gabor et al (normalized to a porosity of 50%).[1-26] The beds involved a mixture of particle sizes, so an effective particle diameter was determined to be 0.32 mm, using Ref 1-27.
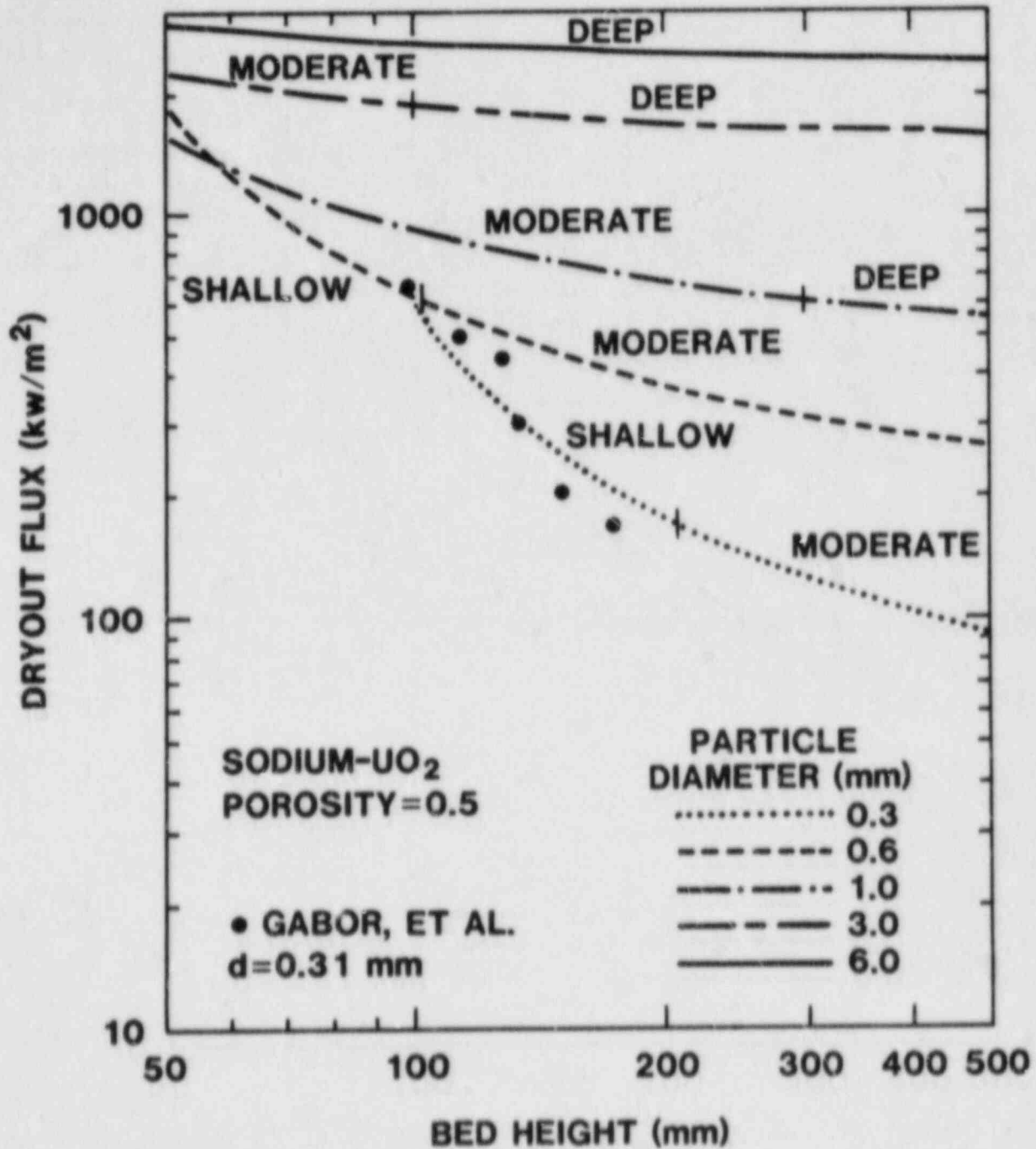
Figure 1.4-2. Dryout Heat Flux vs Bed Thickness for LMFBR Debris in Nonsubcooled Sodium

$$d_e = f_s \left[\sum \frac{w_i}{d_i} \right]^{-1}$$

(1.49)

where w_i is the weight fraction of particles with sieve diameter d_i, and f_s is a shape factor, which is 1 for spheres and 0.78 for rough particles. The average error for the model predictions in Figure 1.4-2 is 31%.

Another parameter that can affect the dryout flux is pressure. The pressure in a LWR vessel can vary from 1 to 170 bars after an accident. The pressure in the containment building can be several times atmospheric. Figure 1.4-3 shows the predicted dryout flux for various beds in Freon-113 as a function of presure. The dryout flux initially increases with increasing pressure. This is due primarily to the increasing vapor density, allowing more heat removal per unit volume of vapor. However, at very high pressures, the heat of vaporization decreases strongly and the dryout flux decreases. Similar behavior is predicted for water, with the peak occurring around 60 bars. Also shown in Figure 1.4-3 are data from Jakobsson et al [1-26] and Tasi et al.[1-22] Some inconsistency exists concerning the dryout flux at 1 bar, but the trend for increasing pressure matches the model predictions.

If postaccident debris falls on a permeable support (e.g., core support plate, grid spacers, permeable core retention device), liquid will be able to enter the base of the debris either by natural or forced convection. This will increase the dryout flux. For small inlet liquid fluxes, there will be a combination of liquid entering the bed from both above and below. As the bottom mass flux increases, the dryout flux approaches the heat removed by vaporizing only the bottom inlet mass flux:

$$q_d = w \, h_{\ell v}$$

(1.50)

If the inlet liquid is subcooled and the bed is deep, the dryout flux is increased by the amount of heat required to raise the incoming liquid to the boiling temperature:

$$q_d = q_0 + w \, C_p \, \Delta T$$

(1.51)

where q_0 is determined by Eq. 1.3, C_p is the specific heat of the liquid, and ΔT is the amount of subcooling.

Figure 1.4-4 shows the predicted dryout flux (using Eq. 1.43 and 1.51) for a deep bed in Freon-113 on a permeable support plate as a function of liquid mass flux entering the bed bottom at 25°C. Also shown in Figure 1.4-4 are the measured dryout fluxes from Tsai et al with a Freon inlet temperature of 298 K (25°C).[1-22] The average error is 10%.

64
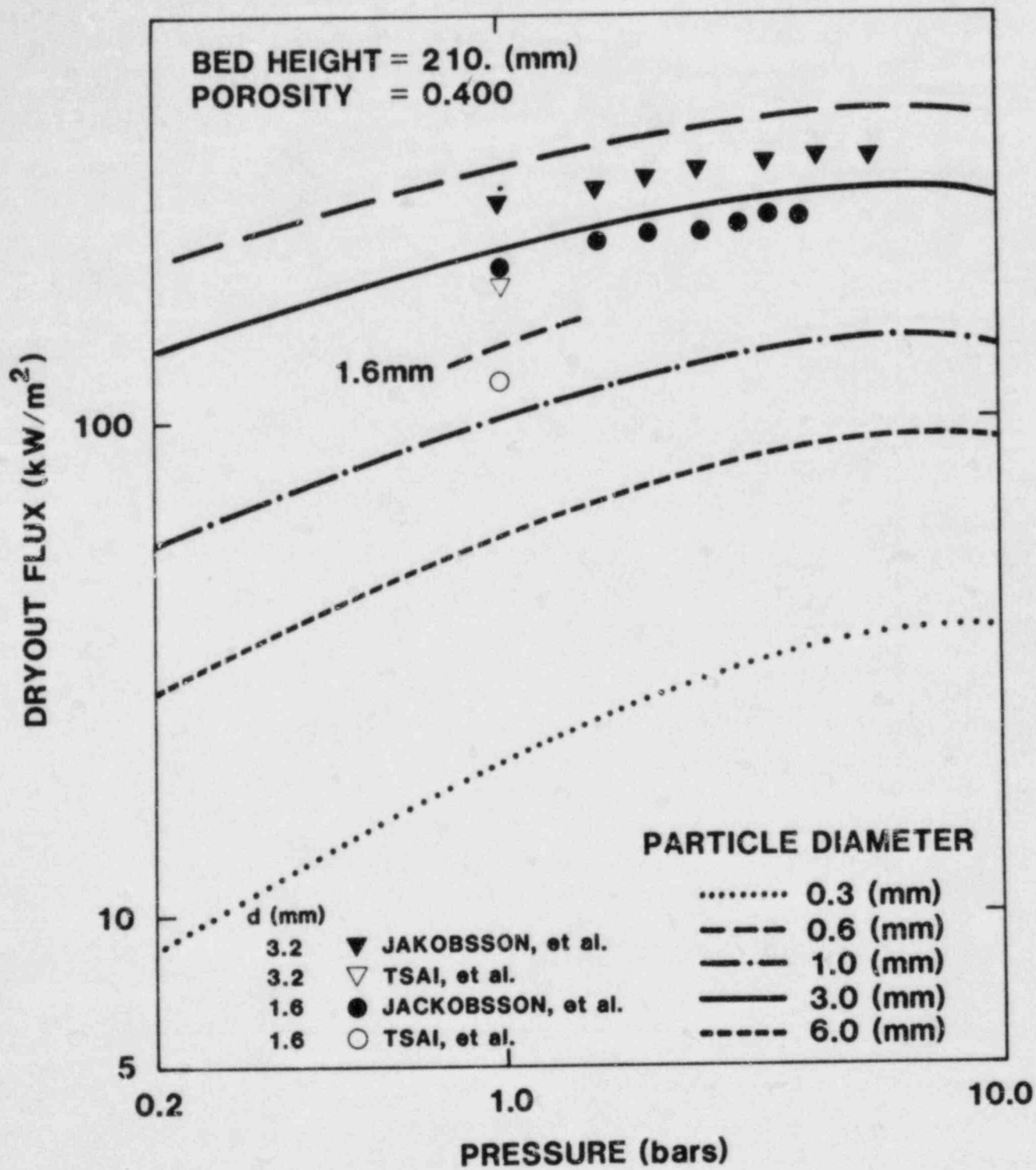
FREON-113

Figure 1.4-3. Dryout Heat Flux vs Ambient Pressure for Freon-113
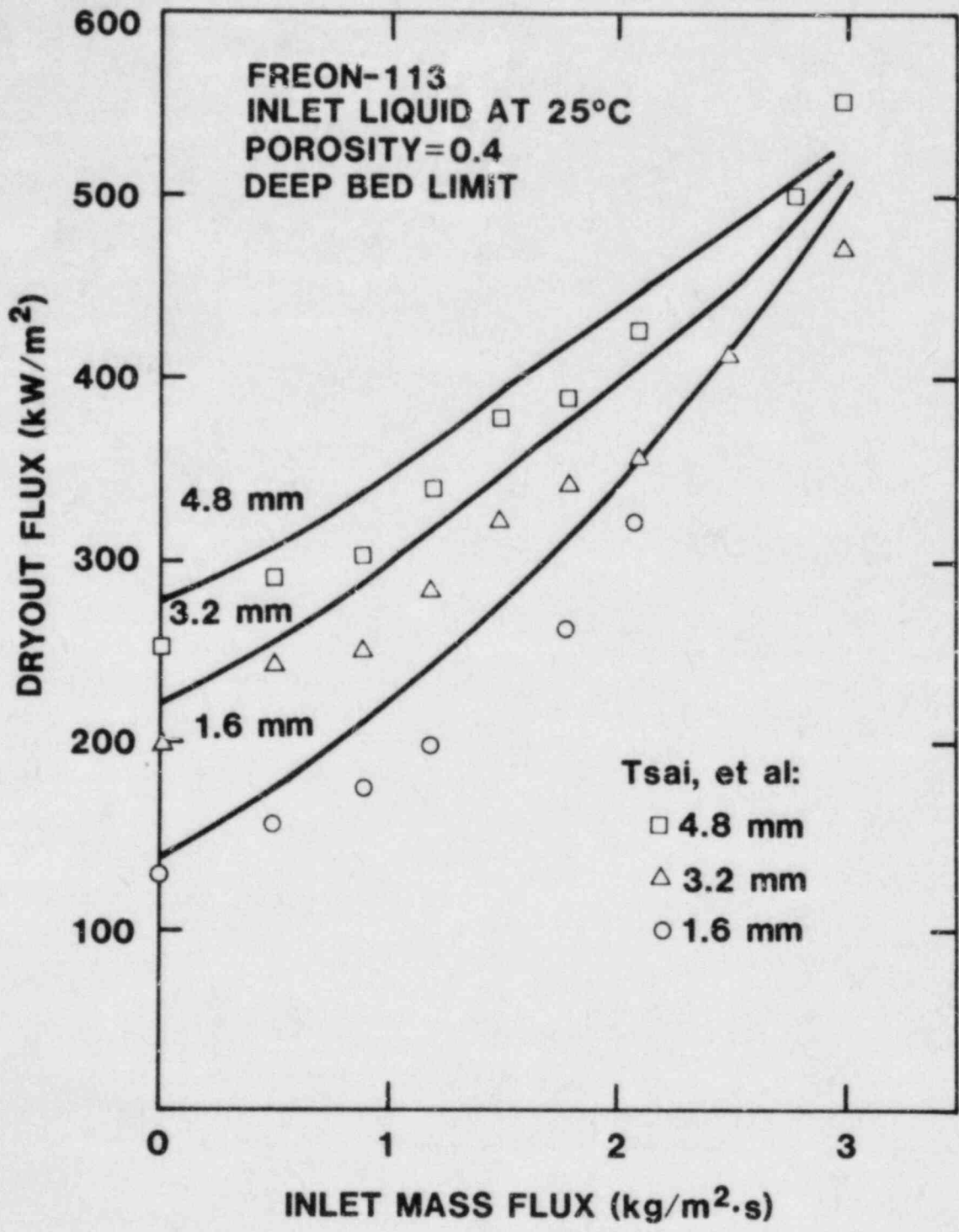
Figure 1.4-4. Dryout Heat Flux for Debris on a Permeable Support Plate

The dryout power in stratified debris is predicted to be lower than for the same debris mixed because of the negative effect of the second term in Eq. 1.43. Such behavior has been observed experimentally. Many experiments involve debris stratified in discrete layers. In such cases, Eq. 1.43 is used within each layer with the second term set to zero; then between the layers the saturation undergoes a step change. The effective saturation below the layer interface is

$$s_- = J^{-1} \left[\frac{\epsilon_- d_- (1 - \epsilon_+)}{\epsilon_+ d_+ (1 - \epsilon_-)} \Big(J(s_+) \Big) \right] \tag{1.52}$$

where J^{-1} is the inverse of the Leverett function, and + and − refer to the upper and lower layers, respectively.

Figure 1.4-5 compares the predicted dryout flux for 0.1- to 1.0-mm-diameter debris stratified into five layers with the data from Gabor et al.[1-28] The average error is 30%.

LMFBR debris has particular cooling phenonema because of the high conductivity of sodium. The sodium will often be subcooled, and heat removal from the bed by conduction and liquid convection must be considered in addition to that by boiling. In addition, cold overlying sodium can suppress channel formation and alter the dryout flux.[1-29] For subcooled debris in which channeling has been suppressed, a nonboiling zone may be assumed to be above the boiling zone in the bed. Heat is removed through the nonboiling zone by conduction (possibly enhanced by convection) in series with the heat produced in the boiling zone.[1-29] The thickness of the boiling zone for a uniform source, Q, is then

$$H_b = \sqrt{H^2 - 2k_b(T_s - T_t)/Q} \tag{1.53}$$

where k_b is the bed conductivity (possibly enhanced by convection), and T_s and T_b are the saturation and bed top temperatures, respectively. Eq. 1.43 may then be applied to the boiling zone.

Figure 1.4-6 compares the model predictions with the results from the D-series experiments.[1-29 through 1-33] (The actual observed bed conductivity was used in the predictions.) Bed disturbances occurred during some of the experiments due to rapid vapor generation. Only data from undisturbed beds are shown in Figure 1.4-6. The bed thicknesses are 106, 158, 83, 114, 74, and 75 mm for D2, D3, D4, D6, D7, and D9, respecitvely. D6, D7, and D9 were stratified. The packed-bed dryout predictions agree reasonably well with the model (average error is 11%). In particular, the dryout powers for the stratified beds D6, D7, and D9 are predicted to be lower than for the uniform beds D2 and D4, and such is the case.

Channeling occurred before dryout in D2 and in D4 with subcoolings of 583 and 468 K (310° and 195°C), respectively. However, this
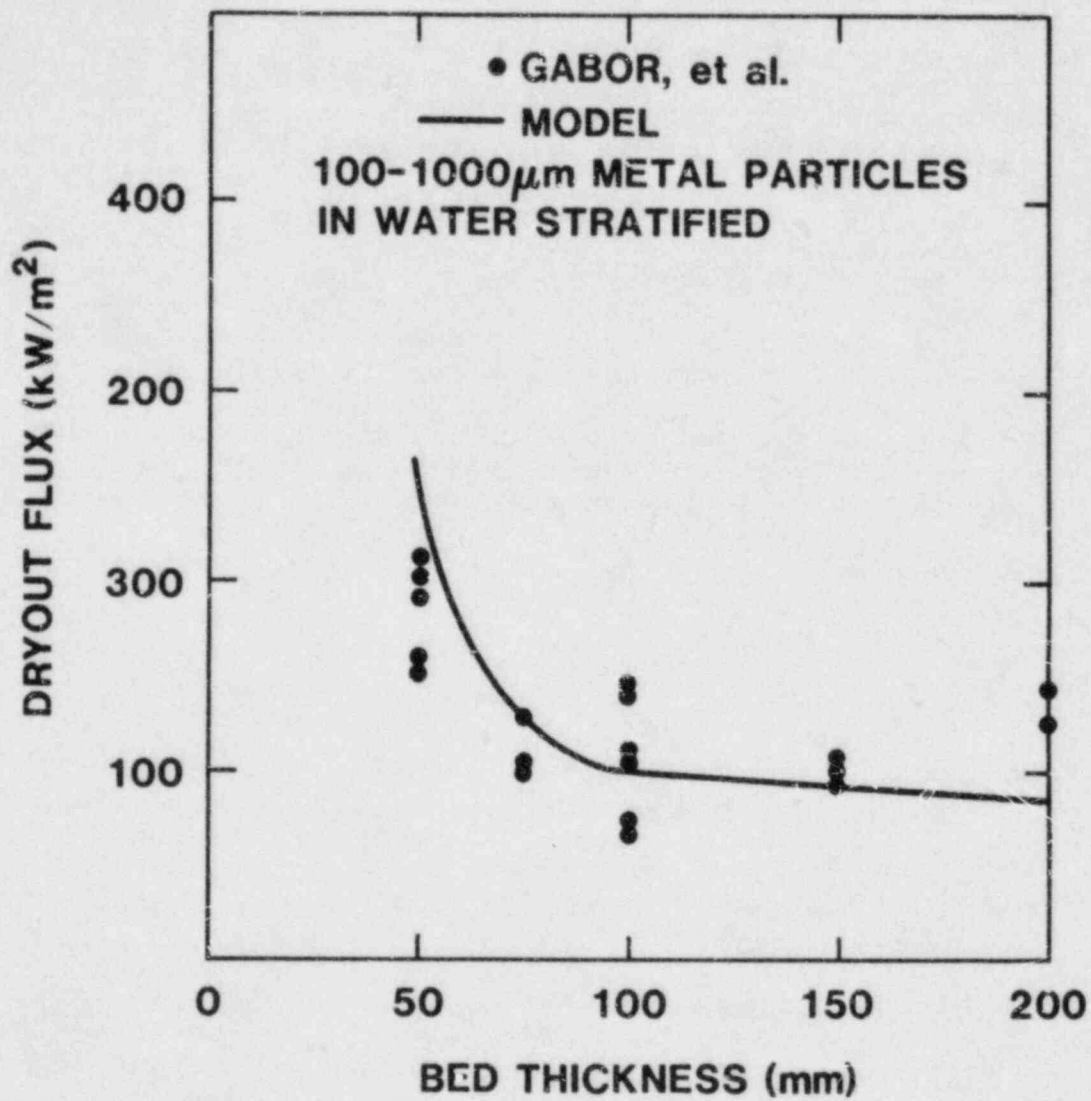
Figure 1.4-5. Dryout Heat Flux for Stratified Debris in Water
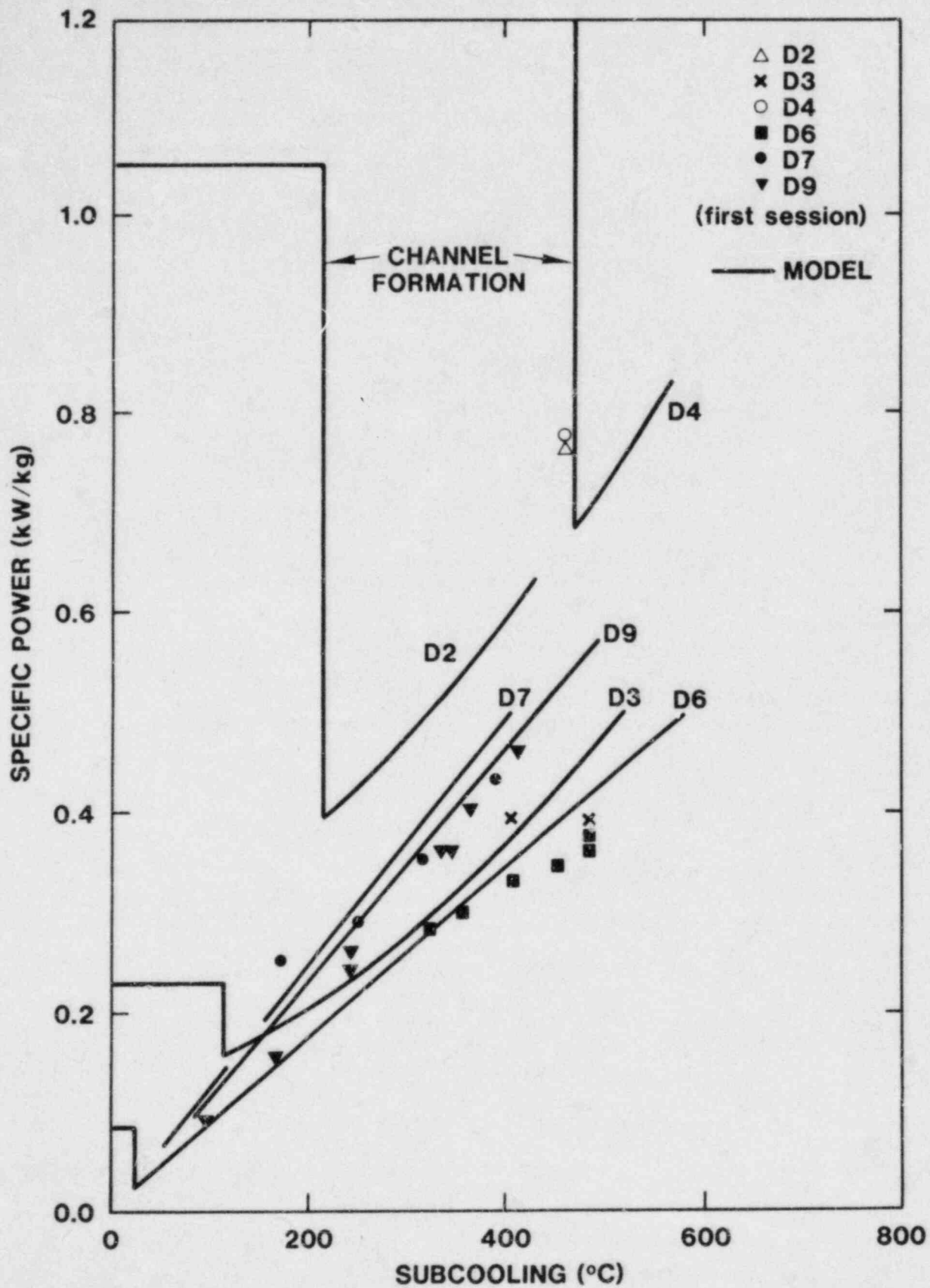
Figure 1.4-6. Dryout Power vs Subcooling for LMFBR Debris

69

occurred after a superheat flashing disturbance in each case, and an accurate determination of the subcooling needed for channeling was not obtained. Whether the disagreement with the channel penetration prediction for D2 is definitive is not certain. The stratified beds are predicted not to channel before dryout, and this agrees with the data.

Eq. 1.43 predicts the steady-state dry zone thickness for powers above the incipient dryout power. The dry zone can be fairly thin if the debris is not too deep. An important class of such beds is post-accident LMFBR debris, which is expected to be much less than a meter thick and composed of submillimeter particles. Again, Eq. 1.53 must be used with Eq. 1.43 if the sodium is subcooled.

Figure 1.4-7 shows the predicted dry zone thickness vs power for the 72-mm-thick stratified D9 bed.[1-33] Channel formation is predicted to occur at about 260 W/kg, and the predicted bottom of the channeled zone is also shown in the figure. Prior to channeling, the dry zone thickness increases strongly with power increase. However, channel penetration of the subcooled zone is predicted to cause a decrease in the dry zone thickness. After channel formation, the dry zone increases less strongly with power increases. Data from D9 is also shown in Figure 1.4-7. The observed dry zone thickness agrees fairly well with the channeled predictions, including the sudden decrease in dry zone thickness as the power was increased.

A similar behavior of the dry zone thickness is predicted for uniform beds. However, if the bed is shallow enough, the dry zone will be eliminated entirely when channeling occurs. Dryout with channels will then require a significantly higher power. Such behavior is believed to have occurred in D2 and D4.[1-29]

1.4.2.3 Simpler Formulae

Numerical solution of Eq. 1.43 can be cumbersome. Fortunately, in various limits, the equations can be simplified. In the deep bed limit, Eq. 1.43 becomes algebraic by setting surface tension equal to zero. The deep bed limit is satisfied when the bed thickness, H, greatly exceeds the capillary head, λ_c (Eq. 1.47); (e.g., for 0.5-mm-diameter UO_2 particles in water, $\lambda_c = 0.113$ m). The incipient dryout power in a deep bed may be determined by varying the saturation at the top of the bed until the bed heat flux, q, reaches a maximum. This process for determining the dryout flux was first proposed by Hardee and Nilson; physically, it determines the maximum amount of vapor that can exit the top of the bed without choking off too much of the liquid flow.[1-34]

Many debris dryout applications involve debris on an impermeable support. In that case, $w = 0$ and the maximization of the heat flux results in a closed form (noniterative) solution in a laminar and turbulent limits with deep beds. However, the range of applicability can be extended somewhat by including beds of moderate thickness, in which capillary force is important but channels are not. Much experimental data is in the moderate range. For example, with 0.7-mm steel particles in water, the range of moderate bed thicknesses is about 80 to 200 mm.
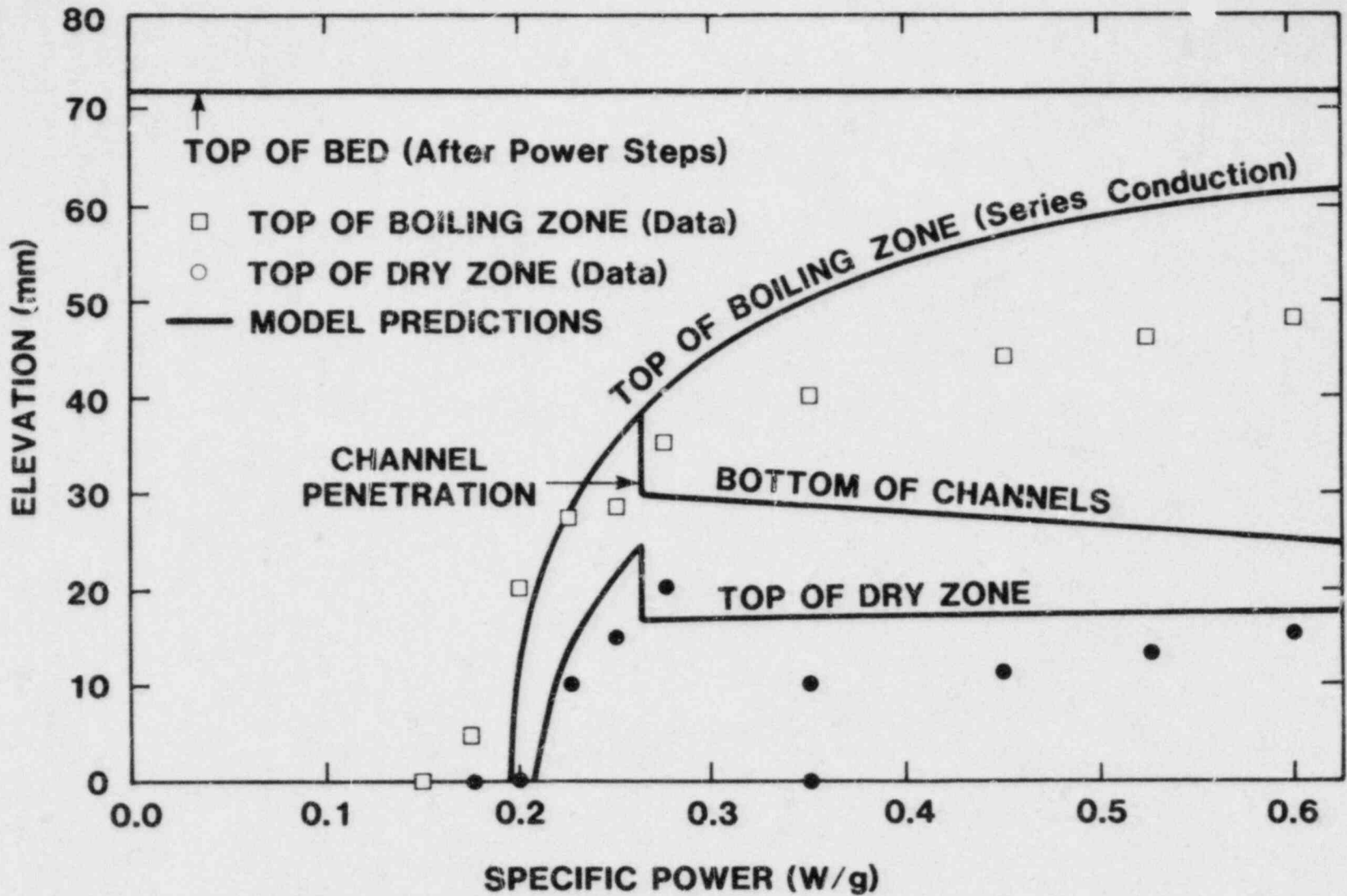
Figure 1.4-7.   Dry Zone Thickness vs Power in LMFBR Debris

For deep and moderate debris, the effect of capillary force on dryout is included in the full one-dimensional model (Eq. 1.43). However, a good approximation can be obtained by simply adding the capillary head to the hydrostatic head. This approach was first introduced by Shires and Stevens and was an important step in developing a physically based dryout model that would agree with dryout data from debris of moderate thickness.[1-35]

Under these assumptions, and using the process of maximizing the bed heat flux with respect to variations in saturation, the dryout criterion becomes:

$$q_d = \left[\frac{q_t^4}{4q_\ell^2} + q_t^2 \right]^{1/2} - \frac{q_t^2}{2q_\ell} \tag{1.54}$$

where

$$q_\ell = \frac{(\rho_\ell - \rho_v) \, g \, d^2 \, \varepsilon^3 \, h_{\ell v} \left[1 + \frac{\lambda_c}{H} \right]}{150 \, (1 - \varepsilon)^2 \, (\nu_v^{1/4} + \nu_1^{1/4})^4} \tag{1.55}$$

and

$$q_t = h_{\ell v} \left[\frac{\rho_v \, \rho_\ell \, (\rho_\ell - \rho_v) \, g \, d \, \varepsilon^3 \, \left(1 + \frac{\lambda_c}{H}\right)}{1.75 \, (1 - c) \, (\rho_v^{1/6} + \rho_\ell^{1/6})^6} \right]^{1/2} \tag{1.56}$$

where ν is kinematic viscosity and λ_c is given in Eq. 1.47. Note that q_ℓ and q_t are also the dryout fluxes in the laminar and turbulent limits, respectively. In the limit of $\lambda_c = 0$, q_ℓ and q_t become the exact solutions for dryout with $w = 0$, which were mentioned earlier. The difference between the dryout fluxes predicted by Eq. 1.43 and 1.54 is worst at the shallow end of the moderate regime. There the difference is about 30%. The difference is less for deeper beds.

1.5 DRY DEBRIS COOLABILITY
(J. T. Hitchcock, 6421; J. E. Kelly, 6425)

The Dry Capsule studies, follow-on to the Molten Pool program, are using prototypic reactor materials to investigate experimentally the progression of a debris bed from dryout to melt and the interaction of the melt with structural and core retention material.

1.5.1   In-Pile Experiment Program

The DC 1 Experiment, the next in-pile test, will investigate the thermal characteristics of an internally heated UO_2 debris bed from 1273 K (1000°C) to melt and the phenomenology and thermal characteristics of a molten pool. During this quarter, the final experiment assembly was essentially completed. The pressure proof tests and preliminary leak checks were performed on the primary and secondary containment vessels. These tests confirmed the stress calculations and demonstrated the sealing capability of the metal K seal. Validyne pressure transducers were tested and calibrated over the experiment temperature and pressure range, with no drift observed. A diffusion welding technique was qualified for attaching the tungsten ultrasonic thermometer positioners to the bottom of the tungsten crucible. This welding was performed at 1673 K (1400°C) using a pressure of 20 ksi for 2 hr. Finally, a prototype ultrasonic thermometer was twice tested for a time period of 4 hr (the planned duration of the DC 1 test) to a peak temperature of 3123 K (2850°C). The instrument functioned reliably throughout the test and the five axial temperature measurements were self-consistent and agreed well with measurements from the optical pyrometer. The DC 1 test is scheduled to run in April.

1.5.2   Postdryout Debris Bed Modeling

Analysis of the postdryout behavior of reactor debris material, the progression of the debris to a molten state, and the subsequent interaction of the core melt with structural and core retention materials are all important in reactor safety analysis. Analytical models are being developed to predict the postdryout behavior of debris beds.

In Reference 1-36, a preliminary model for analyzing the postdryout behavior of debris beds was described. The original model treated the debris bed as one-dimensional and accounted for melt motion in a parametric manner. In order to expand the application of the model, the geometrical modeling was changed to two-dimensional (R-Z) and the melt motion modeling was generalized. While the two-dimensional modeling is not critical for analyzing reactor accident scenarios, this capability is needed for analyzing the in-pile experiments. The increased generalization of the melt motion allows a wider range of problems to be analyzed without relying on empirical factors. Hence, these improvements have extended the range of applications of the meltdown model.

The modification of the geometrical modeling to allow two-dimensional analysis was done by using an Alternating Direction Implicit (ADI) method for the heat transfer calculation. This method has good stability characteristics and is numerically efficient. Basically, this method solves the two-dimensional (R-Z) heat conduction equation using standard finite difference approximations. The model was kept general by allowing for nonuniform mesh size, nonuniform bed porosity, nonuniform power distribution and temperature dependent material properties. Radiation within the bed is accounted for through the use

73

of effective conductivity models. With this model, the two-dimensional temperature distribution can be calculated in debris beds of varying compositions and porosities.

Improvements in the melt relocation modeling were made to eliminate the need of specifying the melt penetration distance. Previously, the melt penetration distance was a fixed parameter, determined from a parametric study. This parameter is difficult to determine due to uncertainties in both the physical properties of the melt (such as viscosity and surface tension) and the appropriate form of the momentum equation. However, a simple model for melt penetration can be developed by considering the physical processes.

The main force driving the melt as it forms is the capillary force, which tends to draw the melt into the bed due to differences in saturation and permeability. For a bed of uniform porosity and particle diameter, this force should act in a spherically symmetrical manner. Gravity acts to move the melt downward while viscous forces tend to prevent melt penetration into the bed. However, for LMFBR in-vessel debris beds, the capillary force dominates until the melt volume becomes very large. The capillary force in a 45% porous bed with a particle diameter of 0.4 mm is equivalent to a gravitational head of 90 mm.

When the melt forms, it is rapidly accelerated and drawn into the porous bed. Once all the liquid is within the bed, the driving force for capillary flow is lost, and gravity moves the liquid downward. However, some of the melt will remain as a film on the particulate. Also, if there is a thermal gradient in the bed, some of the melt may freeze.

The penetration distance of the melt based solely on hydrodynamic mechanisms can be estimated by considering the case of a molten debris reservoir, which is allowed to flow into a porous bed (Figure 1.5-1). If the flow is assumed to be dominated by capillary force and the liquid totally fills the bed as it flows through, then a criterion can be developed to predict the maximum penetration distance. The first assumption implies that when the liquid is totally within the bed, the flow will stop. This assumption is true for horizontal and upward flow but is not always correct for downward flow. A second assumption, together with a mass balance, yields

$$X_o \, \epsilon_R = X_{max} \, \epsilon_B \qquad (1.57)$$

where X_o is the reservoir height, X_{max} is the maximum penetration distance, ϵ_R is the porosity of the reservoir, and ϵ_B is the bed porosity. This equation states that the mass of liquid initially in the reservoir must equal the final mass of liquid in the bed. This equation can be rearranged to find the maximum penetration distance for upward or horizontal flow.

$$X_{max} = X_o \, \epsilon_R / \epsilon_B \qquad (1.58)$$

The relationship X_{max}/X_o to ϵ_B is illustrated in Figure 1.5-1.
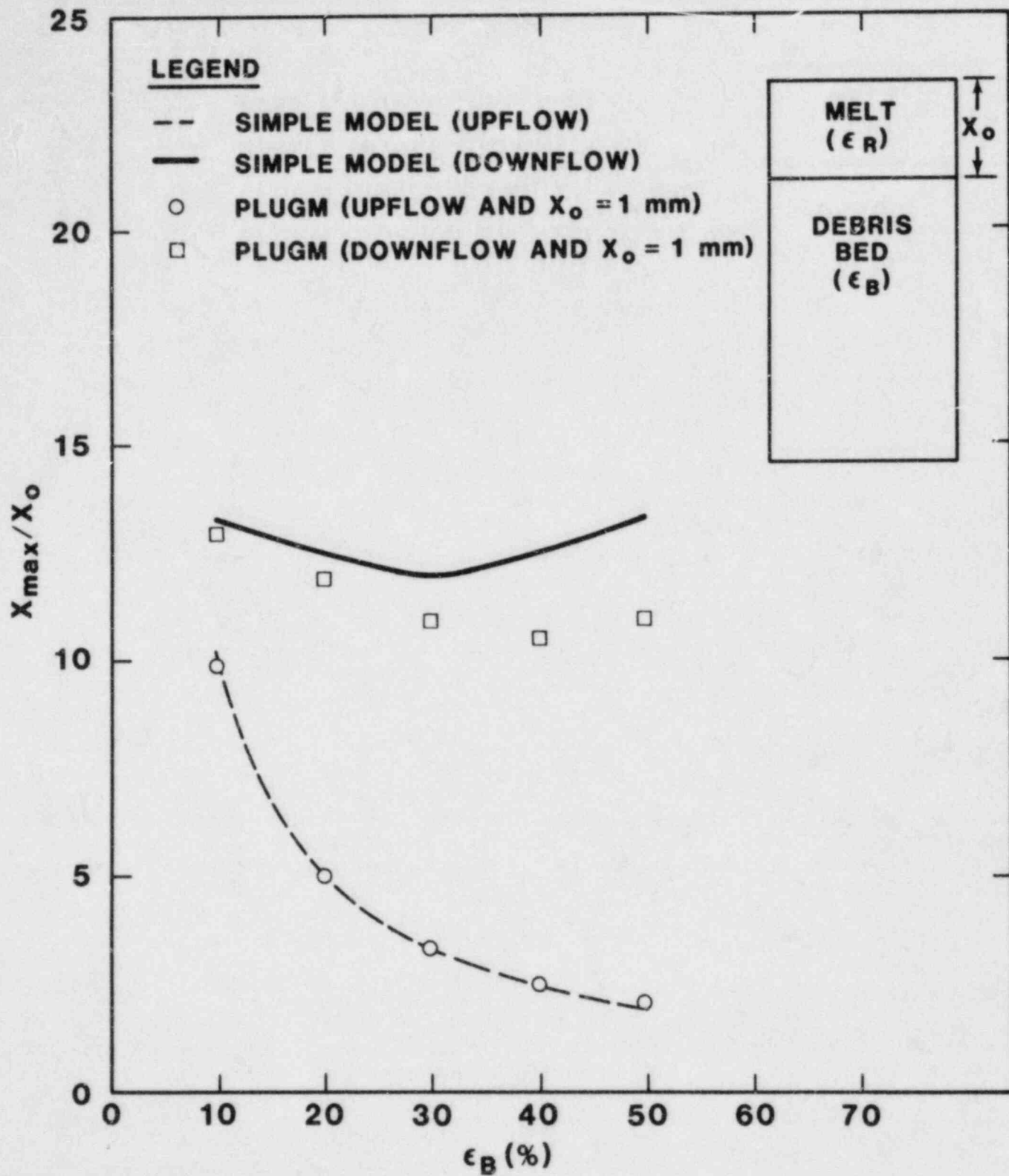
Figure 1.5-1.   Maximum Melt Penetration Distance Comparisons

For downward flow, gravity will continue to move the melt even after the capillary force is lost. However, a liquid film will be deposited on the particulate as the melt flows through the bed. If the bed is large enough, the melt may be totally depleted as a film. The film thickness depends on the bed permeability. Values of the thickness as a fraction of the bed porosity ranges from 0.75 for a bed of 10% porosity to 0.12 for a bed of 60% porosity.[1-37]

By using a mass balance for the melt,

$$X_o \, \epsilon_R = X_{max} \, \epsilon_B \, \gamma \qquad (1.59)$$

is obtained where γ is the film thickness fraction. By rearranging the maximum penetration distance is given as

$$X_{max} = (X_o \, \epsilon_R)/(\epsilon_B \, \gamma) \qquad (1.60)$$

As expected, the maximum penetration distance for downward flow (Eq. 1.60) is greater than that for horizontal or upward flow (Eq. 1.58).

To assess the validity of this model, comparisons have been made between the model and calculations made with PLUGM.[1-38] For horizontal or upward flow, the agreement between the two was found to be satisfactory. Comparison of the simple model predictions and those of PLUGM for upward flow (X_o = 1 mm) are shown in Figure 1.5-1. The agreement is found to be satisfactory. For downward flow, comparisons were also made with PLUGM (X_o = 1 mm) and are shown in Figure 1.5-1. Again, the agreement between the model and PLUGM is satisfactory. Hence, Eq. 1.58 and 1.60 can be used to estimate the hydrodynamic penetration distance of melt into a porous bed.

The above discussion has only considered hydrodynamic effects. In an actual bed, there will be temperature gradients that will allow the melt to freeze and possibly form blockages in the bed (i.e., plug). The hydrodynamic limits are absolute maximum limits and the thermal effects will shorten the penetration distance. In view of these thermal effects, a second criterion has been derived to estimate the penetration distance.

A simplified heat balance for melt that is freezing is given as

$$(1-\epsilon) \left(\rho C_p \right)_s (T_m - T_i) = \epsilon \rho_\ell \, h_{\ell s} \qquad (1.61)$$

where ϵ is the porosity, T_m is the melt temperature, T_i is the local temperature, and $h_{\ell s}$ is the heat of fusion. This equation may be rearranged to find the minimum ΔT that will freeze the liquid:

$$T_m - T_i = \left(\epsilon \rho_\ell h_{\ell s} \right) \Big/ \left| (1 - \epsilon) \left(\rho C_p \right)_s \right| \qquad (1.62)$$

This equation is accurate if the heat transfer from the liquid to the solid is large. Due to the large surface area in the bed, the heat

transfer is expected to be so. This equation, together with a calculated temperature distribution, can be used to predict the penetration distance.

To assess this model, PLUGM predictions were compared to the model predictions for downward flow cases. A temperature gradient of 473 K (200°C)/cm was used, and the plugging penetration distance as a function of porosity was calculated. For PLUGM, three reservoir heights were used to assess the influence of this parameter. The simple thermal model yields an upper bound for the penetration distance for all porosities, even for the large reservoir heights (Figure 1.5.2). In the X_o = 1 mm case, hydrodynamic effects tend to dominate the penetration distance for porosities greater than 30%. In this case, the hydrodynamic penetration distance yields a better limit.

The criteria developed for predicting the penetration distance have been shown to provide an upper limit to the penetration distance calculated using the fully coupled mass, energy, and momentum equations found in PLUGM. While not exactly predicting the correct penetration distance, these criteria are probably sufficient to estimate. In the meltdown model, each of these criteria is evaluated, and the minimum distance is used in the calculation of the melt propagation. Since the melting occurs over a relatively long period of time, many stepwise movements of the melt will occur. In an integral sense, the sum of all these steps should yield a good approximation of the actual melt motion.

An example calculation with this model is illustrated in Figure 1.5-3a and b, where the formation of a molten pool is depicted. In this example, a cylindrical dry bed (7 cm high, 8 cm in diameter) with internal heat generation is allowed to heat up and melt. The boundary temperatures on the top, bottom, and side are held constant. As the bed melts, it is drawn, forming a central void (Figure 1.5-3a). As more of the bed melts, a dense crust is formed and a permanent void is formed. The crust, in turn, supports the molten pool, and eventually a steady configuration is attained (Figure 1.5-3b).
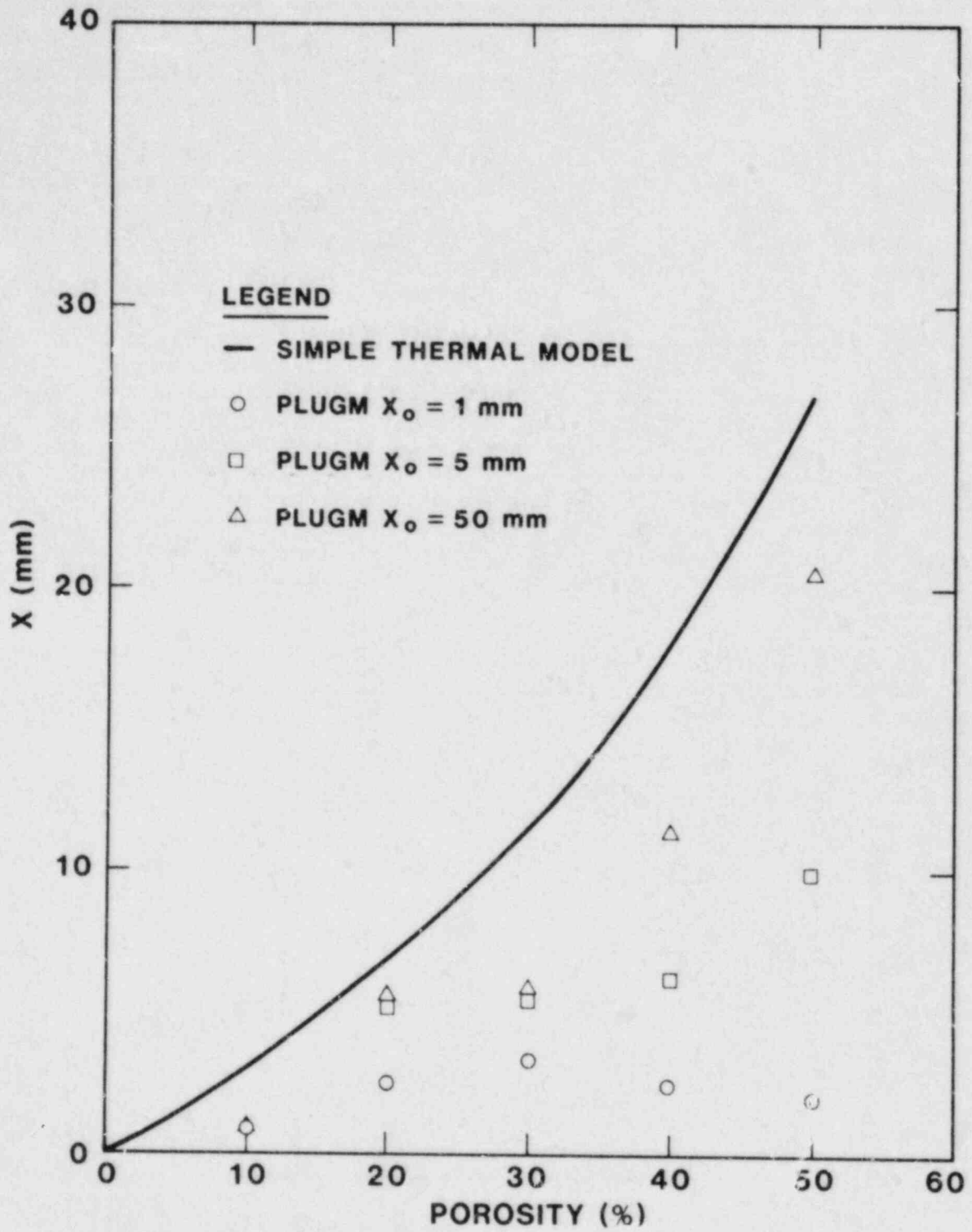
Figure 1.5-2.   Plugging Penetration Distance Comparison
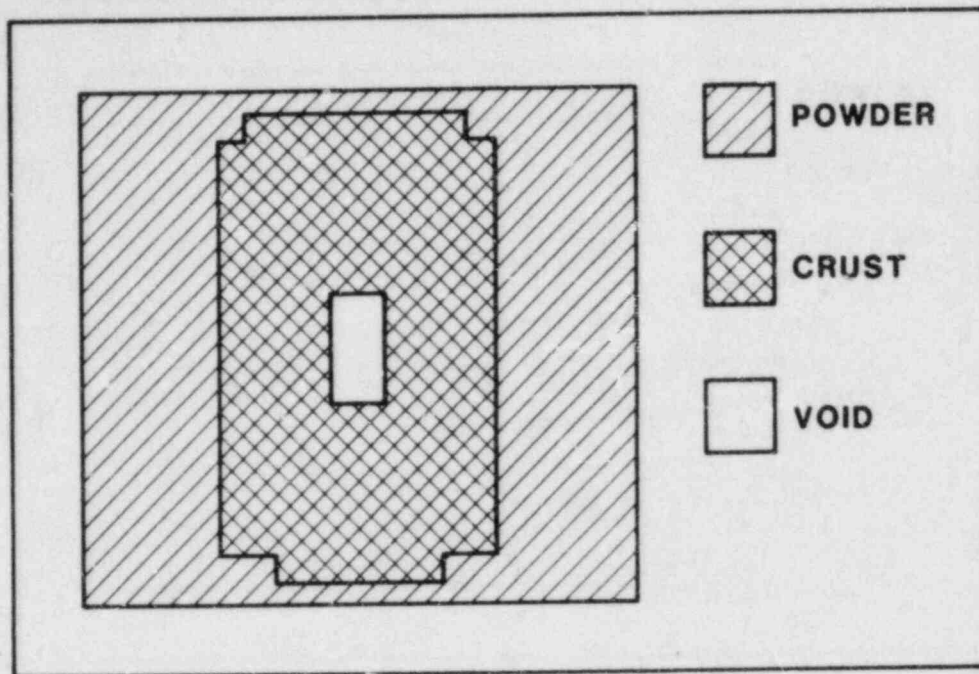
Figure 1.5-3a.   Initial Void Formation
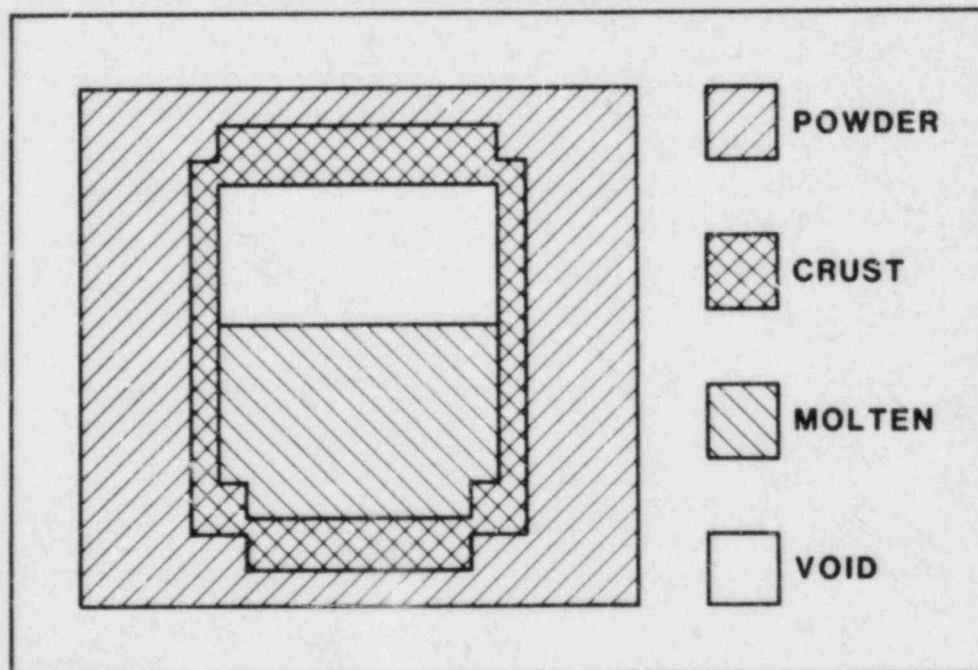
Figure 1.5-3b.   Molten Pool Formation

1.6 REFERENCES

1-1.   Advanced Reactor Safety Research Quarterly Report, April-June 1982, SAND82-0904 (2 of 4), NUREG/CR-2679 (2 of 4) (Albuquerque, NM: Sandia National Laboratories, to be published).

1-2.   Zion Probabilistic Safety Study (Chicago, IL: Commonwealth Edison Co., 1981).

1-3.   G. N. Abramovich, The Theory of Turbulent Jets, translation by Scripta Technica (Cambridge, MA: The MIT Press, 1963).

1-4.   Strategy of Experimentation - Revised Edition (Wilmington, DE: E. I. duPont de Nemours Co., Inc., 1975).

1-5.   G. E. P. Box and D. W. Behnken, "Some New Three-Level Designs for the Study of Quantitative Variables," Technometrics, p. 2, 1960.

1-6.   P. E. Chou and A. K. Hopkins, eds., Dynamic Response of Materials to Intense Impulsive Loading (Wright-Patterson AFB, OH: Air Force Materials Laboratory, 1972).

1-7.   Handbook of Chemistry and Physics, 46th Ed., Chemical Rubber Co. (Cleveland, OH: CRC Press, 1965).

1-8.   H. J. Sutherland and S. Hagen, Acoustically Measured Penetration Profiles for a Molten Metallic Pool into River-Stone Concrete, SAND82-0676, NUREG/CR-2634 (Albuquerque, NM: Sandia National Laboratories, December 1982).

1-9.   D. Buxton and W. B. Benedick, Steam Explosion Efficiency Studies, SAND79-1399, NUREG/CR-0947 (Albuquerque, NM: Sandia National Laboratories, December, 1982).

1-10.   E. Oberg et al, Machinery Handbook, 20th Ed. (New York, NY: Industrial Press, 1978).

1-11.   M. F. Spotts, Mechanical Design Analysis (Englewood Cliffs, NJ: Prentice-Hall, Inc., 1964).

1-12.   D. Powers and F. Arellano, Large-Scale, Transient Tests of the Interaction of Molten Steel with Concrete, SAND81-1753, NUREG/CR-2282 (Albuquerque, NM: Sandia National Laboratories, January 1982).

1-13.   J. F. Pederson, TAC2D - A General Purpose Two Dimensional Heat Transfer Computer Code, GA-8868 (San Diego, CA: Gulf General Atomic, September 1969).

1-14.   M. Pilch and P. K. Mast, "PLUGM, A Coupled Thermal-Hydraulic Computer Model for Freezing Melt Now in a Channel," SAND82-1580 (Albuquerque, NM: Sandia National Laboratories, to be published).

1-15. R. J. Lipinski, A Model for Boiling and Dryout in Particle Beds, NUREG/CR-2646, SAND82-0765 (Albuquerque, NM: Sandia National Laboratories, 1982).

1-16. A. W. Reed, The Effect of Channeling on the Dryout of Heated Particulate Beds Immersed in a Liquid Pool (Cambridge, MA: The MIT Press, 1982).

1-17. M. C. Leverett, "Capillary Behavior in Porous Solids", Transactions of the American Institute of Mechanical Engineers, Vol. 142, 1941.

1-18. L. Barleon et al, "Dependence of Dryout Heat Flux on Particle Diameter and Bed Height and Effects of Stratification and Bed Reconfiguration," Proceedings of the 5th Post Accident Heat Removal Informal Exchange Meeting, Karlsruhe, FRG, 1982.

1-19. G. Hofmann, "On the Location and Mechanisms of Dryout in Top-Fed and Bottom-Fed Particulate Beds," Proceedings of the 5th Post Accident Heat Removal Informal Exchange Meeting, Karlsruhe, FRG, 1982.

1-20. L. Baker et al, "Correlations of Particle Debris Bed Coolability Data," Proceedings of the 5th Post Accident Heat Removal Informal Exchange Meeting, Karlsruhe, FRG, 1982.

1-21. G. F. Stevens and R. Trenberth, "Experimental Studies of Boiling Heat Transfer and Dryout in Heat Generating Particulate Beds in Water at 1 Bar," Proceedings of the 5th Post Accident Heat Removal Informal Exchange Meeting, Karlsruhe, FRG, 1982.

1-22. F. P. Tsai et al, "Dryout Heat Flux in a Debris Bed with Flow from Below," Proceedings of the 5th Post Accident Heat Removal Informal Exchange Meeting, Karlsruhe, FRG, 1982.

1-23. D. Squarer et al, "Effects of Debris Bed Pressure, Particle Size, and Distribution on Degraded Nuclear Reactor Core Coolability," Nuclear Science and Engineering, p. 80, 1082.

1-24. C. Somerton et al, "An Experimental Investigation in Deep Debris Beds," LWR Safety Information Exchange, Gaithersburg, MD, October 26-31, 1981.

1-25. J. Jakobsson et al, Proceedings of the ASME/JSME Thermal Engineering Joint Conference, Honolulu, HI, March 20-24, 1983.

1-26. J. D. Gabor et al, "Studies and Experiments on Heat Removal for Fuel Debris in Sodium," Proceedings of the American Nuclear Society Fast Reactor Safety Meeting, Beverly Hills, CA, April 1974.

1-27. G. M. Fair and L. P. Hatch, "Fundamental Factors in Governing Streamline Flow of Water Through Sand," Journal of American Water Works, Vol. 25, p. 1551, 1933.

1-28. J. D. Gabor et al, "The Effect of Particle Stratification on Debris Bed Dryout", *Proceedings of the 5th Post Accident Heat Removal Informal Exchange Meeting*, Karlsruhe, FRG, 1982.

1-29. R. J. Lipinski, J. E. Gronager, and M. Schwarz, "Particle Bed Heat Removal with Subcooled Sodium: D4 Results and Analysis," *Nuclear Technology*, Vol. 58, p. 369, 1982.

1-30. J. B. Rivard, "In-Reactor Experiments on the Cooling of Fast Reactor Debris," *Nuclear Technology*, Vol. 46, p. 344, 1979.

1-31. G. W. Mitchell, R. J. Lipinski, and M. Schwarz, *Heat Removal from a Stratified UO_2-Sodium Particle Bed*, SAND81-1622, NUREG/CR-2412 (Albuquerque, NM: Sandia National Laboratories, February 1982).

1-32. G. W. Mitchell, C. A. Ottinger, and R. J. Lipinski, "Debris Bed Experiment D7," SAND82-0062 (Albuquerque, NM: Sandia National Laboratories, 1983).

1-33. C. A. Ottinger, G. W. Mitchell, R. J. Lipinski, and J. E. Kelly, "Heat Removal in Stratified UO_2 Debris in Sodium: D9 Results", *Transactions of the Meeting of the American Nuclear Society*, Detroit, MI, 1983.

1-34. H. C. Hardee and R. H. Nilson, "Natural Convection in Porous Media with Heat Generation," *Nuclear Science and Engineering*, Vol. 63, p. 116, 1977.

1-35. G. L. Shires and G. F. Stevens, *Dryout During Boiling in Heated Particulate Beds*, AAEEW-M1779, (Winfrith, UK: Atomic Energy Establishment, April, 1980).

1-36. *Advanced Reactor Safety Research Quarterly Report*, SAND82-0904 (4 of 4), NUREG/CR-2679 (4 of 4) (Albuquerque, NM: Sandia National Laboratories, to be published).

1-37. Brown and Associates, *Unit Operations* (New York, NY: John Wiley and Sons, 1950) p. 223.

1-38. M. Pilch and P. K. Mast, "PLUGM, A Coupled Thermal-Hydraulic Computer Model for Freezing Melt Flow in a Channel," SAND82-1580, NUREG/CR-3190 (Albuquerque, NM: Sandia National Laboratories, to be published).

2. HIGH-TEMPERATURE FISSION-PRODUCT CHEMISTRY AND TRANSPORT

(R. M. Elrick, 6422; R. A. Sallach, 1846)

The purpose of the High-Temperature Fission-Product Chemistry and Transport program is to establish the data base necessary to predict fission-product behavior properly during severe accidents. This experimental task is being pursued by three interrelated activities:

a. Definition of thermodynamic data and chemical reaction characteristics of particular fission products of interest.

b. Examination of the transport properties of fission products in prototypic environments of steam and hydrogen.

c. Comparison of the observed behavior of the fission products with predictions made by purely thermodynamic considerations.

2.1 CsI VAPOR REACTIONS WITH B_4C

The study of the chemistry of the control rod material, boron carbide (B_4C), in steam continued with experiments that examine the behavior of CsI vapor in the B_4C and steam environment.

The Fission Product Reaction Facility was configured as shown in Figure 2.1-1 for the boron carbide experiment. The same physical arrangement was used for the first two experiments in this series: boron carbide in steam alone at 1273 K (1000°C) and boron carbide in steam at 1273 K (1000°C) with the addition of CsOH vapor.[2-1]

Steam at 1273 K (1000°C) enters the reaction tube and flows through a bed of 0.07-cm B_4C particles packed in a sieve that filled the 2.5-cm-diameter flow tube for about 1.2 cm of its length (Figure 2.1-1). The particle surface area was measured by the BET method to be 0.031 m^2/g. The particle bed, placed upstream in the reaction tube, provided a reaction rate limited geometry and distributed any reaction products uniformly across the flow cross section. The B_4C reacts with steam to produce a surface film of liquid B_2O_3. Subsequently, the liquid B_2O_3 reacts with the steam to produce volatile boric acids, HBO_2 and H_3BO_3. The steam, laden with boric acid, mixes with the CsI vapor carried from an alumina crucible heated to 1093 K (820°C) (vapor pressure equals 4 torr). Steam flowed for about 160 min at a rate of 1 g/min with a velocity of 10 cm/s in the reactor tube. Coupons of Inconel 600 (in a system lined with Inconel 600) and of B_4C were placed downstream of the particle bed.

Preliminary analysis consisted of x-ray fluorescence on several of the Inconel and B_4C coupons, atomic absorption spectroscopy, ion chromatography, and titration on the steam condensate and the condensed boric acid plug (Figure 2.1-1). X-ray fluorescence counts that are shown can be compared between coupons of a given material, resulting in a measure of relative concentration. As in the two previous B_4C experiments, a plug of boric acid formed in the condenser

B₄C PARTICLES

B₄C AND INCONEL COUPONS

SUPER-HEATED STEAM

BORATED PLUG

(A) REACTION TUBE

CONDENSER

FISSION PRODUCT IN

(B) STEAM CONDENSATE
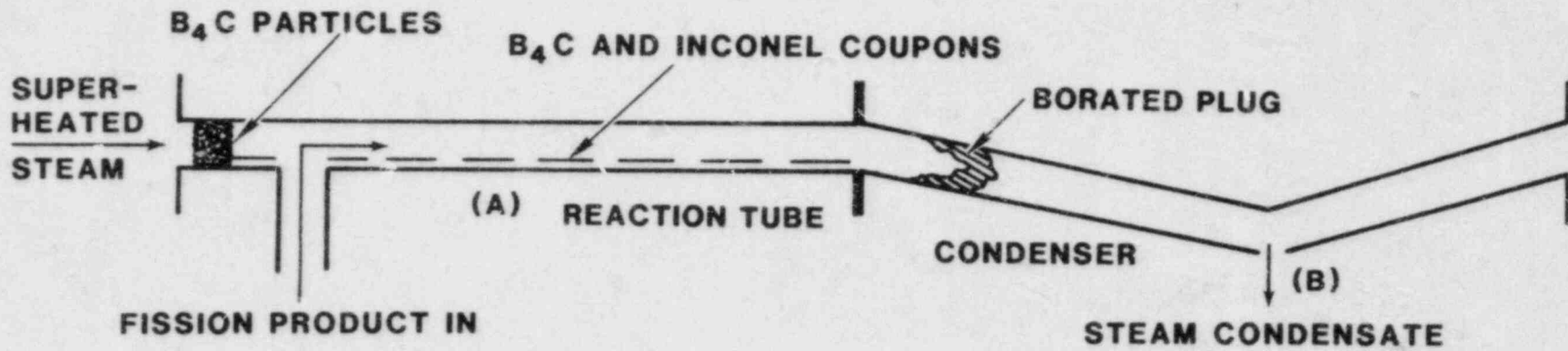
I Cal/B₄C IN STEAM 1000°C/INCONEL

(A) INCONEL	B₄C COUPON	(B)
Cs 200	Cs 9000	Cs 1-2 ppm
Fe 4500	Fe 1200	B 1500 ppm
Ni 25000	Ni 67	I 70 ppm
Cr 4800	Cr 40	
I bkg	I bkg	

Figure 2.1-1. Experiment Arrangement in the Fission-Product Reaction Facility To Study the Reaction Between CsI and Boron Carbide in Steam at 1273 K (1000°C)

84

at a temperature between 473 and 573 K (200° and 300°C). Analysis of the condensed steam showed that very little cesium got through the steam system, 1 ppm to 2 ppm compared to 80 ppm in the same system without B_4C. The level of iodine in the steam condensate was about the same in the system with B_4C as in the one without B_4C (80 ppm). Analysis of the plug showed that iodine was about 10 times as plentiful as cesium and implies that cesium removal had occurred prior to the condensation of the boric acids. Amounts of boron in both the plug and condensate were similar to the boron levels measured in the two previous B_4C experiments. This similarity indicates that the behavior of boron was about the same in the three tests. Some cesium reacted with the Inconel. X-ray fluorescence counts were about 200 counts/s (background count <30 cps) on the Inconel coupons exposed to CsI in tests with B_4C and without B_4C. There was no iodine detected on the Inconel in either of these tests. A very high level (9000 cps) of cesium was detected on the B_4C coupons. The boric oxide on the B_4C coupons, acting as a flux, dissolved iron and smaller amounts of nickel and chromium. Iodine was not detected on the B_4C coupons.

These observations indicate that most of the cesium is retained in the reaction tube. This can happen in two ways: (1) reaction of CsI with and dissolution in the B_2O_3 or (2) vapor phase reaction between CsI and boric acid to form a more stable cesium-boron compound. This compound, which may be $CsBO_2$ could then condense on tube surfaces. In either case, iodine is released in a more volatile form, presumably HI, which could collect in the plug and in the condensate. These resulting cesium and iodine forms are expected to be water-soluble and would pass into the aqueous phase on reflooding of the primary system.

2.2 TELLURIUM INTERACTIONS WITH STRUCTURAL MATERIALS

A new series of experiments was begun to examine the reaction between tellurium vapor and structural materials in a steam and hydrogen environment. Previous work in an argon carrier demonstrated that in the temperature range, 770 K to 1070 K (497° to 797°C), a rapid reaction of tellurium vapor occurred with both unoxidized and lightly oxidized surfaces of the structural alloys, 304 SS and Inconel 600. This data suggested that tellurium might be retained in the primary system should a release of fission products occur. However, at least two conditions must be met for the retention of tellurium on surfaces: (1) that the surfaces are not subsequently heated to decompose the tellurium compounds and (2) that concurrent oxidation (rather than a static oxide) does not impede the formation of tellurides.

These steam experiments were designed to address the importance of simultaneous growth on telluride formation and of temperature and environment in telluride decomposition. A schematic of the experiment apparatus is shown in Figure 2.2-1. Superheated steam at 1073 K (800°C) and tellurium vapor transported from the tellurium crucible at 923 K (650°C) 910-torr vapor pressure) by an argon flow are combined in a section of the reaction tube that is lined with alumina. This alumina liner allowed for the mixing of steam and tellurium vapor before the structural alloy in the reaction tube became exposed to the
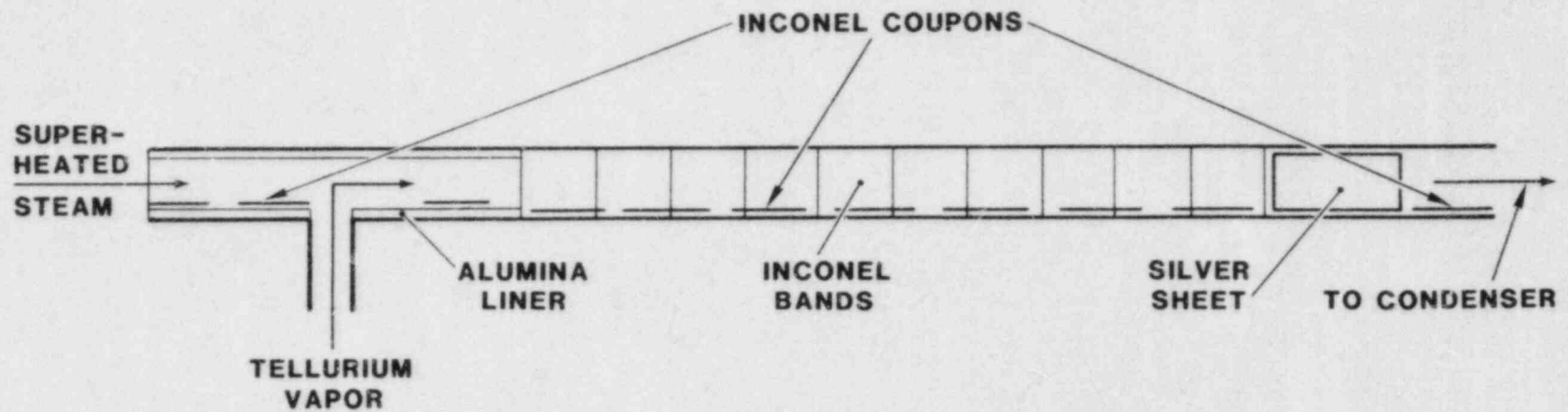
Figure 2.2-1. Reaction Tube in the Fission-Product Reaction Facility
Configured To Examine the Interaction Between Tellurium
Vapor and Inconel 600 in Steam at 873 K (600°C)

combined vapor stream. Residence time in the tube is about 5 s at an average flow speed of 10 cm/s; the experiments are run for 3 to 4 hr.

In the first experiment, the reaction tube was lined with pre-weighted Inconel 600 bands, and Inconel coupons were also placed along the length of the reaction tube. If the weight gained by the Inconel due to tellurium retention is large in comparison to the weight gained by oxidation, then an estimate can be made of the surface reaction rate constant from the weight gain profile along the reaction tube. This estimate is made from a modification to the deposition program FLATDEP written for the microbalance geometry. The modification, called CRCDEP, predicts deposition profiles in pipes with circular cross stion. Oxidation mass gains for the alloys were estimated from those coupons exposed only to steam. These coupons are located up-stream of the point of injection of tellurium and downstream of a sheet of silver positioned at the downstream end of the reaction tube. Mass gains for the 3-cm-wide Inconel bands varied from 11 to 2 mg (the weight gain due to oxidation) in about a 13-cm distance along the reaction tube. This rate of deposition is approximately the same as previously observed for the deposition of tellurium onto preoxidized Inconel in an argon environment.

2.3 TELLURIUM INTERACTIONS WITH URANIA

Earlier work on tellurium interactions were concentrated on its interactions with reactor structural materials and zircaloy cladding. Urania aerosols may be generated during a reactor accident, and the extent of interaction between fission-product tellurium vapor and urania in the 800 to 1100 K (527° to 827°C) temperature range is not known.

Two modes of interaction are likely. First, the surface adsorp-tion of tellurium vapor can be a prelude to condensation of tellurium. Though the adsorption would be taking place at such temperatures and vapor pressures, physical condensation would not be expected, only chemical bonding interactions should be observable. Such adsorption is not believed to be extensive, and thus a large surface area is desired for ease of measurement.

The second mode is incorporation of tellurium into the crystal lattice of the urania. Urania does show a large range in hyper-stoichiometry at high temperatures, which is the result of the incor-poration of additional oxygen atoms into the UO_2 crystal lattice. Tellurium is a member of the oxygen family of elements, and its chemi-cal properties would permit its incorporation. However, the atomic size of tellurium species is much larger than that of the correspond-ing oxygen species. This would limit the amount of tellurium that could be added. Again, large samples are desired for experimental convenience.

The results of several experiments in which tellurium vapor was equilibrated with urania particulate are reported here. For this study the microbalance apparatus used in the earlier tellurium studies was modified by the addition of a porous plug at the end of the balance tube. This plug supported a urania particle bed.

Tellurium interactions with the urania were determined indirectly. A known partial pressure of tellurium was produced in an argon carrier gas by its passage through a heated tellurium particle bed. This tellurium, containing carrier gas, was then directed through the urania particle bed. Subsequently the tellurium was removed from the gas stream by reaction with a nickel coupon suspended from the microbalance. The rate of mass gain by the Ni coupon was a direct measure of the tellurium content of the carrier gas. Interactions with the urania particles would be evidenced by changes in the rate of mass gain.

Experiments were made at temperatures between 773 and 1073 K (500° and 800°C) using two sizes of urania particulate, one at a nominal range of 1.0 to 1.4 mm and the other at a nominal range of 0.090 to 0.125 mm. A steady rate of mass gain by the nickel coupon was established within 4 to 8 min. This rate of mass did not differ significantly from that found in the absence of urania. Hence, there is no extensive interaction of tellurium vapor with urania.

A slight interaction between tellurium vapor and urania was shown in the following experiment. When urania was exposed to tellurium vapor for several hours at 773 K (500°C) and then heated to 1073 K (800°C), there was a transitory increase in the rate of mass gain of the nickel coupon, the rate later falling back to the initial value. Conversely, on decreasing the urania temperature, there was a transitory decrease in the rate of mass gain. These observations are not believed to be an artifact of the experimental procedure since the transition duration is ~40 min while only 10 to 12 min is required to establish a new stabilized urania temperature. The amount of tellurium is small, approximately 6 µg per gram of UO_2. Both urania sizes gave similar values, indicating that the interaction is probably not a surface-related phenomenon.

The long times required to establish equilibrium and the small magnitude of the interaction indicate that this interaction can be ignored in the context of reactor safety issues. Urania aerosol would not be expected to remain in this range of temperature long enough, nor is the interaction extensive enough, to result in any significant effect. Other tellurium/surface reactions would dominate.

REFERENCE

2-1. Advanced Reactor Safety Research Quarterly Report, October-December, 1982, SAND82-0904 (4 of 4), NUREG/CR-2679 (4 of 4) (Albuquerque, NM: Sandia National Laboratories, February 1984).

3. CONTAINMENT ANALYSIS

(M. E. Senglaub, 6424; K. D. Bergeron, 6424; P. Rexroth, 6424; W. Trebilcock, 6424; M. Murata, 6424; F. W. Sciacca, 6424)

The Containment Analysis Programs are centered on the development, testing, and application of the CONTAIN code. CONTAIN is NRC's general-purpose computer code for modeling containment response to a severe accident and for determining the consequences thereof. It provides detailed mechanistic models of phenomena that occur outside the reactor primary system and inside the reactor containment building. These phenomena include interactions between core debris and coolant or concrete, hydrogen combustion, thermal hydraulics of the gases in the various compartments of a containment building, aerosol behavior, and fission-product transport. CONTAIN provides models for LMFBR and LWR containment systems. Major parts of CONTAIN are operational and are being extensively tested and applied to reactor accident analysis.

For core-disruptive accidents in an LMFBR, the code provides models for the thermal hydraulics of the cell atmospheres; heat transfer to and vapor condensation on structures in the cells; sodium-spray fires; chemical interactions of sodium vapor and aerosols; hydrogen combustion; aerosol transport, agglomeration, and deposition; and radioisotope transport and decay. The reactor-cavity debris-pool model is partially completed and can model sodium-pool fires and core debris/concrete interactions. The modeling of core debris/coolant interactions and sodium/concrete interactions is not yet completed, due in part to the lack of adequate mechanistic models.

For severe accidents in an LWR, the code provides models for core debris/concrete interactions; cell-atmosphere thermal hydraulics; containment sprays; structure-heat transfer; steam condensation on structures and on aerosols; hydrogen combustion; aerosol transport, agglomeration, and deposition; and radioisotope transport and decay.

3.1 CONTAIN CODE DEVELOPMENT

3.1.1 Sodium/Concrete Interaction Model

A simple sodium/concrete interaction model has been developed to provide a means of estimating gas release to the reactor cavity and to provide a check on the performance of more complex, mechanistic models. The current model has been designated as the SSCI code. The interaction model includes a concrete zone, a reaction zone, a sodium pool, and a gas space. Within this system, a steady-state reaction is assumed to occur for 2 hr, with concrete penetration at 0.05 mm/s (3 mm/min, 7 in./hr) and constant reaction-heat input. The system lower boundary is assumed to move downward at the same velocity as the penetration rate; thus, new concrete is added to the system at the same rate as it is consumed. The thermal model is one-dimensional and includes temperature nodes for the concrete zone, reaction zone, bulk sodium, sodium surface, and the gas atmosphere. Sodium evaporates from the pool surface into an atmosphere saturated with sodium vapor

at the assumed constant gas temperature. Excess vapor is released from the system. System mass inventory increases by the generation of reaction products and decreases by the amount of released sodium vapor. Temperatures are held constant in the concrete, the reaction zone, and the gas space. Heat added to the system by reaction raises the sodium temperature. A reaction-zone temperature is calculated and compared to the assumed constant temperature.

Preliminary results for a 2-hr run using CRBR input parameters indicate a sodium temperature rise from 800 K to 975 K (527° to 702°C) and a sodium evaporation rate of 0.5 g-mole/s.

Hydrogen generated at the reaction zone is now treated using a bubble-rise model. An auxiliary calculation has determined the average velocity of rise to be 30 cm/s and the average bubble diameter to be between 0.9 and 2.4 cm in a deep (500-cm depth) pool. The bubbles carry an inventory of saturated sodium vapor that is small when compared with that evaporated from the pool surface. A reaction-zone temperature is now calculated at the sodium/concrete interface on the basis of constant reaction-heat input. Once the reaction temperature reaches the local boiling point, excess reaction heat is assumed to vaporize sodium. This vapor is then condensed in the bulk pool, and the heat of condensation is added there. Reaction products are assumed to be uniformly mixed in the pool to determine heat capacity and thermal transport properties. However, the pool is considered to be pure sodium to determine evaporation and condensation rates. The calculation procedure now provides for venting of the gas volume to maintain a constant pressure. Sodium vapor, hydrogen, and nitrogen, components of the gas atmosphere, are assumed to be vented at a rate proportional to their inventory. Fission-product heating is now an input to the bulk-pool temperature node as a function of rated core power. Reaction rate, duration of the reaction, fission-product heating rate, gas pressure (constant), and initial gas temperature can now be specified on input. The calculation can be terminated either on elapsed problem time or on exhaustion of sodium or concrete.

The improved code was tested using with the CRBR extreme penetration case (0.05 mm/s for 2 hr), and, as before, local boiling began at the reaction zone at 1.5 hr, continuing until the reaction was terminated at 2 hr. Now that fission-product heating is included, the bulk sodium temperature continued to rise to a maximum of 1144 K (871°C) at 3 hr and decreased slightly throughout the remainder of the run (to 15 hr). Gas, reaction-product, and pool temperatures were nearly the same at this time, and the gas volume was entirely occupied by sodium vapor. A preliminary validation calculation was made for Sandia Test 3. The reaction rate was assumed to be 0.05 mm/s (3 mm/min), and sodium was consumed in 11.7 min. At this time, 3.4 cm of concrete were calculated to be consumed, while the experiment indicated that all 15.2 cm of limestone concrete had been consumed. At best, calculated results appear to agree with the experimental results to within a factor of 2; a more detailed comparison is underway.

Further improvements planned for the SSCI code include treatment of the contribution to the aerosol source term resulting from breakup

of the hydrogen-bubble film. This assumes conversion of bubble film
into droplets upon burst of bubbles at the sodium surface. In addi-
tion, experiments indicate that a somewhat differ nt set of chemical
reactions is more appropriate; these reactions will be put into the
code, and the results will be compared with the current results.

3.1.2 LMFBR Reactor-Cavity Model

Tests have been performed to check out the moving interface
capability of the new LMFBR reactor-cavity model. With a slowly
moving interface and a very small node next to a large one, severe
instabilities resulted initially. The instabilities were eliminated
by making a small change in the algorithm, and the solution algorithm
now works well under a number of moving-node conditions. Each layer
in the problem will track two independently moving interfaces at most.

The process of developing the grid-behavior mechanism in the pool
layer revealed that the top of the pool needed to be treated in a
special manner. The model now assumes that there is at least one
atmospheric node in the problem. The properties of this node are
reset every cell time step to the values for the atmosphere as calcu-
lated by the main part of the CONTAIN code. A problem may be set up
with a pool layer that is initially dry. Given this condition, the
problem is treated using three nodes, and as the liquid level begins
to rise, the problem is restructured. Initially, a single liquid node
is used, and this node will grow until an internal condition is met
and the node is split. When this occurs, the problem will be treated
using two liquid nodes and a single atmospheric node rather than a
single pool node and two atmospheric nodes.

With the completion and demonstration of the moving-interface
capabilities of the new model, the input and control routines were
prepared for the implementation of various physical models. These
routines, plus an added source option, have been completed and tested.
Sources for individual layers can now be specified without resorting
to the distribution logic that existed in the old SINTER system. Use
of individual-layer sources requires the defining of layer-dependent
common blocks. The logic for loading and storing these blocks is
operational and in place.

Much effort has been spent in developing and testing the trans-
port models used in the new reactor-cavity model. The technique used
by Werner et al seems to work well for physical models in which there
are only one or two materials.[3-1] The situation, however, requires
additional mass conservation equations at the top and bottom half-
nodes of each layer. As a result, gradient-constraint correlations
were no longer used to define the surface densities. The technique
that appears to work is to solve for all the densities at the top or
bottom of a layer at a given point in time and to allow the velocities
at the top of the half-node to vary, thus providing the additional
free parameter. The additional equation to be solved is the volume
fraction constraint equation. This approach has been developed only
recently and needs to be tested some more to verify the potential that
it appears to have.

3.1.3 MEDICI, LWR Reactor-Cavity Model

Work on the MEDICI code/model continued. A working version of the code has been produced in accordance with the structure diagrams and "structured documents" that were generated over the past few months. In the spirit of top-down code design and development, this code is a skeleton of the final version, containing most of the required logic and data management, but using dummy subroutines for many of the physics modules. Most of the effort for this code went into developing and debugging an efficient, interactive input processor.

The skeleton code was recorded on tape and sent to University of Wisconsin personnel, who are developing computer models of the first phase of the core-melt/coolant interactions. They will integrate their models with the structure in the near future.

Meanwhile, model development for the second phase of core-melt/coolant interactions proceeded at Sandia. A new time-dependent debris-bed quench model using steady-state models for dryout flux has been developed by R. Lipinski and E. Gorham-Bergeron. Preliminary calculations with this model have been made, using constant atmospheric conditions, and good agreement can be obtained with results of quench experiments. Work has proceeded on generalizing the model to account for time-varying atmospheric conditions.

Work was finished on the M1 (initial interactions) portion of the MEDICI code. The input was completed using the recently developed INLIB subroutines for processing free-format input. The input routines were checked, comment cards were added to provide documentation, and then a melt-release subroutine was checked. Simple models for falling through air and water were included. The code could then treat a simple problem using the melt-release subroutine, which accumulated a debris bed at the bottom of a water pool. Water level and water property subroutines were also added to the code. This version of the code, along with the appropriate documentation, was sent to the University of Wisconsin so that models developed there can be integrated into the code and checked out.

Model E for tracing quench fronts in a debris bed was analyzed and coded. Model E includes all Model B treatments (channeling, etc.) plus a variable dryout flux. This latter feature entails different equations and numerical solutions of these differential equations rather than the closed-form solutions used in Model B. Model E was coded to make checking with Model B simple. This checking needs to be done, and following this, a library-solver routine needs to be added.

3.1.4 MELCOR Phenomenological Assessment

A substantial effort was directed this quarter to providing input to the MELCOR code-development project document. This document is intended to be a guide for code developers and to provide a rationale for model choices. Personnel involved in the Containment Analysis program are the principal authors of four sections of the report. These sections are containment flow and thermodynamics, reactor-cavity

phenomena, engineered safety features, and aerosol and fission-product behavior. These personnel also contributed to the section of heat transfer.

The containment-flow and thermodynamics section discusses the interrelations between the various models and modules within the code. Several main "building blocks" are identified (i.e., cells, flow paths, structures, a reactor cavity, and engineered features) out of which system models for any type of containment can be built. In addition, the cell-atmosphere thermodynamics and flowpath equations are discussed in detail. Development of mechanistic, pressure-driven-flow models has progressed to the point where they can be used in risk codes where speed is a primary consideration. Use of these models will allow a substantial improvement in the accuracy of modeling over that obtainable using the MARCH code. MELCOR should be able to model each physical compartment with one or more computational cells. More than one cell (or node) per compartment may be needed to model circulation within large compartments adequately, although the capabilities of MELCOR I may be limited in this respect. The cells can be interconnected in an arbitrarily complicated fashion through flow paths that range in complexity from simple holes in the walls to relatively complex BWR suppression pools. Many of these capabilities currently exist in the CONTAIN code, and the MELCOR study has helped identify several areas where CONTAIN can be improved.

The section on reactor-cavity constitutes a document that reviews phenomena unique to the cavity (i.e., excluding such a phenomenon as heat conduction in structures, which is also important in other parts of the containment). The phenomena addressed include high-pressure melt-release (including aerosolization, jet breakup, and sweepout of materials); coarse mixing and fragmentation of molten materials injected into water; steam explosions and subsequent fine fragmentation and expulsion; debris-bed formation, quenching, and dryout; simultaneous core/concrete interactions and debris-bed behavior; and flammable gas generation.

The section on containment heat transfer includes a complete description of the new condensation model that has recently been implemented in CONTAIN. Also included are some sensitivity studies performed with CONTAIN, the results of which show that the thermal resistance of the condensate film is usually negligible. However, the film could be important in certain circumstances, and therefore there should be at least a simple model of the film in any condensation model for LWR containment codes.

3.1.5 MAEROS Aerosol Module

Development work on the aerosol module continued. One concern successfully addressed was the modeling of evaporation and condensation of water on aerosols; the treatment of these processes appears to dominate the execution time in the LWR problems that are now being run. Execution time can be reduced substantially by simply changing the boundary conditions at the maximum and minimum particle sizes. The previous use of closed boundary conditions required an extremely

large range of sizes for the particles to avoid distorting the particle distribution function, and this large range introduced stiffness effects associated with having both very small and very large particles. Open boundary conditions, with an approximate treatment of particles overflowing from the mesh, allow the use of a much more restricted range of sizes and, as a result, much faster execution. The calculated results are also relatively insensitive to the maximum and minimum sizes selected, providing the distribution function is reasonably well bracketed.

When the aerosol concentration is very high (10 to 100 g/m^3), agglomeration occurs very rapidly, and condensation or evaporation can also occur very rapidly. As a result, the differential equations used in modeling the aerosol behavior can become very stiff, requiring very small time steps to perform integrations with the Runge-Kutta integrator currently being used. An increase in speed of execution can be achieved in part through the use of different boundary conditions, which makes the equations less stiff. To provide a further increase in speed, the use of a stiff differential-equation solver was investigated. Preliminary results indicate that the time required for calculations of aerosol behavior at high concentrations can be reduced substantially (an order of magnitude). However, the stiff solver requires substantially more storage space in central memory. The trade-offs involved in using a stiff solver (storage space versus speed) are being investigated further.

The input to the aerosol module has also been improved. A new, alternative-keyword input format allows the user to specify (non-default) values for many of the aerosol-physics parameters that are frequently used in other aerosol codes. The user can also specify keywords to disable the condensation phase, the evaporation phase, or both phases in order to carry out sensitivity studies.

3.1.6 Radionuclide-Transport Modeling

The tasks required for the modeling of radionuclide transport within and of radionuclide release from containment following severe accidents in LMFBR systems have been identified. Processes that require modeling to treat radionuclide redistribution between the various host materials (e.g., sodium, fuel, structures, aerosols, and atmosphere gases) have also been identified. Provisions must be made to treat not only the direct release of radionuclides to the upper RCB (following an energetic CDA) but also the transport of radionuclides that arise from interactions in the reactor cavity (following thermal failure of the vessel). A conceptual plan for modeling these processes was developed, and a preliminary review of the available data base was carried out.

The data base available for use in modeling the behavior of elemental iodine in LWR containments following severe accidents was reviewed. In this review, attention was focused on phenomena governing those natural removal processes that would be present in accident sequences were the containment's engineered safety features (ESFs) not operational. Understanding the rather complex hydrolysis chemistry of

94

elemental iodine received considerable attention. A model was formulated (but not yet implemented) that, though simplified, would allow representation of two important features of iodine behavior: the saturation phenomenon and the reaction kinetics that lead to a time dependence of the effective distribution coefficient governing the partitioning of iodine between aqueous and gaseous phases.

3.1.7 Engineered Safety Features

Modeling and initial coding of the CONTAIN heat-exchanger and recirculation model have been completed. Debugging and checkout are currently underway.

Development of the CONTAIN ice-condenser model has been initiated. A simple model, in which ice is modeled as a structure, is being used to study the suitability of the CONTAIN flow model for treating the highly transient blowdown through the ice compartment and to evaluate the various approaches that might be used in a more detailed model.

The fan-cooler models that are in use in existing containment codes were reviewed. This review was performed for both the CONTAIN and the MELCOR projects. The simplest models, those in which the cooling rate is expressed as a simple function of containment temperature, were deemed inadequate. The model used in the MARCH code is more detailed; it uses an effective heat transfer coefficient that is a function of atmospheric vapor fraction. Using this correlation and the design conditions and capacity, an effective heat transfer area is computed. This area is then used in the computation of capacity for off-design conditions. The correlation for the heat transfer coefficient is based upon cooler capacity curves that were developed assuming saturated conditions and a constant concentration of noncondensable gases.

To test the MARCH correlation, a simple mechanistic fan-cooler model was developed using the condensation formulation that has been adopted for CONTAIN. At saturated conditions, the model results agreed well with the MARCH results. For superheated atmospheres and variable concentrations of noncondensables, the results diverged. The Sandia staff proposes that both MELCOR and CONTAIN include a condensing fan-cooler model, with perhaps the option to use the MARCH correlation where its governing assumptions are known to be valid.

3.1.8 Aerosols

In combined MARCH/CORRAL or MARCH/MATADOR calculations, the thermohydraulic processes calculated by MARCH are assumed to be independent of the detailed aerosol and fission-product behavior calculated by CORRAL or MATADOR. In contrast to the integral treatment in CONTAIN, any coupling or feedback effects from aerosol/fission-product behavior on thermohydraulic processes would therefore have to be calculated in a cumbersome iterative fashion. Several coupling effects were studied in conjunction with the MELCOR phenomenology assessment program. Significant coupling effects are expected from the

thermodynamic behavior of the suspended aerosol mass in the case of water aerosols and from localized heating due to the deposition of fission products on surfaces and heat sinks. A qualitative evaluation is currently in progress and will be available in a forthcoming report.

3.1.9 CONTAIN-CORCON Link

Several runs using the CONTAIN-CORCON link were made to optimize the buffer size for overlay loading. A sample problem (8000-s problem time) was run (a) using CONTAIN (SINTER) and CORCON together and (b) using the CONTAIN-CORCON link. The results were compared with the result of running the same problem using only CONTAIN (SINTER). Compared with the cost of running CONTAIN alone, it costs only twice as much to run CONTAIN with the overlay structure used with the CORCON link and four times as much to run CONTAIN and CORCON together.

3.2 CONTAIN TESTING

The testing of CONTAIN has been underway for some time. Many features of CONTAIN have been tested, and a large number of tests have been completed and documented. The results of this testing are being compiled into a comprehensive report that will summarize the results of the CONTAIN Test program to date. The objective is to make available to the user community the results of the tests that have thus far been performed. The report presents these results so that users may be aware of the areas that have been tested, of the features that have been verified and that therefore may be used with confidence, and of the areas where problems have been identified.

The test-program results presented in this report include several elements. The actual test reports are provided, along with a brief discussion of the supporting analysis used to check the code output. Data sets used in making the CONTAIN runs are also provided. Thus, this report provides information needed by a user to repeat tests of interest in his specific work areas. By repeating certain tests, the user can check the results obtained using his particular version of the code against documented test results.

The test areas listed below will be covered in this report. The general test area is indicated, together with the test series included in that category. The test series identification letters are also shown.

a. Atmosphere Thermodynamics and Heat Transfer

   Series AA - Atmosphere Thermodynamics and Sources
   Series AC - Atmospheric Condensation
   Series VA - Sodium- and Water-Vapor Thermodynamics
   Series HS - Atmosphere-to-Structure Heat Transfer

b. Atmosphere Chemistry

   Series HB - Hydrogen Burning
   Series SB - Sodium-Vapor Combustion
   Series SF - Sodium-Spray Fire

c. Intercell Flow

   Series CF - Intercell Flow of Gases
   Series AF - Intercell Flow of Aerosols

d. Fission Products

   Series FP - Fission-Product Decay and Release

e. Pool Thermodynamics and Heat Transfer

   Series PQ - Pool-to-Atmosphere Heat Transfer
   Series PB - Pool Heatup and Boiling
   Series PS - Pool Sources
   Series PC - Pool Chemistry
   Series PF - Sodium-Pool Fires

f. Aerosol Behavior

g. Integral Tests

   Series ZT - LWR Sample Problem

   A preliminary draft of the report containing Test Summary Reports, Input Data Sets, and Supporting Analyses has been assembled.

3.3 CLINCH RIVER CONTAINMENT ANALYSIS

   During this reporting period, additional features of the CONTAIN code were checked out to ensure that the phenomena associated with severe accidents in the CRBR were being adequately treated. Of particular importance is the treatment of water release from heated concrete. Water release can be important in these accident scenarios because the sodium-water reaction is highly energetic and produces hydrogen. Checks of CONTAIN established that water was being released from heated concrete, but that some of the water present was not being adequately accounted for. Work was initiated to determine whether the water-migration model was working properly.

   A potentially important aspect of aerosol behavior is that of aerosol plateout on walls and ceilings. Aerosol deposits observed in tests tend to be very light and fluffy. These deposits can act as an insulating material if the plateout on heat-transfer surfaces is significant. In the CRBR design, the upper RCB atmosphere is cooled during accident conditions by heat transfer through the steel containment shell. Aerosol deposits on this shell could restrict this heat transfer and lead to potentially higher upper RCB temperatures than have thus far been anticipated. Efforts were initiated to model this

phenomenon in CONTAIN. The present coding treats the aerosol deposition and plateout processes, but modifications need to be made to account for the additional thermal resistance posed by the aerosol deposits.

The CRBRP containment-response analysis requires a good set of data representing the fission-product inventories. Work was started to obtain detailed information on fission products applicable to the CRBR's heterogeneous core. The ORIGIN code (Sandia version) will be used to generate this updated inventory information.

During the quarter, work on aerosol plugging of flow paths was reviewed. A paper by H. Morewitz of Atomics International presents a simple empirical model, which is well verified by tests but which is of limited use for time-scale predictions.[3-2] T. Huang of GE has developed a plugging code called GALP.[3-3]

3.4 LWR CONTAINMENT ANALYSIS

3.4.1 LWR Source-Term Study

A peer-review meeting on the LWR source-term work was held at NRC on 25-26 January. Battelle presented results of calculations for four different (Surry) accident sequences (AB, TMLB', S_2D, and V), with several differing containment failure modes for the first two sequences. Relatively larger retentions are calculated in containment than in the RCS, especially when early containment failure is improbable. The discussion at the meeting indicated that many people attached correspondingly large uncertainties to the containment calculations and that there is considerable skepticism in the community about the experimental support for several of the codes used in the study. It appears that CONTAIN can provide a firmer basis for some of the crucial aspects of the containment retention estimates, and discussions are currently underway with NRC to provide additional support in this area.

Following the peer review of the LWR source-term work in January, a detailed review was performed of the then-current draft of NUREG-0956, "Radionuclide Release Under LWR Specific Accident Conditions, Vol. I: A PWR Analysis." The review included, in certain instances, checks of computer calculations reported in NUREG-0956 against simple analytical calculations.

The review draft shows that NUREG-0956, when completed, will offer the potential for substantially increasing current understanding of radionuclide transport and release in LWR accidents and should improve the ability to identify the major areas of uncertainty requiring further work. Nonetheless, it is also clear that substantially increased care must be taken to ensure that in each scenario the models employed are treating the dominant effects, at least as a first approximation. The analysis of radionuclide release from the reactor coolant system (RCS) in TMLB' sequences appears to be a case in which the dominant effects were not always treated. Simple analyses show that in TMLB' sequences, natural convection processes will

dominate forced-flow processes by some orders of magnitude in governing heat and mass transport within the RCS. However, the modeling used treats only forced flow and neglects natural circulation in some key stages. For example, transport by natural convection between control volumes is ignored, even though some of the control-volume boundaries are essentially artifacts of the calculational procedure and do not correspond to physical boundaries that would present a barrier to natural circulation.

The results quoted for the S_2D sequences also require careful checking. These sequences are the only ones considered in which containment sprays were assumed to be operating. The results given suggest that particle residence times in containment were only a few seconds, while containment-spray experiments indicate that residence times of a few minutes to a few tens of minutes can be expected. The problem may arise in the modeling of the sprays, for which the calculated collection efficiencies for collisions between spray drops and aerosol particles seem to be excessively high.

A letter report, covering these points in some detail and including a substantial number of additional comments, was written and forwarded to the NRC.

In addition to these specific problem areas, three general conclusions or concerns were apparent from the peer-review meeting and from the draft report: (1) although there is considerable uncertainty and variation from one accident scenario to another, the principal fission-product-retention processes appear to occur in containment, outside the RCS; (2) considerable skepticism was voiced concerning the use of essentially unvalidated codes in the study to date; and (3) sensitivity studies are needed to estimate the uncertainty in the modeling and in the input data. In view of these concerns, NRC has urged that CONTAIN be used to provide a more substantial basis for the containment part of the study. Calculations of the Surry accident sequences are being started.

3.5 REFERENCES

3-1. Werner et al, "Treatment of Discontinuity of Derivatives by the ASWR Method," Proceedings of the ITM on Advances in Mathematical Methods for the Solution of Nuclear Engineering Problems, Vol. I, April 27-29, 1981, Munich, FRG.

3-2. H. Morewitz, "Leakage of Aerosols from Containment Buildings," Health Physics, 42, 2, February 1982.

3-3. T. Huang, Revisions and Development of Aerosol Analytical Methods GEAP-14147 (San Jose, CA: General Electric Company, September 1976).

4. ELEVATED TEMPERATURE MATERIALS ASSESSMENT

(C. H. Karnes, 1835; W. B. Jones, 1835)

The primary objectives of the Elevated Temperature Materials Assessment studies are (1) to determine how microstructures evolve due to thermochemical history, which results in mechanical property changes, and (2) to evaluate the validity of material damage and evaluate nondestructive evaluation techniques.

4.1 INCONEL 718 CHARACTERIZATION

The staff completed optical metallography on the thermally aged specimens of Inconel 718 received from INEL. These two heats had shown significantly different age-hardening kinetics even though both heats were well within allowable ASTM Specifications for Inconel 718. The metallography showed that the heat exhibiting more pronounced age hardening had a finer grain size and more obvious banding from the forging process. Some resolvable precipitation seems to have occurred in the harder heat while the microstructure of the second heat appeared unchanged for up to 25,000 hr at 922 K (649°C). Project personnel prepared thin foils so that these can be studied in the transmission electrode microscope to characterize the fine-scale precipitation products, which cannot be resolved by optical techniques.

4.2 BIAXIAL TESTING

Sandia staff members visited Oak Ridge National Laboratory to formulate a detailed test plan for a cooperative study of the elevated temperature biaxial deformation behavior of stainless steel. They determined that the most meaningful initial study would be to evaluate the current design analysis method for biaxial deformation. This design assumes that the only deformation parameter that affects component life under cyclic deformation is the total strain range, regardless of the principle stress path covered. This study will include tests to failure along three different stress paths, one radial and two nonradial. Another part of the study will monitor the motion of the yield surface after the material has been subjected to groups of excursions into different parts of the plastic range.

Trial specimens on 316 SS had previously been obtained on this program, and efforts have been underway to characterize the surface roughness and wall thickness uniformity. It appears that a wall thickness variation of 2% and surface roughness of 11 microinches on the outside and 44 microinches on the inside are typical. Deformation modeling studies on 316 SS continued with additional measurements being made of creep behavior and of kinematic variables in strain transient dip tests.

Other laboratories doing elevated temperature deformation studies using induction heating indicate that radiofrequency fields were coupling into the thermocouple leads and influencing the temperature measurements. Confirmation tests were conducted to establish that

this was not occurring at Sandia. A test specimen identical to the normal configuration was heated inductively. When the induction power was instantaneously turned off, the thermocouple output was observed to be continuous and to follow the anticipated cooling behavior, thus indicating that no voltage was induced into the leads from the radio-frequency coils.

5. ADVANCED REACTOR ACCIDENT ENERGETICS

The Advanced Reactor Accident Energetics program is directed toward developing a data base for the understanding of the key in-core events, in a core disruptive accident, that determine the progression and severity of a reactor accident. For the advanced reactor, understanding in-core events is particularly important because significant energy release from the core is possible. The magnitude of this energy release, and therefore the ultimate threat to the containment, is determined by the competing positive and negative reactivity effects caused by the motion and temperature of fuel, cladding, and coolant.

This program, currently focused on postulated CRBR accidents, involves experimental and analytical efforts to determine the magnitude and characteristics of these reactivity effects in the two phases of a core disruption accident in an advanced reactor. These phases are:

a. Initiation Phase -- Fuel Dynamics
b. Transition Phase -- Fuel Freezing and Streaming.

5.1 INITIATION PHASE -- FUEL DYNAMICS
(S. A. Wright, 6423)

The last two experiments (FD4.4 and FD4.5) in the FD2/4 experiments program are described in this report. The previous seven experiments are described in Ref. 5-1, 5-2, and 5-3. These earlier experiments investigated the influence of power history and burnup on the mode of fuel disruption. In these last two experiments, solid-state cracking (a mode of disruption observed in previous experiments) was investigated in more detail. This mode of disruption is especially interesting because it may lead to early fuel dispersal in some types of LMFBR accidents.

Experiment FD4.4 reproduced the heating conditions of experiment FD4.3, in which dispersive ejection of solid fuel occurred, later followed by fuel melting and slumping. However, in experiment FD4.4, the reactor transient was stopped prior to fuel melting. Solid-state fuel ejection was indeed achieved in this experiment, and the fuel pin remained intact rather than being destroyed, as in experiment FD4.3. The remaining fuel from this experiment will be examined using PIE techniques at KfK to study the details of solid-state cracking.

Experiment FD4.5 investigated the behavior of German-fabricated fuel under the same type heating conditions that produced cracking in U.S.-fabricated fuel. The German fuel was irradiated in the KNK-II reactor at KfK and had a burnup of 4.5 a/o and a linear heat rating of 43.5 kW/m. This fuel was suspected of having a higher gas content than the PNL fuel (for similar burnup and linear heat rating) because of the larger grain size. Thus, for this fuel, the disruption consisted of early solid-state swelling followed by limited sputtering of fuel from the unrestructured zone. This type disruption was very

similar to that observed in experiment FD2.8, which used fuel with a high gas content (8.3 a/o burnup).

The results and analysis of these two experiments are described below.

5.1.1 Fuel Characteristics for Experiments FD4.4 and FD4.5

Experiment FD4.4 used a fuel section from the middle of the PNL10-74 fuel pin. This fuel and irradiation history are described in HEDL-TME-80-20.[5-4] Most of the data used in this report and analysis were taken from Ref. 5-4 and from PIE of a PNL10-12 fuel pin. The FD4.4 fuel pin section had a burnup of 5.62 a/o and a linear heat rating of 25.6 kW/m. Distructive fission gas analysis made on a neighboring fuel pin PNL10-12 indicated that 64% of the fission gas was released. As a consequence, the PNL10-74 fuel pin is estimated to have a retained fission gas content of 1×10^{26} Xe-atoms/(m^3).

The fuel used in experiment FD4.5 was fabricated in Germany and preirradiated in the KNK-II reactor. The fuel had a burnup of 4.5 a/o and a linear heat rating of 43.5 kW/m. The major differences between this German fuel and the U.S. fuel are porosity (14.6% versus 9.09%), grain size (15 versus 10 μm), enrichment (93% versus 40% to 67%) and diameter (6.00 versus 5.84 mm). The fission gas characteristics are not well known at this time. However, since the unrestructured fuel had larger grains than the PNL fuel, it is reasonable to expect that the gas content was larger in spite of its higher linear heat rating. (The gas release fraction is very sensitive to the grain size.) The retained gas concentration is estimated to be greater than 1.0×10^{26} and less than 1.7×10^{26}.

Additional fuel characteristics are described in Table 5-I. This table lists the local fuel characteristics for both experiments. It should be noted that the fuel enrichment for the KfK fuel was 93%; thus, the reactor coupling factor was higher than in the previous FD experiments. The coupling factor, as in all experiments, was determined by calorimetric measurements and is estimated to be accurate to ±3%.

5.1.2 Results and Preliminary Analysis for Experiment FD4.4

This experiment used an ACRR power history that was similar to that used in the FD4.3 experiment. The disruptive power pulse, however, was terminated shortly after its peak. Our precalculations showed that this type power transient would cause solid-state cracking but prevent fuel melting. This was indeed achieved; therefore, fuel specimens are available for PIE tests. These PIE tests should expose the microscopic mechanisms that are causing the cracking phenomena.

Figure 5.1-1 shows the power transient used for this experiment, with an arrow indicating the observed time of fuel disruption. Table 5-II illustrates the major sequence of events as observed in the film, and Figures 5.1-2 and 5.1-3 show the calculated thermal profiles and the temperature histories.

Table 5-I

Fuel Characteristics for Experiments FD4.4 and FD4.5

	FD4.4	FD4.5
PIN	PNL10-74	(KNK-II/15)*
Pellet numbers	35-39	---
BU (a/o)**	5.62	4.5
Linear heat rating (KW/m)	25.6	43.5
Enrichment (%)	67.3	93
Pu/(Pu + u) (%)	25	30
Coupling factor (J/g/MJ)	12.95	14.48
Diameter of fuel	5.08	---
Theoretical density $-TD^\dagger$ (Kg/m^3)	11.0×10^3	11.02×10^3
Fabrication density† (%TD)	90.9	86.5
Smear density† (%TD)	85.5	80.5
Released fission gas (%)	36	36-60
Fission gas concentration (atm/m^3)	1×10^{26}	$1-1.7 \times 10^{26}$

*
Irradiated in KNK-II reactor
**
Local values
† ±2%

The fuel disruption sequence was identical to the FD4.3 experiment, beginning at 4.761 s with an ejection of solid fuel moving at 8 to 10 m/s and consisting of approximately 5% to 10% of a single fuel pellet. The fuel was ejected through molten cladding (35% through the heat of fusion) which had not relocated. The peak temperature of the fuel was 2700 K (2427°C)(fuel centerline), but the ejected fuel (from the center of the unrestructured region) had a temperature of 2150 K (1877°C). The gradient in the unrestructured zone was 2800 K/mm, and the reactor power at the time of disruption was about 10 times P_o.

The ejection lasted for 7 ms, after which a calm period occurred. Following the calm period, the ejection began again but with a much weaker intensity. This ejection consisted of a sputtering of small fuel fragments (0.2 to 0.5 mm) at velocities of 1 to 2 m/s. At 4.800 s, some swelling of solid fuel was observed (32% volume increase), but by this time, the power level was rapidly decreasing so the swelling was terminated before fuel melting occurred (Figures 5.1-2 and 5.1-3). If melting did occur, it was only at the fuel centerline, and even then it would have just barely reached the solidus temperature.
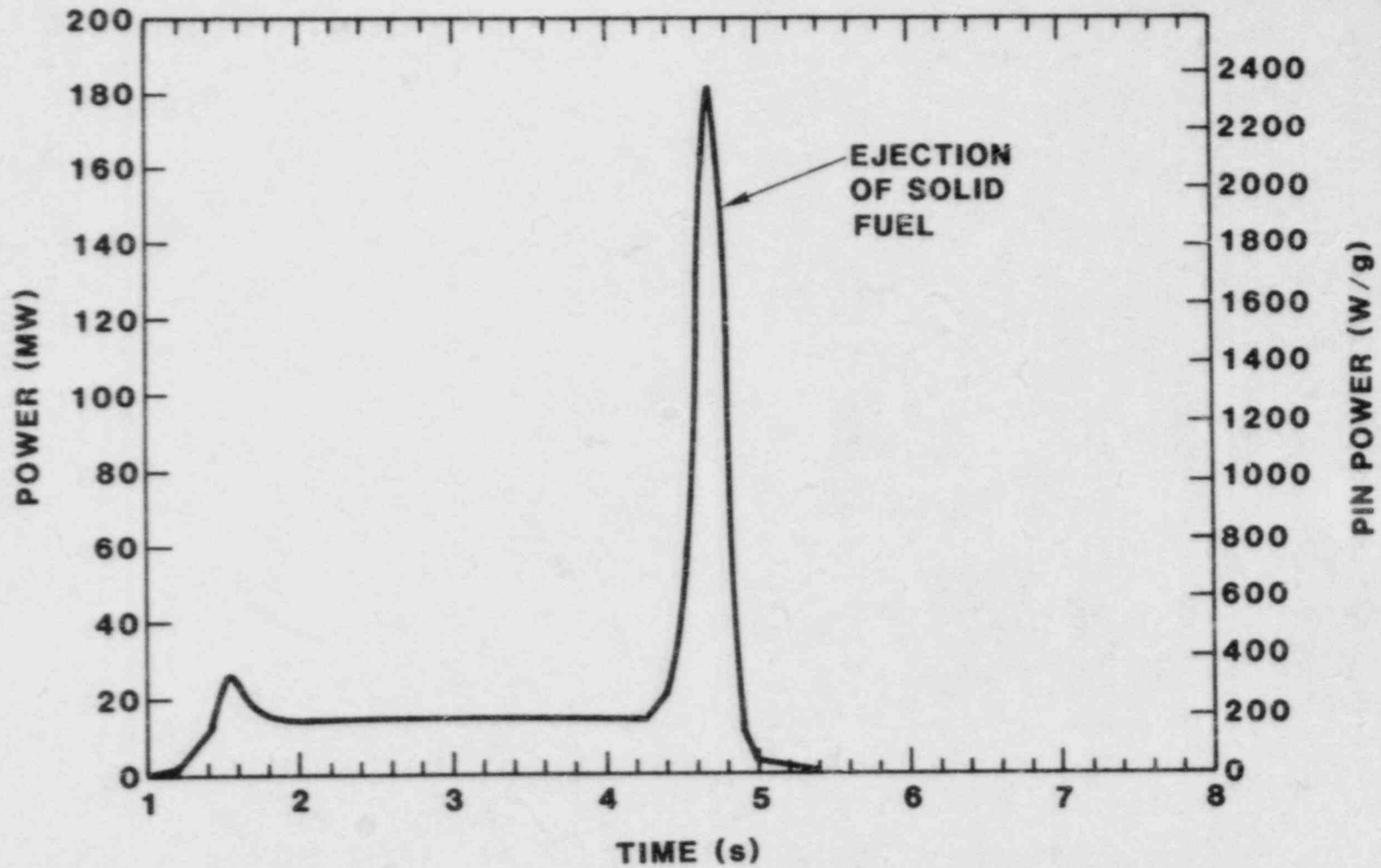
Figure 5.1-1. Measured ACRR Power Transient for FD4.4

Table 5-II

Sequence of Events as Observed from FD4.4 Film

| No.	Event	Time (Rod Timer) (s)
1	One ms before fuel ejection	4.760
2	Start of solid fuel ejection	4.761
3	Cont. ejection of fuel (v=10 m/s)	4.762
4	Cont. ejection of fuel with some solid chunks (1 mm)	4.763
5	Ejection significantly reduced	4.764
6	End of ejection	4.768
7	Calm period, no ejection	4.772
8	Start of mild sputtering	4.777
9	Cont. sputtering	4.784
10	Start of gas release and swelling clad 10% removed	4.800
11	Clad 100% removed	5.179
12	Final State of fuel	5.3 (arb.)
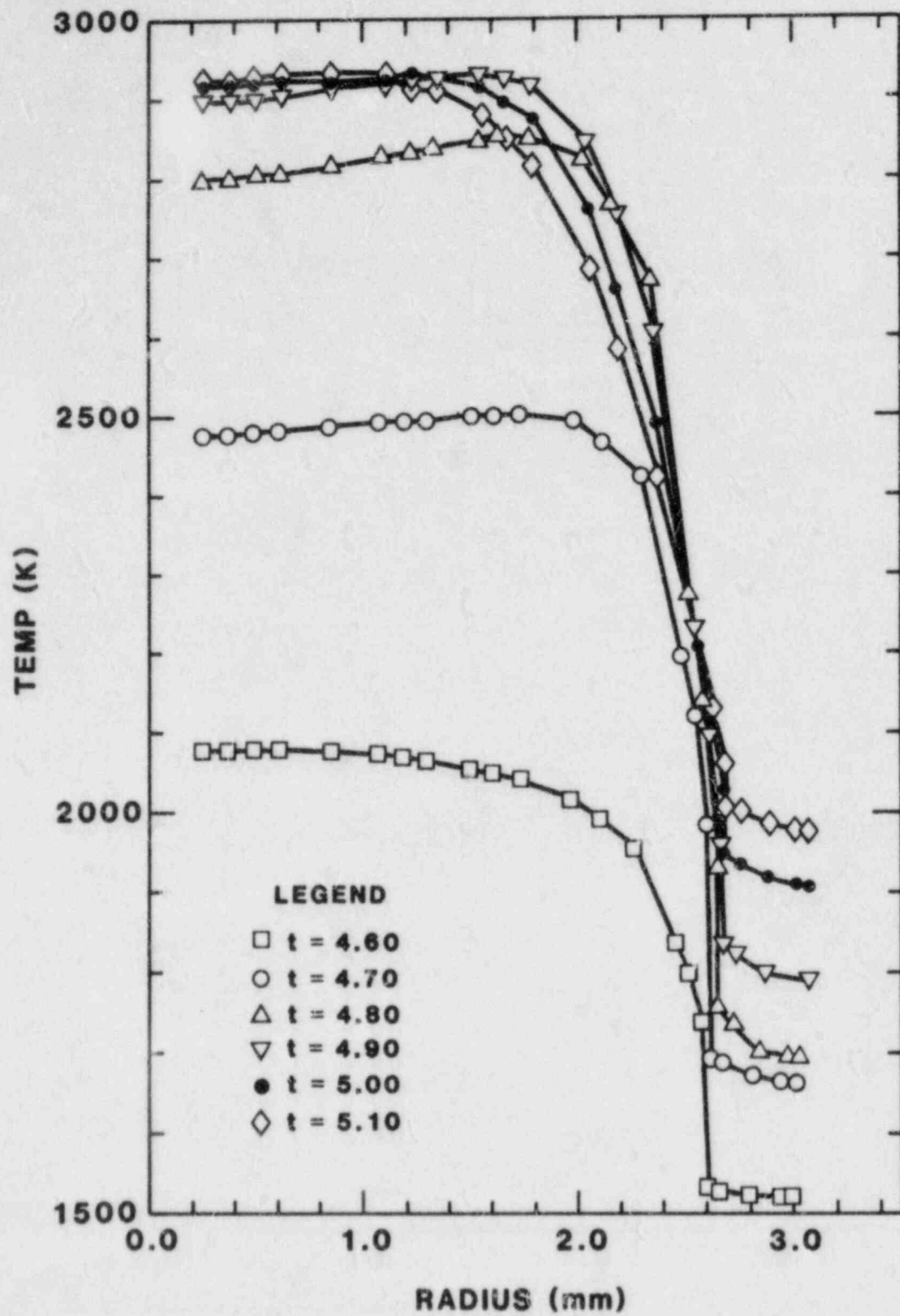
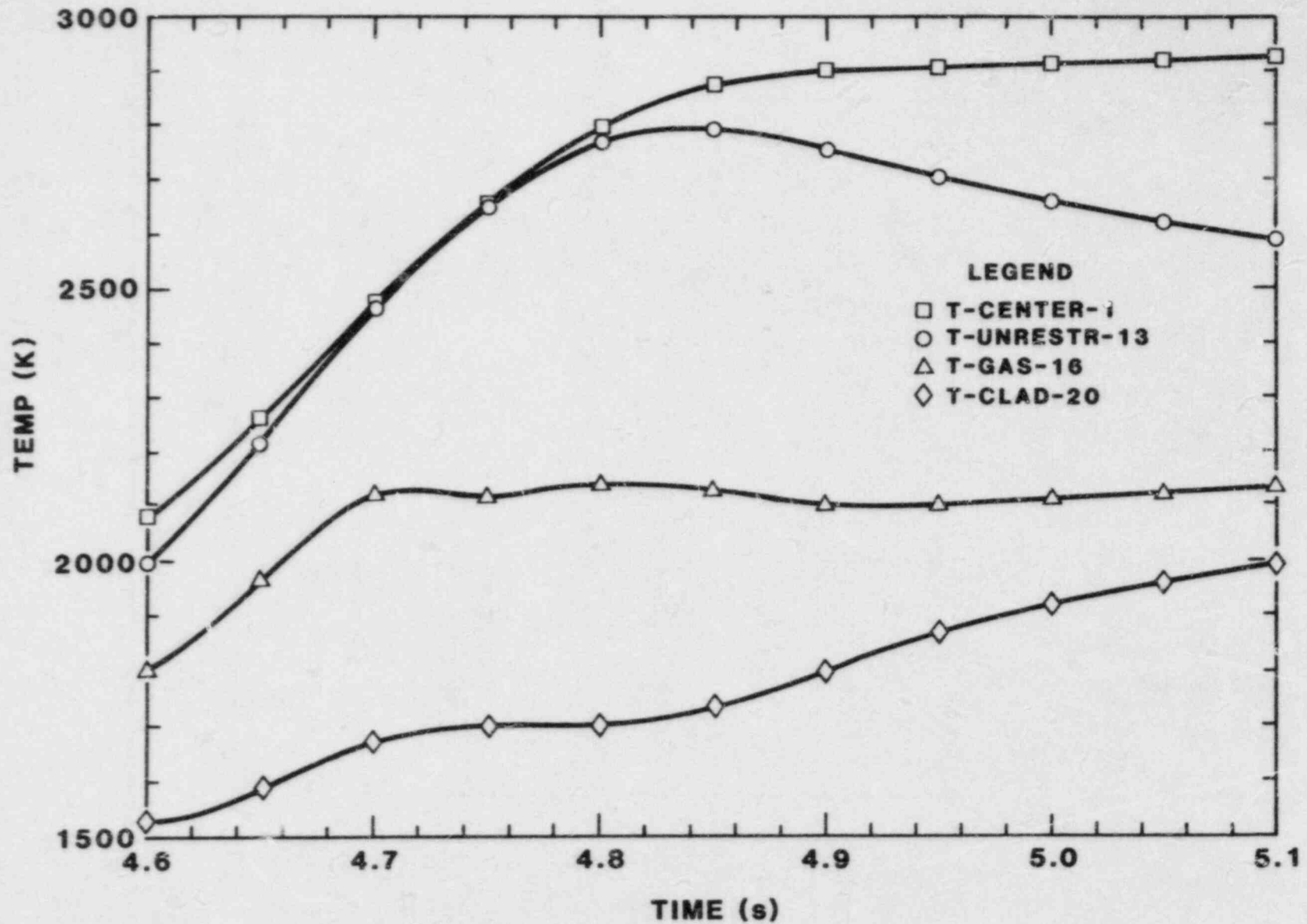Figure 5.1-2. Temperature Profiles at Various Times for Experiment FD4.4

Figure 5.1-3. Temperature History at Thermal Nodes 1, 13, 16, and 20 for FD4.4

The fission gas calculations (performed by SANDPIN) indicated that solid-state cracking should occur at 4.800 s. Since the observed time of disruption was 4.761 s, both the time and mode of disruption are consistent with the observations. The fission gas model says that the cracking is caused by the biased migration (due to the high temperature gradient) of the small intragranular fission gas bubbles to the grain boundary. When enough bubbles collect on the grain boundary, they then have enough potential energy (since they stress the solid fuel matrix) to separate the grain boundary and thus "crack" the fuel.

Since the fuel disruption sequence for this experiment was identical to that of experiment FD4.3, the disruption frames of the film are not shown. Instead, a few frames near the end of the power transient are shown in Figures 5.1-4a, b and c. Figure 5.1-4a shows the fuel shortly after the mild sputtering-type ejection, which coincided with the solid state swelling. Figure 5.1-4b shows the swollen fuel after the clad has drained, and Figure 5.1-4c shows the final configuration of the fuel pin. The fuel was ejected from the upper left side of this last figure.

5.1.3 Results and Preliminary Analysis for FD4.5

Experiment FD4.5 reproduced the heating conditions of FD4.3 but with German-fabricated fuel. The objective of this experiment was to cause fuel disruption while at 10 to 15 x P_0 with the clad molten but not relocation. This type power history reproduces the heating conditions of the "best-estimate" LOF accident scenario calculated by SAS. With the U.S.-irradiated fuel, this type power transient produced dispersive cracking and ejection of solid fuel in moderate burnup fuel (4.0 to 5.6 a/o) and a less energetic disruption consisting of sputtering and swelling (of solid fuel) for high burnup fuel (8.3 a/o).

As mentioned earlier, the German fuel has a larger grain size and it is expected to have a higher gas content than U.S. fuel of similar burnup. Because of the high gas content, the disruption is expected (and calculated by SANDPIN) to be similar to the higher burnup-type disruption seen in experiment FD2.9. This was indeed observed.

Figure 5.1-5 shows the ACRR power transient used for FD4.5, and a few markers indicate the times when important events occurred. Table 5-III lists the times of the major events as observed in the film, and Figures 5.1-6 and 5.1-7 show the SANDPIN calculated temperature profiles and histories. Figures 5.1-8a through d show a few selected frames of the disruption sequence.

At 4.718 s into the transient, an axial crack appeared in the cladding (Figures 5.1-8a and b). This type crack indicates that the fuel had swollen and was pressurizing the partially molten cladding. At this time, the cladding was 25% through the heat of fusion and none of the fuel was molten, thus the swelling at this point was due to solid-state swelling mechanisms. Later, at 4.788 s, some limited sputtering occurred and the swelling began to accelerate. At this
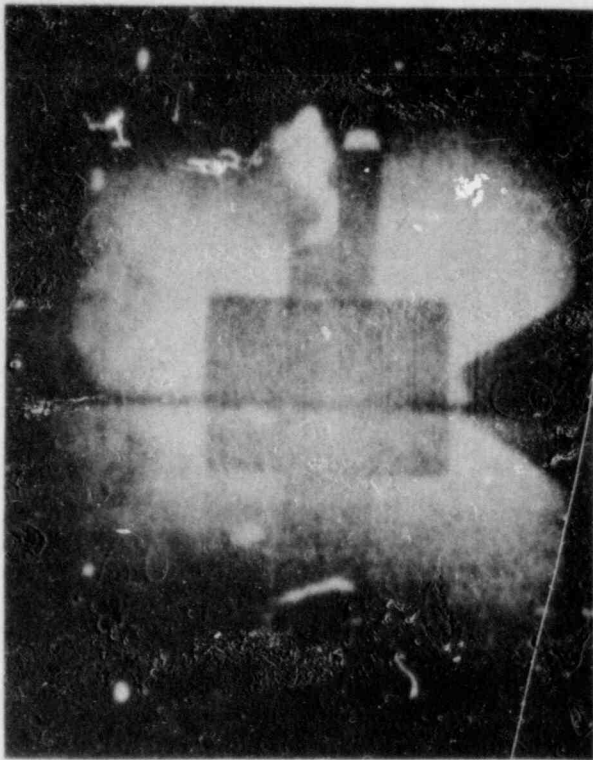
a. Swelling of Fuel after
   Dispersive Ejection of Solid
   Fuel in FD4.4 (t = 4.800 s)
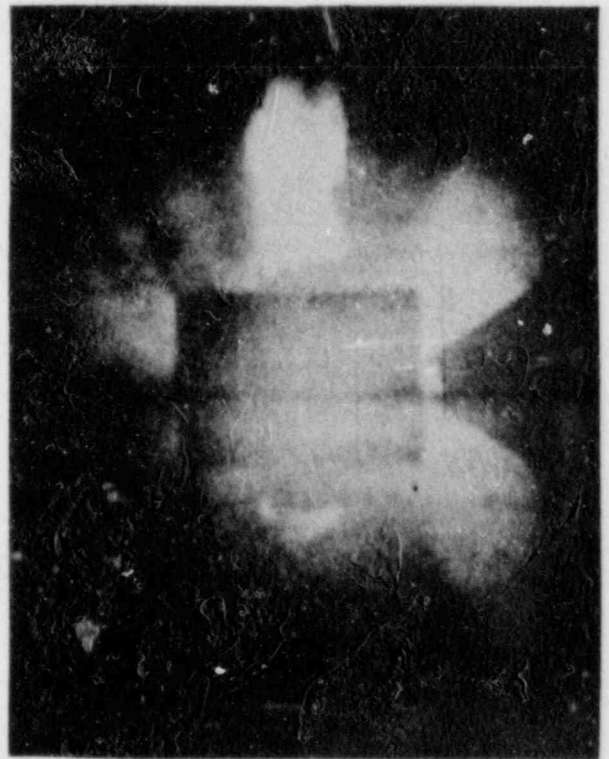
b. Swelling and Clad Removal in
   FD4.4 (t = 5.179 s)

c. Final Fuel Configuration
   (t = 5.3 s)

Figure 5.1-4 Selected Frames of
FD4.4 after Dispersive Solid-
State Fuel Ejection
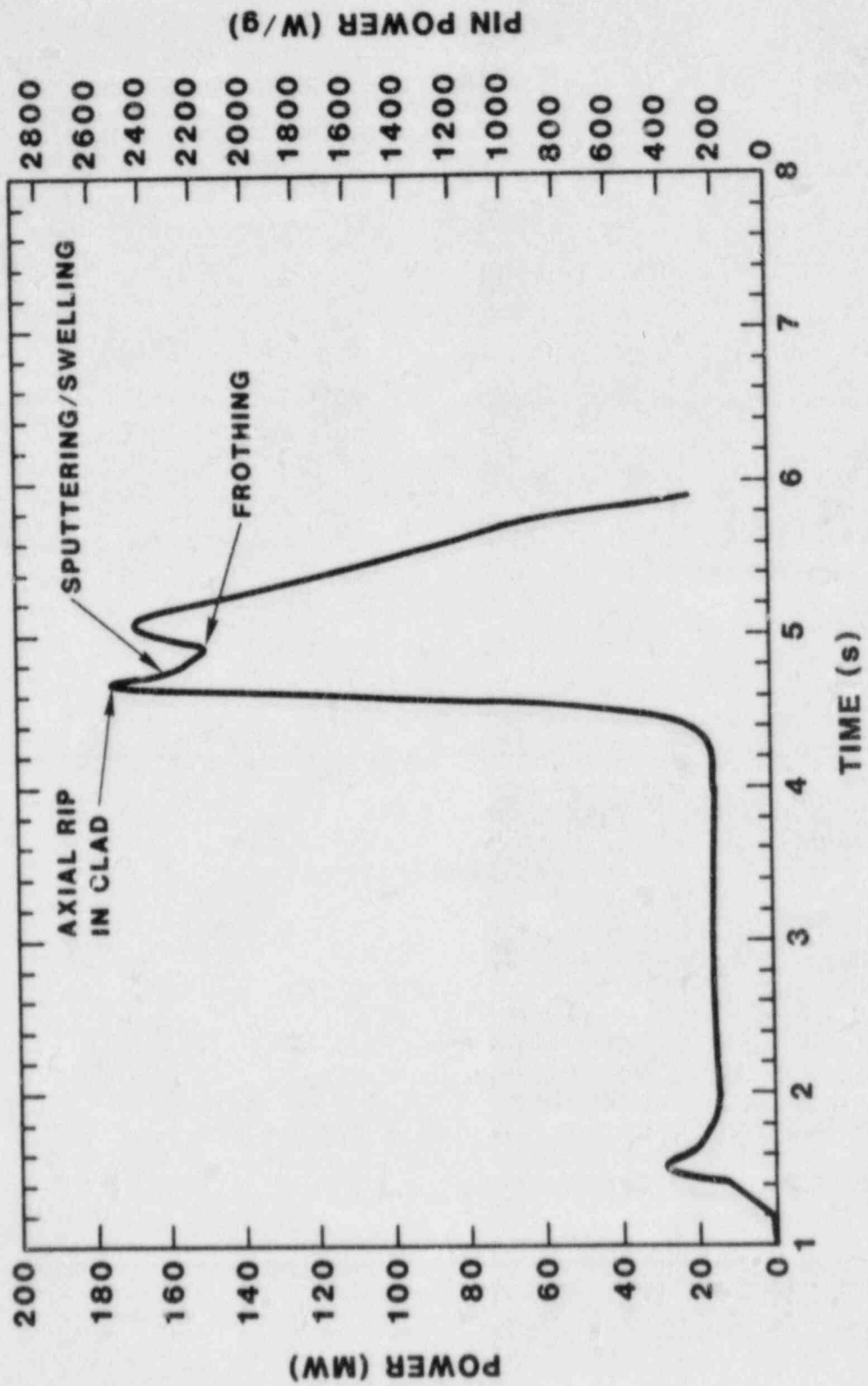
Figure 5.1-5. Measured ACRR Power Transient for FD4.5

111

Table 5-III

Time Sequence of Events as Observed in the FD4.5 Film

No.	Event	Time (Rod Timer) (s)
1	Start of aerosol release	1.850
2	Fully developed aerosol release	1.932
3	New aerosol release	4.705
4	Axial crack in clad due to solid fuel swelling	4.718
5	Sputtering and swelling of solid fuel	4.788
6	Fully developed sputtering and swelling	4.799
7	Massive frothing	4.877
8	Cont. frothing	4.897
9	Start of Slumping	4.913
10	Slumping of upper fuel pellet	4.965

time, the thermal calculations show that the fuel was just beginning to melt (Figure 5.1-7). The SANDPIN fission gas calculations indicate that the cracking criterion had reached a maximum of 0.909 between 4.70 and 4.75 s. Considering the uncertainties in this calculation, this type of disruption (swelling with limited sputtering) is consistent with the SANDPIN calculations. Later, at 4.877 s, significant fuel frothing occurred because of massive fuel melting.

In general, the behavior of the KfK fuel is very similar to the U. S. fuel, especially when considering the higher gas content in the German fuel. The higher enrichment tends to promote early centerline melting, which further causes earlier frothing and swelling.

5.2 TRANSITION PHASE
(D. A. McArthur, 6423; P. K. Mast, 6425)

5.2.1 Posttest Examination Work on TRAN PHASE-I

A longitudinal cut was made through the two blockages observed in TRAN-2. Between 7% and 13% steel was found distributed in the blockages as isolated globules scattered fairly uniformly and randomly. How steel became distributed through the plugs is uncertain, but

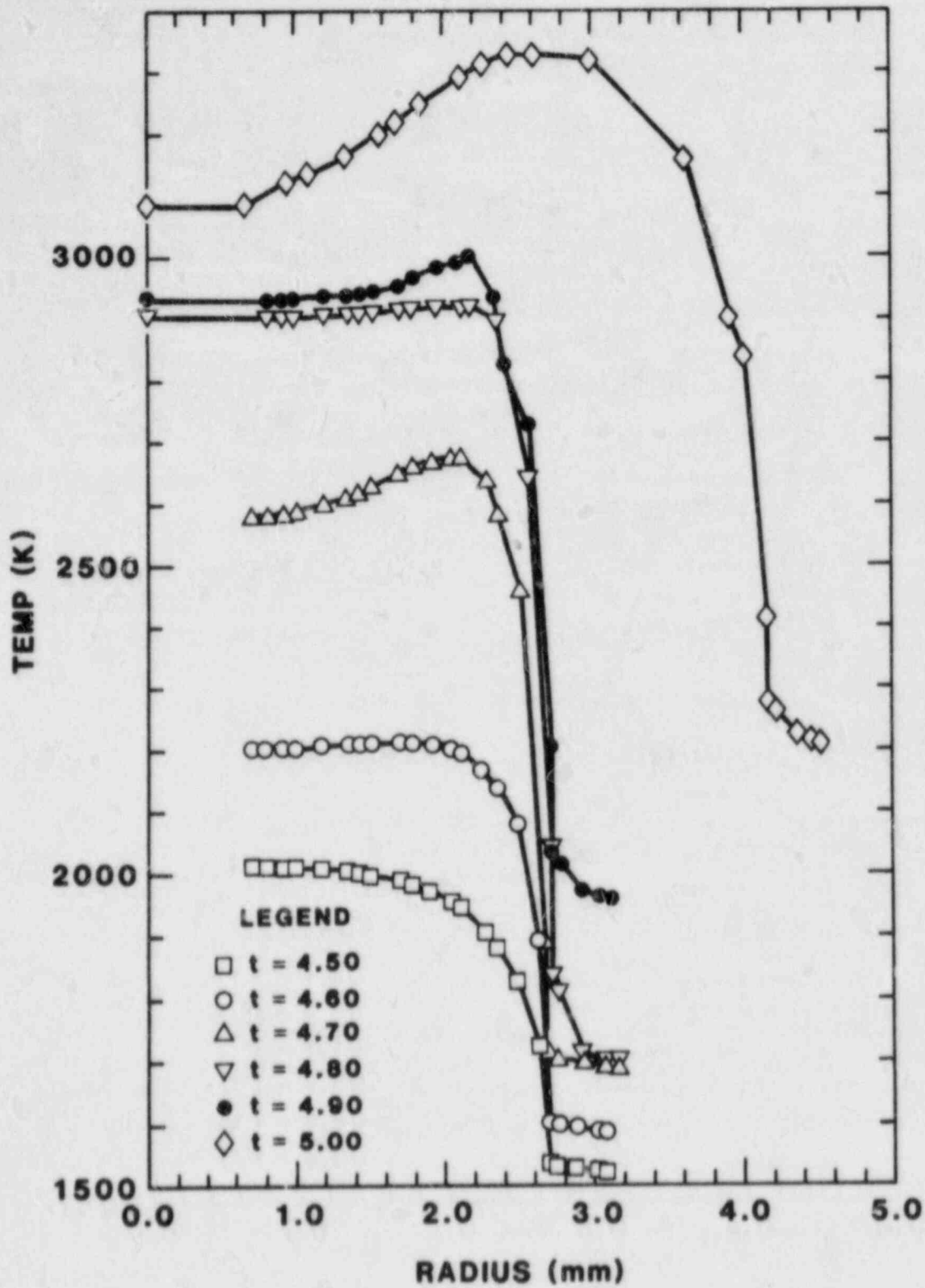Figure 5.1-6. Temperature Profiles at Various Times for FD4.5
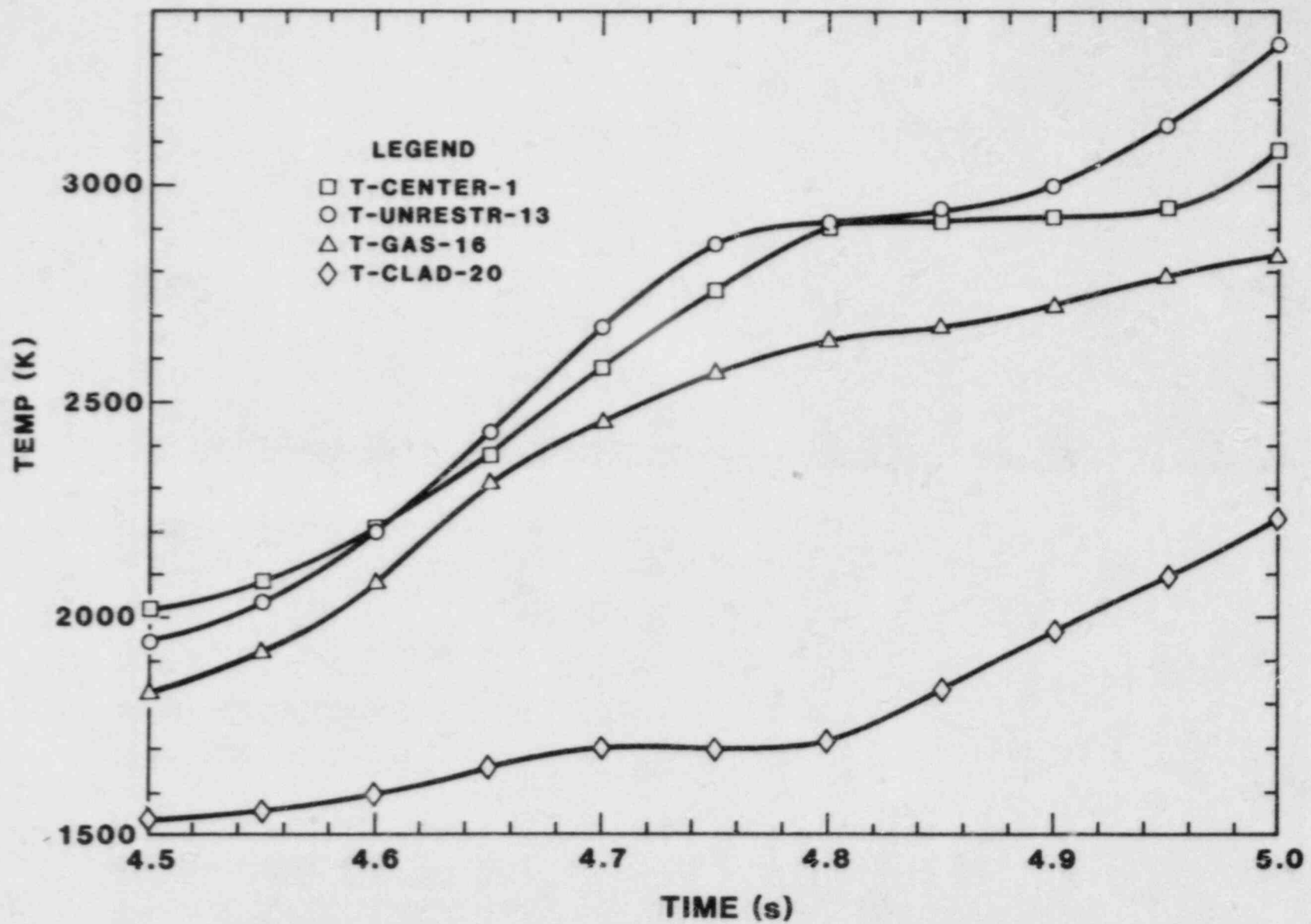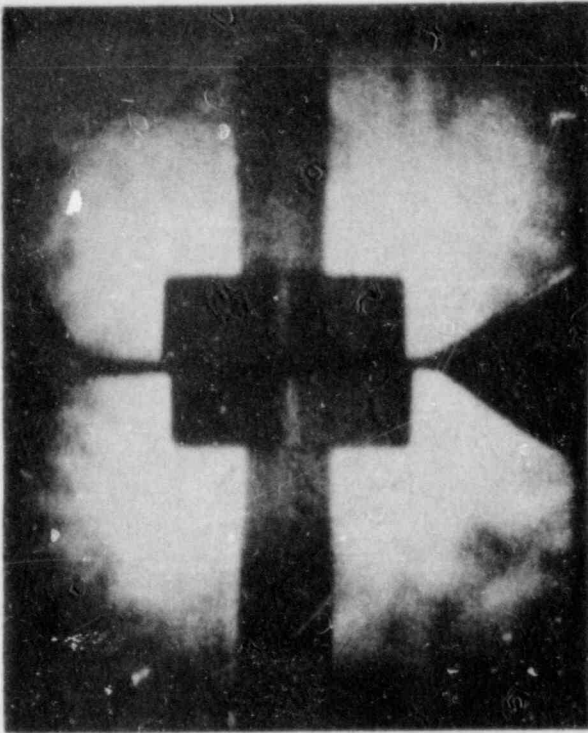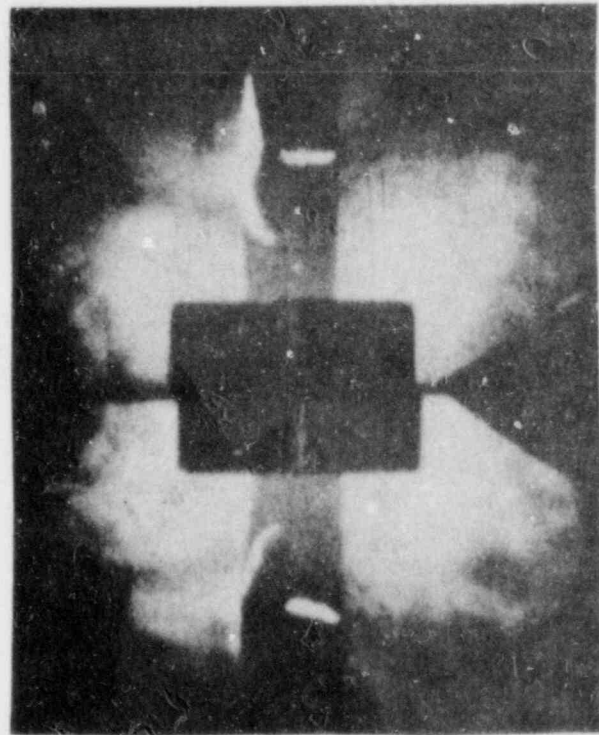
113

Figure 5.1-7. Temperature History Calculated by SANDPIN for FD4.5

a. FD4.5-4
Start of Axial Crack in
Cladding due to Solid
Fuel Swelling

b. FD4.5-6
Fuel Sputtering and Continued
Swelling

c.   FD4.5-7
Frothing of Fuel due to Melting

d.   FD4.5-8
Continued Fuel Frothing

Figure 5.1-8.   Selected Frames from Experiment FD4.5

115

evidence exists for a similar amount of steel in the end of the crust layer located about 8 cm below the plugs. Since the intervening 8 cm of channel wall had essentially no crust, the blockages were assumed to be located initially at the end of this crust layer.

A thick region of melted and refrozen steel was found underneath the thick fuel crust at the entrance of the freezing channel. The steel in the plugs might have been entrained in the fuel flow as it passed by the molten steel at the channel entrance.

5.2.2 Results of the Annular Channel Experiment (B-1)

The first TRAN B-Series experiment, B-1, was performed on February 15, 1983. B-1 used an annular freezing channel with thick steel boundaries, designed to directly compare the stability of fuel crusts formed on steel surfaces of opposite curvature. In accordance with previous concerns about whether enough fuel was available to observe the "final" freezing behavior, the initial fuel load was more than doubled from 44 to 100 g. To avoid the complications of fuel crust stability over molten steel, conditions were chosen to avoid rapid steel melting, but sufficient sensible heat was added to the melt to insure that the channel walls were exposed to a flow of fully molten fuel (TF = 3600 K [3328°C]), TS = 770 K [497°C]). The rod in the center of the annular channel had a diameter of 5.84 mm; and the channel width was 1.5 mm, yielding a hydraulic diameter similar to that of an LMFBR flow subchannel.

The driving pressure of 0.92 MPa was applied about 33 ms before fuel melting. One unusual feature of the B-1 results was that gas flow appeared to occur continuously throughout the flow of fuel into the freezing channel (Figure 5.2-1). In fact, a fairly sharp pressure rise occurred early in the flow (from 0.335 s to 0.345 s) well before pressures were equalized across the column of molten fuel. The pressure then remained fairly constant until about 0.360 s, suggesting that the annular channel was filled with molten fuel until that time.

B-1 also included a limited array of 1-mm-diameter thermocouples, which were used to measure the velocity of the fuel front. Two thermocouples were located at 5 cm from the entrance of the freezing channels, and two more at 25 cm from the entrance. The thermocouples were set into the outer wall of the annular freezing channel, one at each axial location being flush with the channel wall, the other being inset about 0.4 mm. Before installation, an estimate of the response time of each thermocouple was made by plunging it into molten solder at about 523 K (250°C) and recording the rate of temperature rise. Two thermocouples were used at each axial location to provide an estimate of the statistical uncertainty of the measurement, and the recessed thermocouples were used to discriminate against any rapidly moving low-density debris that might precede the main fuel flow.

The arrival of the fuel front was defined as the time at which the temperature began to rise rapidly, found by extrapolating the linear part of the temperature rise back to the initial channel temperature. Figures 5.2-2 through 5.2-5 show the data obtained in B-1.
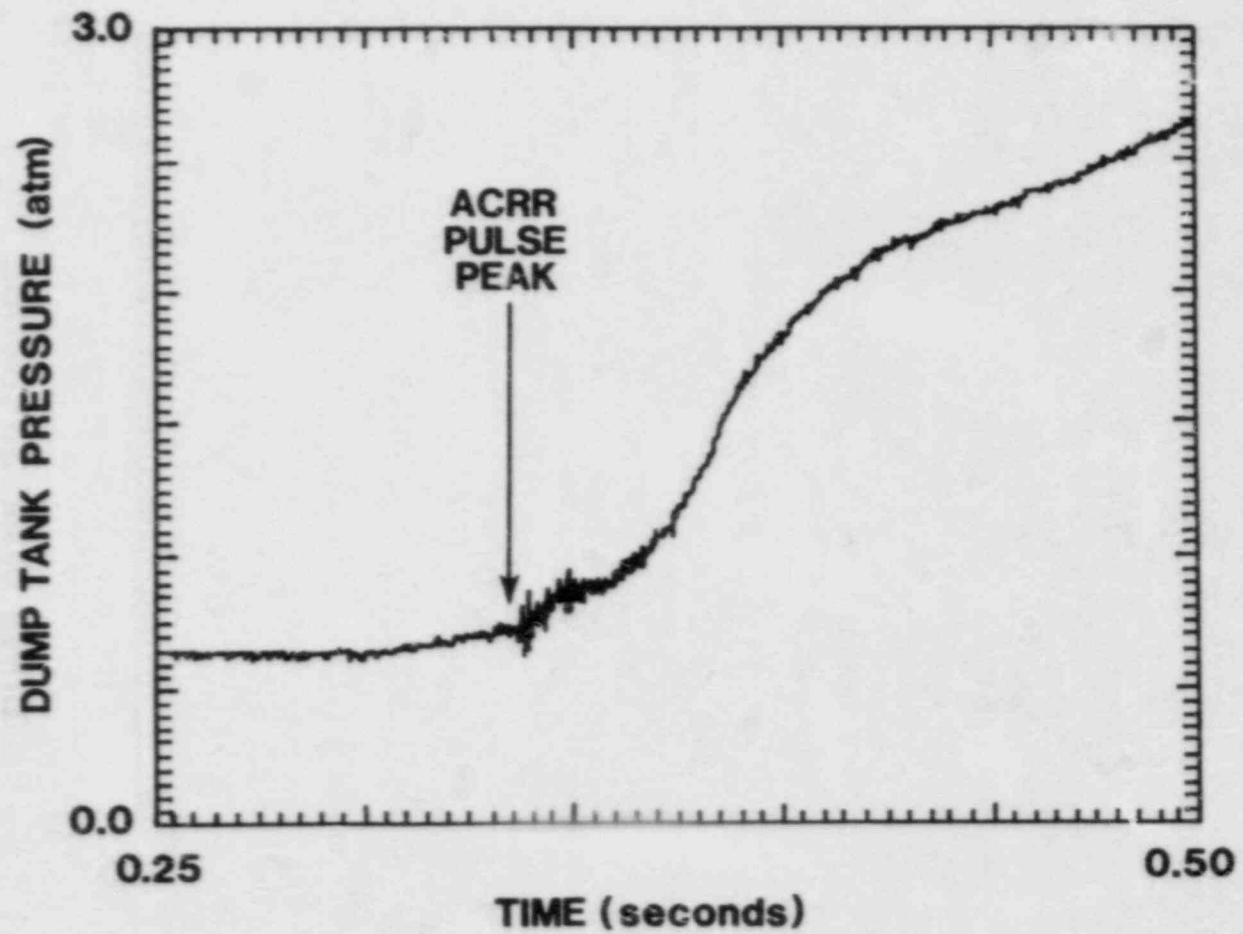
Figure 5.2-1 Dump Tank Pressure History for TRAN B-1

Figure 5.2-2   Temperature History of Flush-Mounted Thermocouple at 5 cm from Channel Entrance (TRAN B-1)
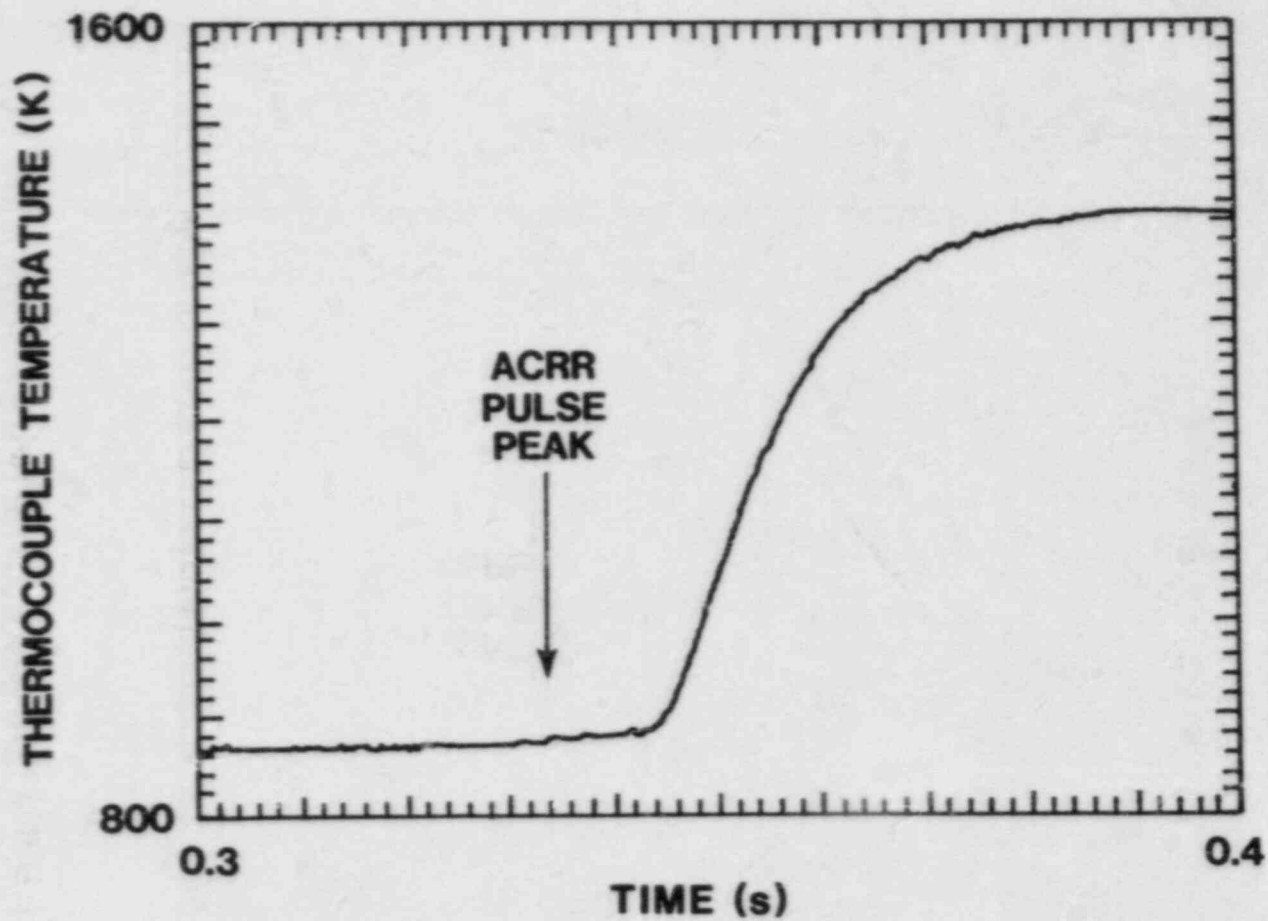
Figure 5.2-3   Temperature History of Recessed Thermocouple at 5 cm
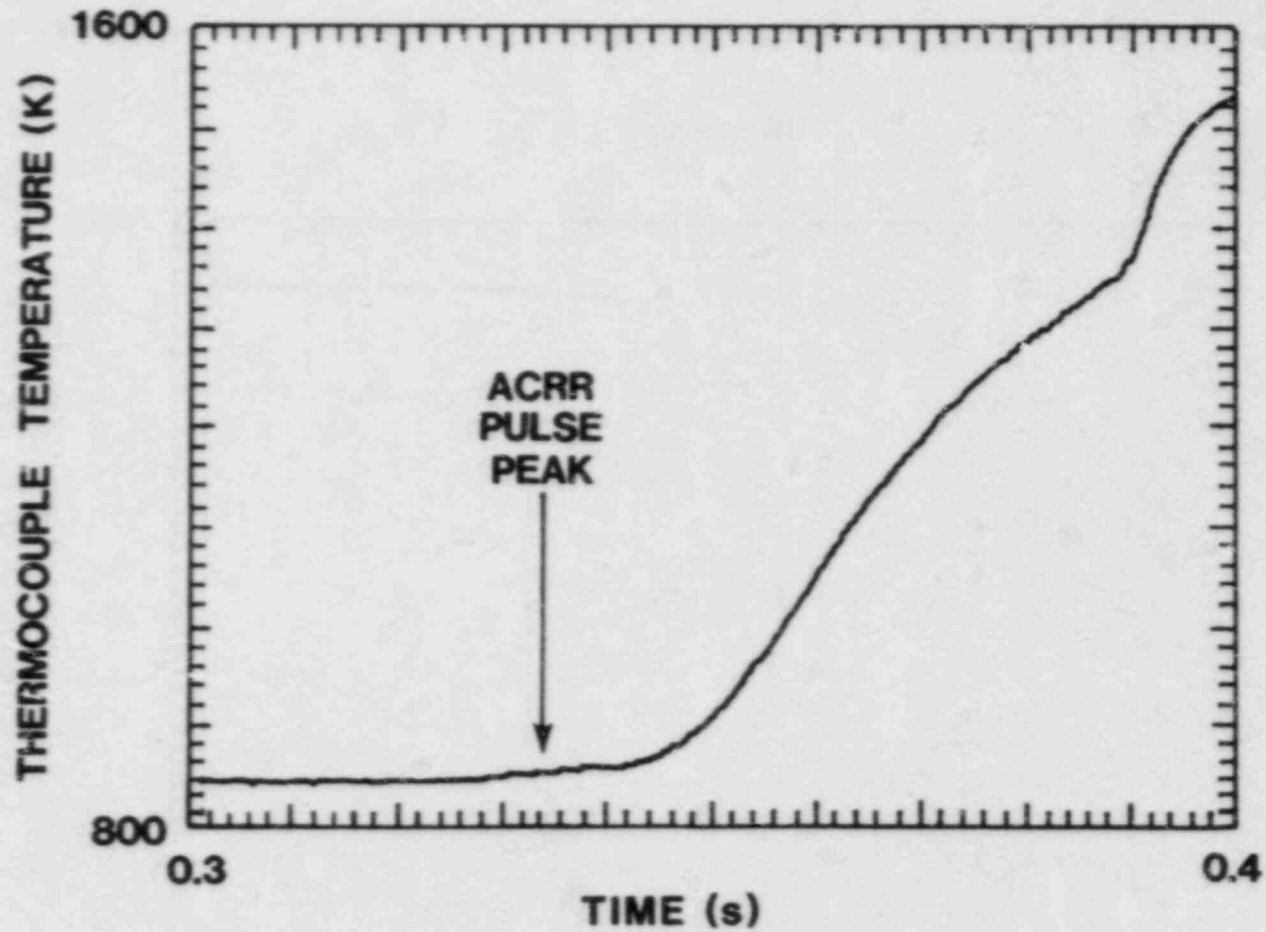from Channel Entrance (TRAN B-1)
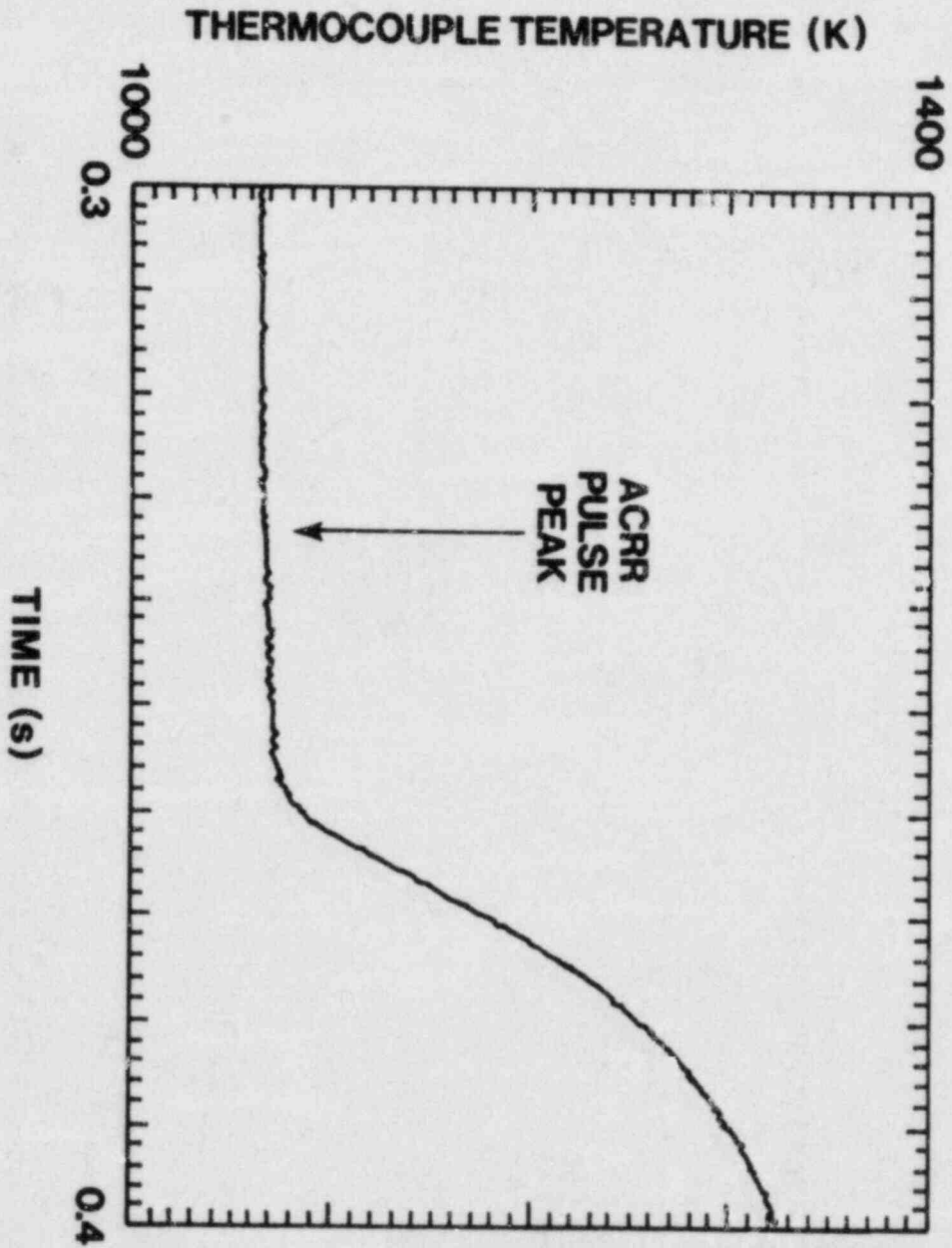
Figure 5.2-4 Temperature History of Flush-Mounted Thermocouple at 25 cm from Channel Entrance (TRAN B-1)
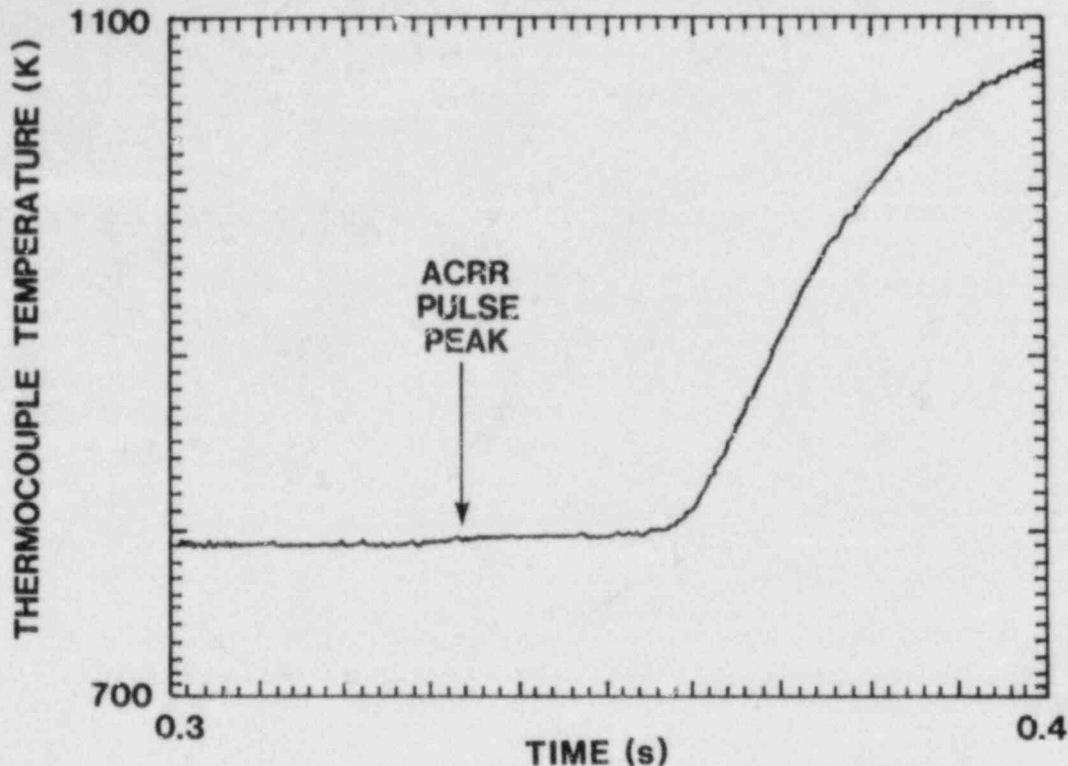
Figure 5.2-5   Temperature History of Recessed Thermocouple at 25 cm
                from Channel Entrance (TRAN B-1)

The fuel front velocities implied by the "flush" and "recessed" ther-
mocouples are similar, with an average velocity of about 16 m/s.

Such fuel slug velocity data are very useful in confirmng the
accuracy of the PLUGM code, since the fuel velocity is determined by
the initial mass in the slug (one of the most important, unknown
parameters that must presently be specified in PLUGM). Since the
current. PLUGM model assumes depletion of the slug mass by both fuel
crust formation and liquid layer deposition, the fuel slug is expected
to accelerate as it moves up the channel. Therefore, essentially all
future TRAN experiments will incorporate such thermocouple arrays, so
that slug motion can be measured all along the channel.

Radiographs of B-1 show a fuel crust, only 40 to 45 cm long,
which is shorter than predicted by a simple conduction-freezing model.
At this time, the cause of this shorter crust is not known. The cause
could be a shortage of fuel in the flow, an enhanced heat transfer
between the molten fuel and the wall (because of crust instability),
or a hydrodynamic effect in which less fuel is swept upward by the gas
as a result of the shape of the annular channel. One possible indica-
tion of the development of a flow instability is that the crust seems
to be more uniform azimuthally and axially in the first 10 cm of the
channel than in the following 30 to 35 cm.

121

The radiographs also show an accumulation of relatively large pieces of debris clustered around one group of the setscrews that were used to position the rod in the center of the annular channel. The large size of some of the pieces indicates that they were initially frozen lower in the channel but later were carried upward by the gas flow. The location of this debris, separated from the end of the main crust, is somewhat analogous to the blockages observed in TRAN-2.

5.2.3 Improved Fuel Temperature Measurements

The accuracy of fuel temperature measurements was greatly improved with a better model of heat transfer between the thermocouple and the fuel. More nodes were used to describe the thermocouple, heat conduction between the fuel and the thermocouple through the He gas was modeled in detail, and the average thermal conductivity of the test fuel was adjusted to fit the late-time behavior of the thermocouple temperature. By adjusting only two parameters (the unknown coupling factor between the fuel energy deposition and the reactor power, and the fuel thermal conductivity), excellent fits to the thermocouple temperature could be obtained (Figure 5.2-6). Based on the fact that the two adjustable parameters do not interact strongly in fitting the data, the estimate is that the coupling factor can now be determined to within less than 5%.

5.2.4 Analysis of TRAN B-1

The B-1 experiment was analyzed with PLUGM, which predicted penetration lengths of about 50 to 70 cm, depending on the amount of mass assumed to be in the initial liquid fuel slug.

5.2.5 PLUGM Code Development and Verification

5.2.5.1 Modeling the Effect of Taylor Instabilities on Film Deposition

During this quarter, modeling was added to the PLUGM code to account for the effect of Taylor instabilities on the film deposition at the trailing edge of an accelerating liquid slug. Previously, the film deposition calculation had assumed steady-state film deposition (negligible slug acceleration) based on the results of simulant-material slug-ejection experiments. These experiment results had indicated that for cylindrical and annular flow channels with hydraulic diameters ranging from 3 to 8 mm, the trailing-edge film thickness was characterized by a liquid fraction (fraction of flow channel area occupied by residual film) of 0.15 for turbulent slug flow. For lower fluid velocities, where the flow is laminar, the film liquid fraction was as high as 0.25.

If the liquid slug is accelerated through the flow channel by a lower density fluid, then Taylor instabilities at the trailing edge of the liquid slug will cause the lighter density fluid to penetrate into the heavier density liquid slug. This action might be expected in LMFBR transition-phase analyses where fuel or steel vapor is the driving force for the flow of molten corium through the various flow
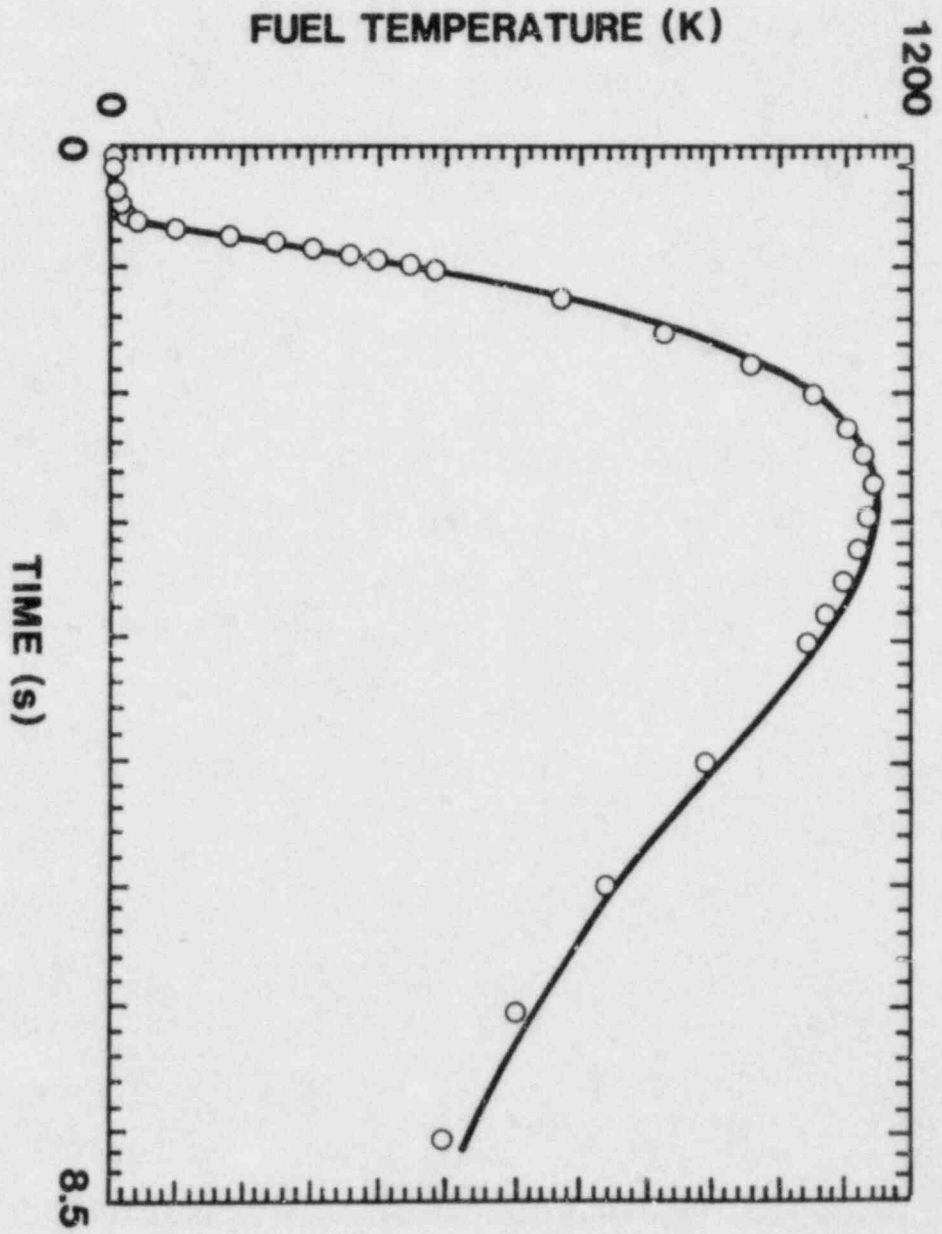
Figure 5.2-6 Measured Fuel Temperature Trace and Calculated
Temperatures for Fuel Geometry of TRAN B-1.
Average coupling factor = 10.8 J/g·MJ.

channels. Such Taylor instabilities would result in the deposition of a thicker liquid film than predicted by the steady-state deposition described previously.

An estimate of the liquid film thickness left by such Taylor instabilities can be obtained by considering the relative velocity between the trailing edge of the flow (the "bubble" velocity) and the bulk liquid velocity near the trailing edge. An upper bound for this relative velocity is obtained from the growth rate of the fastest growing instability wavelength in the channel. Given this relative velocity, it is a simple matter to calculate the resulting film thickness. The procedure used to calculate this film thickness (as well as the steady-state result previously described) is described by the following equations.

Given a trailing edge velocity of v_{trail} and a bulk material velocity of v_{bulk} near the trailing edge of the flow, the residual liquid film is characterized by a liquid fraction, F, of

$$F = 1 - \frac{v_{trail}}{v_{bulk}} \tag{5.1}$$

For steady-state film deposition, the trailing edge velocity is thus given by

$$v_{trail}(ss) = \left[\frac{1}{1 - F_{ss}} \right] v_{bulk} \tag{5.2}$$

where

$$F_{ss} = 0.25 \text{ for Re} < 3500$$
$$F_{ss} = 0.15 \text{ for Re} > 3500$$

If the liquid slug is being accelerated through the channel, the trailing edge velocity must be increased by the relative velocity between the lighter density fluid (bubble) and the liquid slug, v_{Taylor}. Thus,

$$v_{trail} = v_{trail}(ss) + v_{Taylor} \tag{5.3}$$

An upper-bound estimate for the relative velocity v_{Taylor} can be expressed in terms of the bulk slug acceleration, a_{bulk}, and the longest Taylor wavelength, λ, as

$$v_{Taylor} = C_{Taylor} \cdot (a_{bulk} \cdot \lambda)^{1/2} \tag{5.4}$$

The constant, C_{Taylor}, and the longest wavelength, λ, are dependent upon the channel geometry. For slit geometry, these parameters are expressed in terms of the slit spacing, D, and the slit width, W, as

124

$$\lambda = W$$

$$C_{Taylor} = 0.23 + 0.13 \frac{D}{W}$$

For cylindrical geometry these parameters are expressed in terms of the channel diameter, D, as

$$\lambda = D$$

$$C_{Taylor} = 0.345$$

5.2.5.2 Effect of Enhanced Film Deposition on TRAN Results

To determine the importance of Taylor-instability-enhanced film deposition, the TRAN 1, 2, and 3 experiments were analyzed with and without the effect of Taylor instabilities accounted for. Taylor instabilities are most important when the fuel is being accelerated rapidly. Thus, the effect is expected to be most important early, when the fuel is being accelerated from rest in the melt chamber, and late, when the fuel slug is accelerating through the channel because of rapid mass depletion.

The results of these calculations are summarized in Table 5-IV. As in previous analyses of TRAN 1, 2, and 3, the fuel mass used in the calculations is chosen so that the calculated penetration length matches that observed in the experiment.

Table 5-IV

Effects of Taylor Instabilities on PLUGM Predictions
for TRAN 1, 2, and 3 and TRAN B-1

Experiment	Fuel Mass used in Calculation (g)	Calculation with Taylor		Calculation without Taylor	
		Crust Length (cm)	Fuel Mass in Melt Chamber (g)	Crust Length (cm)	Fuel Mass in Melt Chamber (g)
TRAN 1	20.6	69.6	5.4	78.7	4.5
TRAN 2	23.4	85.7	5.7	96.3	4.7
TRAN 3	17.0	66.9	4.4	76.9	3.4

In experiments TRAN 1, 2, and 3, the neglect of Taylor instabilities underestimates (by 1 g) the fuel mass that is calculated to be left behind in the fuel melt chamber (by crust growth and film deposition). The resulting penetration length is overpredicted by about 10 cm. In these experiments, the enhanced film deposition in the melt chamber (the additional 1g of fuel) is the most important effect and accounts for most of the 10 cm difference in crust length.

These calculations clearly show that Taylor instabilities are an important mechanism in the TRAN experiments and must be accounted for in order to explain better observed penetration lengths.

5.2.6 TRAN G-Series II Design (Gap Experiments)

Energy deposition calculations show that a moderator is needed inside the annular initial fuel load to provide more uniform energy deposition in the test fuel. Calculations are being performed to design an active cooling system for such an internal moderator in the event that preheating of the fuel load is necessary.

Various possible ACRR transients are being investigated to determine which ones will be best for melting fuel or fuel/steel mixtures and for producing a uniform initial temperature in the relatively thick fuel loads that are necessary when a 2-kg melt is being prepared. It appears that a double ACRR pulse may have significant advantages.

Preliminary engineering drawings were made of the experiment package. Provisions will be made for driving pressures ranging from 1.0 MPa down to the 0.1 MPa characteristic of the gravity head of a 10-cm-high column of molten fuel. Heat transfer calculations were also performed to examine the safety of the experiment in the event of rapid freezing of the fuel or in the event that fuel is heated but does not move out of the melting chamber.

A new laboratory area is being set up for assembly of the GAP experiments.

5.2.7 Modification to the B-Series Package Design

During fabrication of the fuel housings for B-1 and B-2, aligning the fuel melting chamber with the freezing channel was difficult because they were gun-drilled from opposite directions into the same piece of steel. Therefore, in the future, the two chambers will be machined into separate pieces of steel and joined accurately with a weld. This weld must be a full-penetration weld, and considerable care must also be taken to avoid warping of the fuel housing. Work has begun to develop the weld specification and to qualify welders to perform it.

Since the thermocouples in the freezing channel in B-1 were so helpful in analysis of the experiment, discussions with analysts are underway to determine exactly where such thermocouples should be placed to diagnose the details of the fuel flow in the thin-wall and multiple-subchannel freezing channel experiments.

5.2.8 Development of Fuel/Steel Pellets

The fabrication of fuel/steel pellets by extrusion and sintering has proved to be unexpectedly difficult. The principal difficulty is that the presence of a steel phase inhibits the sintering of fuel, and vice versa. Don Schell, at LANL, reports that varying the usual parameters, such as sintering temperature, initial fuel, and steel particle sizes, have not been effective in producing final densities greater than 70% of theoretical or in producing pellets that have the customary strength required for machining.

Marginally strong pellets have, however, been produced for the 5% steel/95% fuel composition at densities of about 65% (theoretical). Hopefully, such pellets can be used for an initial fuel/steel experiment while other fabrication methods are developed for the other fuel/steel melt loads.

5.2.9 Cooperation with Foreign Research Programs

The current TRAN results were reported to Dr. Wilhelm Peppler, Mr. Guenther Groetzbach, Dr. Reimar Froelich, and Mr. Horst Knuth of KfK during various visits to Sandia. These visitors were typically very supportive of our program, and some of them expressed an interest in performing thermite experiments, which would be closely analogous to certain TRAN experients, for the purpose of clarifying the differences in behavior of thermite and molten fuel.

The current attache from Cadarache, Gaston Kayser, is also closely involved in the analysis of the TRAN B Series experiments and the design of the GAP experiments. Kayser is using PLUGM to calculate the flow of fuel in the B-1 experiment and will also be using PLUGM to estimate the flow of fuel in the complex GAP package geometry.

5.3 REFERENCES

5-1.   *Advanced Reactor Safety Research Quarterly Report*, January-March, 1982, SAND82-0904 (1 of 4), NUREG/CR-2679 (1 of 4) (Albuquerque, NM: Sandia National Laboratories, 1983).

5-2.   *Advanced Reactor Safety Research Quarterly Report*, July-September, 1982, SAND82-0904 (3 of 4), NUREG/CR-2679 (3 of 4) (Albuquerque, NM: Sandia National laboratories, 1984).

5-3.   *Advanced Reactor Safety Research Quarterly Report*, October-December, 1982, SAND82-0904 (4 of 4), NUREG/CR-2679 (4 of 4) (Albuquerque, NM: Sandia National Laboratories, 1984).

5-4.   R. E. Rowley, *Fabrication, Irradiation, and Postirradition Examination of the PNL-10 Mixed-Oxide Fuel Pins*, HEDL-TME 80-20 (Richland, WA: Hanford Engineering Development Laboratories, 1982).

6. LIGHT WATER REACTOR (LWR) DAMAGED FUEL PHENOMENOLOGY

6.1 MELT PROGRESSION PHENOMENOLOGY
(J. B. Rivard, 6420A; M. F. Young, 6425)

The objective of this program is to provide balanced perspectives and capabilities applicable to that phase of severe LWR accidents starting with initial core damage and progressing through to breach of the reactor vessel and discharge of core materials into the containment environment.

The formal elements comprising this program are:

a. Core Damage Sensitivity Studies.

b. Severe Accident Uncertainty Analysis.

c. Melt Progression Model (MELPROG) Development.

Because of the complexity and inherent costs of this program, the important features of severe fuel damage and the magnitude of uncertainties dealing with containment integrity and radiological release in probabilistic risk assessment (PRA) during risk-dominant accident sequences must be estimated as early as possible. These estimates can be used to:

1. Insure that the experiments address issues that are both relevant and of outstanding importance.

2. Establish appropriate initial and boundary conditions for reactor damage experiments.

3. Provide information generally useful for the guidance and focusing of NRC research programs.

The purpose of the Melt Progression Phenomenology program is to contribute to this perspective. Progress and perspectives developed to date in these program elements are discussed below.

6.1.1 Core Damage Sensitivity Studies

The core damage sensitivity studies are directed toward identifying the most influential phenomena governing the behavior of an LWR reactor core during a "beyond-the-design-basis" accident. The phenomena include both those governing the degradation of the core in an unterminated sequence and those occurring during attempts to terminate a severe accident sequence.

A two-level factorial approach for study has been designed to investigate the influence of six "external" factors:

a. Oxidation kinetics
b. Void fraction model

c. Sequence pressure
d. Power level
e. Hydrogen blanketing
f. Axial power distribution

Most of the study has been completed. Preparation for the report documentation is complete.

Additional work is necessary in the preparation of the DFR-DQ matrix because of effects revealed by the experiment simulation code and because of the necessity for limiting experiment conditions with regard to pressure, inlet superheat, and power distribution. A revised set of factors for the matrix may also be necessary.

In conjunction with the phenomena assessment task for the MELCOR code development program, studies of fluid flow and heat transfer regimes in the upper plenum of a PWR have been completed. These and additional studies to be performed will be integrated into the sensitivity study report.

6.1.2 Severe Accident Uncertainty Analysis (SAUNA)

Because of the current importance of PRA in nuclear regulatory activities, improved definition (and where practicable, quantitative evaluation) of the effects of uncertainty on the magnitude of risk estimates coming from PRA is necessary. The staff is pursuing this goal as part of the Sandia cooperative study called Severe Accident Uncertainty Analysis (SAUNA).

Preparation of the report, Identification of Severe Accident Uncertainties, is complete with exception of Chapter 1 and Chapter 8. The report covers a preliminary assessment of the importance of severe accident uncertainties and the approach to evaluating the impact of uncertainties on risk. Major elements in the report include inputs from several related programs such as SASA, SARRP, ASEP, and MELCOR. Although a complete consensus on overall treatment methodology is lacking, the format for all tabular entries in the report was resolved. A completion date for the report was targeted toward the May-June period.

6.1.3 Melt Progression Model (MELPROG) Development

A formal system for integrating knowledge gained through improved understanding of the physical processes governing severe damage during the in-vessel phase of the accident can be constructed by developing computer-based models. The need for improved treatment arises because of limitations and deficiencies that have been identified in existing accident-analysis codes such as MARCH. These limitations and deficiencies yield uncertainties in risk evaluations whose resolutions have sometimes required additional costly analyses and studies by the NRC.

The Melt Progression Model (MELPROG) is a program that is part of the SFDAP code system. Its function is to calculate the in-vessel

part of LWR accident sequences from rubble/debris formation through vessel failure. MELPROG will include models to calculate rubble melting by decay heat and oxidation, structural failure including vessel failure, melt/water interactions, and fission-product transport, plateout, and chemistry.

The Los Alamos code MIMAS was picked as the basis for MELPROG development. MIMAS satisfies the basic criteria of (1) true modular structure, thereby easing the task of adding code functions and (2) extensive fluids treatment, important because essentially all phenomena in the accident sequence interface through fluids transport.

MIMAS has been set up and run on VAX and CRAY-I computer systems at Sandia. Comparisons between transients run on the VAX and CRAY indicate no divergence in the results over 25,000 time steps.

Selection of basic model types for structure heat transfer and mechanical failure was completed, and coding of the structures module was started. The first models will be grid plate structures. Some information was collected appropriate to deciding on models to be incorporated into the fission-products module. Release and thermodynamic equilibrium models along the lines of the VANESA code along with an aerosol description similar to MAEROS were selected. A paper, "MELPROG Methods and Developments" was submitted to the Cambridge International Meeting on LWR Severe Accident Evaluation.

6.2 LIGHT WATER REACTOR (LWR) FUEL DAMAGE EXPERIMENT
    (A. C. Marshall, 6423; K. O. Reil, 6423; K. T. Stalker, 6426; R. O. Gaunt, 6423)

This program is directed toward examining the key phenomena that determine the core-damage configuration during the progression of a core melt sequence in an LWR core-uncovering accident. This program uses the information and perspectives gained in current LWR safety programs and focuses on the design of experiments that can contribute to the resolution of important severe-damage issues.

The two major areas of interest regarding in-vessel phenomena are:

a. The behavior of fuel and cladding during the stages of major core deformation from rod-bundle geometry to a severely degraded geometry and

b. The response of the severely damaged fuel to reintroduction of coolant from the emergency core cooling system (ECCS), especially the questions of redistribution of quenched material, short-term cooldown, increased steam generation, and oxidation reaction kinetics.

Information on the first item is necessary to predict the course and duration of core meltdown and associated effects in containment; resolution of the second provides the essential information to guide

action that would terminate the accident and/or mitigate its conse-
quences and to preclude action that could exacerbate the accident.

The present work under this subtask focuses on the in-pile exper-
iments because neutronic heating allows prototypic heat generation
under severely damaged conditions.

6.2.1 Test Planning and Analysis

Staff members are modifying the DFR·MOD3 code to provide a
lumped-parameter computer code to model the entire steam system. This
code will be used to simulate dynamic response of the system to con-
trol procedures.

Analysis has continued using the DFR·MOD3 code to evaluate DFR
experiment conditions in preparation for DF-1 and 2. The staff cur-
rently plans DF-1 as an initial scoping experiment with relatively low
steam flow and a slow cooldown from an intermediate damage state. The
relative system-rod pressure will be characteristic of a larger break
accident. DF-2 will be a high steam flow rate experiment with system-
rod relative pressure characteristic of small break conditions.

The experiment matrix was reviewed and several modifications were
suggested. The modified DFR experiment matrix includes system pres-
sure and steam flow rate as the principle variables.

For the DF experiments, the fuel condition (fresh, cracked, or
preirradiated) and geometry (PWR vs BWR) are also experiment vari-
ables. For the DQ experiment, the damage level, quench rate, and
quench mode are identified. The tentative matrix for the DF experi-
ment series is given in Table 6-I.

The DFR·MOD3 code has been applied to the analysis of several
recently completed out-of-pile air tests. The initial DFR·MOD3 tem-
perature predictions did not agree well with the air test data at high
temperatures, and modifications to DFR·MOD3 to account for the axial
radiant heat loss have now been implemented. With approximate view
factors for the air tests and this modified DFR·MOD3 code, the staff
obtained substantially improved agreement between the calculations and
the measurements.

6.2.2 In-Pile Experiments

The layout of the steam supply skid (Figure 6.2-1) for the in-
pile experiments has been completed.

A special transportable skid has been fabricated for the in-pile
steam supply system. All of the in-pile steam supply components will
be housed on this skid to facilitate the setup of the in-pile experi-
ments. Assembly of the in-pile steam supply system will begin next.
Procurring is begun for all major in-pile hardware components.

Table 6-I

DF-1
Tentative DF Experiment Matrix

| Experiment	System Pressure (atm)	Steam Flow Rate (g/s/rod)	Fuel Condition	Geometry	Damage Level	System Pressure Rod Pressure (atm)	Flow Rate Rod Power (W/g)	Flow Rate Power Gradient	Inlet Temp. (K)
DF-1	1.0	0.025	Fresh	PWR	Moderate	<0.1	1.2	2/1	500
DF-2	20.0	0.15	Cracked	PWR	High	1.0	1.8	1/1	500
DF-3	1.0	0.15	Cracked	PWR	High	30.0	1.8	1/1	500
DF-4	20.0	0.025	Cracked	PWR	High	1.0	1.2	2/1	500
DF-5	1.0	0.15	Cracked	BWR	High	30.0	1.8	1/1	500
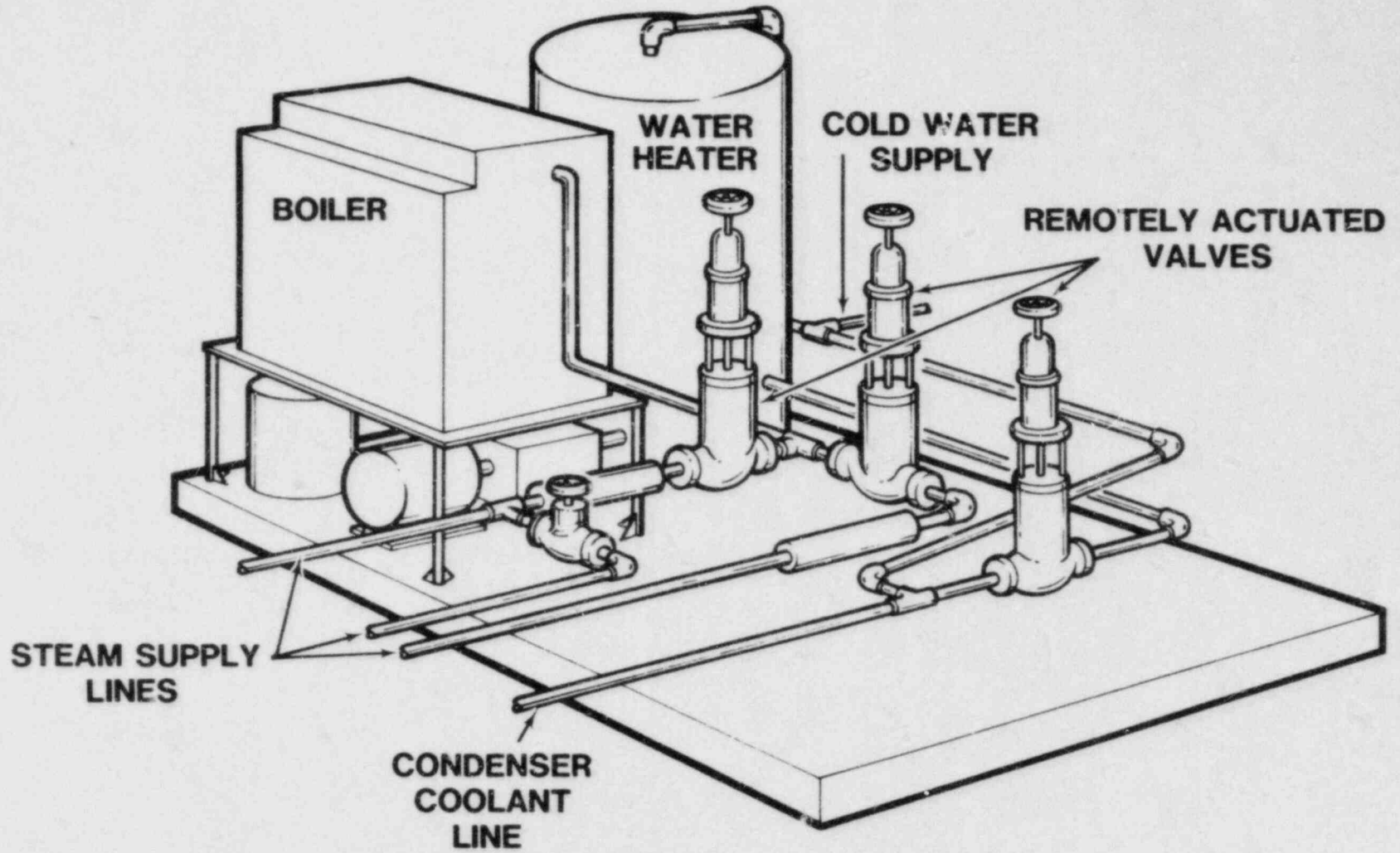
Figure 6.2-1. DFR Steam Supply Skid (Simplified)

The DFR shield plug is designed to block radiation that would otherwise stream up the ACRR experiment tube while allowing instrumentation and diagnostic lines to pass through. The staff completed an analysis of this proposed shield plug and performed several tests with the current ACRR shield plug to establish benchmarks for the analytical models. The major conclusions from this evaluation were:

a. The proposed stovepipe penetration for the DFR shield-plug viewing port should provide effective shielding.

b. The proposed penetrations, which do not include an offset (i.e. no stovepipe), for the steam and instrumentation lines for the DFR shield plug will result in significant neutron and gamma streaming and the design is not recommended. It is recommended, instead, that stovepipe penetrations should be used for these lines also.

c. With the proposed modifications to the DFR shield plug, the plug attenuation effectiveness should be comparable to the current ACRR shield plug.

6.2.3 Out-of-Pile Tests

All of the system plumbing for the out-of-pile steam system has been completed and proof tested. Preliminary boiler operation checks have been completed. The simplified test section, CuO recombination tube, and condensate tank for the Raman diagnostics development tests have arrived. The Raman diagnostic tests will test Raman techniques for measuring H_2 in a steam environment similar to the in-pile system. These tests will be the first out-of-pile steam tests that will include all major components; however, no fuel rod simulators will be present for these tests and only limited superheating will be achieved. Fabrication of the electrically heated out-of-pile test section has begun. Development of the Data Acquisition and Control (DAC) System continued.

Experimenters completed the design for the detailed electrically heated out-of-pile test section (which approximates the in-pile test section very closely). The high-current power supply for the tungsten rod heaters was assembled (Figure 6.2-2).

The signal conditioning chassis for the flowmeters and pressure transducers was assembled. The interface between the data acquisition and control system (DACS) and the cameras was designed, and the fabrication order was placed. A board to provide alarm and status information from the DACS was designed and is being fabricated. An existing power controller was modified to be compatible with DACS for use in controlling trace heaters on pipe runs. The many cables that will connect transducers to the DACS and the interconnecting cables within the DACS are being fabricated.
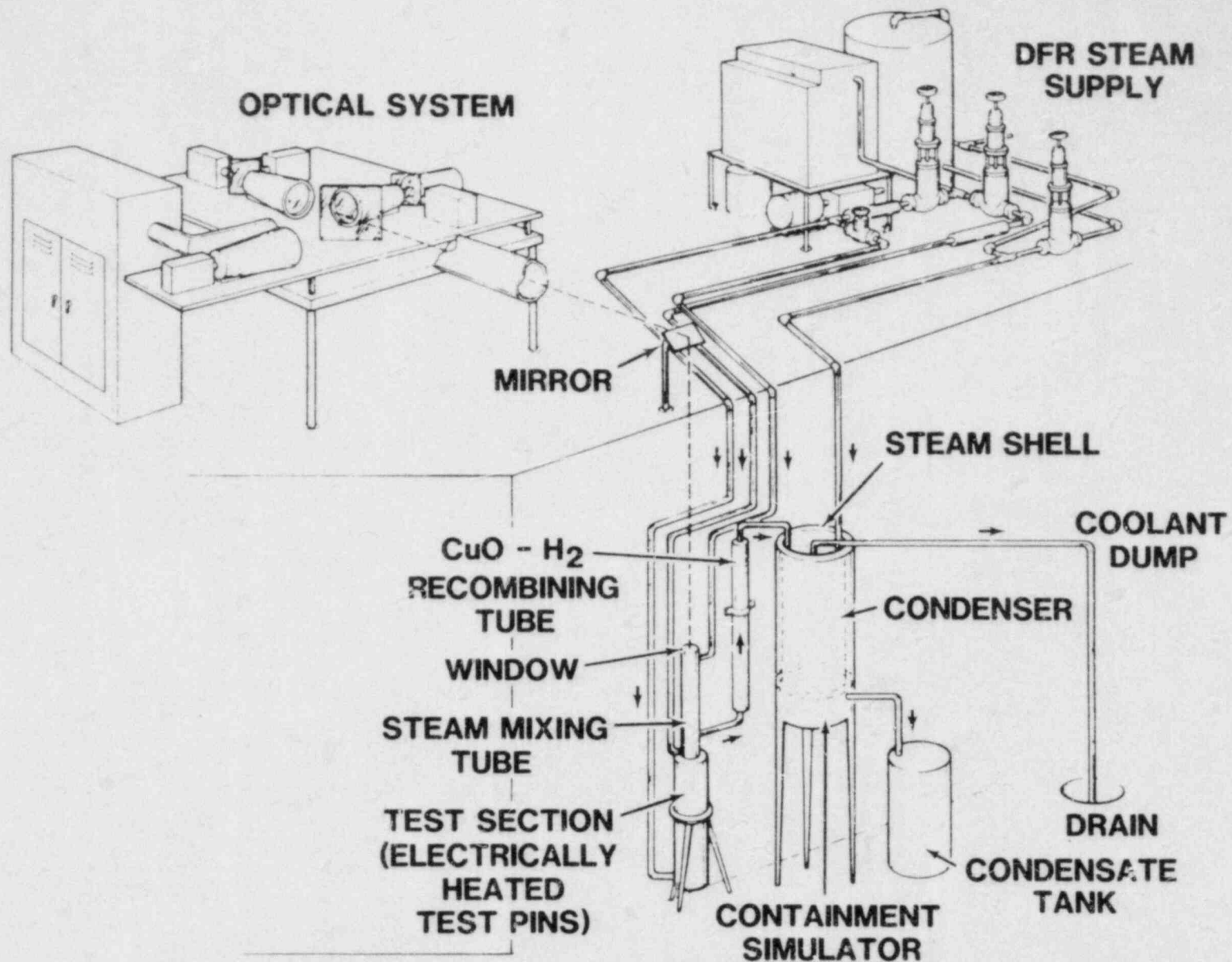
Figure 6.2-2.   DFR Out-of-Pile Steam Test Apparatus

6.2.4 Instrumentation

Optical test bed components for the visual, radiometric temperatures and Raman systems were defined and ordered. Staff members have begun studies to develop calibration techniques for obtaining temperature data from photographic film. Film temperature data will supplement temperature data obtained from thermocouples and the optical pyrometer.

The 35-mm computer-controlled cameras have been ordered. The charge-coupled camera, which will eventually be used as a scanning optical pyrometer, has been interfaced with the DACs. Experimenters have obtained data to determine the feasibility of two-band photographic radiometry and to establish exposure criteria for in-pile and out-of-pile experiments.

6.3 LIGHT WATER REACTOR (LWR) DEGRADED-CORE COOLABILITY (DCC) PROGRAM (K. R. Boldt, 6421; E. Gorham-Bergeron, 6425)

Sandia National Laboratories is pursuing a program to determine the coolability of the LWR degraded cores. The main purpose is to provide an experimental data base for use in evaluating the applicability of LMFBR coolability models to LWR-specific conditions. This will be accomplished by performing a limited number of in-pile experiments using fission-heating of UO_2 rubble to simulate the source of decay power in a severe-fuel-damage accident. This year the scope of the DCC program encompasses the following:

a. Continue design, acquisition of parts, and assembly of the first two DCC experiment packages.

b. Perform DCC-1, the first in-pile coolability experiment containing a UO_2 rubble bed in a water bath.

c. Analyze the DCC-1 results compared to current coolability models, and develop and improve models where necessary.

6.3.1 Experimental Activity

During the current quarter, the DCC program experimental effort focused on the following activities.

a. Acquisition of the DCC-1 experiment hardware continued. Delays in delivery of some critical path components (primarily the urania fuel and the pressure vessels) put off the start of final assembly of the DCC-1 experiment package.

b. Considerable progress was made in fabricating and assemblying test facilities for the DCC-1 experiment. These facilities include a new lab and assembly area, a multilevel platform for final assembly, and a leak-test bell jar capable of enclosing the entire experiment package.

c. Sandia staff members reviewed the particle size distributions for the first three experiments and concluded that DCC-1 will contain a small-sized particle distribution (typical of debris from a partial steam explosion) and DCC-2 will contain a large-sized particle distribution (typical of thermally fractured fuel).

d. Because of the small-sized particle distribution for DCC-1, some design and hardware changes were required for the DCC-1 experiment package. These include the addition of an electric heater, the exclusion of the liquid nitrogen precooler from the cooling loop, and the operation of the cooling loop with nitrogen instead of helium.

e. Most of the hardware and process development tests for DCC-1 were completed. Also, the final package test sequence to insure experiment reliability was formalized.

Each of these items will be summarized in the following discussion. A detailed description of the planned DCC-1 debris bed will also be presented.

During the quarter, the major portion of machining, inspection, and preliminary assembly of DCC-1 parts was completed. The status of each of the main components in the first experiment is as follows:

1. Urania fuel -- A partial shipment of 45 kg of urania fuel was received. The remaining 15 kg of the total 60-kg fuel order has been delayed from early April to May. The reason for the delay is the occurrence of class B chemical explosion in the DCC fuel preparatory room at Los Alamos, the fuel fabricator for this program. Although the DCC fuel was unaffected by the explosion, the investigation into the accident is expected to delay fuel shipment. With the existing fuel on hand, a representative batch of the DCC-1 bed was mixed, and results will be presented later in this section.

2. Crucible -- The double wall insulated crucible was assembled by machining cylindrical sections of Min-K insulation and carefully fitting them into position. A Sandia welder was qualified on Inconel-625 prior to making the closure weld of the crucible. The weld has been leak tested and final machining is in progress.

3. Primary and secondary pressure vessels -- The cylinders have been received and inspected. Machining of the closure bulkheads is complete, and brazing of pass-through fittings into the bulkhead is in progress.

4. Heat exchanger -- Fabrication of the heat exchanger tubes and closures is complete. Thermocouples are being installed to monitor heat removal performance. Final welds and testing of the heat exchanger are expected to be complete by mid-April.

5. Shield plug -- A recent change in design from vacuum-insulated cooling pipes to thermal insulation on the pipes has delayed final assembly and delivery of the shield plug. All other associated hardware has been delivered and is being assembled.

6. Helium loop -- The helium blower, which failed during the D-9 experiment, has been repaired and reinstalled into the loop. The loop has been leak tested and requires some minor modifications before being fully operational. All new piping has been assembled and insulation of piping is proceeding.

7. Instrumentation and pass-throughs -- All pressure transducers and thermocouples have arrived, and have been tested and initially calibrated. The placement and type of secondary transducer have been modified to enable use of a more reliable transducer in a cooler environment. The thermocouples have been cut to length and shipped to a firm specializing in hermetically sealed pass-throughs. Pass-through bodies for the secondary have been received, and work is proceeding on installation of glass-to-metal seals in the bodies.

8. Data acquisition and helium control instrumentation -- All hardware has been assembled for the upgraded data acquisition and helium control consoles. Testing of instrumentation is proceeding concurrently with the completion of assembly of the helium loop. The data acquisition software is nearly complete and will be checked out during the upcoming DC-1 (dry capsule) experiment.

The DCC experiment assembly facilities were improved by the acquisition and setting up of a new lab and assembly room. The room has a 13-m ceiling height and crane facilities able to handle all DCC experiment hardware. Two raised level platforms were built in the room to permit multilevel assembly of the experiment packages. One of these platforms can be enclosed by a plastic sheet to provide a clean room for urania fuel loading. A bell jar (1/2-m diameter and 5-m height) has been set up for integral leak tests of the experiment containments.

DCC program personnel reviewed the primary experiment matrix to formalize the DCC-1 particle distribution. The review included an analysis of the most recent fuel fragmentation and steam explosion experiments performed at PBF, INEL and the FITS program at Sandia.[6-1] The decision was made to have the DCC-1 debris bed be a homogeneously mixed, small-sized particle distribution (mean diameter = 0.75 mm) and the DCC-2 bed be a homogeneously mixed, large-sized particle distribution. This delay in using the large-sized distribution was affected to insure adequate time to implement improvements to the coolant system that may be necessary at higher bed powers. Figures 6.3-1 and 2 show the proposed particle distributions for DCC-1 and DCC-2, respectively. Both distributions are terminated at 0.075 mm on the small end to avoid particle sizes that may fluidize and subsequently change the coolability of the bed. Also shown on the
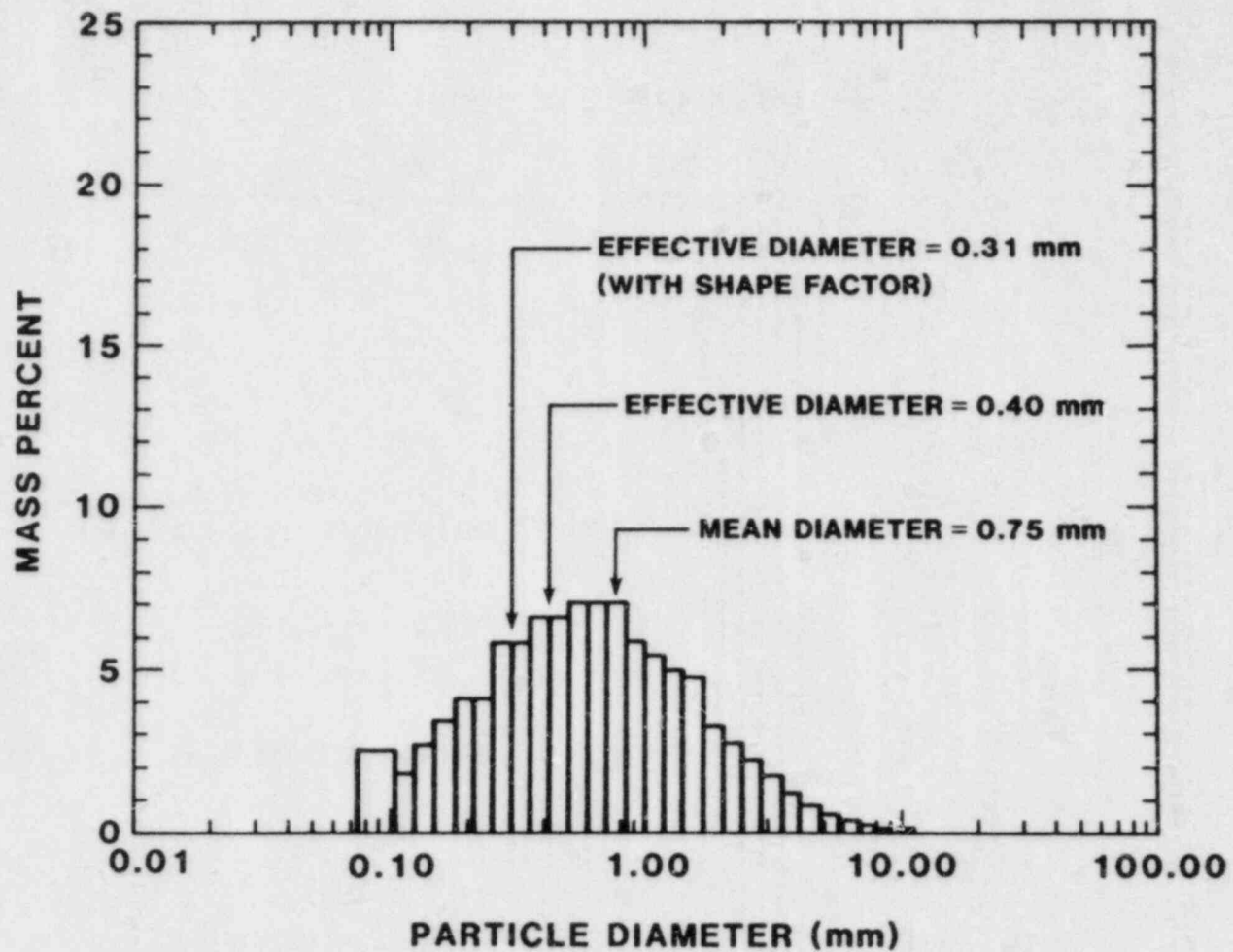
Figure 6.3-1. Particle Size Distribution for DCC-1
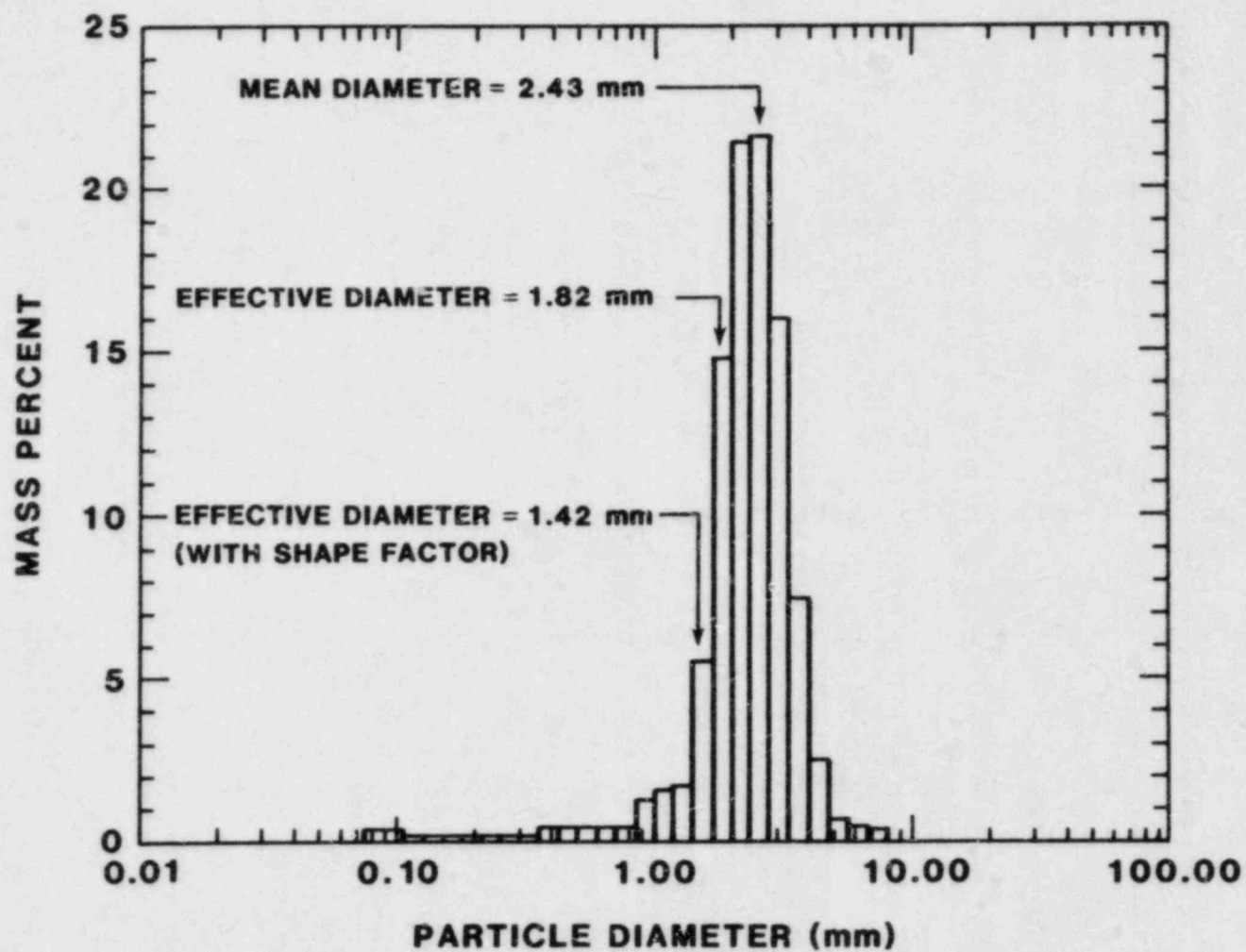Degraded-Core Coolability Program

Figure 6.3-2. Particle Size Distribution for DCC-2 Degraded-Core
Coolability Program

figures are the mean diameter, effective diameter (using an l/D weighting), and effective diameter with a shape factor multiplier of 0.78. It was also decided that DCC-3 would investigate a stratified bed with a medium-sized particle distribution. DCC-3 will investigate the effects of stratification in a deep water bed. All beds will be 50-cm-high, bottom-insulated beds, and all will be pressurized to the full range of pressures found in LWR primary vessels.

Part of the criteria for selecting the DCC-1 and DCC-2 particle size distributions was to operate, if possible, in both the laminar and turbulent coolability regimes. Figure 6.3-3 shows the predicted dryout heat flux at 1.0 bar as a function of particle diameter and at various porosities based on the Lipinski one-dimensional coolability model.[6-2] Also shown is the current predicted dryout heat flux for DCC-1 (assuming 34% porosity) and DCC-2 (assuming 45% porosity). DCC-1 clearly is the laminar coolability regime; whereas, DCC-2 exists in the transition between laminar and turbulent. As pressure is increased, the coolability behavior of the bed becomes more turbulent. A more complete analysis of particle size distributions and predicted coolability is provided in the DCC program plan.[6-3]

As a result of the small particle size distribution for DCC-1, the staff predicts dryout to be at very low bed powers--0.5 to 3.33 kW over the full pressure range. Because the heat removal capability of the experiment package is designed for much higher powers (~30 kW), the following design changes were implemented to accommodate the lower powers:

1. An electric heater (4-kW capacity) was designed into the primary system and components ordered.

2. The liquid nitrogen heat exchanger, which supplements the cooling capacity of the helium trailer, will not be used in the first experiment.

3. The helium cooling system may be operated with nitrogen gas to reduce conductivity.

Most of the hardware and process development tests in support of the DCC program were completed during the quarter. First, a two-stage sealing process for the primary pass-throughs was developed. The process involves a nicrobraze on the thermocouple sheaths with a Kryoflex glass-to-metal seal backing up the braze, sheath, and thermocouple insulation. The advantage of this approach is that two independent seals are effected on the one DCC component that has the highest probability of failure, that being the 10-mil-thick sheath for the 56 thermocouples in the primary. Additional development tests were performed with nicrobraze and S-glass in various environments expected in the experiment. Second, the D-test vessel has been assembled and welded closed. The vessel is being instrumented with strain gauges for the destructive pressure test. Based on actual experiment properties, the vessel is predicted to rupture at 15,000 to 20,000 psi. This is adequate to satisfy the minimum safety factor of 4 required for the 3,000 psi first experiment. Last, a small batch (1 kg) of the DCC-1 fuel was mixed to evaluate methods for determining
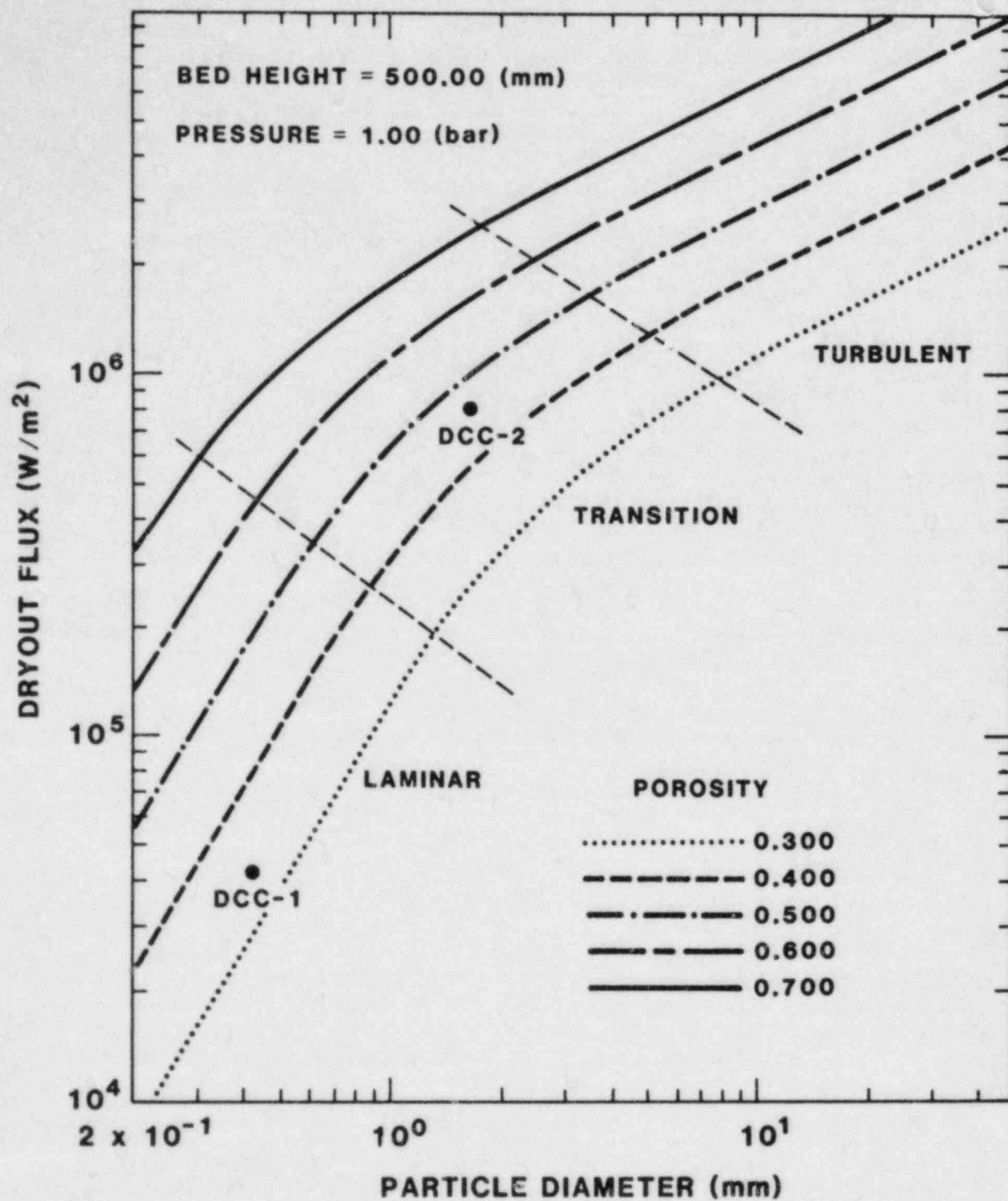
Figure 6.3-3. Predicted Dryout Heat Flux as a Function of Particle Diameter

porosity and identify any problems that may exist in maintaining a homogeneously mixed bed during the fuel loading process. Figure 6.3-4 shows photographs of a packed bed formed from the premixed batch. Even though the distribution was homogeneously mixed prior to pouring into the graduated cylinder, some areas of localized high porosity existed (evident at the 120-ml level in Figure 4), and a disproportionately high amount of large particles were present at the top of the bed. The solution to these localized zones of varying porosity will be to premix the DCC-1 bed (expected to be 25 to 30 kg) in small batches before forming the bed. The porosity for the packed bed shown in Figure 6.3-4 was determined using three methods:

1. Dry mass and volume; porosity = 33.6%.

2. Water displacement based on volumes; porosity = 34.1%.

3. Water displacement based on masses; porosity = 33.8%.

Due to limited experiment hardware and time, the remaining development test sequence has been revised. The planned out-of-pile systems test (OPST) was changed from a single electrically heated integral experiment to several well-defined, smaller scale tests to check performance of individual components and systems. For example, three of the individual systems tests and their purposes are: (1) an electrically heated primary leak test with 3000-psi helium at 623 K (350°C) to determine leak rate under extreme operating conditions, (2) an electrically heated closed primary and secondary system to confirm pressure-transducer response and to confirm no pressure generation mechanism (out-gassing, vaporization, etc.) in the secondary, and (3) an electrically heated test prior to nuclear heat to check out the performance of the helium/liquid-nitrogen cooling system in the final DCC-1 experiment configuration.

6.3.2 LWR Degraded-Core Coolability Analysis

6.3.2.1 Safety Calculations for DCC-1

Two safety calculations were performed for DCC-1. In the first, the heat flux required to dry out the wet annular region between the bed crucible and the walls of the primary vessel was calculated. Secondly, attempts were made to analyze thermocouple leak rates at low temperatures and pressures, in order to extend them to higher temperatures and pressures that might be encountered. The calculations are discussed in the following sections.

a. Calculation of Heat Flux to Dry Out Annular Region

Two methods were used for this calculation.

Method I

Method I uses Wallis' flooding correlation to predict the critical heat flux from the top of the annular section.[6-4]
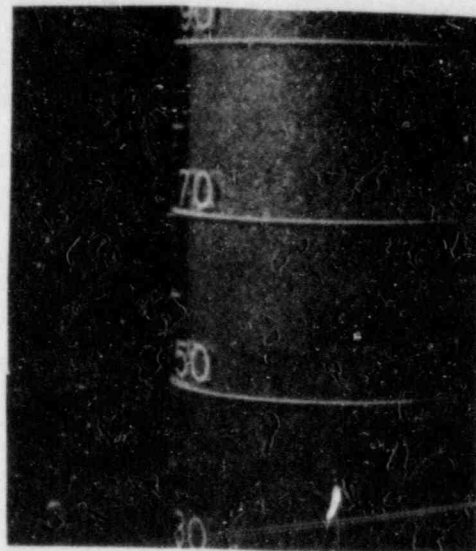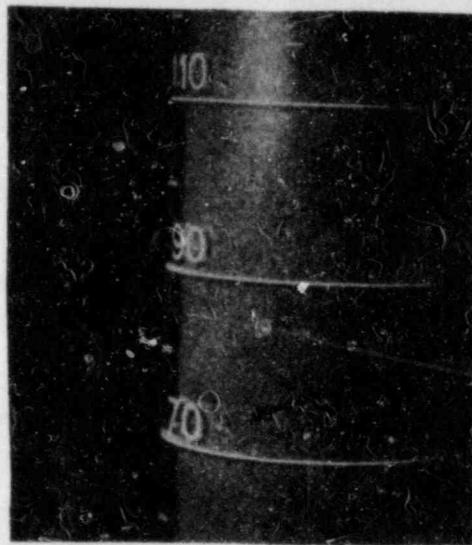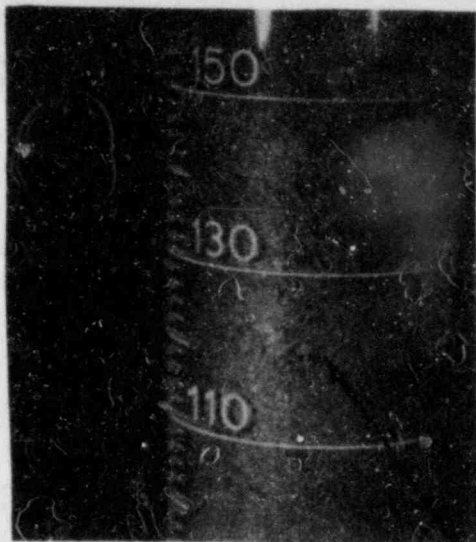
Figure 6.3-4.   Premixed 1-kg Batch of DCC-1 Fuel

144

$$Q = \frac{C^2 h_{fg} A \sqrt{\rho_g g \, \Delta\rho \, D}}{\left[1 + \left(\rho_g / \rho_f \right)^{1/4} \right]^2} \qquad (6.1)$$

where

D = hydraulic diameter,

C = entrance adjustment,

A = flow cross-sectional area

h_{fg} = heat of varporization of water,

ρ_g = density of water vapor,

$\Delta\rho = \rho_1 - \rho_g$

ρ_ℓ = density of liquid, and

g = gravitational constant.

Using a value of 1.1×10^{-3} m^2 for A, fluid properties of water at 100°C, and a hydraulic diameter of 4×10^{-3} mm, Equ. 6.1 yields:

$$Q = (C^2) \, (8.80 \text{ kW}) \qquad (6.2)$$

leaving Q = 4.62 kW for sharp-edged entrances and Q = 8.8 kW for rounded-edged entrances.

Method II

Method II uses a direct comparison with experiments in Ref. 6-4. With zero velocity forced flow, Q_o, the total heat flux was found to vary from 1.69 to 1.84 kW. By assuming that the flooding velocity (vapor flux) is independent of the annulus dimensions, the total heat flux required can be calculated to produce the same flooding velocity found in Ref. 6-4 by:

$$Q_{max} = \frac{Q_o \, A_{DCC}}{A_{exp}} \qquad (6.3)$$

where A_{DCC} = flow cross-sectional area of the DCC-1 experiment and A_{exp} = the flow cross-sectional area for the experiment of Ref. 6-4.

This yields:

$$Q_{max} = Q_o \, (5.5) \qquad (6.4)$$

and $Q_{max} \sim (9.3 \text{ to } 10.1)$ kW. These results are of the same order, although larger than those predicted by using the Wallis correlation.

The lowest value, 4.62 kW, should be used in the DCC-1 safety calculation.

b. Calculation of Heat Loss to Water

If a temperature difference exists across the insulator in the bed crucible, then the heat loss to the water in the annulus is calculated from

$$Q_{loss} = Ak \frac{\Delta t}{\Delta \chi} \tag{6.5}$$

where A = crucible surface area (0.34 m^2), k = insulator thermal conductivity (at highest expected temperature and pressure), and $\Delta \chi$ = thickness of the insulator (0.79×10^{-2}m).

Assuming that the water in the annulus is at the saturation temperature, the entire bed can be up to 873 K (600°C) higher than the water saturation temperature before the water surrounding the bed crucible will begin to boil out. Q_{loss} is equal to 4.62 kW, the lowest value estimated to produce flooding of the annular region.

c. Analysis of Thermocouple Sheath Leak Rate Tests

Attempts were made to analyze thermocouple leak rates at low temperatures and pressures, in order to extend them to higher temperatures and pressures that might be encountered during the experiment and provide an upper bond on leak rates expected.

For compressible, laminar, isothermal flow through a porous medium,

$$P^2 - P_o^2 = \frac{2\mu \bar{P}\bar{Q}\Delta \chi}{k A} \tag{6.6}$$

where

$\bar{Q}$ = volumetric helium flow rate, normalized to 1 bar pressure

$\bar{P}$ = pressure of helium volumetric flow, at 1 bar,

A = helium flow cross-sectional area,

k = permeability of porous medium,

μ = dynamic viscosity, and

$\Delta \chi$ = the length over the flow resistance is encountered.

For compressible, laminar, adiabatic flow through a porous medium,

$$P^{(1+\frac{1}{\gamma})} - P_o^{(1+\frac{1}{\gamma})} = \left(\frac{\mu}{k}\right) \left(1 + \frac{1}{\gamma}\right) \bar{P}^{(\frac{1}{\gamma})} \frac{\bar{Q}}{A} \Delta \chi \tag{6.7}$$

where $\gamma = \dfrac{C_p}{C_v}$. For helium, $\gamma = 1.6$, so

$$p^{1.6} - p_o^{1.6} = \frac{\mu}{k} (1.6) \bar{P}^{.6} \frac{\bar{Q}}{h} \Delta\chi \tag{6.8}$$

For compressible, turbulent, isothermal flow through a porous medium

$$p^2 = \frac{\bar{P} \bar{\rho}_{He} \bar{Q}^2 \Delta\chi}{\eta A^2} \tag{6.9}$$

where η = flow resistance.

For compressible, turbulent, adiabatic flow through a porous medium

$$p^{1.6} = \frac{\bar{P}^{.6} \bar{\rho} \bar{Q}^2 \Delta\chi}{\eta A^2} \tag{6.10}$$

Equations 6.6 through 6.10 are plotted schematically in Figures 6.3-5a and b. In Figures 6.3-5a and b, the upper lines are separated for different distances along which the resistance is measured. Comparing Figures 6.3-5a and b with c, it is apparent that for pressures below 50 psi, the flow is primarily turbulent, but the source of flow resistance operates over a constant length. For pressures above 50 psi, the cause of the flow resistance is no longer operative, and flow is being restricted in some other manner. To predict what will happen for higher pressure drops, more data is needed at higher pressures.

6.3.2.2 Development of MEDICI

Work continued on the development of MEDICI (the ex-vessel module for MELCOR and the LWR version of CONTAIN).[6-5] The following tasks were performed:

a. Review of models B and E.

b. Recommendations for modifications to models B and E to limit the motion of the quench front when there is little sensible heat in the bed.

c. Comments on the implications of fingering of liquid into the bed.

d. Assessment of further modeling requirements.

e. Recommendations for experiments to verify some model predictions.
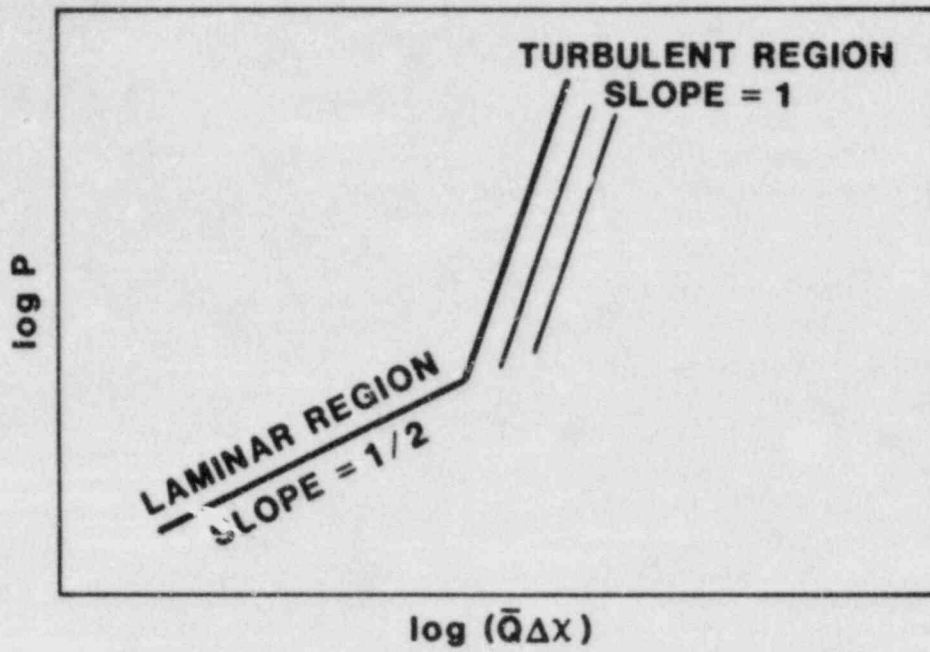
Figure 6.3-5a.   Isothermal Compressible Flow
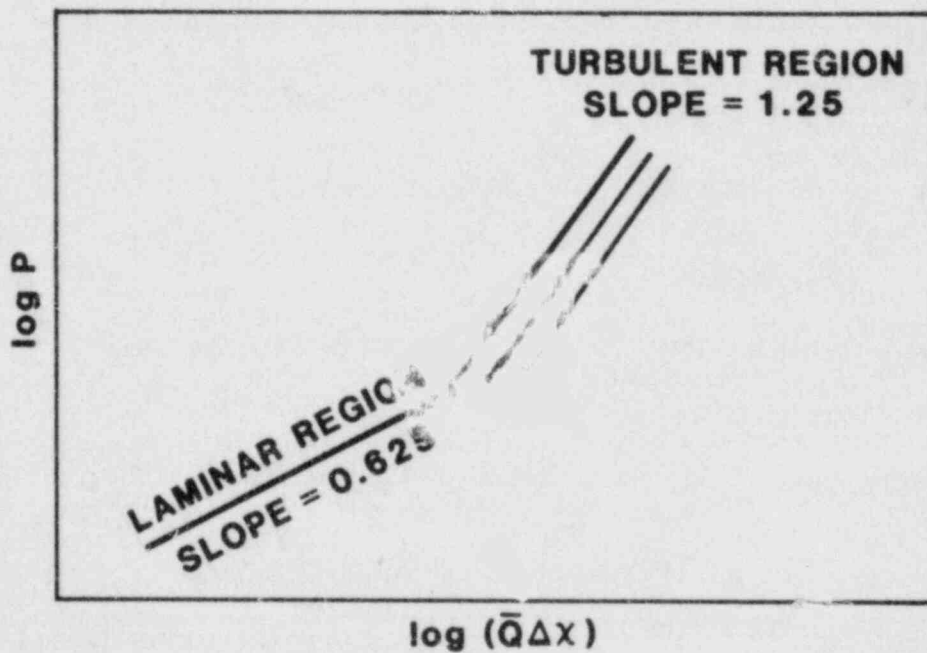
Figure 6.3-5b.   Adiabatic Compressible Flow
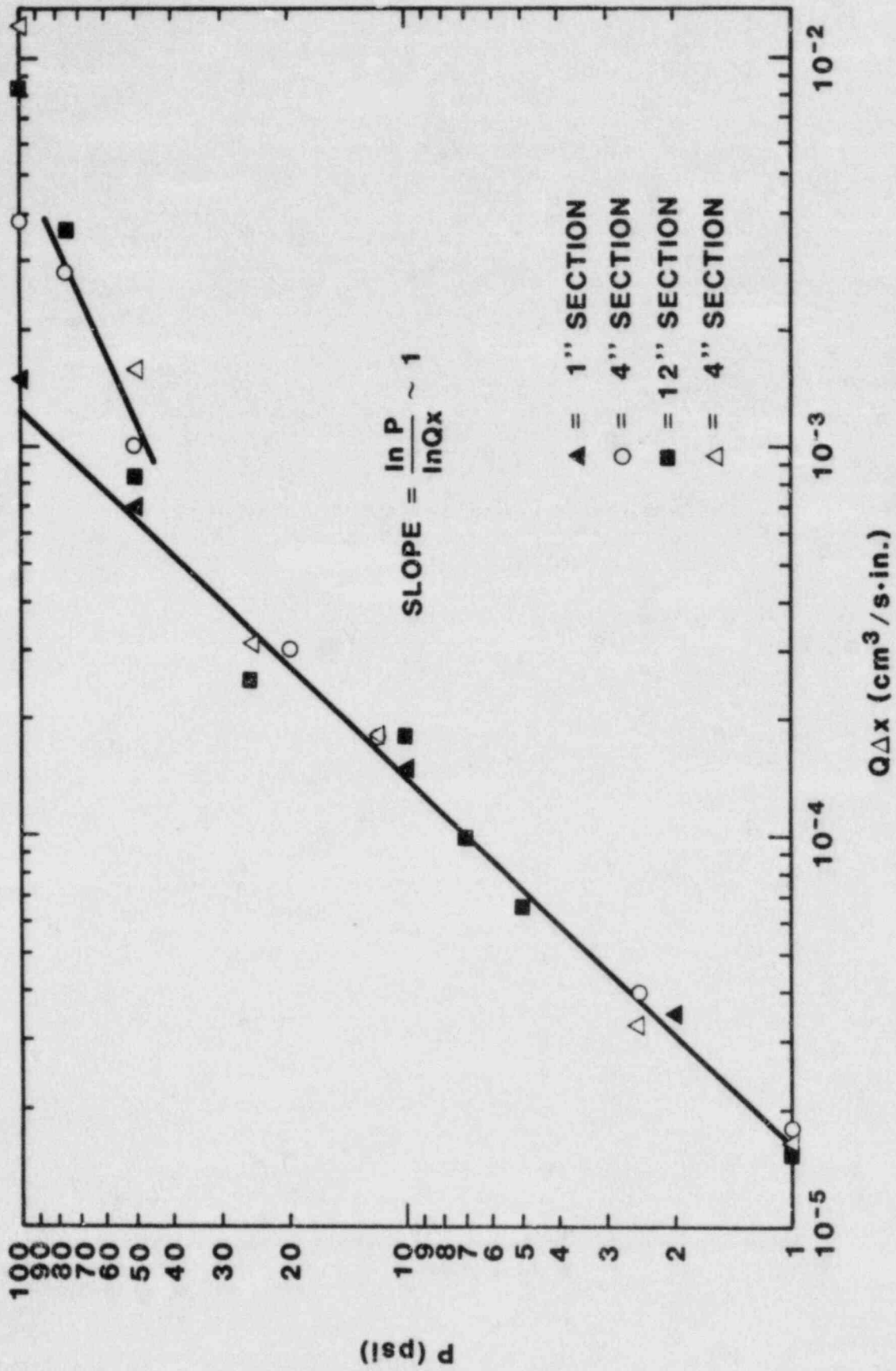
Figure 6.3-5c. Plotted Data

149

6.4 REFERENCES

6-1. D. E. Mitchell, M. L. Corradini, and W. W. Tarbell, _Intermediate Scale Steam Explosion Phenomena: FITS-A and MD-Series Experiments and Analysis_, NUREG/CR-2145, SAND81-0124 (Albuquerque, NM: Sandia National Laboratories, 1981).

6-2. R. J. Lipinski, "A One-Dimensional Particle Bed Dryout Model" _Transactions of American Nuclear Society_, 38:386-7, 1981.

6-3. E. D. Bergeron, K. R. Boldt, R. J. Lipinski, and P. A. Kuenstler, _LWR Severe Core Damage Phenomenology Program Plan, Volume 2: LWR Degraded Core Coolability Program_, SAND 82-1115 (Albuquerque, NM: Sandia National Laboratories, to be published).

6-4. K. Mishima and M. Ishii, _Critical Heat Flux Experiments Under Low Flow Conditions in a Vertical Annulus_, NUREG/CR-2647, ANL-82-6, p. 13 (Argonne, IL: Argonne National Laboratories, 1982).

6-5 E. Bergeron, "Summary of Debris Bed Calculations and Recommendations for MEDICI," Sandia National Laboratories Internal Memorandum to K. D. Bergeron, May 26, 1983.

7. TEST AND FACILITY TECHNOLOGY

7.1 ACRR STATUS

This section contains comments on the general status of overall ACRR operation and remarks concerning experimental activities involving the ACRR.

The ACRR is operating normally in support of weapons program research and advanced reactor safety experiments.

DISTRIBUTION:

US NRC Distribution Contractor
15700 Crabbs Branch Way
Rockville, MD 20850
    (370 Copies for R3 and R7)

US Nuclear Regulatory Commission (4)
Division of Accident Evaluation
Office of Nuclear Regulatory Research
Washington, DC 20555
Attn: C. N. Kelber, Assistant Director
          Advanced Reactor Safety Research
       R. T. Curtis, Chief
          Analytical Advanced Reactor Safety Research, ARSR.
       G. Marino, Chief
          Experimental Fast Reactor Safety
       R. W. Wright
          Experimental Fast Reactor Safety

R. W. Barber
US Department of Energy
Office of Nuclear Safety Coordination
Washington, DC 20545

US Department of Energy (2)
Albuquerque Operations Office
PO Box 5400
Albuquerque, NM 87185
Attn: J. R. Roeder, Director
          Operational Safety Division
       D. L. Krenz, Director
          Energy Research & Technology Division
          For: C. B. Quinn
                R. N. Holton

T. Ginsberg
Department of Nuclear Energy
Bldg. 820
Brookhaven National Laboratory
Upton, NY 11973

University of Michigan
Nuclear Engineering Department
Ann Arbor, MI 48104

General Electric Corporation (3)
Advanced Reactor Systems Department
PO Box 3508
Sunnyvale, CA 94088
Attn: K. Hikido, Mgr., Safety Engineering - M/C S-18
       D. M. Switick, Mgr., Plant Safety
       M. I. Temme, Mgr., Probabilistic Risk Assessment

DISTRIBUTION (Continued):

W. E. Myer
P.O. Box 1845
Idaho Falls, ID 83401

W. Tarbell
K Tech Corp
901 Pennsylvania NE
Albuquerque, NM 87110

Projekt Schneller Brueter (4)
Kernforschungszentrum Karlsruhe GMBH
Postfach 3640
D75 Karlsruhe
West Germany
Attn: Kessler (2)
       Heusener (2)

UKAEA Safety and Reliability Directorate (6)
Wigshaw Lane
Culcheth
Warrington WA3 4NE
Chesire
England
Attn: J. H. Gittus
       F. R. Allen
       A. R. Edwards
       F. Abbey
       M. J. Hayn
       R. S. Peckover

AERE Harwell
Didcot
Oxfordshire OX11 ORA
England
Attn: J. R. Matthews, Theoretical Physics Division

UKAEA (2)
Risley
Warrington WA3 6AT
Cheshire
England
Attn: B. Cowking, FRDD
       D. Hicks, TRDD

Dr. F. Briscoe
Culham Laboratory
Culham
Abingdon
Oxfordshire OX14 3DB
England

DISTRIBUTION (Continued):

Atomic Energy Establishment (2)
Winfrith,
Dorset DTZ 8DH
England
Attn: C. P. Gratton
       R. Potter

A. J. Manley
EG&G Idaho, Inc.
T.S.B.
LWR Fuel Research Div.
P.O. Box 1625
Idaho Falls, ID 83415

K. S. Norwood
Mail Stop B 12
Bldg 4500 N
Oak Ridge National Laboratory
P. O. Box X
Oak Ridge, TN 37830

Joint Research Centre (3)
Ispra Establishment
21020 Ispra (Varese)
Italy
Attn: R. Klersy
       H. Holtbecker
       P. Fasoli-Stella

Power Reactor & Nuclear Fuel
  Development Corporation (PNC) (3)
Fast Breeder Reactor Development Project (FBR)
9-13, 1-Chome, Akasaka
Minato-Ku, Tokyo
Japan
Attn: Dr. Watanabe

Sandia National Laboratories
1230   J. E. Powell
1231   T. P. Wright
1510   J. W. Nunziato
1530   L. W. Davison
1534   J. R. Asay
1541   H. C. Hardee
1830   M. J. Davis
1840   R. J. Eagan
1846   R. A. Sallach
1846   R. K. Quinn
2150   J. A. Hood
3141   C. M. Ostrander (5)
3151   W. L. Garner
6310   T. O. Hunter
6320   R. M. Jefferson

DISTRIBUTION (Continued):

6400	A. W.	Snyder
6410	J. W.	Hickman
6412	J. W.	Hickman (acting)
6415	D. C.	Aldrich
6420	J. V.	Walker (2)
6420	M. M.	Watkins
6420A	J. B.	Rivard
6421	T. R.	Schmidt
6421	K. R.	Boldt
6421	J. T.	Hitchcock
6421	G. W.	Mitchell
6421	C.	Ottinger
6422	D. A.	Powers
6422	J. E.	Brockman
6422	E. R.	Copus
6422	R. M.	Elrick
6422	J. E.	Gronager
6422	E.	Randich
6422	A. R.	Taig
6423	P. S.	Pickard
6423	A. C.	Marshall
6423	D. A.	McArthur
6423	K. O.	Reil
6423	S. A.	Wright
6425	W. J.	Camp
6425	D. R.	Bradley
6425	J. E.	Kelly
6425	R. J.	Lipinski
6425	P. K.	Mast
6425	M.	Pilch
6425	A.	Suo-Anttila
6425	A.	Wickett
6425	M. F.	Young
6427	M.	Berman (5)
6427	B. W.	Marshall
6427	L. S.	Nelson
6427	E. W.	Shepherd
6427	M. P.	Sherman
6427	S. R.	Tieszen
6427	C. C.	Wong
6430	N. R.	Ortiz
6440	D. A.	Dahlgren
6442	W. A.	Von Riesemann
6449	K. D.	Bergeron

DISTRIBUTION (Continued):

6450	J. A. Reuscher
6451	T. Luera
6452	M. Aker
6453	W. J. Whitfield
6454	G. L. Cano

7100	C. D. Broyles
7530	T. B. Lane (1)
	Attn: N. R. Keltner, 7537
	R. U. Acton, 7537
	T. Y. Chu, 7537
7550	F. W. Neilson (1)
	Attn: O. J. Burchett, 7552
	J. H. Gieske, 7552
8424	M. A. Pound

3. TITLE AND SUBTITLE	4. RECIPIENT'S ACCESSION NUMBER
Reactor Safety Research Quarterly Report, January-March 1983, Volume 25	
	5. DATE REPORT COMPLETED
	MONTH / YEAR

6. AUTHOR(S)	7. DATE REPORT ISSUED
Reactor Safety Research Program	MONTH March / YEAR 1984
	9. PROJECT/TASK/WORK UNIT NUMBER

8. PERFORMING ORGANIZATION NAME AND MAILING ADDRESS (Include Zip Code)	
Sandia National Laboratories Albuquerque, NM 87185	10. FIN NUMBER
	A-1016 etc.

11. SPONSORING ORGANIZATION NAME AND MAILING ADDRESS (Include Zip Code)	12a. TYPE OF REPORT
Division of Accident Evaluation Office of Nuclear Regulatory Research U.S. Nuclear Regulatory Commission Washington, DC 20555	Technical-Quarterly
	12b. PERIOD COVERED (Inclusive dates)
	January-March 1983

13. SUPPLEMENTARY NOTES

14. ABSTRACT (200 words or less)

Sandia National Laboratories is conducting, under USNRC's sponsorship, phenomenological research related to the safety of commercial nuclear power reactors.

The overall objective of this work is to provide NRC a comprehensive data base essential to (1) defining key safety issues, (2) understanding risk-significant accident sequences, (3) developing and verifying models used in safety assessments, and (4) assuring the public that power reactor systems will not be licensed and placed in commercial service in the United States without appropriate consideration being given to their effects on health and safety.

Together with other programs, the Sandia effort is directed at assuring the soundness of the technology base upon which licensing decisions are made.

This report describes progress in a number of activities dealing with current safety issues relevant to both light water and breeder reactors. The work includes a broad range of experiments to simulate accidental conditions to provide the required data base to understand important accident sequences and to serve as a basis for development and verification of the complex computer simulation models and codes used in accident analysis and licensing reviews. Such a program must include the development of analytical models, verified by experiment, which can be used to predict reactor and safety system performance under a broad variety of abnormal conditions.

Current major emphasis is focused on providing information to NRC relevant to (1) its deliberations and decisions dealing with severe LWR accidents, and (2) its safety evaluation of the proposed Clinch River Breeder Reactor.

15a. KEY WORDS AND DOCUMENT ANALYSIS	15b. DESCRIPTORS

16. AVAILABILITY STATEMENT	17. SECURITY CLASSIFICATION (This report)	18. NUMBER OF PAGES
GPO Sales and NTIS	Unclassified	177
	19. SECURITY CLASSIFICATION (This page) Unclassified	20. PRICE $

ORG.	BLDG.	NAME	REC'D BY*	ORG.	BLDG.	NAME	REC'D BY*

Sandia National Laboratories